INFORMATION TO USERS

This manuscript has been reproduced from the microfilm master. UMI films the text directly from the original or copy submitted. Thus, some thesis and dissertation copies are in typewriter face, while others may be from any type of computer printer.

The quality of this reproduction is dependent upon the quality of the copy submitted. Broken or indistinct print, colored or poor quality illustrations and photographs, print bleedthrough, substandard margins, and improper alignment can adversely affect reproduction.

In the unlikely event that the author did not send UMI a complete manuscript and there are missing pages, these will be noted. Also, if unauthorized copyright material had to be removed, a note will indicate the deletion.

Oversize materials (e.g., maps, drawings, charts) are reproduced by sectioning the original, beginning at the upper left-hand corner and continuing from left to right in equal sections with small overlaps. Each original is also photographed in one exposure and is included in reduced form at the back of the book.

Photographs included in the original manuscript have been reproduced xerographically in this copy. Higher quality 6" x 9" black and white photographic prints are available for any photographs or illustrations appearing in this copy for an additional charge. Contact UMI directly to order.

UMI

A Bell & Howell Information Company
300 North Zeeb Road, Ann Arbor MI 48106-1346 USA
313/761-4700 800/521-0600

UNIVERSITY OF OKLAHOMA

GRADUATE COLLEGE

A COMPREHENSIVE GEOLOGICAL, GEOCHEMICAL, AND PETROGENETIC STUDY OF HOTSPOT RELATED OCEANIC BASALT-RHYOLITE SERIES ROCKS FROM ASCENSION ISLAND, SOUTH ATLANTIC OCEAN

A Dissertation
SUBMITTED TO THE GRADUATE FACULTY
in partial fulfillment of the requirements for the
degree of
Doctor of Philosophy

By

ADITYAMOY KAR
Norman, Oklahoma
1997

A COMPREHENSIVE GEOLOGICAL, GEOCHEMICAL, AND PETROGENETIC STUDY OF HOTSPOT RELATED OCEANIC BASALT-RHYOLITE SERIES ROCKS FROM ASCENSION ISLAND, SOUTH ATLANTIC OCEAN

A Dissertation APPROVED FOR THE

SCHOOL OF GEOLOGY AND GEOPHYSICS

BY

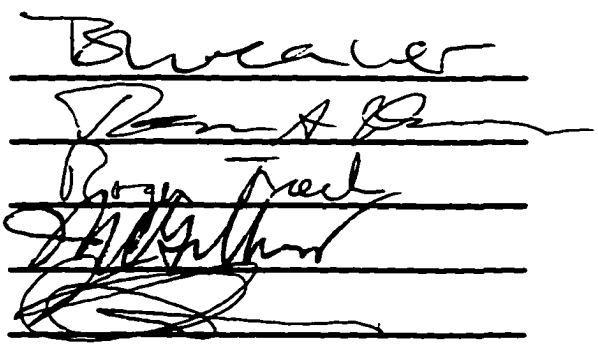

Acknowledgements

First and foremost I thank my parents, Mr. Kalyan Moy Kar and Dr. Minati Kar, and my brother, Mr. Anandamoy Kar for believing in me, supporting me all through these years of hard work, encouraging every new step I took in life, and loving and caring for me for what I am.

I extend my heartfelt thanks to the Chair of my Ph.D. committee, Dr. Barry Weaver, who has taught me "igneous geochemistry" and at the same time extended his friendship to me. From my initial days in Oklahoma to these last minute of my dissertation writing he has been by the side of me, has supported me financially, and through his National Science Foundation grant I was able to travel to a remote island in the middle on South Atlantic Ocean, Ascension, which is the topic of my dissertation. I also came to know through Barry some unique people on Ascension called "Saints" whose friendship during the two summer fieldtrips I would never forget. I have tremendous respect and admiration for Dr. Weaver as a scientist, person, and a friend. If I had to do it over again (not in this life but as Indian I have more to come), I would gladly choose Dr. Weaver as my advisor (I am not sure if its true the other way round or not!).

Dr. Charles Gilbert, Chairman of the School of Geology & Geophysics and also my committee member has always helped me every time I have approached him. I have been to several field trips with him and have benefited tremendously from his knowledge. I acknowledge his support and all the opportunity he has given me. I extend my regards to him.

I thank my other committee members, Dr. David London, Dr. Thomas Dewers (my squash partner), and Dr. Roger Frech for their comments and suggestions.

Dr. Jon Davidson from UCLA has been like my second advisor. I spent two summers with him on Ascension and then a month in UCLA in his lab. His belief in me, his comments, and his wit has made this dissert.ation work full of fun and a leaming experience.

I also thank my new employer, Dean of School of Arts & Sciences, Dr. Isaac J. Crumbly at Fort Valley State University in Georgia for believing in me and giving me a chance to teach geology and explore new opportunities in academics and research. The friends I have made in Georgia, Ms. Jackie Hodges, Dr. Singli Garcia, Ms. Vickie Halbert, and Mr. James Brown makes teaching fun and life enjoyable.

Last but not the least I thank all my friends at the School of Geology and Geophysics. Dr. John and Karen Hogan, the American family I have known for the longest time; they have been wonderful friends and have lend a helping hand during the most distressing times. Dr. Sanjay Banerjee, Mr. Sankar Muhuri, and Ms. Satavisa Sarkar, are friends whose help and friendship I cannot elucidate in words. Mr. Jon Price, Ms. Donna Montgomery, Ms. Sara Moody, Ms. Patti Mershon, Ms. Shirley Blanchard, and Mr. Bill Buchanan have also been wonderful friends and have extended their helps at all times. I enjoyed every moment being all these great people.

I also thank the School of Geology and Geophysics for the financial support. A part of this dissertation was supported through NSF grant EAR-9204079.

Table of Contents

Title page i

Signature page ii

Copyright page iii

Acknowledgements iv

Table of Contents v

Abstract vii

Chapter IA

Introduction 1-1

Chapter IB

Regional Tectonic Setting 1-8

Chapter IC

Geology of Ascension Island 1-11

Chapter II

Small-scale mantle heterogeneities: Evidence from incompatible element and isotopic ratios of mafic volcanic rocks of Ascension Island, South Atlantic Ocean 2-1

Chapter III

Felsic oceanic island magmatism: Origin of high $^{87}Sr/^{86}Sr$ evolved volcanic and plutonic rocks from Ascension Island, South Atlantic Ocean 3-1

Chapter IV

Geochemical characteristics of borehole samples recovered from Ascension Island, South Atlantic Ocean 4-1

Chapter V

Anomalous phosphorous behavior in OIB basalt and hawaiite from Ascension Island, South Atlantic Ocean: Evidence of apatite resorption during low pressure crystal fractionation 5-1

Chapter VI

Mafic clasts with unusual REE patterns in felsic volcanic rocks: Evidence of subsolidus alteration of mafic rocks from Ascension Island, South Atlantic Ocean .. 6-1

Chapter VII

CONCLUSIONS 7-1

Appendix 1 XRF, INAA, radiogenic, & stable isotope analytical procedures & techniques A1-1

Appendix 2 Location of rock samples collected from Ascension Island A2-1

Appendix 3 Petrographic (thin-section) study of Ascension rocks A3-1

Appendix 4 Major element, trace element, radiogenic & stable isotope data A4-1

Abstract

The mafic rocks (basalt-hawaiite-mugearite-benmoreite) of Ascension Island form four distinct groups: low Zr/Nb hawaiite, high Zr/Nb basalt, intermediate Zr/Nb basalt to benmoreite, and Dark Slope Crater (DSC) hawaiite and mugearite.

The geochemical characteristics of the felsic rocks are largely consistent with an origin by fractional crystallization of high Zr/Nb mafic magmas (identical $^{143}Nd/^{144}Nd$ and similar Pb isotopic ratios). Syenite, monzonite, and granite xenoliths are cumulate rocks from, and intrusive equivalents of, fractionating felsic magmas. Internal (mineral) isochrons for two granite xenoliths give ages of ~1.0 Ma. Most of the felsic volcanic rocks and granite are also characterized by high $^{87}Sr/^{86}Sr$ (> 0.706) compared to mafic rocks ($^{87}Sr/^{86}Sr < 0.703$), although $^{143}Nd/^{144}Nd$ of the felsic rocks is similar to that of the low $^{87}Sr/^{86}Sr$ mafic lavas; elevated $^{87}Sr/^{86}Sr$ suggests interaction of the felsic rocks with geothermal fluids derived from seawater under subsolidus conditions. In addition, evidence for the involvement of a high $^{87}Sr/^{86}Sr$ component during magmatic differentiation is also provided by the high initial $^{87}Sr/^{86}Sr$ of the granitic xenoliths, and of high $^{87}Sr/^{86}Sr$ (> 0.704) in some of the feldspar phenocrysts from felsic rocks. $d^{18}O$ ranges of +5.5 to +8.1‰ (whole rock) and +5.5 to +7.2‰ (feldspar) in the felsic rocks also indicate the involvement of a high $d^{18}O$ component, and suggest that hydrothermally-altered pre-existing volcanic basement may have been cannibalized during felsic magma differentiation.

Crystal fractionation controls compositional variation within each mafic group, however, it cannot be the cause of the differences between the groups. The high and intermediate Zr/Nb groups have similar Sr-Nd-Pb isotopic characteristics and were derived from the same mantle source (HIMU-type). The low Zr/Nb and DSC groups have different radiogenic isotopic characteristics due to contributions from enriched

mantle components (HIMU-type). The dominant component, present in the high, intermediate, and low Zr/Nb groups, has the composition of the St. Helena hotspot and has mixed to varying degrees with the depleted upper mantle. The more minor component, present only in the DSC group and some intermediate Zr/Nb samples, has higher $^{208}Pb/^{204}Pb$ relative to $^{208}Pb/^{204}Pb$ than the St. Helena hotspot. This component may be of local lithospheric origin.

Chapter IA
Introduction

The majority of the world's volcanism occurs at convergent or divergent plate boundaries. A small yet significant amount of volcanism, however, occurs within the interior of the continental and oceanic plates; that occurring on the oceanic plates forms some of the world's largest volcanic structures in the Atlantic, Pacific, and Indian Oceans. This intra-plate volcanism is associated with localized regions of anomalous heat sources in the Earth's mantle and voluminous magma production called hotspots which can be situated under oceanic or continental lithosphere. Hotspot-related volcanism, especially that occurring in the interior of oceanic plates, is one of the best means to study the composition of the mantle of the Earth as those coming through the oceanic plates are less contaminated as compared to the continental crust, during their ascent from their deep mantle source through the thin oceanic lithosphere to the surface of the Earth. The volcanic rocks of hotspot oceanic islands, called ocean island basalt (OIB), have crystallized from mantle derived magmas produced by decompression melting of upwelling "mantle plumes". Questions still exist as to exactly where "plumes" originate within the Earth, at the upper to lower mantle boundary or the core-mantle boundary? Questions also exist about the nature of the "plumes" - are they "thermal plumes" and/or "chemical plumes"?

Hotspot volcanic rocks have major chemical differences compared to mid-oceanic ridge basalt (MORB). They typically are SiO_2 undersaturated and mildly alkaline with the degree of undersaturation being very variable with rocks ranging from alkali basalt to trachyte and comendite, and basanite to phonolite (Harris, 1983; Hoernle & Schmincke, 1993; le Roex et al., 1990). Tholeiite is erupted on some oceanic islands (e.g., Hawaii

and Gran Canaria), however, the geochemistry is distinct from tholeiite erupted at mid-oceanic ridges. The more evolved compositions (trachyte and phonolite) found on oceanic islands generally are considered to be produced by low pressure fractional crystallization from parental mafic magmas (Harris, 1983; le Roex, 1985; Weaver, 1990).

Mantle heterogeneity

Numerous studies in the last few decades on the major and trace element geochemistry and isotope characteristics of hotspot-related magmatism have thrown light on the chemical heterogeneities that exist amongst the mantle derived intra-plate volcanic rocks from different parts of the world. Hart (1988) puts forward some intriguing questions regarding mantle heterogeneity - how many discrete mantle domains exist, where are they located, and how do they form? Are chemical heterogeneities being created faster than they are being convectively destroyed? Do primitive, chemically undifferentiated reservoirs still exist on Earth? There are many models that have been envisioned to account for the sources of OIB magmas, ranging from melting of a chemically primordial lower mantle (?), melting of ancient subducted oceanic crust (Dupuy et al., 1989; Hofmann & White; 1982; Weaver, 1991; Weaver et al., 1986; Weaver et al., 1987; Woodhead & McCulloch, 1989), melting of ancient sub-continental lithosphere in the deep mantle (Davies et al., 1989; McKenzie & O'Nions, 1983), components of recycled sediment in OIB genesis (Weaver, 1991), or a combination of some or all of the above mentioned processes.

White (1985) subdivided the mantle source for oceanic basaltic rocks into five distinct groups based on their radiogenic isotopic (Sr, Nd, and Pb) characteristics. These groups are represented by MORB, St. Helena, Keguelen, the Society Islands, and the Hawaiian Islands and may represent different but internally heterogeneous

mantle reservoirs or merely distinct groups within which chemical evolution has proceeded in a similar manner (White, 1985). The primitive mantle is identifiable in the Sr, Nd, Hf, and Pb isotope characteristics of only the Hawaiian source. The evolution of St. Helena-type sources remains enigmatic. White (1985) acknowledges the existence of multiple reservoirs in the mantle and that several processes have been involved in their evolution.

Two contrasting models have been suggested for convection in the mantle; Loper (1985) proposed a mantle-wide single cell convection model whereas independent convection cells in the upper and lower mantle have been proposed by Richter & McKenzie (1981). In the latter model, the upper mantle consists of depleted material (the MORB source) and is underlain by a primitive lower mantle. The two layers are convectively isolated, and chemical transfer between them is limited. Part of the subducted oceanic crust (along with part of its sedimentary veneer) sinks to the bottom of the upper mantle, where it becomes embedded in the convective boundary layer between the upper and lower mantle. The remainder of the subducted oceanic crust is recycled into the upper, depleted layer where it is eventually homogenized by convective mixing, but small volumes may survive for upto 10^9 years. These small heterogeneities may be the source of some anomalous regions of mid-ocean ridges and isolated seamounts. Long-lived hotspots are the result of mantle plumes rising from the convective boundary layer. These instabilities result from both internal heating (due to a relatively high K, U, and Th abundance) and heating from below. More rarely, plumes composed of primitive material may rise directly from the lower mantle.

OIB characteristically are enriched in incompatible trace elements, and have high abundance of Rb, Ba, Th, Nb, etc., and generally are enriched in light rare earth elements (LREE) relative to heavy rare earth elements (HREE). This enrichment

requires OIB magmas to be derived from an enriched mantle source very different to the MORB source. Some distinctions in the trace element characteristics of the OIB end-members have been recognized by Palacz and Saunders (1986), Weaver et al. (1986, 1987), Loubet et al. (1988), Saunders et al. (1988) and Weaver (1991). Zindler and Hart (1986), Hart (1988), and Weaver (1991a,b) report three distinctive OIB sources (HIMU, EMI, and EMII) that exist in the suboceanic mantle. OIB with unusually radiogenic Pb isotope ratios are derived from a source with a high $^{238}U/^{204}Pb$ (HIMU source), whereas OIB with unusually radiogenic Sr and unradiogenic Nd isotope ratios are derived from mantle sources (EMI and EMII) enriched in large ion lithophile elements (LILE) and LREE (Weaver, 1991a). Weaver (1991a) suggests that oceanic crust subducted into the mantle forms the major component in the OIB magma source, with HIMU OIB sources being pure basaltic crust compared to EMI and EMII OIB sources which contain variable amounts of pelagic and terrigenous sediment, respectively, together with the very old (1 to 2 Ga) recycled oceanic crust. In addition to the three mantle sources for OIB, Hart (1988) identifies a fourth mantle component that exists with unusually low $^{87}Sr/^{86}Sr$ and high $^{143}Nd/^{144}Nd$ which is the MORB source, the depleted MORB mantle (DMM).

Hart (1988) addresses the generation of the different mantle components. The MORB source is depleted in incompatible elements, with the missing budget of these elements now largely residing in the continental crust. The exact pathway(s) by which these elements have migrated from the upper mantle into the crust involves both melt removal processes occurring at spreading centers, and melt-fluid extraction processes occurring in subduction zones.

Zindler and Hart (1986) proposed explanations for the existence of large-scale and small-scale chemical heterogeneity in the mantle. Large-scale chemical heterogeneities

(similar in scale to the depth of the convecting layer) require very long time scales for dispersal and will likely persist for the age of the Earth. Small-scale chemical heterogeneities will be mixed over "regional" volumes on time scales significantly shorter than the age of the Earth. Total destruction of even the smallest scale chemical heterogeneities depends on chemical diffusion. Zindler and Hart (1986) contended that convective isolation is not necessary to preserve ancient mantle heterogeneity. They propose: (1) that kilometer-size chemical heterogeneities can survive diffusive equilibration for billions of years, even in the presence of a melt phase. The situation for the rare gases is not drastically different than that for other elements. (2) The mantle is chemically heterogeneous on both very small (10 m) and very large (>1000 km) scales. (3) Isotopic heterogeneities in the mantle require the existence of four "end-member" components (DMM, HIMU, EMI, and EMII) and are consistent with the existence of at least two additional components, bulk silicate Earth (BSE) and prevalent mantle (PREMA). BSE is defined as the primitive, undifferentiated segment of the Earth's mantle and PREMA represents isotopic compositions of ocean islands and enriched MORB, which are intermediate between the DMM, BSE, HIMU, and EM components (Zindler & Hart, 1986).

The Azores hotspot in the North Atlantic Ocean is an example of heterogeneity on a single island scale. Davies et al. (1987) propose that away from the influence of hotspots, the isotope composition of MORB tends to be relatively constant. In the proximity of hotspots, MORB develops the chemical and isotopic signatures of hotspot volcanism (e.g., South Atlantic, Hanan et al., 1987). Davies et al. (1987) further propose that MORB and hotspot reservoirs are generally isolated from each other. The presence of Northern Hemisphere Reference Line (NHRL), HIMU, and DUPAL (Dupre & Allegre) signatures in the Azores magmas demonstrates their source region to be

extremely heterogeneous. Woodhead and McCulloch (1989) present evidence from Pitcairn Island in the southeast Pacific Ocean of small length-scale (~10 km) chemical heterogeneities in ocean islands.

South Atlantic Ocean mantle heterogeneity

It is, therefore, well established that the Earth's mantle in general is chemically heterogeneous (Sun & McDonough, 1989; Zindler & Hart, 1986). Hotspot-related magmatism produces rocks which are extremely diverse in their geochemistry. Volcanic and plutonic rocks from the hotspot-related islands of the South Atlantic Ocean illustrate this diversity in Sr-Nd space (Fig. 1.1). This chemical diversity suggests that large-scale chemical heterogeneity on the scale of hundreds or thousands of kilometers exists in the suboceanic mantle (White, 1985, Allegre et al., 1987, Hart, 1988). Major geochemical diversity is also increasingly being noted in OIB from individual oceanic islands, implying that heterogeneities also exist in OIB sources on small (kilometer) scales (Dupre et al., 1982, Weaver et al., 1987: Woodhead and McColloch, 1989; Barling and Goldstein, 1990; Halliday et al., 1992). The significant variation in the Pb isotope composition of samples from individaul hotspot-related South Atlantic Ocean islands (Fig. 1.1) substantiates the presence of small-scale chemical heterogeneities in the mantle.

Ascension Island mantle heterogeneity

A substantial geochemical data base now exists for hotspot-related ocean island basalt (OIB) from different parts of the world (Budhan and Schimtt, 1985; Bohrson and Reid, 1995; Clague and Frey, 1982; Dupre et al., 1982; Harris, 1983; Hoernle and Schmincke, 1993; Loubet et al., 1988; Harris and Sheppard, 1987; Weaver et al., 1991; Weis, 1983; West and Leeman, 1994; White, 1985). Yet, prior to this study, Ascension

Island, situated at 7°56'S and 14°22'W in the South Atlantic Ocean, had not been comprehensively studied. This is the first project that aims at a comprehensive volcanological, geochemical, and petrogenetic study of the hotspot-related volcanic rocks of Ascension Island. Some data exist on the surface and subsurface geology, mineralogy, geochemistry, fluids associated with magmatism, and age of the different varieties of rocks and plutonic xenoliths of Ascension Island (Atkins et al., 1964; Baker, 1973; Roedder & Coombs, 1967; Harris & Bell, 1982; Harris et al., 1982; Harris, 1983; Weis, 1983; Harris, 1985; Sheppard & Harris, 1985; Harris & Sheppard, 1987; Weis et al., 1987; Adams, 1996; Nielson & Sibbett, 1996; Nielson & Stiger, 1996). These studies show there to be substantial diversity within the geochemical data. Volcanic rocks from Ascension Island have radiogenic Nd isotope compositions ($^{143}Nd/^{144}Nd$ of 0.5130 to 0.5131) which are similar to the compositions of MORB magmas erupted from the MAR in the South Atlantic Ocean (Weis et al., 1987). Ascension volcanic rocks have low $^{87}Sr/^{86}Sr$ similar to St. Helena, and Pb isotope compositions similar to Fernando de Noronha, Trindade, and Bouvet (Weis, 1983; Weis et al., 1987). A suite of gabbroic xenoliths from Ascension have much lower $^{206}Pb/^{204}Pb$ (17.9 to 18.8) than the volcanic rocks and there is particularly wide isotopic diversity among the volcanic and plutonic rocks of Ascension Island (Harris et al., 1982; Weis 1983). The present study confirms the diversity that exists in the mantle and is directed to understand the cause of this variation in the geochemical data and its implications for large-scale and small-scale mantle chemical heterogeneities, as reflected in the petrogenesis of mafic and felsic volcanic and plutonic rocks of Ascension Island.

Chapter 1B

Regional Tectonic Setting

Ascension Island is situated at 7°56'S and 14°22'W in the South Atlantic Ocean (Fig. 1.2) and is located about 80 km west of the median valley of the Mid-Atlantic Ridge (MAR) and about 50 km south of the Ascension Fracture Zone (AFZ, Fig. 1.2). The AFZ is the first large right lateral offset of the MAR south of the equator. The Ascension hotspot is located 225 km southeast of Ascension Island at 9°50'S and 13°20'W (not under Ascension Island) and has produced two seamount chains (Fig 1.3). One chain, to the east, follows the trend of Fracture Zone A and the small offset slightly to the south and includes two seamounts near the MAR and a large topographic bulge 450 km east of the ridge. The second chain includes Ascension Island, which sits on 5- to 6-Ma-old oceanic crust, and two large seamounts (Seamount A and Seamount B) that are 300 km and 610 km west of Ascension Island, respectively, and sit on oceanic crust that is 20 and 36 Ma old, respectively, and are on the same spreading flow line (Fig. 1.4). The evidence for this hotspot includes: (1) the existence of Ascension Island and the two seamounts to the west; (2) a 500 to 700 m positive ridge crest anomaly and lack of a well defined rift valley in historical bathymetric data of this region; (3) the marked lack of seismicity along the central anomaly, from 8°30'S to 10°S; (4) a seamount reaching to within 72 m of the surface located at 9°14'S 12°50'W and several large seamounts to the east; and (5) a spike in La/Sm and Nb/Zr of MORB dredge samples from the MAR at 9°45'S (Schilling & Thompson, 1983; Schilling et al., 1985). The two seamounts are similar in size to Ascension Island. The three major volcanic edifices were produced by the hotspot but do not mark the trail of the South

American plate over a fixed hotspot. The model requires that the spreading axis resided relatively close to the hotspot for the past 36 Ma. The seamounts were produced by the channeled subaxial flow of the excess basaltic melt beneath the MAR. This flow is dammed by the older and thicker crust encountered at the Ascension Fracture Zone leading to an excess of volcanism at the intersection of the spreading axis and the fracture zone. This mechanism explains why the seamounts are along a flow line close to the fracture zone rather than marking a hotspot trail. The fact that the three lie along a flow line requires the South American plate to have no north-south component of motion over the mantle for the past 36 Ma or so, if the hotspot is under Ascension. This would also leave the other seamount chain unexplained. Brozena (1986) proposes that, taking into account subsidence and ignoring erosion, seamounts A and B were both islands approximately 1000 m high, similar to Ascension Island.

The hotspot influences the MAR for approximately 450 km from the Ascension Fracture Zone to the Bode Verde Fracture Zone (Fig. 1.3). The effects of the hotspot on the MAR include an anomalously shallow ridge axis with a poorly defined rift valley and a lack of seismicity. The additional heat and magma available from the hotspot give this section of the MAR a structure more typical of fast spreading ridges such as the East Pacific Rise (Brozena, 1986).

Hotspots near, but not on ridge axes channel a portion of the upwelling asthenosphere to the ridge crest. The effect once the material is channeled to the ridge is the same as if the hotspot were located beneath the ridge, although the volume of material may be reduced. Ascension Island may, in fact, be a third type of hotspot island in which the hot plume material is first channeled along the base of the lithosphere to a spreading axis and then flows along the axis to a fracture zone. The flow is dammed at this point and a seamount is formed at a considerable distance from

the hotspot. This process may be responsible for some of the many seamounts and ridges which occur along fracture zones (Brozena, 1986). This feature is well documented between 8°S and 10°S; the plume has a strong influence on the isotopic and trace element ratios of N-MORB, especially Pb and La_N/Sm_N, which are much higher in the plume source compared to the N-MORB (Fontignie & Schilling, 1996).

Ascension and the 20 Ma seamount were probably formed by the damming of plume material which has been channeled along the ridge crest by the Ascension Fracture Zone. Their locations therefore do not correspond to plate motion over a fixed hotspot (Brozena, 1986). On the other hand, the 36 Ma seamount to the west was probably formed over the hotspot (Brozena, 1986). The seamount chains oriented along fracture zone trends can be produced only while the hotspot is sufficiently near the MAR to supply excess melt. This period may be extended by flow toward the ridge of hot material from the hotspot along the base of the lithosphere. The hotspot causes temporal as well as spatial variability by episodic activity. Volcanic events seem to occur for a few Ma separated by about 10 to 15 Ma of inactivity. This implies that the ridge crest morphology and the topography which is rafted away from the ridge may also be affected episodically, thus alternating in type from normal slow spreading to fast spreading (Brozena, 1986).

Chapter IC

General Geology of Ascension Island

Introduction to Geology of Ascension Island

Ascension Island has a very varied topography (Fig. 1.4). The island has a steep, rugged eastern half and much flatter, less rugged western half. In the eastern half, the island rises from the coast to the tallest peak of the island, Green Mountain (859 m elevation) which is made up of massive, thick pyroclastic (mostly pumice) deposits with the southwestern flanks mostly consisting of trachyte. The western half of the island is covered by lava plains of mostly aa flows (only one pahoehoe flow was identified) punctuated by scoria cones, some of which rise to considerable heights (Fig. 1.4).

The exposed volcanic rocks on the island comprise transitional to mildly alkaline basaltic-trachytic series lava flows, trachytic domes, scoria cones, and pyroclastic deposits. The geological map presented in this section (Fig. 1.5 and Fig. 1.6) is modified after Nielson and Sibbett (1996). Essential modifications that were made include adding geochemical classification of the different rock types from detailed compositional data from the present study, and changing and adding a number of flow boundaries to separate flows of different geochemical characteristics.

Ascension Island is a composite volcano with in excess of fifty scoria cones scattered over the island (Fig. 1.7; Table 1.1). Pyroclastic (pumice and scoria) deposits make up about 43% of the island's total areal extent. Prior to this study, the pyroclastic deposits have been uncharacterized. The largest scoria cones occur in the central to southwestern to south-central parts of the island (Fig. 1.4). Some of the scoria cones rise above 305 m in height, with the highest cone (Mountain Red Hill) reaching a height

of 546 m above sea level. The scoria varies in size, vesicularity content, and freshness. Some scoria is extremely fresh, while other scoria is moderately to heavily oxidized. The scoria generally is fine-grained, although phenocrysts can be identified in some scoria deposits. In general, the scoria cones are asymmetric with a gentle northwestern flank and a steep southeastern flank due to the South East trade winds that blow over the island. At the waning stages of cone activity breach flows have erupted from the thinned, weakened southeastern flank of some of the scoria cones. These breach flows are of variable volume and areal extent.

Other than pyroclastic deposits, most of the island is covered by mafic lava flows and felsic lava flows and flow domes. The mafic flows, wherever traceable, are found to emanate from a scoria cone. Some of the smaller scoria cones are associated with tongue-shaped flows of small spatial dimensions. The flows range in chemical composition from basalt through hawaiite and mugearite to benmoreite. Basalt and hawaiite flows are more common than any other variety of mafic and felsic flows. Some of the youngest geological features of the island are hawaiite flows related to the Sisters Peak and South Gannet Hill and these flows may have been erupted within the last few hundred years (Atkins et al., 1964). A few mugearite flows occur in the north-central part of the island. In the northern part of the island three cones (Cones ; Fig. 1.7) form a linear NW-SE trending chain and have each erupted benmoreite breach flows. The western most of these cones, termed Broken Tooth (Fig. 1.7) has erupted both mugearite and benmoreite lava flows that contain xenocrysts disaggregated from entrained syenite xenoliths (Harris & Bell, 1982). There are two distinctive felsic eruptive centers on the island - 1) the central complex is comprised of the Middleton Ridge felsic center and Green Mountain (Fig. 1.6). Middleton Ridge is composed primarily of trachyte, pumice, and some rhyolite and rhyolitic obsidian; 2) the eastern

part of the island is made up mostly by trachyte flows and lava domes (Fig. 1.6), most noticeable of which is a voluminous trachyte flow in the northeastern part of the island tha originated from Devil's Cauldron and flowed northward and eastward.

Previous work on Ascension Island

Ascension Island was discovered in 1501 but regular human settlement started only in 1815. Since 1815, numerous expeditions have touched the shores of Ascension but not until Darwin visited the island was a scientific and geological investigation conducted on Ascension. Darwin made some excellent scientific observations and this classic work was published in 1844. Daly (1925) studied the island's geology in great detail and his article is the first detailed geological document on Ascension Island. Since then various people have investigated the island's geology in an attempt to characterize the volcanic and plutonic rocks. They include Atkins et al. (1964), Roedder and Coombs (1967), Baker (1973), Harris & Bell (1982), Harris et al. (1982), Harris (1983), Weis (1983), Harris (1985), Sheppard and Harris (1985), Harris & Sheppard (1987), Weis et al. (1987), Weaver et al. (1987), Adams (1996), Nielson and Sibbett (1996), and Nielson and Stiger (1996).

Detailed geology of Ascension Island

The most widely exposed rocks of Ascension are basalt and hawaiite lava flows. Compared to these more mafic rocks, lesser volumes of mugearite and benmoreite are present on the island. Trachyte and rhyolite are more abundant than rocks of mugearitic and benmoreitic compositions. A description of the detailed geology of the exposed rocks of Ascension follows. For the location and characteristics of the scoria cones refer to Table 1.1 and Fig. 1.7, for the distribution of the different mafic rocks refer to Fig. 1.5, and for the distribution of the felsic rocks refer to Fig. 1.6.

Mafic volcanic rocks (basalt-hawaiite-mugearite-benmoreite)

There are four distinct basalt to benmoreite suites defined, based on trace element characteristics: **(1)** in the southwestern part of the island there are hawaiite flows and scoria cones which have Zr/Nb of 4.1; **(2)** in the southern and the southeastern parts of the island basalt flows and extensive lapilli deposits have Zr/Nb of 5.6 to 6.1; **(3)** over the rest of the island basalt and hawaiite flows and scoria cones have Zr/Nb of 4.5 to 5.6; and **(4)** hawaiite flows from Dark Slope Crater have Zr/Nb of 4.9 to 5.4, but have unusually high Ni (28 to 52 ppm) and Sr (596 to 902 ppm) relative to Zr compared to other hawaiite flows and scoria with similar Zr/Nb (Ni < 20 ppm and Sr < 540 ppm at equivalent Zr content).

(1) Low Zr/Nb (4.1) hawaiite

Low Zr/Nb pyroclastic deposits and flows were erupted only locally from a few eruptive centers, Cotar Hill, Horse Shoe Crater, and two unnamed nearby craters, Cone 37 and Cone 38 (Fig. 1.7) in the southwestern part of the island. All these cones are hawaiitic in composition with almost identical major and trace element chemistry and radiogenic isotopic signature (Fig. 1.5). These are comparatively small scoria cones and the flows associated with them flow in a west-southwest direction and are very limited in spatial extent. The small tongue shaped flow from Cotar Hill is the youngest of the low Zr/Nb flows.

(2) High Zr/Nb (5.6 - 6.1) basalt

High Zr/Nb pyroclastic deposits and flows are more widespread than low Zr/Nb hawaiite occupying the southeastern part of the island. These mafic rocks are uniformly basaltic in composition with one exception, a flow south of Sharp Cliff which is hawaiitic. Associated with the high Zr/Nb flows there are only three scoria cones which

include the biggest scoria cone on the island, Mountain Red Hill reaching a height of 546 m (Fig. 1.7). South West Bay Red Hill in the southwestern part and Sisters Red Hill (Fig. 1.7) in the northern part are the exceptions. These two high Zr/Nb cones are located in the midst of intermediate Zr/Nb pyroclastic deposits and flows.

High Zr/Nb flows cover the southeastern part of the island (Fig. 1.5) and extend on the coast line from southeast of South Red Crater (Fig. 1.7) in the southern part of the island to Sharp Cliff in the eastern part of the island. Few apparent flow breaks and little significant variation in geochemistry is noticeable over this area. The sources of these flows are not visible but lie somewhere in the east-central section underneath the southern flank of Green Mountain (Fig. 1.4). Two flows in the cliff sequence of Cricket Valley have a slightly evolved chemistry compared to the other high Zr/Nb flows.

(3) <u>Intermediate Zr/Nb (4.5 - 5.6) basalt-hawaiite-mugearite-benmoreite</u>

The intermediate Zr/Nb scoria and mafic flows are more ubiquitous than any other type of mafic rocks. A number of scoria cones are associated with the flows. Most of the flows are voluminous with younger flows covering older flows and making it difficult to trace the origin of the older flows back to their eruptive centers.

Basalt and hawaiite

The major eruptive centers of intermediate Zr/Nb basalt and hawaiite in the western half of the island include Sisters Peak, the second largest scoria cone on the island and a complex eruptive center (Fig. 1.7). A young hawaiite flow from the north side of the Sisters Complex (Fig. 1.5) flowed north and extends between North Point and Porpoise Point. Two very young breach flows on the southern side are of much more limited extent and volume (Fig. 1.5). A lava lake is found on the southern side of the Sisters Complex. These two young flows are considered to have erupted within the past few hundred years (Atkins et al., 1964).

Mugearite and benmoreite

Only a few scoria cones and associated flows are of mugearite composition (Table 1.1, Fig. 1.7). There are some notable scoria cones and flows of benmoreite composition (Figs.s 5 & 6). In the western part of the island are the small cones of Fort Thornton, Fort Hayes, and Cat Hill (Fig. 1.7). Cat Hill has a breach flow (Fig. 1.5) and the "Wireless station" flows (Daly, 1925; Fig. 1.5) from an unnamed cone (Cone , Fig. 1.7) are benmoreite. Benmoreite flows are relatively young as compared to other mafic flows all over the island with the youngest fissure eruption flow being on South East Head (Fig. 1.5). This flow only has a limited areal extent and is amongst some of the youngest volcanic features on the island. This flow is probably no older than 1,000 years old (Atkins et al., 1964). In the northern part of the island three cones (Broken Tooth, Hollow Tooth, and an unnamed cone (Cone 3; Fig. 1.7) have erupted breach flows of benmoreitic composition. The cones have a northwest-southeast trend. Broken Tooth erupted mugearitic and, subsequently, benmoreitic lavas. These flows contain disaggregated xenocrysts from entrained syenite blocks.

(4) <u>Intermediate Zr/Nb (4.9 - 5.4) hawaiite and mugearite flows of Dark Slope Crater</u>

Hawaiite and mugearite flows from Dark Slope Crater (Fig. 1.7) occur in a very localized area in the southwestern part of the island (Fig. 1.5). These flows have high Ni (28-52 ppm) and Sr (596-902 ppm) with respect to Zr (318-558 ppm) and differ from the other, more ubiquitous intermediate Zr/Nb hawaiite flows and scoria (Ni < 20 ppm and Sr < 540 ppm at equivalent Zr content).

Felsic rocks

There are two distinctive felsic eruptive centers on the island, the central complex and the eastern complex. The central complex is comprised of the Middleton Ridge

felsic center and Green Mountain (Fig. 1.6). Middleton Ridge is composed primarily of trachyte, pumice, and some rhyolite and rhyolitic obsidian. The highest peak on the island, Green Mountain (859 m), is made up of massive, thick pyroclastic (mostly pumice) deposits with the southwestern flanks mostly constituted of trachyte.

The eastern part of the island is made up mostly by trachyte flows and lava domes (Fig. 1.6). A voluminous trachyte flow in the northeastern part of the island originated from Devil's Cauldron and flowed northward and eastward. Devil's Cauldron is interpreted to be an explosion crater with the trachyte dome of Weather Post occurring on the southern side of the crater. Southeast of Devil's Cauldron and Weather Post is the massive trachytic flow dome of White Horse, and to the east of White Horse is the comenditic coulee of Little White Hill (Fig. 1.6). At the extreme eastern end of the island, South East Head is constituted of trachyte. In the southeastern part of the island trachyte occurs at Round Hill, Cocoanut Bay, Ragged Hill, and in Pillar Bay (Fig. 1.6). Trachyte from Ragged Hill and Cocoanut Bay contains unusually high concentrations of alkali feldspar phenocrysts.

In the western part of the island trachyte is found locally at Devil's Riding School, Daly's Crags, and Cross Hill (Fig. 1.6).

Rhyolitic compositions are relatively rare, being restricted to the rhyolite flow on Middleton Ridge in the central felsic complex, and the Little White Hill flow dome and a flow in the cliff section to the north of White Horse in the eastern felsic complex.

Plutonic and volcanic xenoliths

Felsic plutonic xenoliths (monzonite, syenite, and granite) and volcanic xenoliths (trachyte and rhyolite) occur mainly in pyroclastic deposits on the western flanks of Green Mountain. The granite, syenite, and monzonite xenoliths have been described in

great detail by Roedder & Coombs (1967), Harris & Bell (1982), Harris et al. (1982), Harris (1983), Sheppard & Harris (1985), and Harris & Sheppard (1987). The granite xenoliths from Five Mile Post vary in size from extremely small (a few cm) to 25 to 30 cm in length and generally are fine-grained with a few which are more coarse-grained. Monzonite xenoliths occur on Middleton Ridge and syenite xenoliths in the Broken Tooth flows (Harris, 1983). Trachytic and rhyolitic xenoliths from the same general area vary vastly in size and generally have a schistose texture.

Ages of the volcanic rocks of Ascension Island

Ascension Island sits on 5- to 6-Ma-old oceanic crust. A deep geothermal exploration well records much of the history of the formation of the island (Nielson & Stiger, 1996). Below 1966 m, the sequence is largely mafic and the felsic rocks mostly occur above 887 m depth. Nielson & Stiger (1996) suggest that felsic volcanism is relatively recent in the growth of the volcanic edifice, although felsic rocks are the oldest exposed rocks on the island.

There is a distinct clustering of ages among the exposed rocks on the island (Fig. 9) with the higher SiO_2 rocks being significantly older (range from 1.2 to 0.56 Ma) than the mafic volcanic rocks (range from 0.47 to 0.12 Ma, with a basaltic dike from Middleton Ridge dated at 0.80 Ma).

Felsic magmatism:

A limited number of age dates (K-Ar) for Ascension trachyte, rhyolite, and pumice exist in the literature (Harris et al., 1982, Nielson and Sibbett, 1996); we have added four new Ar-Ar age dates on feldspar phenocrysts. The first phase of felsic volcanism occurred in the central part of the island. A rhyolite flow east of Middleton Ridge is dated at 0.99±0.02 Ma; this is overlain by a trachyte flow with an age of 0.82±0.02 Ma,

and this flow is overlain by a trachyte dome closely associated with a trachyte lava flow dated at 0.65±0.02 (Nielson & Sibbett, 1996). From field and age relationships we suggest that the build up of the Middleton Ridge felsic center started around 1 Ma ago and continued until 0.65 Ma ago.

Felsic magmatism next occurred:

1) west of Middleton Ridge, where the Devil's Riding School trachyte is dated at 0.66±0.02 and is overlain by pumice with an age of 0.61±0.02 Ma;
2) east of Middleton Ridge, where build up of Green Mountain started around 0.65±0.02 Ma and ended around 0.56±0.06 Ma; and,
3) in the eastern felsic complex where (there is only one age date for this region) the trachyte dome of Weather Post is dated at 0.67±0.02 Ma. The lack of age dates from the eastern felsic complex makes it difficult to conclude its relationship with the Middleton Ridge felsic center. The eastern felsic complex may be contemporaneous, if not slightly younger than, the Middleton Ridge center.

These age dates suggest areal exposure of the central and the eastern parts of the island was built up over a period of half a million years, from 1 Ma to 0.56 Ma. Nielson & Sibbett (1996) suggest that, since the oldest dated rocks in both the felsic complexes are rhyolite, with time silica content decreased with eruption of trachyte from a magma chamber that initially tapped rhyolite from the top of the chamber with the chamber being active for > 0.4 Ma.

Mafic magmatism:

Seven holes drilled for geothermal prospecting (GH1 to GH6, and LDTGH; Neilson & Sibbett, 1996) recovered almost continuous core and penetrated the volcanic pile to a maximum depth of 200 m below sea level. Basalt and hawaiite flows from the deepest levels of three boreholes to the east and north of Devil's Riding School have

higher Zr/Nb (7.4 to 7.7 in GH1; 6.8 to 7.1 in GH6; 6.6 in LDTGH) than any surface basalt or hawaiite lava flows (maximum Zr/Nb of 6.1). This suggests that higher Zr/Nb magmas were erupted earlier in the history of mafic magmatism followed by lower Zr/Nb magmas.

The exposed mafic rocks on Ascension Island are somewhat younger in age compared to the felsic rocks. Overlapping the end of the felsic volcanism, or starting very shortly thereafter, high Zr/Nb basaltic lavas were erupted in the southeastern part of the island. In the southwestern part of the island all four mafic magma types of different ages are present. Field relationships of non-overlapping phases of eruption provide an understanding of the change in the nature of mafic magmatism with time on the island. The basalt flows on the flanks of Devil's Riding School were uplifted by intrusion of trachyte magma which subsequently erupted through the basalt carapace (Atkins et al., 1964). These basalt flows have high Zr/Nb, and as the K-Ar age of the Devil's Riding School trachyte is 0.66±0.02 Ma (Nielson & Sibbett, 1996) there was eruption of high Zr/Nb magma prior to this time. In addition, a high Zr/Nb basalt flow on the southern flank of Green Mountain has a K-Ar age of 0.47±0.10 Ma (Harris et al., 1982) and thick high Zr/Nb basalt flow exposed in the walls of Cricket Valley has a K-Ar age of 0.35±0.03 Ma (Harris et al., 1982). Thus, high Zr/Nb magma may have erupted over at least a 300,000 year period (Weaver et al., 1996).

Dark Slope Crater is adjacent to Devil's Riding School (Fig. 1.7), and flows on the eastern flank of Dark Slope Crater bank up against the western flank of Devil's Riding School (Fig. 1.5). In the cliff section exposed in South West Bay, low Zr/Nb flows overlie flows with the chemical characteristics (high Zr and Ni relative to Zr) of Dark Slope Crater lavas. The highly porphyritic intermediate Zr/Nb flow from Command Hill cone (Fig. 1.6) ramps over the South West Bay cliffs, and also forms a pronounced

flow front on the low Zr/Nb flow to the southeast of Cotar Hill (Fig. 1.5). Elsewhere on the island, the youngest flows (e.g., Sisters flows, Fig. 1.5) are of intermediate Zr/Nb type (Weaver et al., 1996).

Therefore in summary:

1) Borehole data suggest that higher Zr/Nb (> 6.6) mafic magmatism occurred earlier in the history of the island followed by lower Zr/Nb (< 6.6) mafic magmatism.
2) The oldest exposed lava flows are of the high Zr/Nb basalt; limited K-Ar age dates suggest that this magma type may have erupted between ca. 0.66 and 0.35 Ma.
3) Subsequently, there was localized eruption of the Dark Slope Crater magma type.
4) This was followed by equally localized eruption of the low Zr/Nb magma type.
5) The most recent eruptions (which have continued to possibly within the past few hundred years, Atkins et al., 1964) have been much more widespread and of the intermediate Zr/Nb magma type.

REFERENCES

Adams, M.C., 1996. Chemistry of fluids from Ascension #1, a deep geothermal well on Ascension Island, South Atlantic Ocean. Geothermics 25: 561-579.

Allegre, C.J., Hamelin, B., Provost, A., & Dupre, B., 1987. Topology in isotopic multispace and origin of mantle chemical heterogeneities. Earth and Planetary Science Letters 81: 319-337.

Atkins, F.B., Baker, P.E. & Smith, D.G.W., 1964. Oxford expedition to Ascension Island. Nature 204: 722-724.

Baker, P.E., 1973. Islands of the South Atlantic. In: The Ocean Basins and Margins, vol. 1, The South Atlantic: 493-553. Plenum Press, New York.

Barling, J., & Goldstein, S.L. 1990. Extreme isotopic variations in Heard Island lavas and the nature of mantle reservoirs. Nature 348: 257-276.

Bohrson, W.A., & Reid, M.R. 1995. Petrogenesis of alkaline basalts from Socorro Island, Mexico: Trace element evidence for contamination of ocean island basalt in the shallow ocean crust. Journal of Geophysical Research 100, 24: 555-576.

Brozena, J.M.1986. Temporal and spatial variability of seafloor spreading processes in the northern South Atlantic. Journal of Geophysical Research 91: 497-510.

Budhan, J.R., & Schimtt, R.A. 1985. Petrogenetic modelling of Hawaiian tholeiitic basalts: A geochemical approach. Geochimica et Cosmochimica Acta 49: 67-87.

Chaffey, D.J., Cliff, R.A., & Wilson, B.M. 1989. Charaterization of the St. Helena magma source. In: Magmatism in the ocean basins (Saunders, A.D., and Norry, M.J. editors), Geological Society of London Special Publication 42: 257-276.

Clauge, D.A., & Frey, F.A. 1982. Petrology and trace element geochemistry of the Honolulu Volcanics, Oahu: Implications for the oceanic mantle below Hawaii. Journal of Petrology 23: 447-504.

Cohen, R.S., and O'Nions, R.K. 1982. Identification of recycled continental material in the mantle from Sr, Nd, and Pb isotope investigations. Earth and Planetary Science Letters 61: 73-84.

Cornen, G., Daniel, C., and Joron, J. -L. 1990. Meeting with a new oceanic carbonatite on Trindade Island (South Atlantic). Abstracts, IAVCEI, Mainz.

Cliff, R.A., Baker, P.E., and Mateer, N.J. 1991. Geochemistry of Inaccessible Island volcanics. Chemical Geology 92: 251-260.

Daly, R.A., 1925. The geology of Ascension Island. Proc. Am. Acad. Arts Sci. 60: 1-80.

Davies, G.R., Norry, G.R., Gerlach, D.C., & Cliff, R.A., 1989. A combined chemical and Pb-Sr-Nd isotope study of the Azores and CapeVerde hot-spots: the geodynamic implications. In: Magmatism in the ocean basins (Saunders, A.D., and Norry, M.J. editors), Geological Society of London Special Publication 42: 231-255.

Dupre, C., Lambert, B., & Allegre, C.J. 1982. Isotopic variations within a single oceanic island: The Terceira case. Nature 299: 620-622.

Dupuy, C., Barsczus, H.G., Dostal, J., Vidal, P., & Liotard, J., -M., 1989. Subducted and recycled lithosphere as the mantle source of ocean island basalts from southern Polynesia, central Pacific, Chemical Geology 77: 1-18.

Fontignie, D. & Schilling, J.-G., 1996. Mantle heterogeneities beneath the South Atlantic: a Nd-Sr-Pb isotope study along the Mid-Atlantic Ridge (3°S-46°S). Earth and Planetary Science Letters 142: 209-221.

Gerlach, D.C., Stormer, J.C., and Mueller, P.A. 1987. Isotopic geochemistry of Fernando de Noronha. Earth and Planetary Science Letters 85: 129-144.

Halliday, A.N., Davies, G.R., Lee, D-C, Tommasini, S., Paslick, C.R., Fitton, J.G., & James, D.E. 1992. Lead isotope evidence for young trace element enrichment in the oceanic upper mantle. Nature 359: 623-627.

Hanan, B.B., Kingsley, R.H., & Schilling, J.-G., 1986. Pb isotope evidence in the South Atlantic for migrating ridge-hotspot interactions. Nature 322: 137-144.

Harris, C., 1983. The petrology of lavas and associated plutonic inclusions of Ascension Island. Journal of Petrology 24: 424-470.

Harris, C., 1985. Guano-derived rare earth-rich phosphate amygdales in gabbroic inclusions from Ascension Island. Earth and Planetary Science Letters 72: 141-148.

Harris, C., & Bell, J.D., 1982. Natural partial melting of syenite blocks from Ascension Island. Contributions to Mineralogy and Petrology 79: 107-113.

Harris, C., Bell, J.D., & Atkins, F.B., 1982. Isotopic composition of lead and strontium in lavas and coarse-grained blocks from Ascension Island, South Atlantic. Earth and Planetary Science Letters 60: 79-85.

Harris, C., & Sheppard, S.M.F., 1987. Magma and fluid evolution in the lavas and associated granite xenoliths of Ascension Island. In: Fitton, J.G., & Upton, B.G.J. (eds.) Alkaline Igneous Rocks, Geological Society of London Special Publication 30: 269-272.

Hart, S.R., 1984. A large-scale isotope anomaly in the Southern Hemisphere mantle. Nature 309: 753-757.

Hart, S.R. 1988. Heterogeneous mantle domains: Signatures, genesis and mixing chronologies. Earth and Planetary Science Letters 90: 27-296.

Hoernle, K.A., & Schmincke, H.-U., 1993. The role of partial melting in the 15 Ma geochemical evolution of Gran Canaria: A blob model for the Canary hotspot. Journal of Petrology 34: 599-626.

Hofmann, A.W., & White, W.M., 1982. Mantle plumes from ancient oceanic crust. Earth and Planetary Science Letters 57: 421-436.

le Roex, A.P. 1985. Geochemistry, mineralogy and magmatic evolution of the basaltic and trachytic lavas from Gough Island, South Atlantic. Journal of Petrology 26: 149-186.

le Roex, A.P., Cliff, R.A., & Adir, B.J.I., 1990. Tristan da Cunha, South Atlantic: Geochemistry and petrogenesis of a basanite-phonolite lava series. Journal of Petrology 27: 779-812.

Loper, D.E., 1985. A simple model of whole-mantle convection. Journal of Geophysical Research 90: 1809-1836.

Loubet, M., Sassi, R., & Di Danto, G. 1988. Mantle heterogeneities: A combined isotopic and trace element approach and evidence for recycled continental crust materials in some OIB sources. Earth and Planetary Science Letters 89: 299-315.

McKenzie, D., & O'Nions, R.K., 1983. Mantle reservoirs and ocean island basalts. Nature 301: 229-231.

Nielson, D.L., 1996. Introduction to geothermal exploration on Ascension Island, South Atlantic Ocean. Geoethermics 25: 419-425.

Nielson, D.L., & Sibbett, B.S., 1996. Geology of Ascension Island, South Atlantic Ocean. Geothermics 25: 427-448.

Nielson, D.L., & Stiger, S.G., 1996. Drilling and evaluation of Ascension #1, a geothermal exploration well on Ascension Island, South Atlantic Ocean. Geothermics 25: 543-560.

O'Nions, R.K., Hamilton, P.J., & Evensen, N.M., 1977. Variations in $^{143}Nd/^{144}Nd$ and $^{87}Sr/^{86}Sr$ ratios in oceanic basalts. Earth and Planetary Science Letters 34: 13-22.

Palacz, Z.A., & Saunders, A.D., 1986. Coupled trace element and isotope enrichment in the Cook- Austral-Samoa islands, S.W. Pacific. Earth and Planetary Science Letters 79: 270-280.

Richter, F.M., & McKenzie, D.P., 1981. On some consequences and possible causes of possible layered mantle convection. Journal of Geophysical Research 86: 6133-6142.

Roedder, E., & Coombs, D.S., 1967. Immiscibility in granitic melts indicated by fluid inclusions in ejected granite blocks of Ascension Island. Journal of Petrology 8: 417-451.

Sheppard, S.M.F., & Harris, C., 1985. Hydrogen and oxygen isotope geochemistry of Ascension Island lavas and granites: variation with crystal fractionation and interaction with seawater. Contributions to Mineralogy and Petrology 91: 74-81.

Schilling, J.G., & Thompson, G., 1983. Hotspot-MAR interactions and mixing from 80°N to 47°S, Eos Transactions, AGU 64: 324.

Schilling, J.G., Thompson, G., Kingsley, R., & Humphris, S., 1985. Hotspot-migrating ridge interaction in the South Atlantic, Nature 313: 187-191.

Sun, S. –S. 1980. Lead isotopic study of young volcanic rocks from mid-ocean ridges, ocean islands and island arcs. Phil. Trans. Royal Society of London A297: 405-445.

Sun, S.-s., & McDonough, W.F., 1989. Chemical and isotopic systematics of oceanic basalts: implications for mantle composition and processes. In: Magmatism in the ocean basins (Saunders, A.D., and Norry, M.J. editors), Geological Society of London Special Publication 42: 313-345.

Weaver, B.L., Wood, D.A., Tarney, J., & Joron, J., -L. 1986. Role of subducted sediment in the genesis of ocean island basalts: Geochemical evidence from South Atlantic Ocean Islands, Geology 14: 275-278.

Weaver, B.L., Tarney, J., & Joron, J., -L. 1987. Geochemistry of ocean island basalts from the South Atlantic: Ascension, Bouvet, St. Helena, Gough, and Tristan da

Cunha. Alkaline Igneous Rocks (Fitton, J.G. and Upton, B.G.J. editors). Geological Society of London Special Publications 30: 253-267.

Weaver, B.L., 1990. Geochemistry of highly-undersaturated ocean island basalt suites from the South Atlantic Ocean: Fernando de Noronha and Trinidade islands. Contributions to Mineralogy and Petrology 105: 502-515.

Weaver, B.L., 1991a. Trace element evidence for the origin of ocean island basalts. Geology 19: 123-126.

Weaver, B.L., 1991b. The origin of ocean island basalt end-member compositions: Trace element and isotopic constraints. Earth and Planetary Science Letters 104: 381-397.

Weaver, B., Kar, A., Davidson, J., & Colucci, M., 1996. Geochemical characteristics of volcanic rocks from Ascension Island, South Atlantic Ocean.

Weis, D., 1983. Pb isotopes in Ascension Island rocks: Oceanic origin for the gabbroic to granitic plutonic xenoliths. Earth and Planetary Science Letters 62: 273-282.

Weis, D., Demaiffe, D., Cauet, S., & Javoy, M., 1987. Sr, Nd, O and H isotopic ratios in Ascension Island lavas and plutonic inclusions; cogenetic origin. Earth and Planetary Science Letters 82: 255-268.

West, H.B., & Leeman, W.P. 1994. The open-system geochemical evolution of alkalic cap lavas from Haleakala Crater, Hawaii, USA. Geochimica et Cosmochimica Acta 58: 773-796.

White, W.M. 1985. Sources of oceanic basalts: Radiogenic isotope evidence. Geology 13: 115-118.

White, W.M., & Hofmann, A.W., 1982. Sr and Nd isotope geochemistry of oceanic basalts and mantle evolution. Nature 296: 821-825.

Woodhead, J.D., McCulloch, M.T., 1989. Ancient seafloor signals in Pitcairn Island lavas and evidence for large amplitude, small length-scale mantle heterogeneities. Earth and Planetary Science Letters 94: 257-273.

Zindler, A., & Hart, S.R. 1986. Chemical geodynamics. Annual Reviews of Earth and Planetary Sciences 14: 493-571.

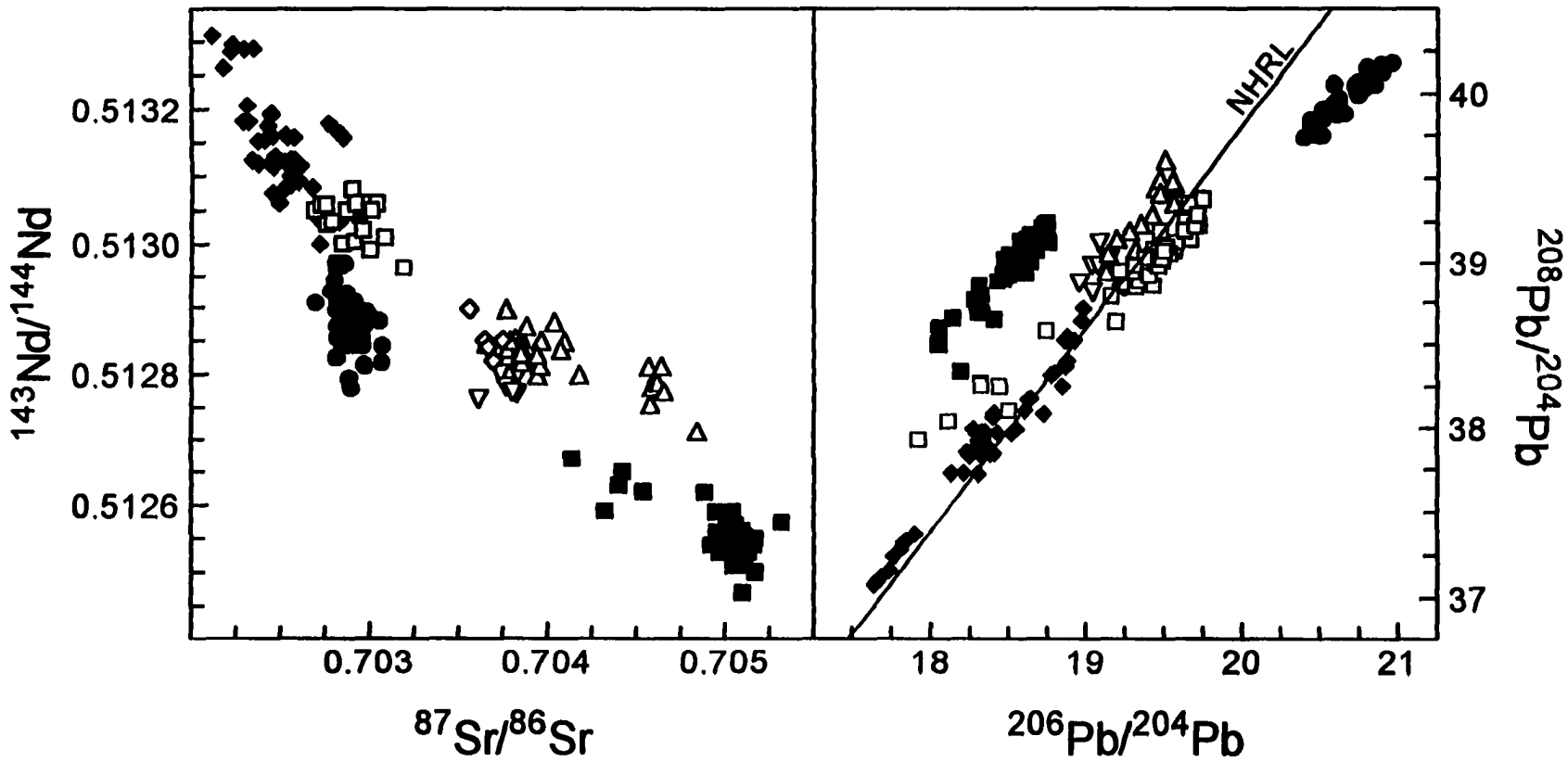

Figure 1.1. Variation in $^{87}Sr/^{86}Sr$ *vs.* $^{143}Nd/^{144}Nd$ and $^{206}Pb/^{204}Pb$ *vs.* $^{208}Pb/^{204}Pb$ for OIB and N-MORB from the South Atlantic Ocean. OIB are: □ Ascension; ◇ Bouvet; △ Fernando de Noronha; ■ Gough and Tristan da Cunha; ▽ Trindade; ● St. Helena. ◆ N-MORB from the Mid-Atlantic Ridge in the South Atlantic Ocean (only MORB samples with $^{87}Sr/^{86}Sr < 0.703$, $^{143}Nd/^{144}Nd > 0.5130$, $^{206}Pb/^{204}Pb < 19$, and $\Delta 8/4 < +30$ are plotted). The Northern Hemisphere Reference Line (NHRL; Hart, 1984) is shown on the $^{206}Pb/^{204}Pb$ *vs.* $^{208}Pb/^{204}Pb$ diagram. Data sources: O'Nions *et al.* (1977), Sun (1980), Cohen & O'Nions (1982), Harris *et al.* (1982), White & Hofmann (1982), Weis (1983), Hanan *et al.* (1986), Gerlach *et al.* (1987), Weis *et al.* (1987), Chaffey *et al.* (1989), Cornen *et al.* (1990), Le Roex *et al.* (1990), Cliff *et al.* (1991), Halliday *et al.* (1992), Fontignie & Schilling (1996).

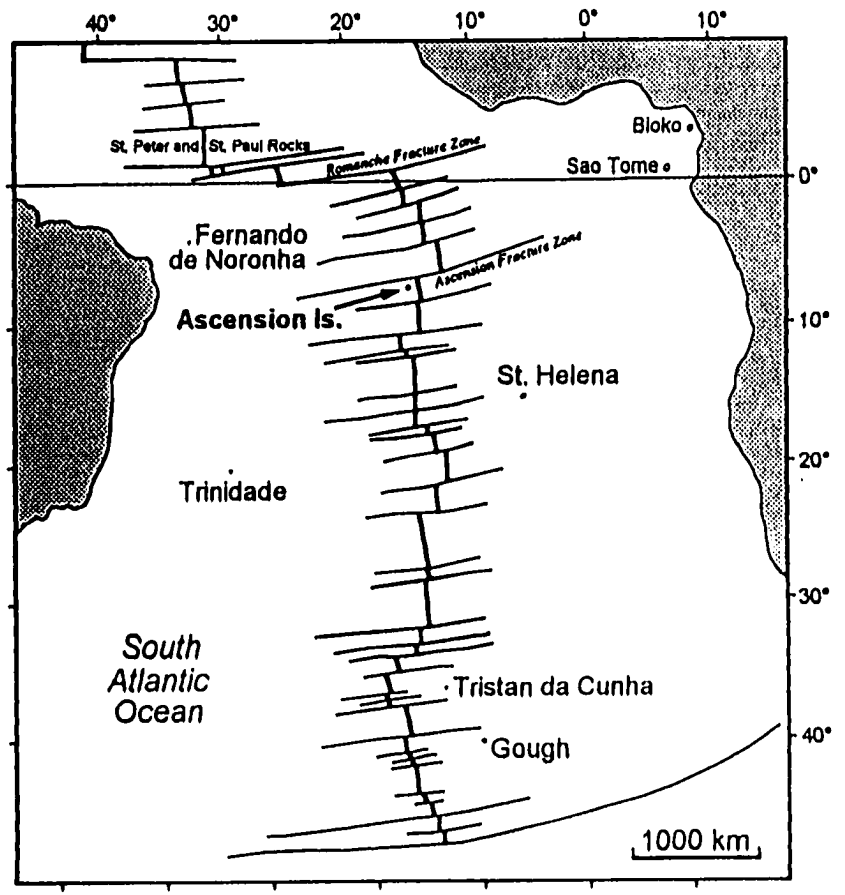

Figure 1.2. Map of part of the South Atlantic Ocean showing the locations of oceanic islands, the axis of the Mid-Atlantic Ridge, and major transform faults and fracture zones. After Nielson (1996).

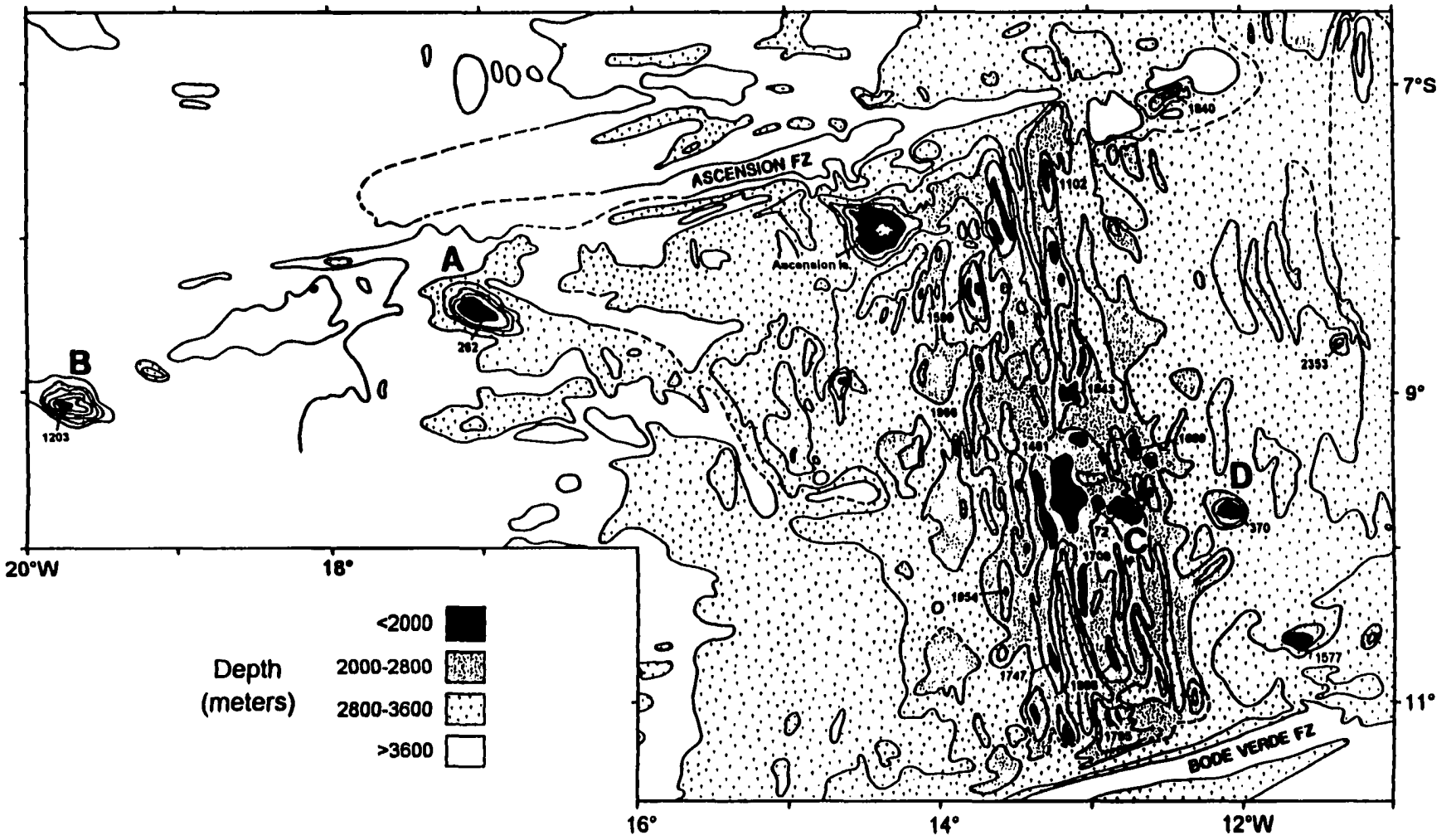

Figure 1.3. Map of the bathymetry of the ocean floor in the South Atlantic Ocean in the vicinity of Ascension Island. After Brozena (1986).

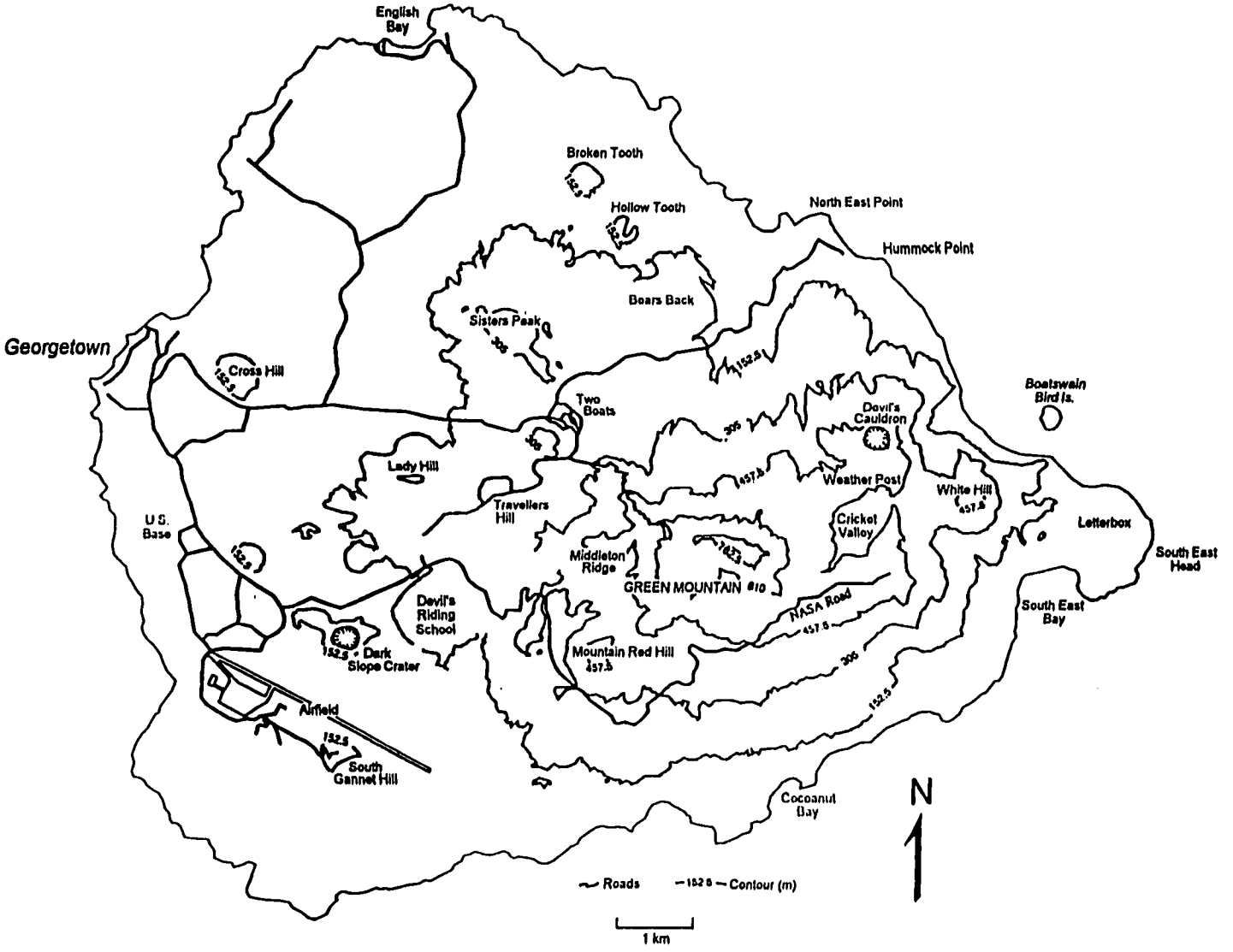

Figure 1.4. Simplified topographic map of Ascension Island showing some of the principal features.

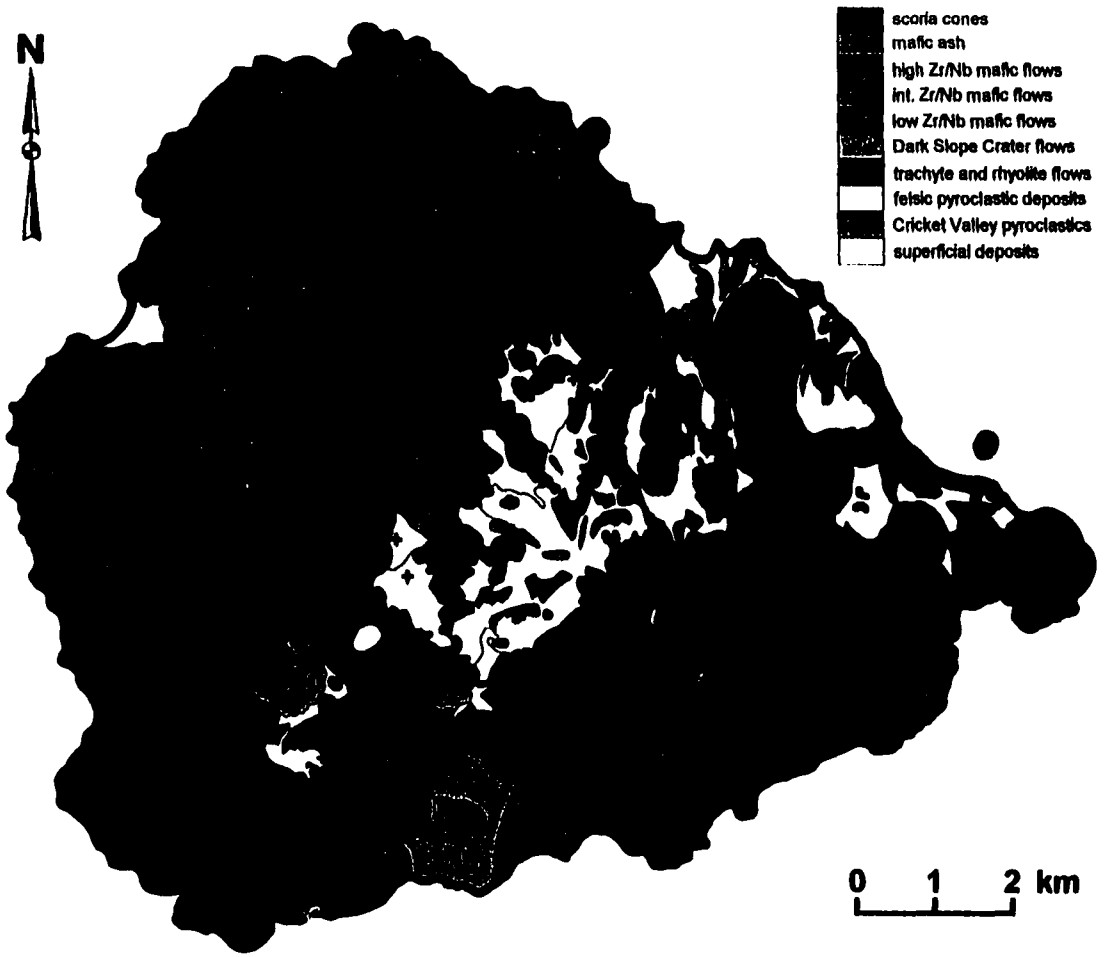

Figure 1.5. Geological map of Ascension Island, somewhat modified from Nielson and Sibbett (1996). The four geochemically distinct mafic rock types (high Zr/Nb, intermediate Zr/Nb, low Zr/Nb, and Dark Slope Crater) are identified and the compositions of selected flows are indicated as: **B** basalt, **H** hawaiite, **M** mugearite, **Be** benmoreite.

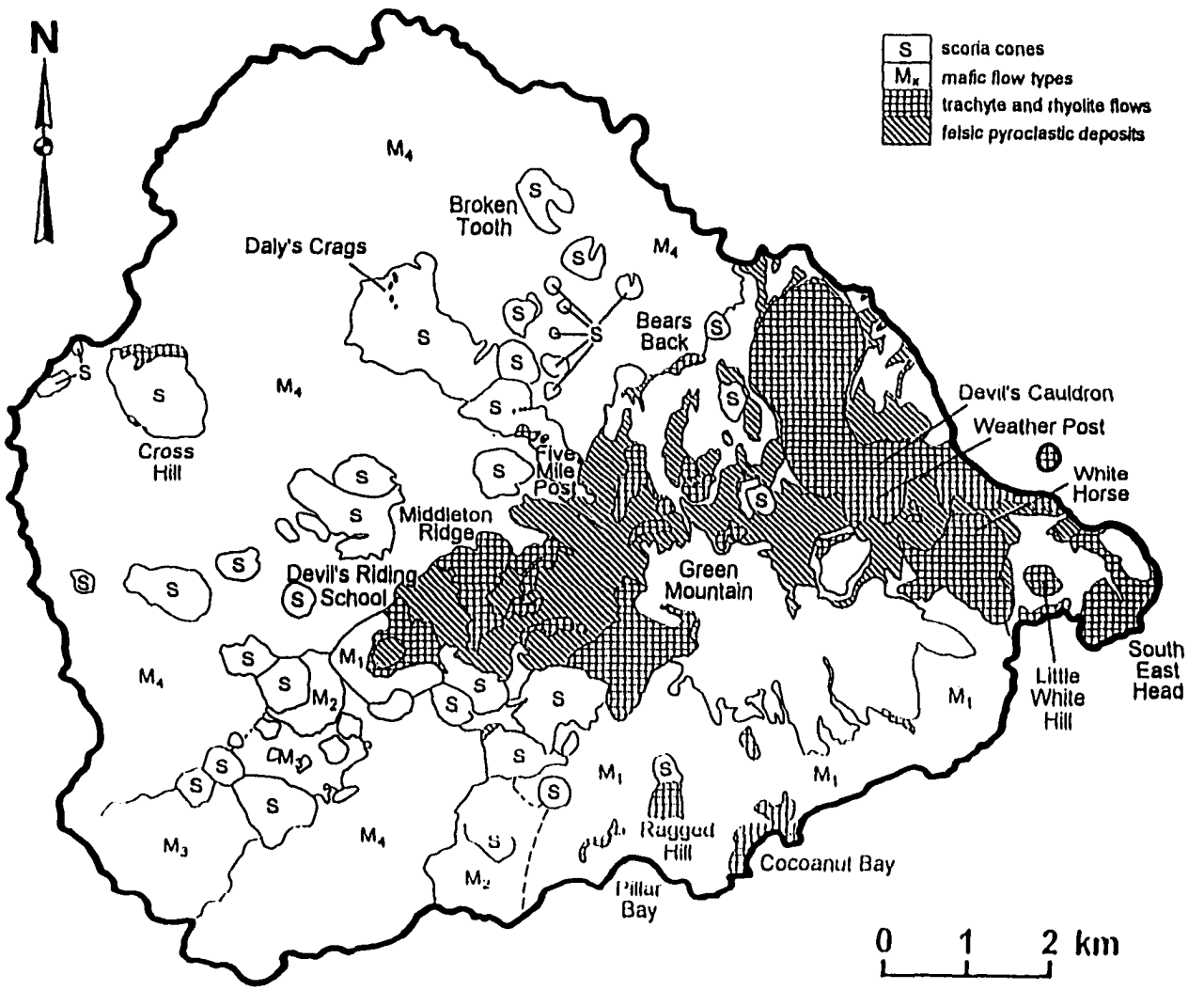

Figure 1.6. Simplified geological map of Ascension Island highlighting the distribution of felsic rock types. Mafic lava flow types are: M_1 high Zr/Nb basalt; M_2 Dark Slope Crater hawaiite and mugearite; M_3 low Zr/Nb hawaiite; M_4 intermediate Zr/Nb basalt to benmoreite. For a more detailed geological map see Kar et al. (Felsic MS).

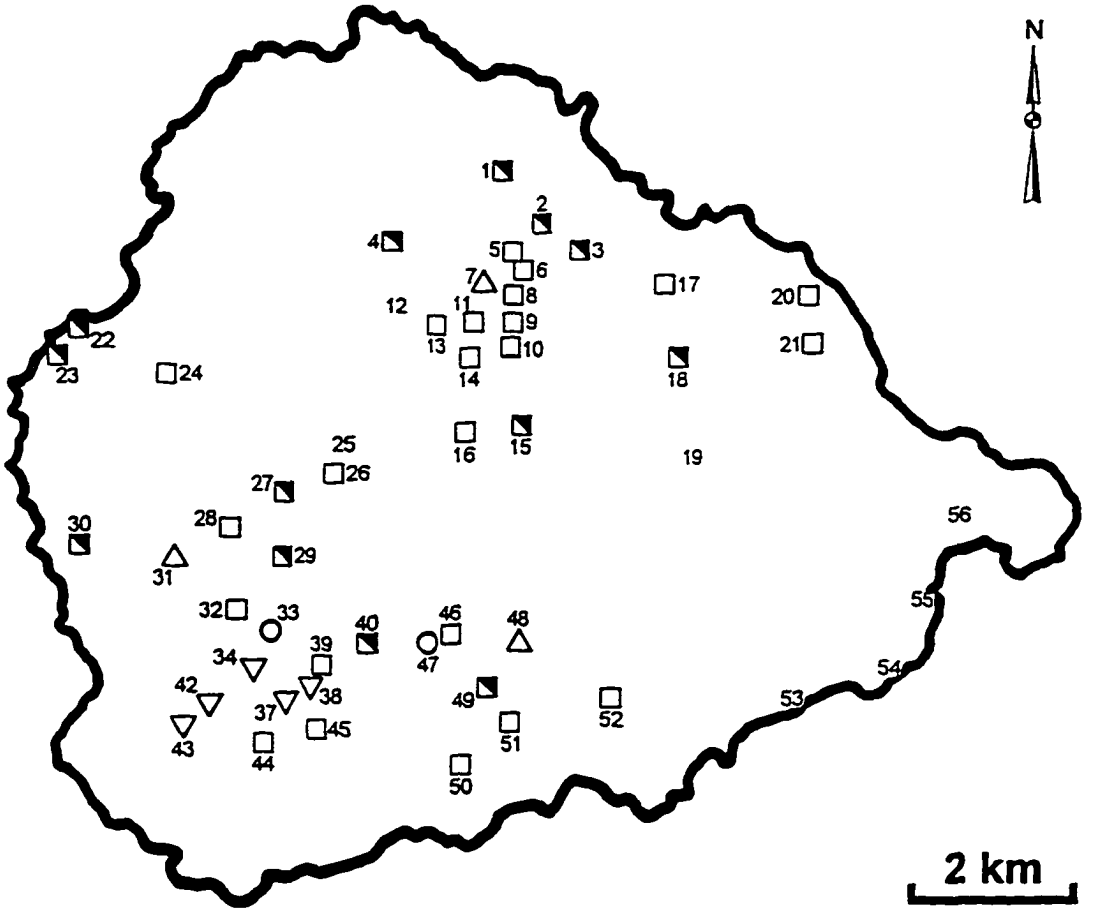

Figure 1.7. Map of Ascension Island showing the location and compositional characteristics of the scoria cones listed in Table 1.1. Symbols used to designate the composition of the cones are: △ high Zr/Nb basalt, ▽ low Zr/Nb hawaiite, □ intermediate Zr/Nb basalt and hawaiite, ◹ intermediate Zr/Nb mugearite and benmoreite, and O Dark Slope Crater hawaiite and mugearite.

Table 1.1. Locations and chemical characteristics of Ascension Island scoria cones.

Cone No.	Name	Grid Reference	Composition	Sample scoria	Sample flow
1	Broken Tooth	703258	Mugearite to benmoreite	✓	✓
2	Hollow Tooth	709251	Benmoreite	✓	
3	unnamed	714247	Benmoreite	✓	✓
4	unnamed	689248	Mugearite		✓
5	unnamed	704247	Hawaiite (intermediate Zr/Nb)	✓	
6	unnamed	706245	Hawaiite (intermediate Zr/Nb)	✓	
7	Sisters Red Hill	700244	Basalt (high Zr/Nb)	✓	
8	unnamed	704242	Hawaiite (intermediate Zr/Nb)	✓	
9	Street Crater	705238	Hawaiite (intermediate Zr/Nb)		✓
10	Butt Crater	704235	Hawaiite (intermediate Zr/Nb)	✓	✓
11	Perfect Crater	699239	Hawaiite (intermediate Zr/Nb)	✓	
12	unnamed	687241	not known		
13	Sisters Peak	693239	Hawaiite (intermediate Zr/Nb)	✓	✓
14	unnamed	699234	Hawaiite (intermediate Zr/Nb)	✓	
15	Thistle Hill	705225	Mugearite	✓	
16	Travellers Hill	697225	Hawaiite (intermediate Zr/Nb)	✓	✓
17	Lower Valley Crater	724243	Basalt (intermediate Zr/Nb)	✓	
18	Upper Valley Crater	726234	Mugearite		✓
19	unnamed	730221	not known		
20	unnamed	743241	Hawaiite (intermediate Zr/Nb)		✓
21	unnamed	744233	Hawaiite (intermediate Zr/Nb)		✓
22	Fort Thornton	647240	Benmoreite		✓
23	Fort Hayes	645236	Benmoreite	✓	
24	Cross Hill	658233	Basalt (intermediate Zr/Nb)	✓	✓
25	unnamed	682222	not known		
26	Lady Hill	681219	Hawaiite (intermediate Zr/Nb)	✓	✓
27	unnamed	674218	Benmoreite	✓	✓
28	unnamed	667213	Hawaiite (intermediate Zr/Nb)	✓	
29	Table Crater	674209	Mugearite	✓	
30	Cat Hill	648211	Benmoreite	✓	✓
31	South West Bay Red Hill	660209	Basalt (high Zr/Nb)	✓	✓
32	Command Hill	668202	Basalt (intermediate Zr/Nb)		✓
33	Dark Slope Crater	672199	Hawaiite to mugearite (DSC-type)		✓
34	Horse Shoe Crater	670193	Hawaiite (low Zr/Nb)		✓
35	unnamed	666193	not known		
36	unnamed	670190	not known		
37	unnamed	674190	Hawaiite (low Zr/Nb)	✓	
38	unnamed	678192	Hawaiite (low Zr/Nb)	✓	✓
39	unnamed	679195	Hawaiite (intermediate Zr/Nb)	✓	
40	unnamed	684196	Mugearite	✓	
41	unnamed	681192	not known		
42	Round Hill	664190	not known		
43	Cotar Hill	661187	Hawaiite (low Zr/Nb)		✓
44	South Gannet Hill	671185	Basalt (intermediate Zr/Nb)	✓	✓
45	Booby Hill	678186	Hawaiite (intermediate Zr/Nb)	✓	✓
46	Spoon Crater	696198	not known		
47	unnamed	694197	Hawaiite (DSC-type)		✓
48	Mountain Red Hill	705197	Basalt (high Zr/Nb)	✓	
49	unnamed	701192	Mugearite	✓	
50	South Red Crater	697181	Hawaiite (intermediate Zr/Nb)		✓
51	Green Top Crater	705187	Hawaiite (intermediate Zr/Nb)	✓	
52	South East Crater	717190	Hawaiite (intermediate Zr/Nb)	✓	
53	Coast Red Nipple	741188	not known		
54	Round Hill	752193	not known		
55	Crater Cliff	758202	not known		
56	unnamed	763212	not known		

Cone number has been assigned arbitrarily. Scoria cone names and grid references are from the 1:25,000 Ascension Island topographic map, series G 892, edition 4-GSGS, 1992.

CHAPTER II

(To be submitted to Journal of Petrology)

Small-scale mantle heterogeneities: Evidence from incompatible element and isotopic ratios of mafic volcanic rocks of Ascension Island, South Atlantic Ocean

Running head: *Geochemistry of Ascension Island mafic rocks*

Kar, A.[1,2]
School of Geology and Geophysics
University of Oklahoma
Norman, OK 73019, USA

Weaver, B.
School of Geology and Geophysics
University of Oklahoma
Norman, OK 73019, USA

Davidson, J.
Department of Earth and Space Sciences
University of California Los Angeles
Los Angeles, CA 90024, USA

Colucci, M.
Department of Geology
Southern Methodist University
Dallas, TX 75275, USA

[1] Department of Mathematics and Physics
Fort Valley State University
Fort Valley, GA 31030, USA

[2] Corresponding Author
Telephone: (912) 825 6844
FAX: (912) 825 6618
email: kara@mail.fvsc.peachnet.edu

ABSTRACT

The basalt-hawaiite-mugearite-benmoreite-trachyte-rhyolite suite of Ascension Island has much greater geochemical diversity than hitherto recognized. Among the mafic (basalt to benmoreite) rocks four distinct groups are identified: low Zr/Nb hawaiite, high Zr/Nb basalt, intermediate Zr/Nb basalt to benmoreite, and Dark Slope Crater hawaiite and mugearite. Although crystal fractionation controls compositional variation within each group it cannot be the cause of the differences between the groups. The high Zr/Nb and intermediate Zr/Nb groups have similar Sr, Nd, and Pb isotopic characteristics and were derived from the same mantle source which has undergone lesser degrees of partial melting through time. The low Zr/Nb and Dark Slope Crater groups have different isotopic characteristics (less radiogenic Nd, more radiogenic Sr and Pb) due to contributions from enriched mantle components. In both cases the enriched component is of HIMU type. The dominant component, present in the high Zr/Nb, intermediate Zr/Nb, and low Zr/Nb groups, has the composition of the St. Helena hotspot and has mixed to varying degrees with the depleted upper mantle. The more minor component, present only in the Dark Slope Crater group and some intermediate Zr/Nb samples, has higher $^{208}Pb/^{204}Pb$ relative to $^{206}Pb/^{204}Pb$ than the St. Helena hotspot. This component may be of local lithospheric origin.

Fractional Crystallization / Mantle Heterogeneity / Pb-Sr-Nd isotopes / REE / Zr/Nb

INTRODUCTION

Hotspot-related volcanism, especially that occurring in the interior of oceanic plates, is one of the best means to study the composition of the Earth's mantle. These volcanic rocks, termed ocean island basalt (OIB), represent magmas derived directly from the

mantle and which are least contaminated during their ascent from the mantle through the thin oceanic lithosphere to the surface. Zindler & Hart (1986), Hart (1988), and Weaver (1991a,b) recognize three distinctive OIB mantle sources, HIMU, EMI, and EMII. OIB with unusually radiogenic Pb isotope ratios are derived from a source with high $^{238}U/^{204}Pb$ (HIMU source), whereas OIB with unusually radiogenic Sr and unradiogenic Nd isotope ratios are derived from mantle sources (EMI and EMII) enriched in large ion lithophile elements (LILE) and light rare earth elements (LREE) (Weaver, 1991a). Weaver (1991a) suggested that oceanic crust subducted into the mantle forms the major component in the OIB magma source, with HIMU OIB sources being pure basaltic crust compared to EMI and EMII sources which contain variable amounts of pelagic and terrigenous sediment, respectively, together with the very old (1 to 2 Ga) recycled oceanic crust. In addition to the three mantle sources for OIB, a fourth mantle component with low $^{87}Sr/^{86}Sr$ and high $^{143}Nd/^{144}Nd$ is the source for mid-oceanic ridge basalt (MORB) (Hart, 1988).

Numerous studies in the last few decades on the major and trace element geochemistry and isotope characteristics of hotspot-related magmatism have thrown light on the heterogeneities that exist between and among intra-plate volcanic rocks from different parts of the world. The substantial differences in Sr, Nd, and Pb isotopic compositions between volcanic and plutonic rocks from the various hotspot-related islands of the South Atlantic Ocean (Fig. 2.1) illustrate this diversity and suggests the existence of large-scale chemical heterogeneity on the scale of hundreds or thousands of kilometers (Zindler & Hart, 1986) in the suboceanic mantle. Major geochemical diversity is also increasingly being noted in OIB from individual oceanic islands, implying that heterogeneities also exist in OIB sources on small (kilometer) scales (Weaver et al., 1987; Woodhead & McCulloch, 1989; Barling & Goldstein, 1990;

Halliday et al., 1992). The significant variations in Sr, Nd, and Pb isotopic compositions (Fig. 2.1) among the OIB from individual South Atlantic Ocean islands substantiate the presence of small-scale mantle heterogeneities.

This is the first project that aims at a comprehensive geochemical and petrogenetic study of the hotspot-related volcanic rocks of Ascension Island. Although a substantial geochemical database exists for hotspot-related ocean island basalt (OIB) from different parts of the world, Ascension Island has not previously been comprehensively studied. Some data exist on the geology, mineralogy, major, minor and trace element, and isotope geochemistry, fluids associated with magmatism, and age of the different varieties of rocks and plutonic xenoliths of Ascension Island (Atkins et al., 1964; Roedder & Coombs, 1967; Harris & Bell, 1982; Harris et al., 1982; Harris, 1983; Weis, 1983; Harris, 1985; Sheppard & Harris, 1985; Harris & Sheppard, 1987; Weis et al., 1987; Adams, 1996; Nielson & Sibbett, 1996; Nielson & Stiger, 1996). These studies show that a substantial diversity is present within the geochemical data. The present study confirms and extends this diversity and is directed to understand the cause(s) of the variation of the geochemical data and its implications for mantle heterogeneity and the petrogenesis of the mafic volcanic rocks.

GENERAL GEOLOGY OF ASCENSION ISLAND

Ascension Island, situated at 7°56'S and 14°22'W in the South Atlantic Ocean, is located 80 km west of the Mid-Atlantic Ridge and 50 km south of Ascension Fracture Zone (Fig. 2.2) on oceanic crust which is 5- to 6-Ma-old. The island rises about 2700 m from the ocean floor and has a maximum elevation of 860 m above sea level and an areal exposure of about 98 km^2. The oldest dated volcanic rocks from the island are about 1 Ma (Harris et al., 1982; Nielson & Sibbett, 1996) and volcanism possibly has

continued to within the past few hundred years (Atkins et al., 1964).

Ascension is a composite volcano and the exposed volcanic rocks on the island comprise basalt-trachyte series lava flows, flow domes, scoria cones, and pyroclastic deposits (Fig. 2.3). Pyroclastic (pumice and scoria) deposits make up about 43% of the surface area of the island (Harris, 1983). There are in excess of fifty scoria cones (Table 2.1 and Fig. 2.4) distributed over the island with some of the largest cones occurring in the central to southwestern to south-central parts of the island with the highest cone (Mountain Red Hill) reaching a height of 546 m above sea level. A more detailed geology of the mafic rocks is presented in the geochemistry section of this paper. Prior to this study, the pyroclastic deposits have been largely uncharacterized. In this study we geochemically and petrogenetically characterize the voluminous mafic lava flows and scoria deposits.

SAMPLING AND ANALYTICAL TECHNIQUES

For details on sampling techniques and analytical procedure for major and trace element analyses obtained at the University of Oklahoma refer to Weaver et al. (1996), for radiogenic isotope analysis performed at University of California, Los Angeles refer to Davidson et al. (1993), and for oxygen isotope analysis performed at Southern Methodist University to Borthwick & Harmon (1982).

GEOCHEMISTRY

Alteration of lava flows and scoria

The climate of Ascension Island is (at the present day) quite arid and most of the sampled lava flows have no to little petrographic evidence of alteration and there is unlikely to have been any significant modification of primary chemical characteristics. Scoria samples, however, invariably are oxidized. Sampling of the scoria and lava flow

erupted from the same vent allows assessment to be made of chemical changes due to oxidation (Table 2.2) although there may be slight chemical differences due to degree of fractionation (based on immobile incompatible element abundance, Al-208 is slightly more evolved than Al-211 and Al-179 is more evolved than Al-180; Table 2.2). Oxidized (brown) scoria is hydrated as indicated by elevated H_2O- and LOI (Table 2.2, data for Cones 38 and 16) and, compared to a fresh flow sample from the same vent, there is loss of Na_2O (0.75 to 0.90 wt% for Al-208 and Al-180). Scoria from Cone 44 is not oxidized (black lapilli were sampled from a quarry in the cone) and is not significantly hydrated compared to samples of the flow from this cone, but has ~0.40 wt% depletion in Na_2O (Table 2.2). The massive bomb from Cone 44 petrographically is fresh and has low H_2O- and LOI but has ~0.20 wt% depletion in Na_2O compared to flow samples (Table 2.2). The K_2O content of the scoria samples is unchanged but, because of Na_2O loss, Na_2O+K_2O and Na_2O/K_2O are low in scoria compared to the cogenetic flow (Table 2.2). In addition to Na_2O loss, CaO is lower and MgO higher in scoria relative to flow for Cones 38 and 16 (Table 2.2), and the loss of Na_2O and CaO results in a significant apparent increase in SiO_2 in Al-208 and Al-180 (Table 2.2).

There are also noticeable alteration effects on some trace element abundances. Sr is slightly depleted and Rb slightly enriched in scoria Al-180 and Al-26 relative to flow samples and Ba is slightly depleted in scoria Al-208 and Al-180 relative to flow samples. Th and Pb are constant within analytical error. Zr and Nb are immobile elements in hydrous fluids and Zr/Nb is constant between the scoria and lava flow samples.

Chemical homogeneity of lava flows

Multiple samples were taken from a number of lava flows, allowing assessment of the chemical homogeneity of individual flows (Table 2.3). In many cases, scoria from the

associated vent was also sampled. The flow from Command Hill (Fig. 3, Fig. 4) is quite extensive and forms some 2.5 km of the coast line which is as far as 3 km from the vent. This flow is very distinctive as, unusually for Ascension flows, it is moderately phyric. There are only very small variations in the chemistry of the five samples (Table 2.3); for example, limited variation in MgO probably reflects slightly variable concentration of olivine phenocrysts. Incompatible element ratios are constant (Table 2.3), with the exception of the bomb from the cone (AI-1) which has slightly different ratios to the four flow samples. Nonetheless, despite the phyric nature of this flow there is no significant indication of chemical variability due to flow differentiation.

An extensive hawaiite flow issued from a breach high on the northeast side of Sisters Peak have flowed around Broken Tooth and its flows (Fig. 2.3). This flow apparently is relatively young and very fresh (low H_2O- and negative LOI, Table 2.3). The chemical compositions of the four samples from this flow (Table 2.3) are very consistent, for major and trace elements and for incompatible element ratios.

A benmoreite flow from (unnamed) Cone 27 (Fig. 3, Fig. 4) extends for ~3.5 km to the coast (this is the older of the two "Wireless Station" flows described by Daly, 1925). Although only sampled in two places the chemical analyses are almost identical (Table 2.3) demonstrating that the more evolved flows also are compositionally very uniform.

A number of other flows were sampled in multiple locations. In all such instances the indication is that the lava flows on Ascension are compositionally very homogeneous and, therefore, that a single sample of a flow is well representative of the composition of that flow.

Major and trace element geochemistry

The Ascension volcanic rocks are a transitional to mildly alkaline fractionation series from basalt through hawaiite, mugearite and benmoreite, to the highly fractionated

products of trachyte and rhyolite (Fig. 2.5). Basalt and hawaiite are the most common eruptive products, with lesser volumes of mugearite and benmoreite flows and scoria. Representative chemical analyses of the mafic rock types are presented in Table 2.4. Trachyte flows and domes are volumetrically more abundant than mugearite and benmoreite flows.

In the Ascension basalt to rhyolite suite the major element variations conform to those expected from crystal fractionation of the observed phenocryst phases from a basalt parent magma (Harris, 1983); variation of Al_2O_3, TiO_2, and MgO with respect to SiO_2 define segmented linear correlations indicating fractionation of olivine, feldspar, clinopyroxene, and titanomagnetite. Here we consider the petrogenesis of the mafic (basalt to benmoreite) rock types of Ascension Island which are geochemically more diverse than hitherto recognized (Table 2.4). For petrogenesis of Ascension felsic rocks and their relationship to the mafic rocks refer to Kar et al. (Felsic MS). All of the Ascension mafic rocks have undergone significant crystal fractionation; none have MgO > 7 wt% (Fig. 2.6) and those with > 6 wt% MgO have accumulated olivine ± clinopyroxene phenocrysts. SiO_2 is < 50 wt% for rocks with 7 to 4.5 wt% MgO but then increases with greater degrees of fractionation (Fig. 2.6). Fe_2O_3 and TiO_2 increase from 7 to 4.5 wt% MgO then decrease with decreasing MgO (Fig. 2.6) whereas Al_2O_3 behavior is the opposite, although with considerable scatter in the data (Fig. 2.6). CaO constantly decreases and K_2O constantly increases with fractionation (Fig. 2.6).

The Ascension mafic flows and scoria have a significant range in Zr/Nb, from 4.0 to 6.0 (Fig. 2.7). There are four distinct mafic rock types that are identified based on trace element variations (Table 2.3 and Fig. 2.7):

(1) High Zr/Nb basalt

Basalt lava flows (SiO_2 47.6 to 50.6 wt%) from the southeastern part of the island and

extensive basaltic lapilli deposits on Green Mountain (Fig. 2.4) have relatively low Zr (160 to 248 ppm) but high Zr/Nb (5.6 to 6.1; Fig. 2.7). Only three scoria cones have high Zr/Nb; Mountain Red Hill and South West Bay Red Hill in the southwestern part of the island, and Sisters Red Hill in the northern part of the island (Table 2.2.1, Fig. 2.4). This latter cone is anomalous as it occurs distant from the major surface exposures of high Zr/Nb flows. Ni contents are high (30 to 50 ppm) for Ascension mafic rocks (Fig. 2.8) and incompatible element contents are relatively low (Fig. 2.8). REE patterns are moderately LREE enriched (Ce_N/Yb_N 4.7 to 6.1; Fig. 2.9). Incompatible element normalized patterns are typical for OIB with pronounced enrichment in Nb (and Ta) relative to other highly incompatible elements (Fig. 2.2.10). P/Zr is low (normal) in the high Zr/Nb basalt group (P/Zr = 7.7 to 12.9).

The high Zr/Nb basalt flows are sparsely to moderately phyric with a phenocryst and microphenocryst assemblage mostly of plagioclase and olivine, the relative abundance varying from flow to flow, together with titanomagnetite and rare patchy clinopyroxene.

(2) Low Zr/Nb hawaiite

Localized hawaiite lava flows in the southwestern part of the island (Fig. 2.3) have a restricted range of compositional variation (SiO_2 47.3 to 47.9 wt%; Zr 235 to 259 ppm) and have low Zr/Nb (4.1; Fig. 2.7). These flows originated from a number of small scoria cones, e.g., Cotar Hill, Horse Shoe Crater, and two unnamed cones (Table 2.1, Fig. 2.4) to the south and southwest of Dark Slope Crater. The low Zr/Nb flows also have higher Ba/Zr and Rb/Zr than the other mafic rock types (Fig. 2.8) and REE patterns (Fig. 2.9) that are more fractionated (e.g., Ce_N/Yb_N 6.2 to 6.6 compared to 4.7 to 6.1 in high Zr/Nb basalt). A very distinctive feature of the low Zr/Nb group is a strong enrichment in P relative to other incompatible elements, manifest in elevated P/Zr (16.8 to 19.0 compared to 7.7 to 12.9 in the high Zr/Nb group) and a P "spike" in the

incompatible element normalized patterns (Fig. 2.10).

The low Zr/Nb hawaiite flows are aphyric with rare plagioclase phenocrysts and some are moderately vesicular with small vesicles scattered throughout the groundmass.

(3) Intermediate Zr/Nb basalt-hawaiite-mugearite-benmoreite

Most of the western and northern parts of Ascension Island (Fig. 2.3) are covered by basalt to benmoreite lava flows (SiO_2 47.25 to 60.95 wt%) with a wide range in Zr (140 to 610 ppm) and intermediate Zr/Nb (4.5 to 5.6). Most of the scoria cones on the island are of intermediate Zr/Nb composition (Fig. 2.4). A description of the intermediate Zr/Nb mafic rocks follows.

Basalt and hawaiite

Basalt and hawaiite flows and scoria have 47.3 to 51.6 wt% SiO_2, 140 to 387 ppm Zr, and a range in Zr/Nb of 4.6 to 5.6 (Fig. 2.7), although Zr/Nb < 4.8 or Zr/Nb > 5.2 is rare. The only intermediate Zr/Nb samples with Zr < 221 ppm (Fig. 2.7) are from highly phyric basalt flows associated with the Command Hill cone. Some of the youngest lava flows on Ascension, for example those from South Gannet Hill and Sisters Peak (Atkins et al., 1964), are of intermediate Zr/Nb basalt and hawaiite. Sr is buffered in the 400 to 500 ppm range (Fig. 2.8), although hawaiite flows from Bears Back have higher Sr (close to 650 ppm); these flows also have somewhat lower Y than the other intermediate Zr/Nb flows. REE patterns have Ce_N/Yb_N of 5.3 to 6.5 (slightly more fractionated than the high Zr/Nb group) although highly phyric samples from Command Hill have lower Ce_N/Yb_N of 4.5 to 4.7. P behavior is highly variable in intermediate Zr/Nb basalt and hawaiite; P/Zr ranges from 8.1 to 24.0 and there are large P spikes in the incompatible element patterns (Fig. 2.10) of samples with high P/Zr.

The intermediate Zr/Nb basalt flows typically are sparsely phyric and contain

plagioclase and common olivine phenocrysts that rarely form glomerocrystic clusters with plagioclase. Hawaiite flows mostly are aphyric and slightly to moderately vesicular although some flows are massive; they contain rare microphenocrysts of plagioclase, olivine, and clinopyroxene with the crystals embayed and resorbed. Titanomagnetite microphenocrysts are also present.

Mugearite and benmoreite

Mugearite flows and scoria have 50.2 to 55.3 wt% SiO_2, 333 to 470 ppm Zr, and Zr/Nb of 4.7 to 5.9 whereas benmoreite flows and scoria have 54.7 to 61.0 wt% SiO_2, 429 to 610 ppm Zr, and Zr/Nb of 4.9 to 6.0.

Only a few scoria cones (Fig. 2.4) and associated flows (Fig. 2.3) are of mugearite composition (Fig. 2.7). There are some notable scoria cones (Fig. 2.4) and flows (Fig. 2.3) of benmoreite composition; in the western part of Ascension are the small cones of Fort Thornton, Fort Hayes, Cat Hill (which has a breach flow), and the "Wireless station" flows (Daly, 1925) from an unnamed cone, and at the eastern end of the island is the young benmoreite fissure flow on South East Head. In the northern part of the island three cones form a linear NW-SE trending chain (Fig. 2.4) and have each erupted benmoreite breach flows. The westernmost of these cones is Broken Tooth which erupted both mugearite and benmoreite lava flows that contain xenocrysts disaggregated from entrained syenite xenoliths (Harris & Bell, 1982).

The mugearite flows are aphyric to moderately phyric and contain variable proportions of feldspar, plagioclase, and titanomagnetite phenocrysts and olivine microphenocrysts and phenocrysts. Feldspar phenocrysts are rare and olivine microphenocrysts are very rare. The groundmass is medium grained with feldspar laths defining patchy, irregular flow alignment. The benmoreite flows are aphyric with plagioclase, olivine, and titanomagnetite forming the rare microphenocrysts and vary

from massive to highly vesicular. The groundmass plagioclase laths show some development of flow alignment. The benmoreite fissure flow on Letterbox is moderately phyric and vesicular and contains plagioclase phenocrysts and clinopyroxene, olivine, and titanomagnetite microphenocrysts. The flows from Broken Tooth are petrographically distinctive in that they contain alkali feldspar xenocrysts derived by desegregation of entrained syenite inclusions.

(4) Dark Slope Crater

Hawaiite and mugearite flows (SiO_2 48.2 to 52.1 wt%) originating from Dark Slope Crater (Fig. 2.4) have intermediate Zr/Nb (4.9 to 5.2; Fig. 2.7) but have high Ni (28 to 52 ppm) and Sr (596 to 902 ppm) relative to Zr (318 to 558 ppm) compared to other intermediate Zr/Nb hawaiite flows and scoria (Ni < 20 ppm and Sr < 540 ppm at equivalent Zr content; Fig. 2.8). To the east of Dark Slope Crater, a small unnamed cone (Fig. 2.4) which is partially covered by Spoon Crater has similar characteristics; a dyke exposed on the flank of the cone and a small breach flow are hawaiite, and to the south of this cone is a mugearite flow (Fig. 2.3) which likely originated from the cone. In the Dark Slope Crater group, Sr increases with increasing Zr, as opposed to the other rock types where Sr is buffered at around 500 ppm (Fig. 2.8), implying lesser amounts of plagioclase fractionation from the Dark Slope Crater magmas. The Dark Slope Crater flows also have low Y (Fig. 2.7) and more fractionated REE patterns (Ce_N/Yb_N 8.0 to 12.4; Fig. 2.9) compared to the other mafic rock types. P behaviour is not anomalous; P/Zr is low (11.0 to 13.0 in hawaiite; lower in mugearite due to apatite fractionation) and there is no P spike on incompatible element normalized patterns (Fig. 2.10).

The Dark Slope Crater flows are aphyric (rare olivine microphenocrysts) and moderately vesicular.

DISCUSSION

The wide variation of Zr/Nb observed for the mafic Ascension rocks could be generated by: (1) crystal fractionation, particularly involving clinopyroxene and Fe-Ti oxide fractionation, (2) by variable low degrees (<10%) of partial melting of the mantle source of the mafic magmas, (3) by magmas being tapped from mantle sources of different Zr/Nb with or without source mixing, or (4) a combination of these processes.

Crystal fractionation

Low to moderate degrees of fractional crystallization do not strongly fractionate ratios of incompatible trace elements. Of the observed phenocryst phases in the mafic lava flows, olivine and plagioclase fractionation will not change Zr/Nb (as both elements are highly incompatible in these phases), whereas clinopyroxene fractionation will decrease Zr/Nb in evolved liquids (as $D_{Zr} > D_{Nb}$) and Fe-Ti oxide fractionation will increase Zr/Nb in evolved liquids (as $D_{Zr} < D_{Nb}$). In the highly phyric flows from the Command Hill cone, Zr/Nb is slightly higher (5.4 to 5.5) than in other intermediate Zr/Nb flows (average Zr/Nb of 5.0), most likely due to accumulation of clinopyroxene phenocrysts. However, co-crystallization of clinopyroxene and titanomagnetite will produce little change in Zr/Nb and this is evident from the Ascension mafic rocks; in the high Zr/Nb group there is a slight increase in Zr/Nb with fractionation (Zr/Nb of 5.5 to 5.7 in rocks with 143 to 162 ppm Zr; Zr/Nb of 5.6 to 6.0 in rocks with 244 to 259 ppm Zr) and in the Dark Slope Crater flows there is little change in Zr/Nb (range 4.9 to 5.2) over a wide range in fractionation (Zr 318 to 583 ppm). Similarly, in the intermediate Zr/Nb group there is little change in Zr/Nb over a wide fractionation interval (average Zr/Nb of 5.0 in basalt and hawaiite, 5.0 in mugearite, and 5.3 in benmoreite).

A crystal fractionation controlled liquid line of descent can be quantitatively modeled using least squares regression of major element data for parent and daughter liquids

and phenocryst phases. The derived degree of crystallization and proportions of phenocryst phases can be used to model trace element behaviour during Rayleigh crystal fractionation (e.g., Davidson & Wilson, 1989).

There is wide chemical variation in the intermediate Zr/Nb group and fractionation has been modeled from basalt to hawaiite, hawaiite to mugearite, and mugearite to benmoreite (Table 2.5). The sum of squares of residuals (ΣR^2) is very low in the models (Table 2.5). The largest residual in each model is for Na_2O (Table 2.5) and most likely this reflects the mobility of Na_2O even in apparently "fresh" samples. The phase proportions of olivine, clinopyroxene, and plagioclase (ol:plg:cpx) change from 6:57:37 to 8:50:42 to 15:26:59 with increasing fractionation. Modeled incompatible trace element abundance generally agree extremely well with observed abundance (Table 2.5) and there is little change in Zr/Nb over the large fractionation interval (66% crystallization) from basalt to benmoreite.

The high Zr/Nb group is almost exclusively restricted to basaltic compositions; only one sample (AI-128) from this group is hawaiitic. The least squares solution (Table 2.5) is not as good as for the intermediate Zr/Nb group but the error in Na_2O accounts for 77% of the sum of squares of residuals. Calculated trace element abundances agree well with observed abundances and there is no change in Zr/Nb with fractionation (Table 2.5).

Fractionation of a Dark Slope Crater hawaiite composition to a mugearite composition yields an excellent least squares result (Table 2.5) but there are some notable discrepancies in the trace element model. In contrast to the other groups where Sr is buffered with increasing fractionation, in the Dark Slope Crater group Sr increases with increasing fractionation (Fig. 2.8). This suggests a less important role for plagioclase in the fractionating phenocryst assemblage, but the least squares model

requires that plagioclase is the dominant phenocrysts phase (ol:plg:cpx 15:53:31) and consequently the modelled Sr abundance is much lower than the observed abundance in the mugearite composition (Table 2.5). A similar problem exists for Ni which also does not decrease significantly in abundance with fractionation in the Dark Slope Crater group (Fig. 2.8).

There is only very limited chemical variation within the low Zr/Nb group and least squares modelling has not been done for these compositions.

The combined major element and trace element models therefore indicate that crystal fractionation processes can adequately account for the chemical variation *within* each of the distinct groups of mafic rocks. More significantly, can the different groups be related to a common parent magma type by crystal fractionation?

From field evidence, eruption of lavas of the high Zr/Nb group preceded the eruption of lavas of the other groups. Consequently, models were tested for the derivation of the other magma types from a parental high Zr/Nb mafic magma (Table 2.6). The models for generation of an intermediate Zr/Nb basalt and a Dark Slope Crater hawaiite yield very poor sums of squares of residuals; large residuals for a number of individual oxides contribute to the high sum of squares of residuals (Table 2.6). The model for generation of a low Zr/Nb hawaiite has a better sum of squares of residuals (Table 2.6), but is still inferior to the models for crystal fractionation within the groups (Table 2.5). The trace element models do not account well for either the absolute abundance of individual incompatible elements or for the difference in Zr/Nb between the groups (Table 2.6) and crystal fractionation processes are not the primary control on the relatively wide range in Zr/Nb (4.1 to 6.0) in Ascension mafic rocks.

Partial melting

Variable extents of partial melting at low degrees of melting can significantly

fractionate incompatible trace element ratios. For example, for an enriched mantle source with 15 ppm Zr, 1.5 ppm Nb and D_{Zr} = 0.1, D_{Nb} = 0.01 during melting, magma with Zr/Nb of 4.0 would be generated by 5% batch melting whereas magma with Zr/Nb of 6.0 would be generated by 11% batch melting. Although none of the Ascension mafic lava flows have the chemical characteristics of primary magmas, aspects of the compositions of the high Zr/Nb group compared to the low Zr/Nb group are consistent with the latter being derived from magmas produced by a lower degree of melting. Incompatible element abundances are generally higher in the low Zr/Nb group than in the high Zr/Nb group (Fig. 2.8) and the more highly incompatible elements are more strongly enriched relative to the less incompatible elements (Figs. 9 and 10). The low Zr/Nb group also has higher Na_2O + K_2O relative to SiO_2 (Fig. 2.5). The intermediate Zr/Nb group might then be derived from magmas produced by a degree of melting between those for the high and low Zr/Nb magmas. These general considerations do not, however, necessarily imply a common mantle source for these three magma types. The Dark Slope Crater lava flows are unusual in that they have intermediate Zr/Nb but are substantially more enriched in the more incompatible elements (Fig. 2.8) than are the other mafic rock types, suggesting a distinctive source.

Combined with trace element data, Sr, Nd, and Pb isotopes can provide valuable insights into the characteristics and mixing of the source components involved in the generation of OIB magmas. Previously reported Nd isotope data for Ascension is limited (Weis et al, 1987, Halliday et al., 1992), but $^{143}Nd/^{144}Nd$ has only restricted variation from 0.51299 to 0.51321 in all rock types. $^{87}Sr/^{86}Sr$ is uniformly low (about 0.7030), except in some trachyte and pumice samples where even age corrected ratios are > 0.705 (Harris et al., 1982; Weis et al., 1987; Kar et al., Felsic MS).

Our Nd isotope data for Ascension Island mafic rocks (Table 2.7) extend to less

radiogenic compositions ($^{143}Nd/^{144}Nd$ 0.512918) than previously reported (lowest $^{143}Nd/^{144}Nd$ 0.513000, Halliday et al., 1992) but we do not find $^{143}Nd/^{144}Nd$ as high as the 0.51313 value reported for a basaltic tuff by Weis et al. (1987). There are distinctions in the Nd isotope compositions of some of the four mafic groups recognized from trace element data. The high Zr/Nb compositions have $^{143}Nd/^{144}Nd$ of 0.512992 to 0.513066 (Table 2.3, Fig. 2.11) whereas $^{143}Nd/^{144}Nd$ is lower in the low Zr/Nb group (0.512969 to 0.512972) and, particularly, the Dark Slope Crater group (0.512918 to 0.512974). The intermediate Zr/Nb group mostly has $^{143}Nd/^{144}Nd$ within the range of the high Zr/Nb group although three samples have lower $^{143}Nd/^{144}Nd$ (Fig. 2.11). The Broken Tooth flows have the highest $^{143}Nd/^{144}Nd$ of the mafic rocks (Table 2.7, Fig. 2.11); this is not related to the presence of the disaggregated syenite xenoliths in these flows, which have lower $^{143}Nd/^{144}Nd$ (Table 2.7). The Nd data therefore suggests that the high and (most) intermediate Zr/Nb magmas were derived from an isotopically similar source whereas the low Zr/Nb and Dark Slope Crater magmas were derived from a different, more enriched, source.

Ascension mafic rocks have a general trend of slightly increasing $^{87}Sr/^{86}Sr$ with decreasing $^{143}Nd/^{144}Nd$ (Fig. 2.12) although the range in $^{87}Sr/^{86}Sr$ is not large. Dark Slope Crater group rocks have the highest $^{87}Sr/^{86}Sr$ (Fig. 2.12), with the exception of samples which probably are altered and have secondary elevation of $^{87}Sr/^{86}Sr$ (powders analyzed for Sr isotopes were not leached). Sr isotope compositions of the high and intermediate Zr/Nb groups largely overlap, and the low Zr/Nb group has $^{87}Sr/^{86}Sr$ at the upper end of the range of the high and intermediate Zr/Nb groups (Fig. 2.12) from 0.702766 to 0.703263 and $^{143}Nd/^{144}Nd$ ranging from 0.512918 to 0.513066.

The Dark Slope Crater group has the most radiogenic Pb isotope compositions ($^{206}Pb/^{204}Pb$ ~19.85; Fig. 2.12) and the high Zr/Nb group less radiogenic Pb

($^{206}Pb/^{204}Pb$ ~19.4 to ~19.6; Fig. 2.12). Pb isotope ratios for the intermediate Zr/Nb group mostly overlap with the high Zr/Nb group, but extend toward the composition of Dark Slope Crater flows (Fig. 2.12). The low Zr/Nb group has Pb isotope ratios slightly higher than the high Zr/Nb group, but substantially lower than the Dark Slope Crater group (Fig. 2.12).

The Dark Slope Crater magmas were therefore derived from an enriched source having relatively radiogenic Sr and Pb and unradiogenic Nd (Fig. 2.12). Although the low Zr/Nb magmas were erupted in close proximity to Dark Slope Crater and have similar $^{143}Nd/^{144}Nd$ to the Dark Slope Crater flows, they have significantly less radiogenic $^{87}Sr/^{86}Sr$ and $^{206}Pb/^{204}Pb$ (Fig. 2.12), requiring a distinct source. The low Zr/Nb group lies at the enriched (low $^{143}Nd/^{144}Nd$, high $^{87}Sr/^{86}Sr$ and $^{206}Pb/^{204}Pb$) end of the isotopic arrays defined by the high Zr/Nb group and most of the intermediate Zr/Nb group (Fig. 2.12), suggesting that the isotopic variation in the high Zr/Nb, intermediate Zr/Nb, and low Zr/Nb groups is controlled by mixing between a depleted and a more enriched source. A Dark Slope Crater source component is, however, present in some of the intermediate Zr/Nb compositions (Fig. 2.12). There are, therefore, three distinct source components represented in the compositions of Ascension mafic volcanic rocks, a depleted source and two slightly different enriched sources. The overall similarity in Sr, Nd, and Pb isotope ratios in the high Zr/Nb and intermediate Zr/Nb groups suggests that the latter is derived from the same source region as the former but by a smaller degree of melting. Field relationships suggest that the intermediate Zr/Nb flows are younger than the high Zr/Nb flows, and data for shallow borehole samples (Kar et al., 1995) shows that flows with higher Zr/Nb than, but similar $^{143}Nd/^{144}Nd$ to, any of the surface flows are present in the subsurface; this indicates a temporal decrease in the degree of melting during the more recent magmatic evolution of Ascension Island.

Oxygen isotopes also provide an important tool for investigating the geochemical characteristics of the mantle source regions of OIB and alteration they undergo during their ascent and interaction with seawater. Sheppard & Harris (1985) report that whole rock $^{18}O/^{16}O$ of fresh alkali basalt, hawaiite, trachyandesite, trachyte, and comendite from Ascension range from +6.0 to +6.9‰ with $\delta^{18}O$ tending to increase with increase in SiO_2. Our data (Table 2.7) generally corresponds with that of Sheppard & Harris (1985) but also shows a significant spread in $\delta^{18}O$ values. Low Zr/Nb hawaiite have $\delta^{18}O$ values ranging from +6.5 to +7.1‰, high Zr/Nb basalt have $\delta^{18}O$ from +5.7 to +7.8‰, intermediate Zr/Nb mafic rocks have $\delta^{18}O$ between +5.0 and +7.8‰, and Dark Slope Crater flows have $\delta^{18}O$ between +6.8 to +7.5‰.

South Atlantic Ocean Mantle Heterogeneity and Ascension Island mafic rocks

The variable isotopic signatures of South Atlantic OIB suites (Fig. 2.1) suggests that the suboceanic mantle under the South Atlantic Ocean is geochemically heterogeneous on a large scale. However, this diversity also exists on a single island like Ascension (Fig. 2.1). The cause of this heterogeneity could result from; (1) mixing of different OIB mantle source components (HIMU, EMI, EMII), (2) mixing during ascent of a plume with the depleted upper mantle, and (3) interaction of magma with altered oceanic crust during magma ascent and residence in high level magma storage reservoirs.

The HIMU end-member is represented by volcanic rocks from St. Helena and has unusually radiogenic Pb ($^{206}Pb/^{204}Pb$ > 20.3), radiogenic Nd ($^{143}Nd/^{144}Nd$ 0.5128 to 0.5130), and unradiogenic Sr ($^{87}Sr/^{86}Sr$ 0.7027 to 0.7031) isotope compositions (Fig. 2.1). In marked contrast, volcanic rocks from the EMI islands of Tristan da Cunha and Gough have relatively unradiogenic Pb ($^{206}Pb/^{204}Pb$ 18.2 to 18.8), unradiogenic Nd ($^{143}Nd/^{144}Nd$ 0.5125 to 0.5127), and radiogenic Sr ($^{87}Sr/^{86}Sr$ 0.7042 to 0.7057) isotope

compositions (Fig. 2.1). Volcanic rocks from the islands of Fernando de Noronha, Trindade, and Bouvet have isotopic compositions between these extremes. Volcanic rocks from Ascension Island are distinctive in having radiogenic Nd isotope compositions ($^{143}Nd/^{144}Nd$ 0.5130 to 0.5131) which are similar to the compositions of mid-ocean ridge basalt (MORB) magmas erupted from the Mid-Atlantic Ridge in the South Atlantic (Weis et al., 1987). Ascension rocks have low $^{87}Sr/^{86}Sr$ similar to St. Helena, and Pb isotope compositions similar to Fernando de Noronha, Trindade, and Bouvet (Weis, 1983; Weis et al., 1987). In Sr-Nd space, the compositions of Ascension mafic volcanic rocks plot between compositions typical of Mid-Atlantic Ridge basalt and the compositions of St. Helena volcanic rocks (Weis et al., 1987). Weis et al. (1987) suggested that the isotopic compositions of Ascension lava flows reflect mixing between the N-MORB source and St. Helena-type (HIMU) OIB.

Ascension Island appears not to be hotspot-centered, the geophysical indications being that the Ascension hotspot presently is located east of the Mid-Atlantic Ridge (MAR) at approximately 10°S, some 225 km southeast of Ascension Island (Brozena, 1986). Hotspot derived magma would be channeled northward by sub-axial flow along the MAR, then deflected and erupted upon encountering the Ascension Fracture Zone (Brozena, 1986). Analysis of dredge samples from the MAR between 3°S and 15°S shows the influence of the hotspot on MORB chemistry (Schilling et al., 1986; Hanan et al., 1986; Fontignie & Schilling, 1996). North of the Ascension Fracture Zone is a typical N-MORB domain (La_N/Sm_N ~0.5, $^{206}Pb/^{204}Pb$ < 18; Fig. 2.13) and south of the Bode Verde Fracture Zone the MORB is of fairly uniform composition but somewhat more enriched (higher La_N/Sm_N, $^{206}Pb/^{204}Pb$) than typical N-MORB (Fig. 2.13). Between the Ascension and Bode Verde Fracture Zones there is a geochemical gradient (best defined by La_N/Sm_N) which suggests that the hotspot is located between 9°S and 10°S

(Fig. 2.13).

MORB from the 3°S to 15°S MAR segment define linear arrays in Sr-Nd and Pb-Pb space (Fig. 2.14) due to mixing between depleted, N-MORB source, mantle and an enriched mantle component. In Sr-Nd space the enriched component could be a St. Helena-type HIMU hotspot (Fig. 2.14), although it could also be a hotspot with higher $^{87}Sr/^{86}Sr$ and lower $^{143}Nd/^{144}Nd$ than the St. Helena HIMU source. In Pb-Pb space (Fig. 2.14) the 3°S to 15°S MORB define a trend parallel to the Northern Hemisphere Reference Line (NHRL; Hart, 1984) but displaced to higher $^{208}Pb/^{204}Pb$ (positive Δ8/4). The enriched end-member is therefore a HIMU-type source, but one with higher $^{208}Pb/^{204}Pb$ relative to $^{206}Pb/^{204}Pb$ compared to St. Helena OIB (which plot significantly displaced to the right hand side of the NHRL and have large negative Δ8/4).

Ascension Island mafic rocks have Sr-Nd compositions that plot on the 3°S to 15°S MORB array (Fig. 2.14) but have Pb-Pb compositions distinct from the 3°S to 15°S MORB array, and which plot on the other side (negative Δ8/4) of the NHRL (Fig. 2.14). Within the Ascension data there may be two subtle but distinct isotopic sub-sets. The high Zr/Nb, low Zr/Nb, and most of the intermediate Zr/Nb group samples define a trend from a depleted end-member toward the isotopic composition of St. Helena HIMU OIB (Fig. 2.13, Fig. 2.14), as suggested by Weis et al. (1987), The Dark Slope Crater, and some intermediate Zr/Nb, samples do not, however, fall on this trend, but rather define a separate trend which is more parallel to the NHRL in Pb-Pb space and extends to higher $^{87}Sr/^{86}Sr$ than St. Helena OIB in Sr-Nd space (Fig. 2.13, Fig. 2.14). The dominant enriched component in Ascension magmas is the St. Helena HIMU OIB composition (high Zr/Nb and intermediate Zr/Nb compositions volumetrically are predominant on Ascension). The second, subordinate, enriched component (which is only manifested in the Dark Slope Crater type flows erupted from just two scoria cones) is a HIMU

component with higher $^{208}Pb/^{204}Pb$ relative to $^{206}Pb/^{204}Pb$ than the St. Helena HIMU component.

The Dark Slope Crater gabbro xenoliths are not discussed in detail here. They have Pb isotope compositions (Harris et al., 1982; Weis et al., 1987) which plot to the left of the NHRL but have higher $^{208}Pb/^{204}Pb$ than the MAR MORB and define a mixing trend toward a component with low $^{206}Pb/^{204}Pb$ but elevated $^{207}Pb/^{204}Pb$ and $^{208}Pb/^{204}Pb$, although they have Sr and Nd compositions that plot within the range of the Ascension mafic volcanic rocks. However, our Pb isotope data for the Dark Slope Crater gabbro xenoliths is very similar to that for the lava flows and not as unradiogenic as previously reported.

The isotopic systematics of the Ascension mafic volcanic rocks therefore suggest that the hotspot component is of HIMU type with characteristics very similar to the St. Helena hotspot. Although hotspots can influence the composition of the MORB magmas at ridge axes over considerable distances from the hotspot (Schilling et al., 1986), it is doubtful that the St. Helena hotspot, some 1000 km distant, could have a significant effect on the mantle in the vicinity of Ascension Island. Rather, the Ascension hotspot may be sampling the same mantle source region as tapped by the St. Helena hotspot, but subaxial flow of the hotspot-derived magmas along the MAR results in greater interaction with the depleted upper mantle and dilution of the hotspot signature.

The Dark Slope Crater group represents very localized, relatively small volume volcanism. The different HIMU component present in the Dark Slope Crater group is perhaps most likely to represent a local enriched lithospheric source. However, the lithosphere under Ascension Island is very young (5- to 6-Ma-old) and even very high U/Pb would not be able to generate $^{206}Pb/^{204}Pb$ of close to 20 in such a short period of

time. The exact origin of this component remains somewhat uncertain.

CONCLUSIONS

1) Based on trace element characteristics, four distinct groups of mafic rocks are identified on Ascension Island: a low Zr/Nb hawaiite group, a high Zr/Nb basalt group, an intermediate Zr/Nb basalt to benmoreite group, and, a subset of the intermediate Zr/Nb group, the Dark Slope Crater hawaiite and mugearite group.

2) Crystal fractionation controls the chemical variation within each group, but cannot account for the chemical differences between the groups.

3) There are significant differences in the Sr, Nd, and Pb isotopic compositions of some of the groups. Lava flows from Dark Slope Crater have the lowest $^{143}Nd/^{144}Nd$ and the highest $^{87}Sr/^{86}Sr$ and $^{206}Pb/^{204}Pb$. The low Zr/Nb group has similar $^{143}Nd/^{144}Nd$ to the Dark Slope Crater group, but lower $^{87}Sr/^{86}Sr$ and $^{206}Pb/^{204}Pb$. The high Zr/Nb and intermediate Zr/Nb groups have generally similar Sr-Nd-Pb systematics, with higher $^{143}Nd/^{144}Nd$ and lower $^{87}Sr/^{86}Sr$ and $^{206}Pb/^{204}Pb$ than the Dark Slope Crater and low Zr/Nb groups. These relationships can be explained by mixing between three mantle components, one depleted component and two distinct enriched components.

4). The similarity of Sr, Nd, and Pb isotopic compositions between the younger intermediate Zr/Nb group and the older high Zr/Nb group, and the presence in the subsurface of flows with higher Zr/Nb but similar $^{143}Nd/^{144}Nd$, implies that the degree of partial melting of the same overall mantle source has decreased over time.

5) In $^{208}Pb/^{204}Pb$ - $^{206}Pb/^{204}Pb$ space the Ascension volcanic rocks are displaced to the right of the NHRL and define two mixing trends, one to a HIMU component with the composition of the St. Helena HIMU source, the other also a HIMU component but with higher $^{208}Pb/^{204}Pb$ relative to $^{206}Pb/^{204}Pb$ than the St. Helena source.

6) The St. Helena HIMU component represents the composition of the hotspot which

has mixed with the depleted upper mantle to varying degrees to produce the magmas of the high Zr/Nb, intermediate Zr/Nb, and low Zr/Nb groups.

7) The second HIMU component is only represented in the volumetrically minor Dark Slope Crater group, and this may represent a local enriched lithospheric source.

ACKNOWLEDGMENTS

This paper is a part of a Ph.D. dissertation by Aditya Kar. The project was supported by NSF grant EAR-9204079.

REFERENCES

Adams, M.C., 1996. Chemistry of fluids from Ascension #1, a deep geothermal well on Ascension Island, South Atlantic Ocean. Geothermics 25: 561-579.

Atkins, F.B., Baker, P.E., & Smith, D.G.W., 1964. Oxford expedition to Ascension island. Nature 204: 722-724.

Barling J., & Goldstein, S.L., 1990. Extreme isotopic variations in Heard Island lavas and the nature of mantle reservoirs. Nature 348: 59-62.

Borthwick, J., & Harmon, R.S., 1982. A note regarding ClF_3 as an alternative to BrF_5 for oxygen isotope analyses. Geochimica et Cosmochimica Acta 46: 1665-1668.

Brozena, J.M., 1986. Temporal and spatial variability of seafloor spreading processes in the northern South Atlantic. Journal of Geophysical Research 91: 497-510.

Chaffey, D.J., Cliff, R.A., & Wilson, B.M., 1989. Characterization of the St. Helena magma source. In: Magmatism in the ocean basins (Saunders, A.D., & Norry, M.J. editors), Geological Society of London Special Publication 42: 257-276.

Cliff, R.A., Baker, P.E., & Mateer, N.J., 1991. Geochemistry of Inaccessible Island volcanics. Chemical Geology, 92: 251-260.

Cohen, R.S., & O'Nions, R.K., 1987. Identification of recycled continental material in the mantle from Sr, Nd and Pb isotope investigations. Earth and Planetary Science Letters

Cornen, G., Deniel, C., & Joron, J. -L., 1990. Meeting with a new oceanic carbonatite on Trindade Island (South Atlantic). Abstracts, IAVCEI, Mainz.

Daly, R.A., 1925. The geology of Ascension Island. Proc. Am. Acad. Arts Sci. 60: 1-80.

Davidson, J.P., & Wilson, I.R., 1989. Evolution of an alkali basalt-trachyte suite from Jebel Marra volcano, Sudan, through assimilation and fractional crystallization. Earth and Planetary Science Letters 95: 141-160.

Davidson, J.P., Boghossian, N.D., & Wilson, B.M., 1993. The Geochemistry of the Igneous Rock Suite of St. Martin, Northern Lesser Antilles. Journal of Petrology 34: 839-866.

Fontignie, D. & Schilling, J.-G., 1996. Mantle heterogeneities beneath the South Atlantic: a Nd-Sr-Pb isotope study along the Mid-Atlantic Ridge (3°S-46°S). Earth and Planetary Science Letters 142: 209-221.

Gerlach, D.C., Stormer, J.C., & Mueller, P.A., 1987. Isotopic geochemistry of Fernando de Noronha. Earth and Planetary Science Letters 85: 129-144.

Halliday, A.N., Davies, G.R., Lee, D-C, Tommasini, S, Paslick, C.R., Fitton, J.G., & James, D.E., 1992. Lead isotope evidence for young trace element enrichment in the oceanic upper mantle. Nature 359: 623-627.

Hanan, B.B., Kingsley, R.H., & Schilling, J.-G. 1986. Pb isotope evidence in the South Atlantic for migrating ridge-hotspot interactions. Nature 322, 137-144.

Harris, C., 1983. The petrology of lavas and associated plutonic inclusions of Ascension Island. Journal of Petrology 24: 424-470.

Harris, C., 1985. Guano-derived rare earth-rich phosphate amygdales in gabbroic inclusions from Ascension Island. Earth and Planetary Science Letters 72: 141-148.

Harris, C., & Bell, J.D., 1982. Natural partial melting of syenite blocks from Ascension Island. Contributions to Mineralogy and Petrology 79: 107-113.

Harris, C., Bell, J.D., & Atkins, F.B., 1982. Isotopic composition of lead and strontium in lavas and coarse-grained blocks from Ascension Island, South Atlantic. Earth and Planetary Science Letters 60: 79-85.

Harris, C., & Sheppard, S.M.F., 1987. Hydrogen and oxygen isotope geochemistry of Ascension Island lavas and granites: Variation with crystal fractionation and interaction with seawater. Contributions to Mineralogy and Petrology 91: 74-81.

Hart, S.R., 1984. A large-scale isotope anomaly in the Southern Hemisphere mantle. Nature 309: 753-757.

Hart, S.R., 1988. Heterogeneous mantle domains: Signatures, genesis and mixing chronologies. Earth and Planetary Science Letters 90: 27-296.

Hart, S.R., & Dunn, T., 1993. Experimental cpx/melt partitioning of 24 trace elements. Contributions to Mineralogy and Petrology 113: 1-8.

Kar, A., Weaver, B.L., Davidson, J.P., & Nielson, D., 1995. Geochemical characteristics of borehole samples recovered from Ascension Island, South Atlantic Ocean. GSA Abstracts with Programs 27 no. 6: A-254.

Kar, A., Weaver, B., Davidson, J., & Colucci, M., (Felsic MS). Felsic oceanic island magmatism: Origin of high $^{87}Sr/^{86}Sr$ evolved volcanic and plutonic rocks from Ascension Island, South Atlantic Ocean. Journal of Petrology (in review).

Le Bas, M.J., Le Maitre, R.W., Streckeisen, A., & Zanelttiu, B., 1986. A chemical classification of volcanic rocks based on the total alkali-silica diagrams. Journal of Petrology 27: 745-750.

Le Roex, A.P., Cliff, R.A., & Adair, B.J., 1990. Tristan da Cunha, South Atlantic: Geochemistry and petrogenesis of a basanite-phonolite lave series. Journal of Petrology 31: 779-812.

McDonough, W.F., & Sun, S., -S., 1995. The composition of the Earth. Chemical Geology 120: 223-253.

Nielson, D.L., 1996. Introduction to geothermal exploration on Ascension Island, South Atlantic Ocean. Geothermics 25: 419-425.

Nielson, D.L., & Sibbett, B.S., 1996. Geology of Ascension Island, South Atlantic Ocean. Geothermics 25: 427-448.

Nielson, D.L., & Stiger, S.G., 1996. Drilling and evaluation of Ascension #1, a

geothermal exploration well on Ascension Island, South Atlantic Ocean. Geothermics 25: 543-560.

O'Nions, R.K., Hamilton, P.J., & Evensen, N.M., 1977. Variations in $^{143}Nd/^{144}Nd$ and $^{87}Sr/^{86}Sr$ ratios in oceanic basalts. Earth and Planetary Science Letters 34: 13-22.

Roedder, E., & Coombs, D.S., 1967. Immiscibility in granitic melts indicated by fluid inclusions in ejected granite blocks of Ascension Island. Journal of Petrology 8: 417-451.

Schilling, J.G., Thompson, G., Kingsley, R., & Humphris, R.E., 1986. Hotspot-migrating ridge interaction in the South Atlantic. Nature 313:187-191.

Sheppard, S.M.F., & Harris, C., 1987. Magma and fluid evolution in the lavas and associated granite xenoliths of Ascension Island. Alkaline Igneous Rocks (Fitton, J.G. and Upton, B.G.J. ed.), Geological Society of London Special Publication 30: 269-272.

Sun, S. -S., 1980. Lead isotopic study of young volcanic rocks from mid-ocean ridges, ocean islands and island arcs. Phil. Trans. Royal Society of London, A297: 405-445.

Weaver, B.L., Tarney, J., & Joron, J. L., 1987. Geochemistry of ocean island basalts from the South Atlantic: Ascension, Bouvet, St. Helena, Gough and Tristan da Cunha. Alkaline Igneous Rocks (Fitton, J.G. and Upton, B.G.J. editors), Geological Society of London Special Publication 30: 253-267.

Weaver, B.L., 1990. Geochemistry of highly-undersaturated ocean island basalt suites from the South Atlantic Ocean: Fernando de Noronha and Trinidade islands. Contributions to Mineralogy and Petrology 12 105, 502-515.

Weaver, B.L., 1991a. Trace element evidence for the origin of ocean island basalts. Geology 19: 123-126.

Weaver, B.L., 1991b. The origin of ocean island basalt end-member compositions: Trace element and isotopic constraints. Earth and Planetary Science Letters 104: 381-397.

Weaver, B.L., Rubenstone, J.L., Zindler, A., & Sachi-Kocher, A., 1991. Geochemistry of volcanic rocks from Saint Helena and implications for the origin of HIMU OIB. EOS 72: 318.

Weaver, B.L., Kar, A., & Davidson, J.P., 1995. Unusual behaviour of phosphorus in mafic lavas from Ascension Island, South Atlantic Ocean. EOS 76 no. 46: F698

Weaver, B.L., Kar, A., Davidson, J.P., and Colucci, M., 1996. Geochemical characteristics of volcanic rocks from Ascension Island, South Atlantic Ocean. Geothermics 25: 449-470.

Weis, D., 1983. Pb isotopes in Ascension Island rocks: Oceanic origin for the gabbroic to granitic plutonic xenoliths. Earth and Planetary Science Letters 62: 273-282.

Weis, D., Demaiffe, D., Cauet, S., & Javoy, M., 1987. Sr, Nd, 0 and H isotopic ratios in Ascension Island lavas and plutonic inclusions, cogenetic origin. Earth and Planetary Science Letters 82: 255-268.

White, W.M., 1985. Sources of oceanic basalts: Radiogenic isotope evidence. Geology 13: 115-118.

White, W.M., & Hofmann, A.W., 1982. Sr and Nd isotope geochemistry of oceanic basalts and mantle evolution. Nature 296: 821-825.

Woodhead, J.D., & McCulloch, M.T., 1989. Ancient seafloor signals in Pitcairn Island lavas and evidence for large amplitude, small length-scale mantle heterogeneities. Earth and Planetary Science Letters 94: 257-273.

Zindler, A., & Hart, S.R., 1986. Chemical geodynamics. Annual Reviews of Earth and Planetary Science 14: 493-571.

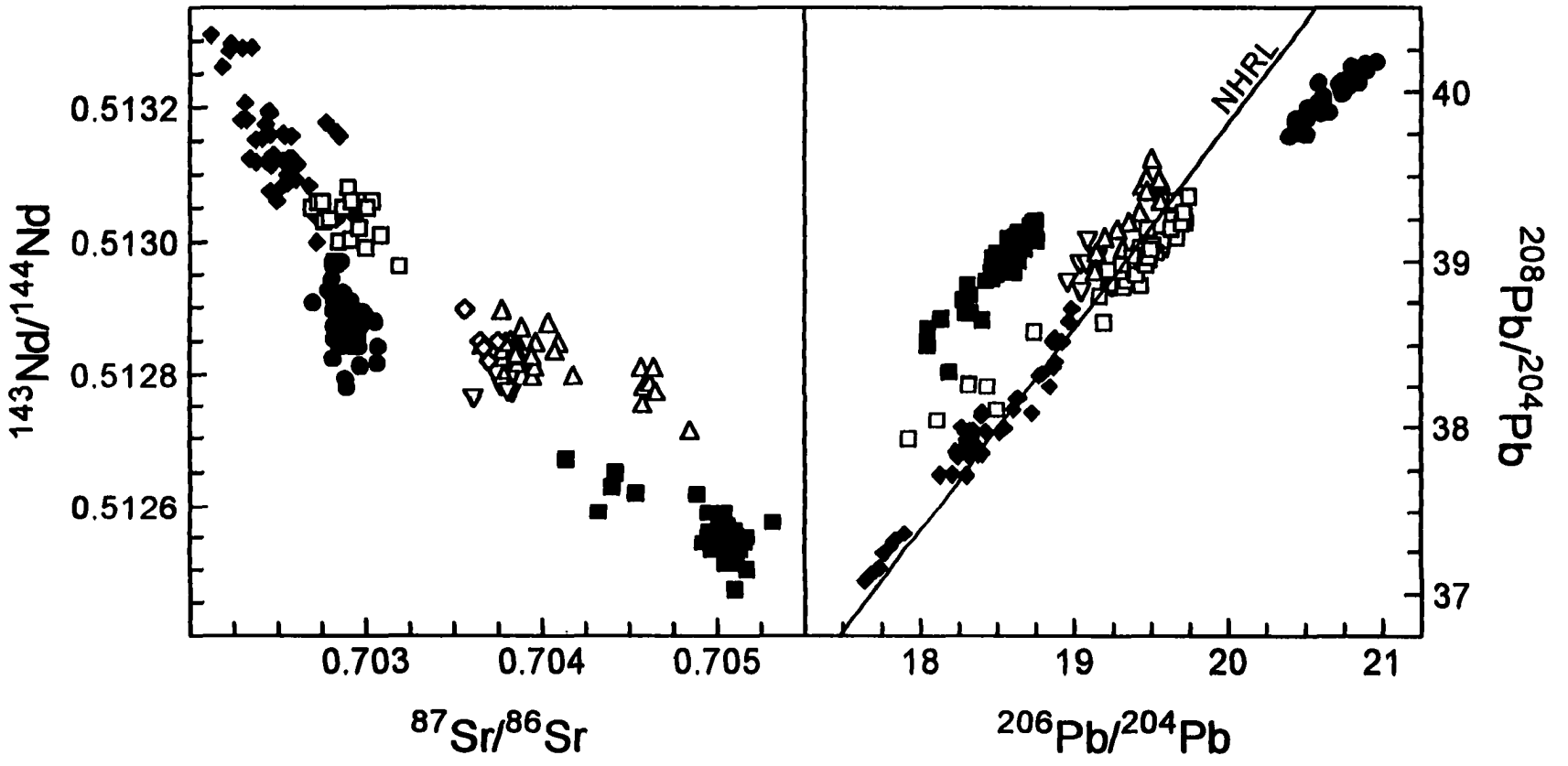

Figure 2.1. Variation in $^{87}Sr/^{86}Sr$ *vs.* $^{143}Nd/^{144}Nd$ and $^{208}Pb/^{204}Pb$ *vs.* $^{208}Pb/^{204}Pb$ for OIB and N-MORB from the South Atlantic Ocean. OIB are: □ Ascension; ◇ Bouvet; △ Fernando de Noronha; ■ Gough and Tristan da Cunha; ▽ Trindade; ● St. Helena. ◆ N-MORB from the Mid-Atlantic Ridge in the South Atlantic Ocean (only MORB samples with $^{87}Sr/^{86}Sr < 0.703$, $^{143}Nd/^{144}Nd > 0.5130$, $^{206}Pb/^{204}Pb < 19$, and $\Delta 8/4 < +30$ are plotted). The Northern Hemisphere Reference Line (NHRL; Hart, 1984) is shown on the $^{206}Pb/^{204}Pb$ *vs.* $^{208}Pb/^{204}Pb$ diagram. Data sources: O'Nions et al. (1977), Sun (1980), Cohen & O'Nions (1982), Harris et al. (1982), White & Hofmann (1982), Weis (1983), Hanan et al. (1986), Gerlach et al. (1987), Weis et al. (1987), Chaffey et al. (1989), Cornen et al. (1990), Le Roex et al. (1990), Cliff et al. (1991), Halliday et al. (1992), Fontignie & Schilling (1996).

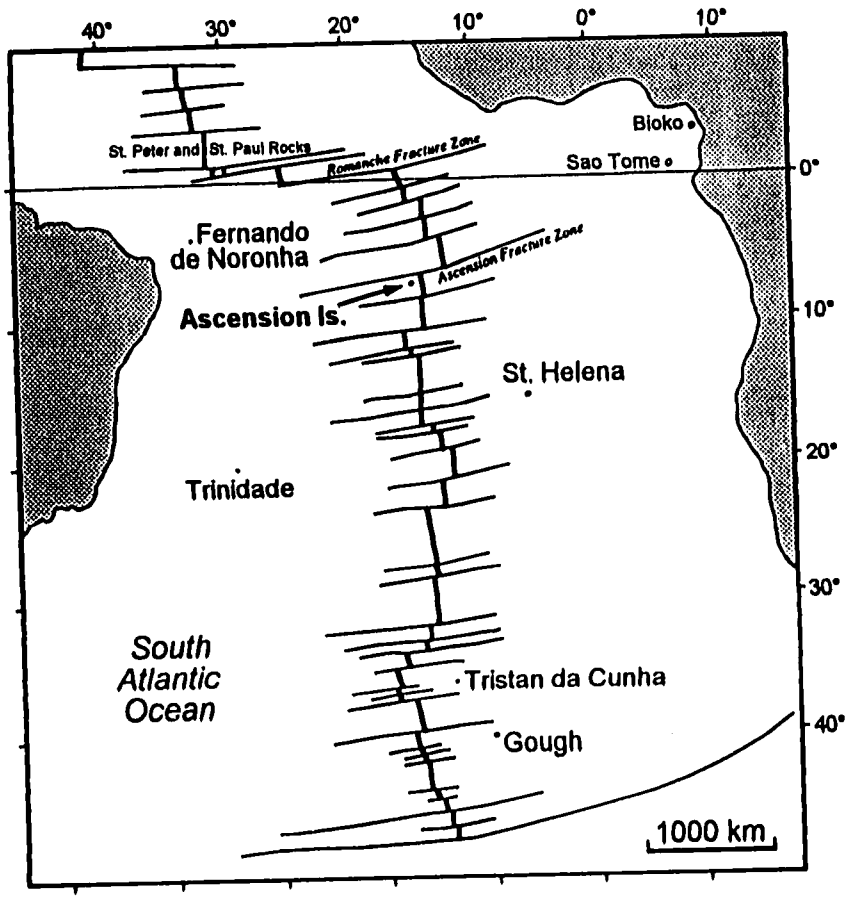

Figure 2.2. Map of part of the South Atlantic Ocean showing the locations of oceanic islands, the axis of the Mid-Atlantic Ridge, and major transform faults and fracture zones. After Nielson (1996).

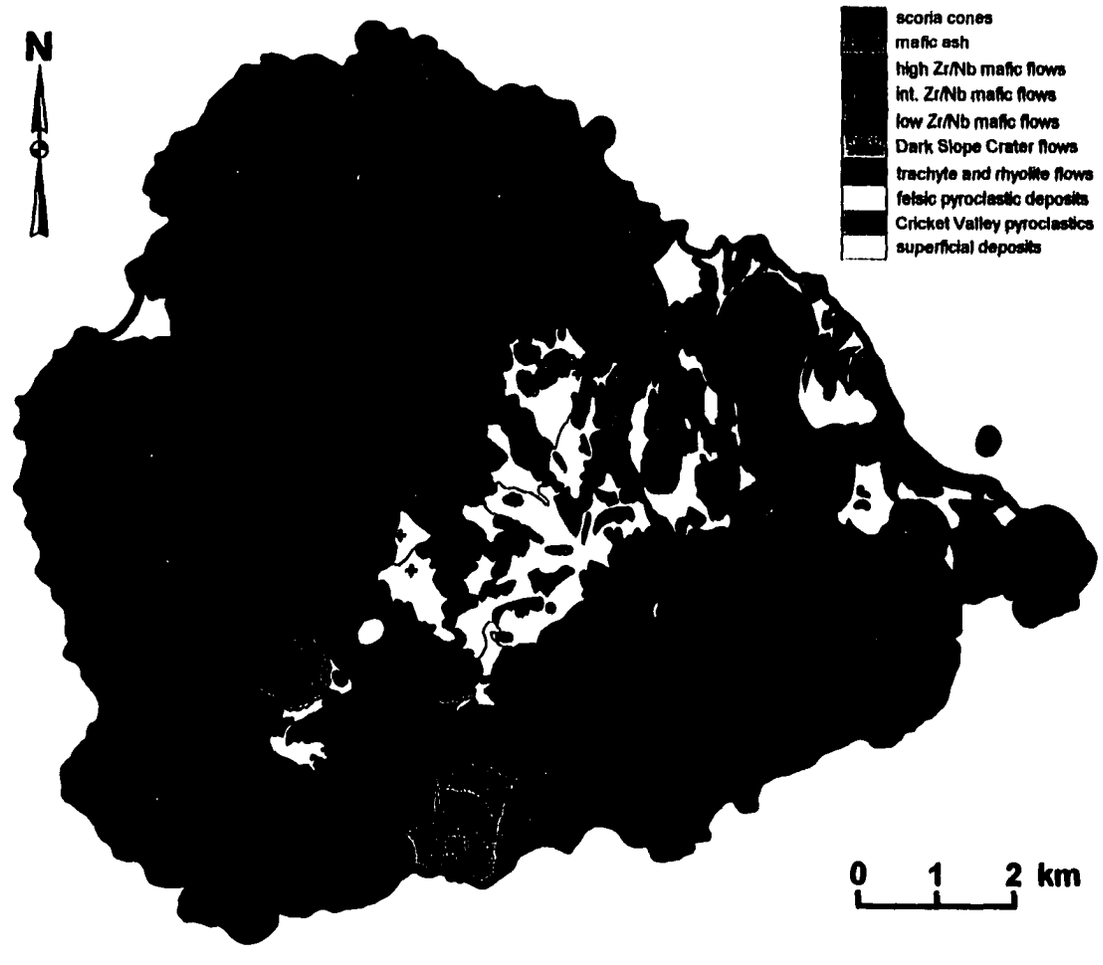

Figure 2.3. Geological map of Ascension Island, somewhat modified from Nielson and Sibbett (1996). The four geochemically distinct mafic rock types (high Zr/Nb, intermediate Zr/Nb, low Zr/Nb, and Dark Slope Crater) are identified and the compositions of selected flows are indicated as: **B** basalt, **H** hawaiite, **M** mugearite, **Be** benmoreite.

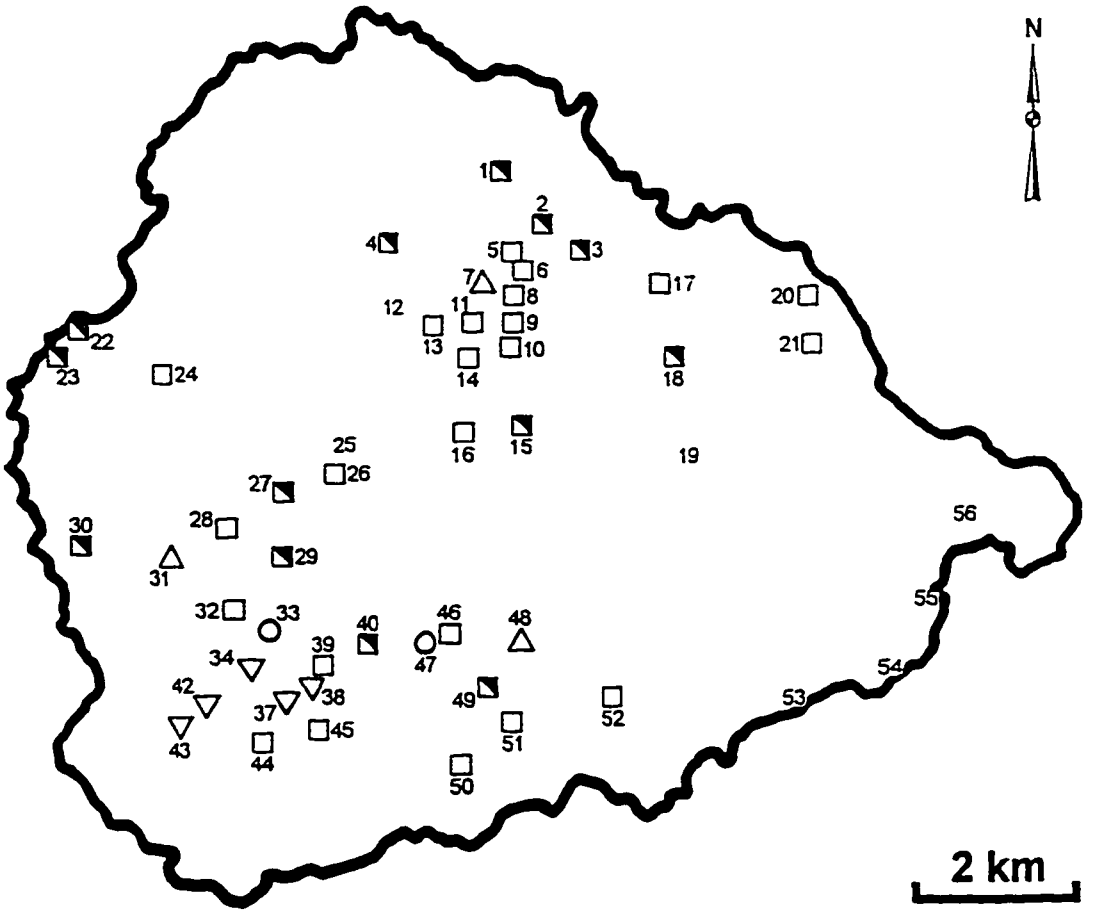

Figure 4. Map of Ascension Island showing the location and compositional characteristics of the scoria cones listed in Table 2.1. Symbols used to designate the composition of the cones are: △ high Zr/Nb basalt, ▽ low Zr/Nb hawaiite, □ intermediate Zr/Nb basalt and hawaiite, ◪ intermediate Zr/Nb mugearite and benmoreite, and ○ Dark Slope Crater hawaiite and mugearite.

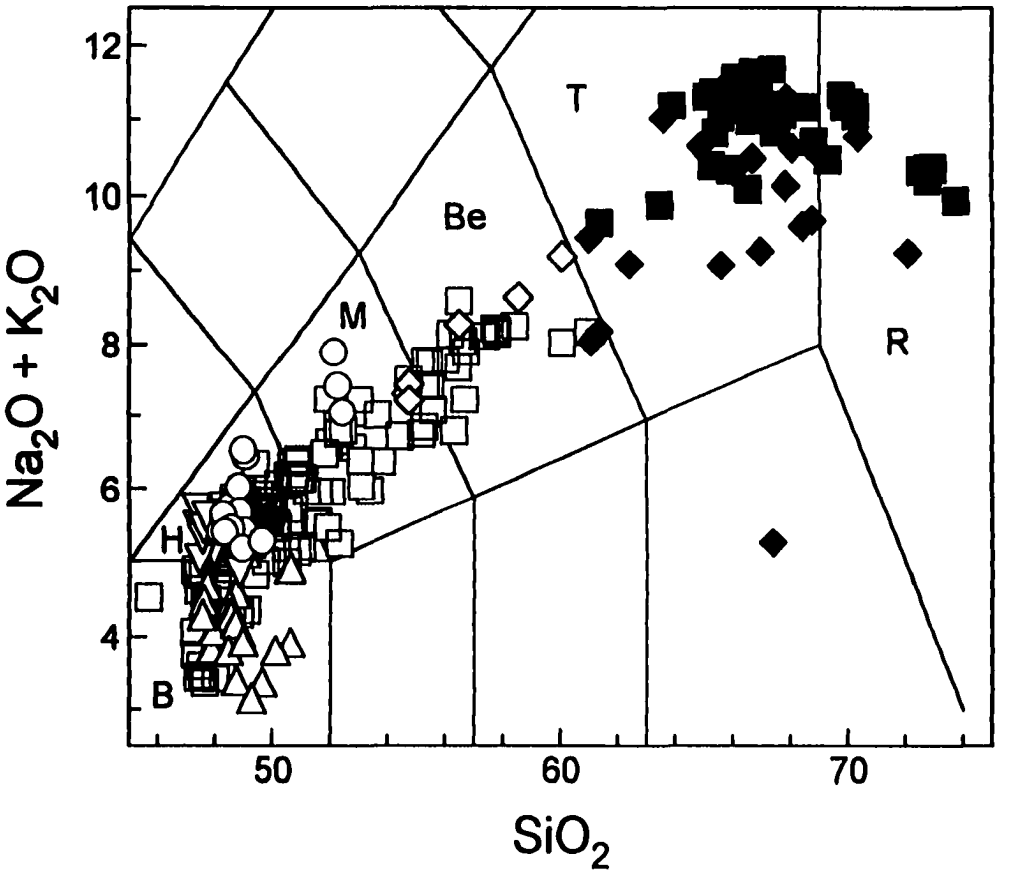

Figure 2.5. Variation in SiO_2 (wt%) *vs.* Na_2O+K_2O (wt%) for volcanic rocks from Ascension Island. The classification fields (B basalt; H hawaiite; M mugearite; Be benmoreite; T trachyte; R rhyolite) are those of Le Bas et al. (1986). △ high Zr/Nb basalt; □ intermediate Zr/Nb basalt to benmoreite; ▽ low Zr/Nb hawaiite; O Dark Slope Crater hawaiite and mugearite; ◇ Broken Tooth mugearite and benmoreite; ◆ trachyte and rhyolite pumice; ■ trachyte and rhyolite flows and flow domes.

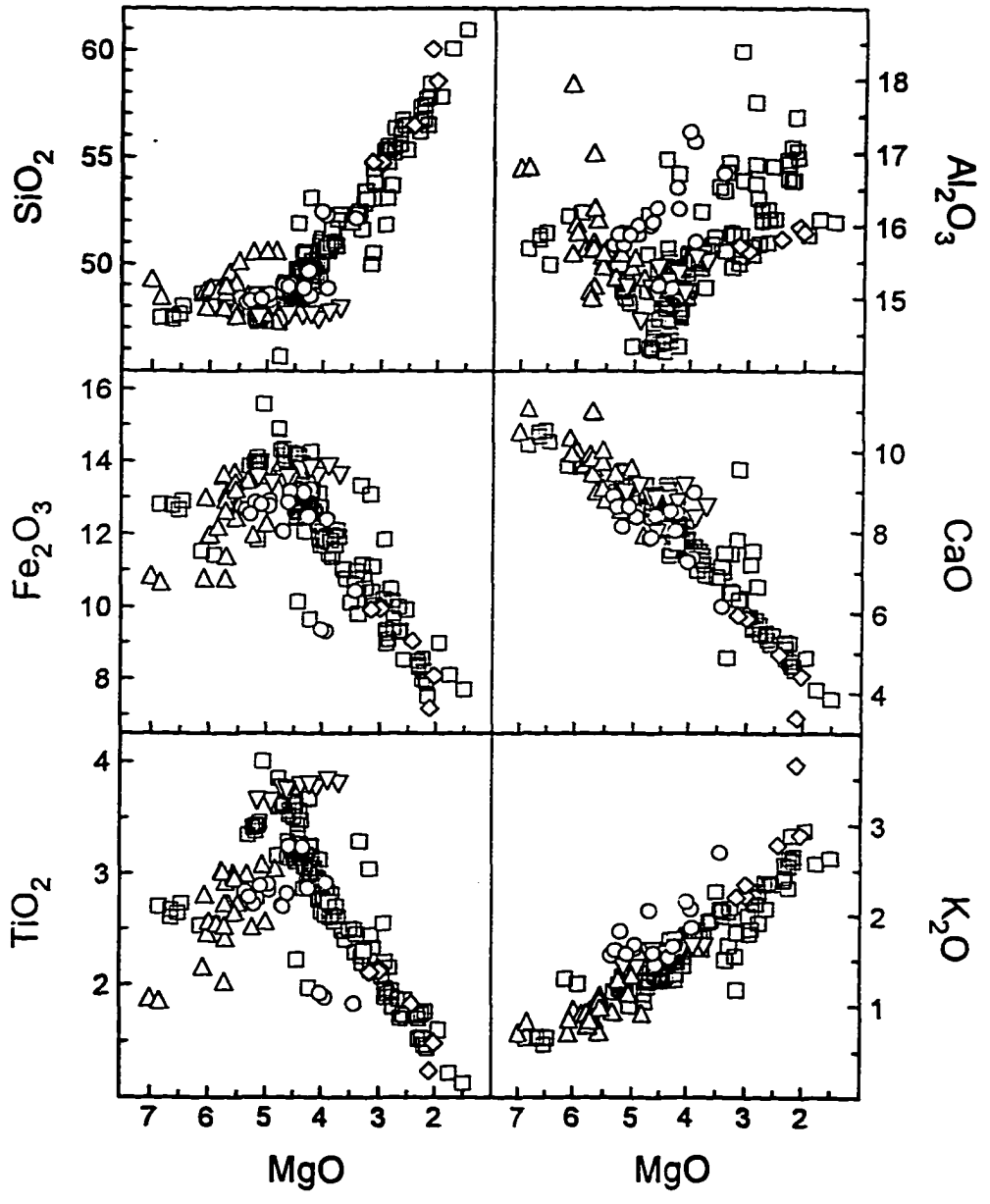

Figure 6. Variation in MgO *vs.* SiO_2, Al_2O_3, Fe_2O_3, CaO, TiO_2, and K_2O (all in wt%) for mafic rocks (basalt to benmoreite) of Ascension Island. Symbols denote compositional groups as defined in Fig. 2.5.

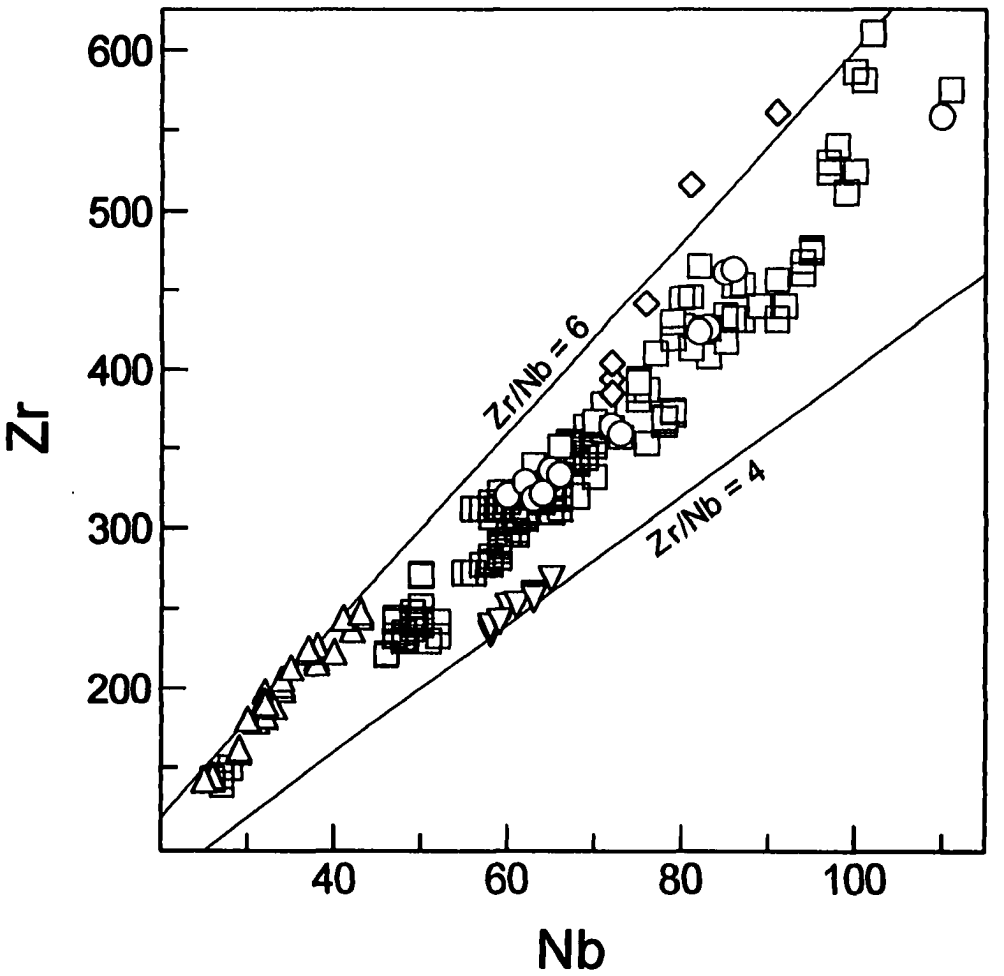

Figure 2.7. Variation in Nb *vs.* Zr (both in ppm) for basalt to benmoreite volcanic rocks from Ascension Island. Symbols denote compositional groups as defined in Fig. 5.

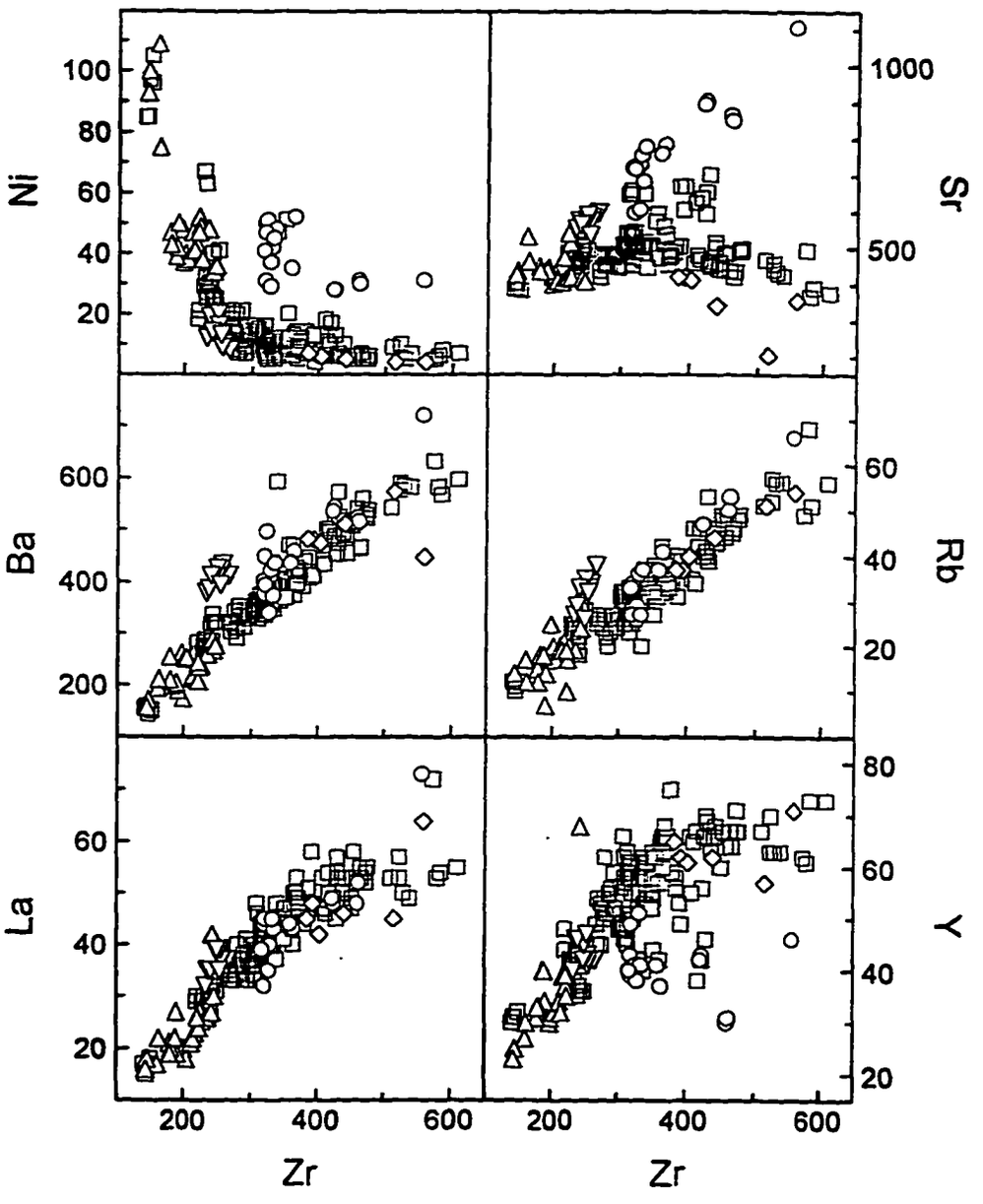

Figure 8. Variation in Zr *vs.* Ni, Sr, Ba, Rb, La, and Y (all in ppm) for basalt to benmoreite volcanic rocks from Ascension Island. Symbols denote compositional groups as defined in Fig. 2.5.

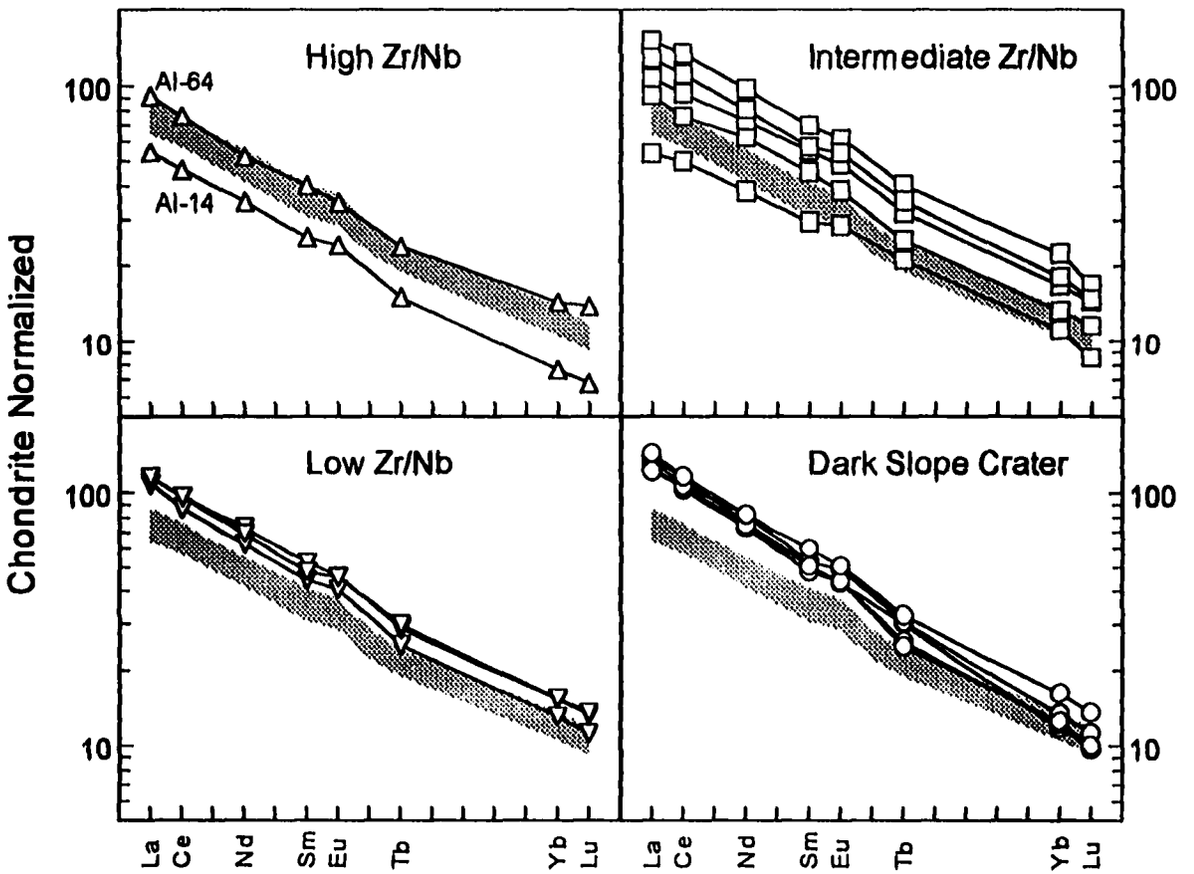

Figure 2.9. Rare earth element patterns (normalized to chondrite values of Nakamura, 1974) for mafic rocks from Ascension Island. For the high Zr/Nb group, the shaded field (also shown on the diagrams for the other groups) represents the range of REE patterns for six high Zr/Nb basalt samples; Al-14 (a highly phyric sample from South West Bay Red Hill) and Al-64 (Cricket Valley flow) are distinguished separately. For the intermediate Zr/Nb group, only basalt and hawaiite compositions are plotted and for the Dark Slope Crater group only hawaiite compositions are plotted.

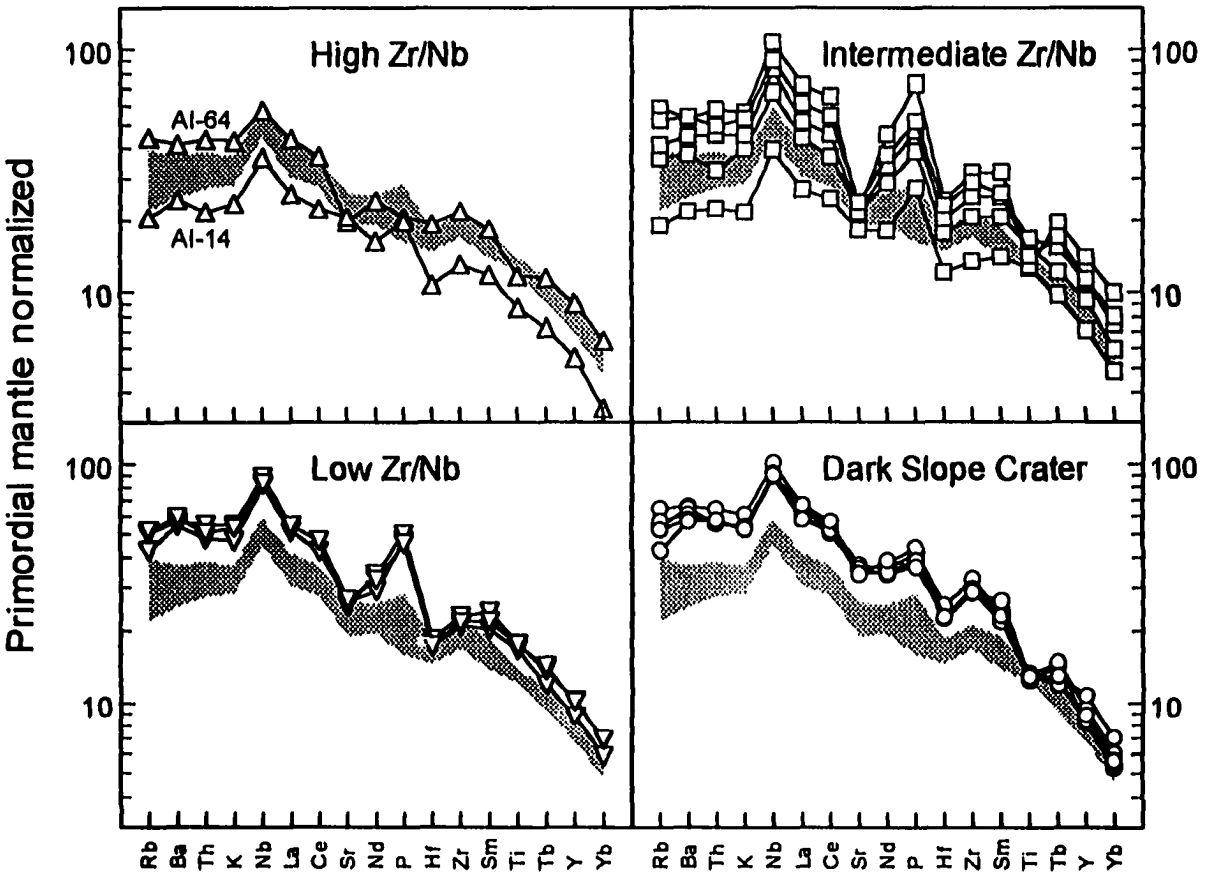

Figure 2.10. Incompatible element patterns (normalized to primordial mantle values of McDonough & Sun, 1995) for mafic rocks from Ascension Island. For the high Zr/Nb group, the shaded field (also shown on the diagrams for the other groups) represents the range of six high Zr/Nb basalt samples; Al-14 (a highly phyric sample from South West Bay Red Hill) and Al-64 (Cricket Valley flow) are distinguished separately. For the intermediate Zr/Nb group only basalt and hawaiite compositions are plotted and for the Dark Slope Crater group only hawaiite compositions are plotted.

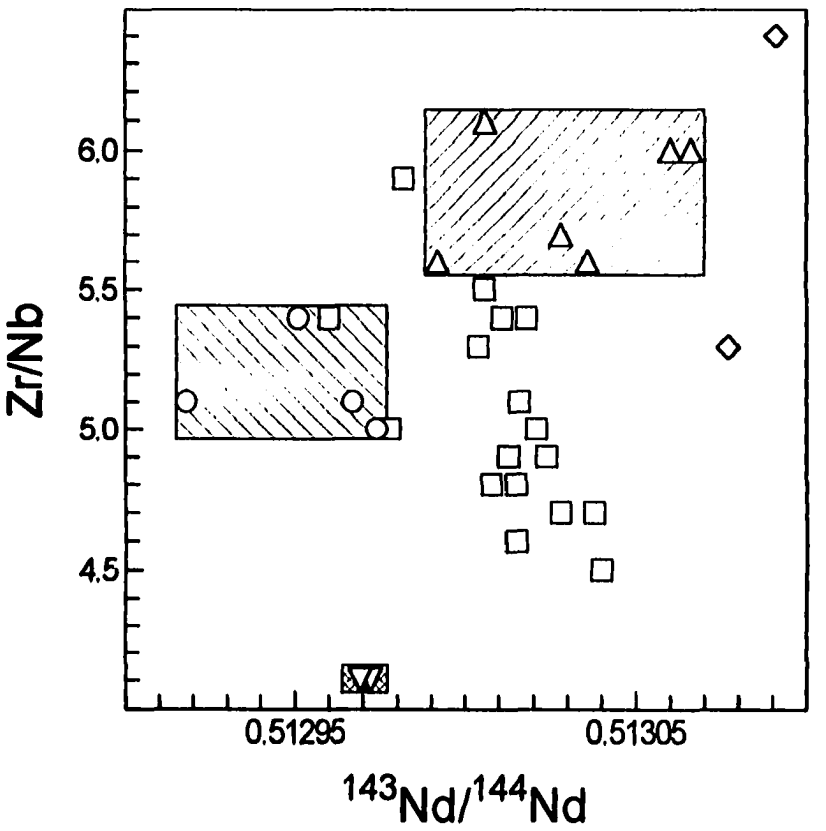

Figure 2.11. Variation in $^{143}Nd/^{144}Nd$ *vs.* Zr/Nb for mafic rocks from Ascension Island. Symbols denote compositional groups as defined in Fig. 5 and the compositional fields for the high and low Zr/Nb groups and the Dark Slope Crater group are outlined by rectangles.

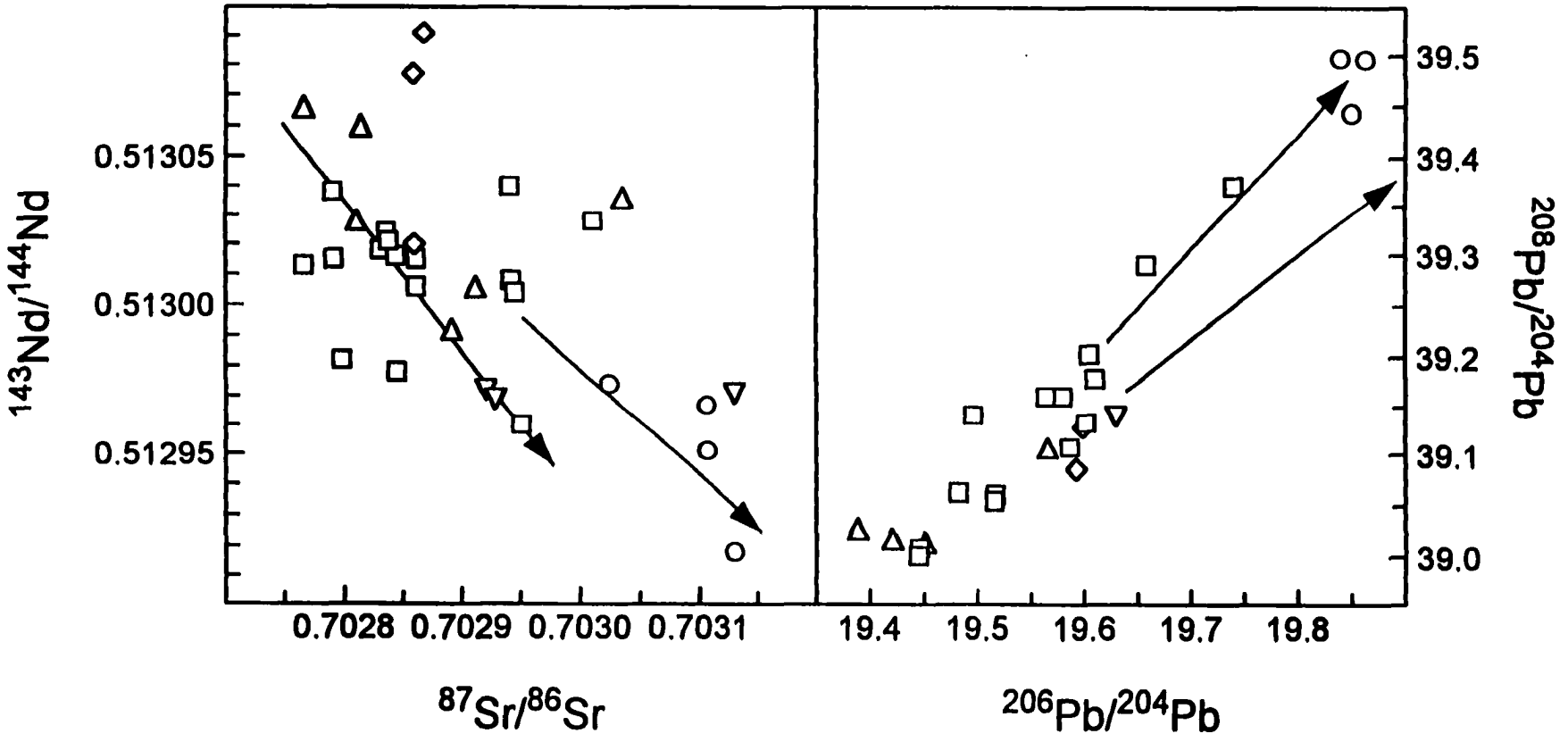

Figure 12. Variation in $^{87}Sr/^{86}Sr$ *vs.* $^{143}Nd/^{144}Nd$ and $^{206}Pb/^{204}Pb$ *vs.* $^{208}Pb/^{204}Pb$ for mafic rocks from Ascension Island. Symbols denote compositional groups as defined in Fig. 2.5.

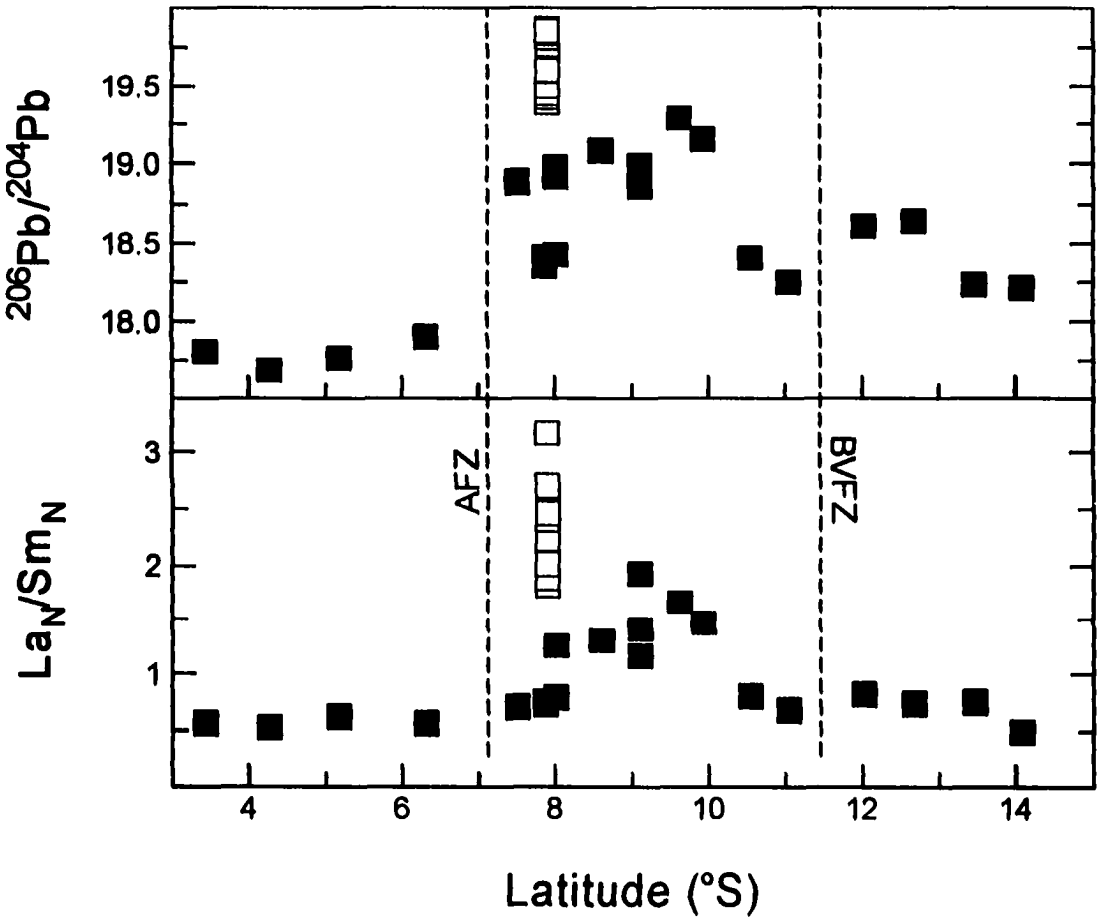

Figure 2.13. Variation in $^{206}Pb/^{204}Pb$ and La_N/Sm_N with latitude between 3°S and 15°S on the Mid-Atlantic Ridge. ■ MORB dredged from the ridge axis (Hanan et al., 1986; Fontignie & Schilling, 1996); □ Ascension Island volcanic and plutonic rocks.

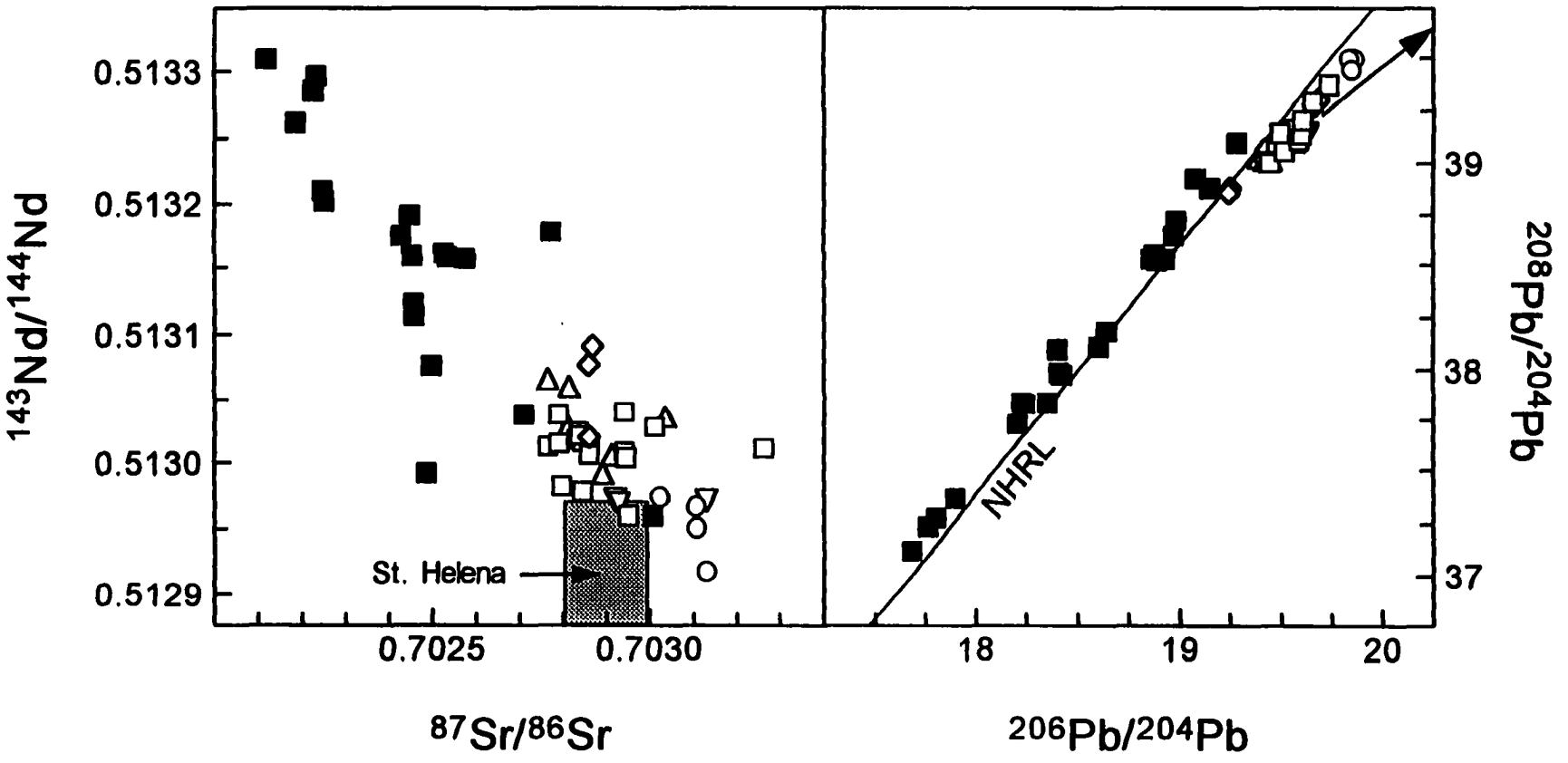

Figure 2.14. Variation in $^{87}Sr/^{86}Sr$ *vs.* $^{143}Nd/^{144}Nd$ and $^{208}Pb/^{204}Pb$ *vs.* $^{206}Pb/^{204}Pb$ for MORB from the MAR axis between 3°S and 15°S (■; Hanan et al., 1986; Fontignie & Schilling, 1996) and Ascension Island mafic rocks (symbols as defined in Fig. 5). The Northern Hemisphere Reference Line (NHRL; Hart, 1984) is shown on the $^{206}Pb/^{204}Pb$ *vs.* $^{208}Pb/^{204}Pb$ diagram and the arrow labeled SH points to the compositional field for volcanic rocks from St. Helena (see also Fig. 1).

Table 2.1. Locations and chemical characteristics of Ascension Island scoria cones.

Cone No.	Name	Grid Reference	Composition	Sample scoria	Sample flow
1	Broken Tooth	703258	Mugearite to benmoreite	✓	✓
2	Hollow Tooth	709251	Benmoreite	✓	
3	unnamed	714247	Benmoreite	✓	✓
4	unnamed	689248	Mugearite		✓
5	unnamed	704247	Hawaiite (intermediate Zr/Nb)	✓	
6	unnamed	706245	Hawaiite (intermediate Zr/Nb)	✓	
7	Sisters Red Hill	700244	Basalt (high Zr/Nb)	✓	
8	unnamed	704242	Hawaiite (intermediate Zr/Nb)	✓	
9	Street Crater	705238	Hawaiite (intermediate Zr/Nb)		✓
10	Butt Crater	704235	Hawaiite (intermediate Zr/Nb)	✓	✓
11	Perfect Crater	699239	Hawaiite (intermediate Zr/Nb)	✓	
12	unnamed	687241	not known		
13	Sisters Peak	693239	Hawaiite (intermediate Zr/Nb)	✓	✓
14	unnamed	699234	Hawaiite (intermediate Zr/Nb)	✓	
15	Thistle Hill	705225	Mugearite	✓	
16	Travellers Hill	697225	Hawaiite (intermediate Zr/Nb)	✓	✓
17	Lower Valley Crater	724243	Basalt (intermediate Zr/Nb)	✓	
18	Upper Valley Crater	726234	Mugearite		✓
19	unnamed	730221	not known		
20	unnamed	743241	Hawaiite (intermediate Zr/Nb)		✓
21	unnamed	744233	Hawaiite (intermediate Zr/Nb)		✓
22	Fort Thornton	647240	Benmoreite		✓
23	Fort Hayes	645236	Benmoreite	✓	
24	Cross Hill	658233	Basalt (intermediate Zr/Nb)	✓	✓
25	unnamed	682222	not known		
26	Lady Hill	681219	Hawaiite (intermediate Zr/Nb)	✓	✓
27	unnamed	674218	Benmoreite	✓	✓
28	unnamed	667213	Hawaiite (intermediate Zr/Nb)	✓	
29	Table Crater	674209	Mugearite	✓	
30	Cat Hill	648211	Benmoreite	✓	✓
31	South West Bay Red Hill	660209	Basalt (high Zr/Nb)	✓	✓
32	Command Hill	668202	Basalt (intermediate Zr/Nb)		✓
33	Dark Slope Crater	672199	Hawaiite to mugearite (DSC-type)		✓
34	Horse Shoe Crater	670193	Hawaiite (low Zr/Nb)		✓
35	unnamed	666193	not known		
36	unnamed	670190	not known		
37	unnamed	674190	Hawaiite (low Zr/Nb)	✓	
38	unnamed	678192	Hawaiite (low Zr/Nb)	✓	✓
39	unnamed	679195	Hawaiite (intermediate Zr/Nb)	✓	
40	unnamed	684196	Mugearite	✓	
41	unnamed	681192	not known		
42	Round Hill	664190	not known		
43	Cotar Hill	661187	Hawaiite (low Zr/Nb)		✓
44	South Gannet Hill	671185	Basalt (intermediate Zr/Nb)	✓	✓
45	Booby Hill	678186	Hawaiite (intermediate Zr/Nb)	✓	✓
46	Spoon Crater	696198	not known		
47	unnamed	694197	Hawaiite (DSC-type)		✓
48	Mountain Red Hill	705197	Basalt (high Zr/Nb)	✓	
49	unnamed	701192	Mugearite	✓	
50	South Red Crater	697181	Hawaiite (intermediate Zr/Nb)		✓
51	Green Top Crater	705187	Hawaiite (intermediate Zr/Nb)	✓	
52	South East Crater	717190	Hawaiite (intermediate Zr/Nb)	✓	
53	Coast Red Nipple	741188	not known		
54	Round Hill	752193	not known		
55	Crater Cliff	758202	not known		
56	unnamed	763212	not known		

Cone number has been assigned arbitrarily. Scoria cone names and grid references are from the 1:25,000 Ascension Island topographic map, series G 892, edition 4-GSGS, 1992.

Table 2.2. Chemical analyses of scoria and lava flow pairs from scoria cones of Ascension Island.

	Cone 38		Cone 16		Cone 44			
	Al-208 scoria	Al-211 flow	Al-180 scoria	Al-179 flow	Al-26 scoria	Al-27 bomb	Al-28 flow	Al-62 flow
SiO_2	48.84	47.88	49.11	48.67	47.61	47.40	47.28	47.38
TiO_2	3.73	3.80	3.62	3.51	3.42	3.41	3.38	3.43
Al_2O_3	15.40	15.48	14.45	14.39	15.09	15.08	14.99	15.12
Fe2O3	13.42	13.61	14.04	13.62	13.92	13.99	13.76	13.93
MnO	0.21	0.19	0.23	0.21	0.21	0.20	0.20	0.20
MgO	4.57	3.69	4.67	4.48	5.22	5.21	5.17	5.12
CaO	7.96	8.60	8.37	8.67	9.24	9.28	9.50	9.13
Na2O	3.25	4.00	3.07	3.97	3.21	3.43	3.69	3.63
K2O	1.60	1.65	1.28	1.30	1.23	1.19	1.19	1.20
P2O5	1.02	1.10	1.16	1.18	0.85	0.81	0.84	0.86
H_2O-	1.90	0.76	1.27	0.10	0.42	0.17	0.30	0.30
LOI	2.13	0.62	0.40	-0.78	0.03	-0.20	-0.31	-0.76
Ni	8	10	7	9	30	32	29	29
Sc	30	27	29	26	29	29	28	30
V	278	322	239	209	303	303	296	291
Zn	116	122	132	111	118	108	108	115
Rb	38	34	27	27	25	23	23	21
Sr	596	584	452	480	455	464	469	466
Ba	413	433	291	346	260	268	262	268
Th	5	5	3	4	4	2	3	3
Pb	2	2	<2	<2	2	<2	<2	<2
Zr	268	259	279	292	237	232	230	240
Nb	65	63	58	59	49	48	48	50
La	37	37	36	38	28	26	25	26
Y	42	42	52	56	42	42	42	44
$Na_2O + K_2O$	4.85	5.65	4.35	5.27	4.44	4.62	4.88	4.83
Na_2O/K_2O	2.03	2.42	2.40	3.05	2.61	2.88	3.10	3.03
Zr/Nb	4.1	4.1	4.8	4.9	4.8	4.8	4.8	4.8
Ba/Nb	6.4	6.9	5.0	5.9	5.3	5.6	5.5	5.4
Rb/Nb	0.58	0.54	0.47	0.46	0.51	0.48	0.48	0.42
K/Nb	204	217	183	183	208	208	206	199
Zr/Y	6.4	6.2	5.4	5.2	5.6	5.5	5.5	5.5

Major and trace element data obtained by XRF at the University of Oklahoma (see footnote to Table 2.4).
Al-208 lapilli, Al-211 lava flow from (unnamed) Cone 38; Al-180 lapilli, Al-179 lava flow from Travellers Hill (Cone 16); Al-26 lapilli, Al-27 bomb, Al-28 and Al-62 lava flow from South Gannet Hill (Cone 44).

Table 2.3. Chemical analyses of multiple samples from individual lava flows of Ascension Island.

	Cone 32					Cone 13				Cone 27	
	Al-1 bomb	Al-100 flow	Al-102 flow	Al-158 flow	Al-259 flow	Al-269 block	Al-79 flow	Al-85 flow	Al-251 flow	Al-272 block	Al-199 flow
SiO_2	47.39	47.53	48.00	47.47	47.63	49.52	49.41	49.76	49.42	56.63	56.17
TiO_2	2.60	2.67	2.73	2.70	2.64	3.14	3.17	3.22	3.17	1.70	1.73
Al_2O_3	15.85	15.80	15.45	15.67	15.89	15.23	15.32	15.40	15.30	16.85	16.90
Fe_2O_3	12.79	12.78	12.90	12.81	12.66	12.78	12.69	12.83	12.76	8.38	8.48
MnO	0.18	0.17	0.17	0.17	0.17	0.22	0.21	0.22	0.22	0.26	0.24
MgO	6.65	6.65	6.46	6.86	6.52	4.43	4.47	4.47	4.36	2.29	2.31
CaO	10.46	10.35	10.23	10.14	10.50	8.09	8.14	8.15	8.14	5.11	5.26
Na_2O	2.77	2.81	2.77	2.94	2.78	4.17	4.09	3.48	4.18	5.61	5.75
K_2O	0.66	0.65	0.65	0.65	0.58	1.50	1.52	1.52	1.51	2.42	2.39
P_2O_5	0.65	0.59	0.64	0.59	0.63	0.92	0.98	0.95	0.94	0.75	0.77
H_2O-	0.30	0.33	0.36	0.22	0.38	0.55	0.17	0.18	0.09	0.31	0.44
LOI	0.10	–0.44	–0.04	–0.49	–0.04	–0.54	–0.70	–0.86	–0.36	0.32	0.18
Ni	85	97	96	105	85	16	14	14	12	6	5
Sc	28	29	29	25	28	24	25	28	24	17	17
V	283	248	255	250	269	244	207	218	233	49	56
Zn	91	92	96	96	90	122	112	122	123	151	149
Rb	12	11	12	12	10	32	32	30	30	49	48
Sr	386	385	381	382	401	502	506	502	503	496	495
Ba	155	144	149	152	159	346	351	345	362	538	522
Th	<2	<2	2	2	<2	5	3	4	4	7	7
Pb	<2	<2	<2	<2	<2	<2	<2	3	<2	3	3
Zr	140	145	150	150	143	305	307	309	307	477	474
Nb	27	27	28	28	26	61	62	62	61	95	95
La	17	16	18	17	15	37	38	39	40	55	54
Y	30	31	32	32	31	48	48	49	49	67	71
Na_2O/K_2O	4.20	4.32	4.26	4.52	4.79	2.78	2.69	2.29	2.77	2.32	2.41
Zr/Nb	5.2	5.4	5.4	5.4	5.5	5.0	5.0	5.0	5.0	5.0	5.0
Ba/Nb	5.7	5.3	5.3	5.4	6.1	5.7	5.7	5.6	5.9	5.7	5.5
Rb/Nb	0.44	0.41	0.43	0.43	0.38	0.52	0.52	0.48	0.49	0.52	0.51
K/Nb	203	200	193	193	185	204	204	204	205	211	209
Zr/Y	4.7	4.7	4.7	4.7	4.6	6.4	6.4	6.3	6.3	7.1	6.7

Major and trace element data obtained by XRF at the University of Oklahoma (see footnote to Table 2.4). Al-1, Al-100, Al-102, Al-158, Al-259 are samples from the Command Hill cone (Cone 32) and associated flow; Al-1 is from a bomb on the north flank of Command Hill and Al-100, Al-102, Al-158, and Al-259 are flow samples from ~400 m NNW, ~1 km NW, ~2 km WSW, and ~2.4 km SW, respectively, of Command Hill. Al-269, Al-79, Al-85, and Al-251 are samples from Sisters Peak (Cone 13) and associated flow; Al-269 is from a massive block in the vent area close to the top of Sisters Peak and Al-79, Al-85, and Al-251 are flow samples from ~1.9 km NE, ~3.2 km NNE, and ~3.2 km N, respectively, of Sisters Peak. Al-272 and Al-199 are samples from (unnamed) Cone 27 and associated flow; Al-272 is from a scoria block from the cone and Al-199 is a flow sample from ~2.7 km WNW of the cone.

Table 2.4. Representative chemical analyses of basalt to benmoreite lava flows from Ascension Island.

	High Zr/Nb			Low Zr/Nb		Intermediate Zr/Nb				Dark Slope Crater		
	Al-107 B	Al-37 B	Al-64 B	Al-60 H	Al-157 H	Al-100 B	Al-161 H	Al-171 M	Al-176 Be	Al-4 H	Al-2 H	Al-6 M
SiO_2	48.55	47.59	50.58	47.94	47.69	47.53	49.58	53.39	57.30	48.49	48.51	52.12
TiO_2	3.00	2.98	2.52	3.64	3.83	2.67	3.21	2.19	1.52	2.89	2.72	1.83
Al_2O_3	15.28	15.43	15.61	14.67	15.54	15.80	15.42	15.41	16.64	16.22	15.73	16.71
Fe_2O_3	13.48	13.43	11.98	13.37	13.84	12.78	12.62	10.79	8.31	13.23	12.88	10.44
MnO	0.16	0.18	0.17	0.21	0.20	0.17	0.21	0.24	0.23	0.18	0.18	0.18
MgO	5.33	5.55	5.23	4.90	3.88	6.65	4.43	3.27	2.30	4.21	5.20	3.43
CaO	9.46	9.74	8.56	9.12	8.32	10.35	8.16	7.44	4.85	8.47	8.13	6.15
Na_2O	3.34	3.42	3.61	3.72	3.96	2.81	3.88	4.31	5.55	3.74	3.92	5.20
K_2O	0.94	1.06	1.29	1.41	1.65	0.65	1.50	1.66	2.56	1.62	1.82	2.69
P_2O_5	0.46	0.62	0.45	1.02	1.09	0.59	0.99	1.30	0.74	0.95	0.91	1.25
H_2O-	0.42	0.31	0.31	0.41	0.70	0.33	0.34	1.16	0.17	0.70	0.72	0.53
LOI	0.18	-0.20	-0.40	0.54	0.61	-0.44	-0.30	0.46	0.13	0.40	0.18	0.28
Ni	39	48	34	12	13	97	12	8	5	50	52	31
Cr	28	54	27	2.6	1.8	156	6.7	2.0	2.0	41	52	12
Sc	33.5	28.1	28.9	27.9	28.8	30.0	24.6	20.6	13.7	24.5	21.7	13.1
V	304	248	201	294	287	248	214	83	44	245	221	90
Zn	93	101	87	132	140	92	119	147	139	142	131	154
Ga	26	24	26	24	24	23	24	27	28	27	25	30
Rb	18	19	28	27	32	11	30	32	56	34	41	66
Sr	436	551	414	551	533	385	498	479	431	721	782	1105
Ba	201	259	289	379	395	144	343	374	584	449	458	720
Th	2.33	2.94	3.69	4.06	4.67	1.70	4.14	4.58	6.56	4.67	5.44	8.93
Pb	<2	<2	<2	<2	2	<2	<2	<2	2	3	3	<2
Zr	188	237	244	235	256	145	306	364	530	320	364	558
Hf	4.88	5.72	5.96	5.36	5.67	3.51	6.61	7.87	11.3	6.92	7.83	11.6
Nb	33	42	41	58	63	27	62	69	97	64	72	110
Ta	2.27	3.09	3.03	3.85	4.06	2.02	3.91	4.27	5.77	3.95	4.64	7.35
La	23.3	28.5	29.9	35.3	37.3	17.5	36.3	44.0	56.4	43.4	45.0	73.2
Ce	53.4	65.7	65.5	75.2	83.1	42.9	87.1	104	118	92.3	97.2	158
Nd	31.4	34.7	32.7	39.3	46.0	24.0	42.8	56.8	62.7	51.7	48.2	67.0
Sm	7.36	8.34	8.13	8.98	10.6	5.95	10.8	13.3	13.6	10.7	10.3	14.3
Eu	2.44	2.67	2.67	3.12	3.54	2.20	3.56	4.62	4.30	3.76	3.30	4.75
Tb	1.08	1.21	1.23	1.30	1.50	1.09	1.41	1.84	2.04	1.60	1.57	1.90
Yb	2.90	2.73	3.16	2.88	3.38	2.43	3.49	4.65	4.84	2.95	2.58	3.23
Lu	0.36	0.34	0.47	0.38	0.45	0.29	0.44	0.59	0.66	0.38	0.34	0.38
Y	40	40	41	40	47	31	48	64	63	43	37	46
Zr/Nb	5.7	5.6	6.0	4.1	4.1	5.4	4.9	5.3	5.5	5.0	5.1	5.1
Ba/Nb	6.1	6.2	7.0	6.5	6.3	5.3	5.5	5.4	6.0	7.0	6.4	6.5
Rb/Nb	0.55	0.45	0.68	0.47	0.51	0.41	0.48	0.46	0.58	0.53	0.57	0.60
K/Nb	236	210	261	202	217	200	201	200	219	210	210	203
Th/Nb	0.071	0.070	0.090	0.070	0.074	0.063	0.067	0.066	0.068	0.073	0.076	0.081
La/Nb	0.71	0.68	0.73	0.61	0.59	0.65	0.59	0.64	0.58	0.68	0.63	0.67
P/Zr	10.7	11.4	8.0	18.9	18.6	17.8	14.1	15.6	6.1	13.0	10.9	9.8
Zr/Y	4.7	5.9	6.0	5.9	5.4	4.7	6.4	5.7	8.4	7.4	9.8	12.1
Ce_N/Yb_N	4.7	6.1	5.3	6.6	6.3	4.5	6.3	5.7	6.2	8.0	9.6	12.4

B basalt; H hawaiite; M mugearite; Be benmoreite. Al-107 flow in Grazing Valley; Al-37 flow on south flank of Devil's Riding School; Al-64 flow exposed in walls of Cricket Valley; Al-60 flow lobe from Cotar Hill; Al-157 flow in cliff section at South West Bay; Al-100 flow from Command Hill; Al-161 young flow from Sisters Peak; Al-171 flow along English Bay Road; Al-176 fissure flow on Letterbox; Al-4 flow on southeast rim of Dark Slope Crater; Al-2 bomb from northwest flank of Dark Slope Crater; Al-6 flow on southeast flank of Dark Slope Crater. Major element oxides are recalculated to sum to 100% on an anhydrous basis. H_2O- is weight loss after drying for 12 hours at 110°C. LOI is weight loss after ignition at 950°C for 1 hour (oxidation of Fe^{2+} to Fe^{3+} in near-anhydrous samples results in weight gain, expressed as negative LOI). Trace elements are in parts per million; Ni, V, Zn, Ga, Rb, Sr, Ba, Pb, Zr, Nb, and Y determined by XRF, other trace elements determined by INAA.

Table 2.5. Major element least squares and trace element Rayleigh crystal fractionation models for the liquid line of descent for compositions within different mafic rock groups.

Intermediate Zr/Nb group

basalt (Al-28) to hawalite (Al-118)

	SiO_2	TiO_2	Al_2O_3	FeO	MnO	MgO	CaO	Na_2O	K_2O	P_2O_5
Al-28	47.94	3.43	15.20	12.56	0.20	5.24	9.63	3.74	1.21	0.85
Al-118	48.63	3.66	14.81	12.76	0.21	4.73	8.86	3.92	1.38	1.03
R	-0.04	0.00	0.00	0.00	-0.01	0.01	0.03	0.11	0.03	-0.01

0.009 Fo_{84} + 0.084 An_{65} + 0.055 Cpx1 + 0.016 Mt1 + 0.835 Al-118 $\Sigma R^2 = 0.02$

	Th	Rb	Sr	Ba	Zr	Nb	La	Y	Zr/Nb
Al-28	2.7	23	469	262	230	48	30.0	42	4.8
Al-118 observed	3.8	26	454	312	281	59	35.1	50	4.8
Al-118 calculated	3.3	27	464	308	271	57	35.4	48	4.8

hawaiite (Al-118) to mugearite (Al-101)

	SiO_2	TiO_2	Al_2O_3	FeO	MnO	MgO	CaO	Na_2O	K_2O	P_2O_5
Al-118	48.63	3.66	14.81	12.76	0.21	4.73	8.86	3.92	1.38	1.03
Al-101	51.60	2.65	15.59	10.85	0.23	3.85	7.60	4.37	1.79	1.47
R	-0.07	0.00	-0.02	0.00	-0.06	0.03	0.05	0.24	0.03	-0.05

0.018 Fo_{76} + 0.107 An_{65} + 0.088 Cpx3 + 0.027 Mt6 + 0.023 Ilm1 + 0.738 Al-101 ΣR^2=0.08

	Th	Rb	Sr	Ba	Zr	Nb	La	Y	Zr/Nb
Al-118	3.8	26	454	312	281	59	35.1	50	4.8
Al-101 observed	4.8	34	475	402	367	78	49.9	66	4.7
Al-101 calculated	5.1	35	475	412	367	77	46.6	62	4.8

mugearite (Al-101) to benmoreite (Al-130)

	SiO_2	TiO_2	Al_2O_3	FeO	MnO	MgO	CaO	Na_2O	K_2O	P_2O_5
Al-101	51.60	2.65	15.59	10.85	0.23	3.85	7.60	4.37	1.79	1.47
Al-130	55.87	1.88	16.25	9.01	0.25	2.56	5.49	5.48	2.36	0.85
R	0.06	0.00	0.04	0.00	-0.03	-0.03	-0.04	-0.28	0.04	0.05

0.033 Fo_{63} + 0.127 An_{52} + 0.057 Cpx6 + 0.029 Mt1 + 0.015 Ilm1 + 0.019 Ap + 0.721 Al-130 ΣR^2=0.09

	Th	Rb	Sr	Ba	Zr	Nb	La	Y	Zr/Nb
Al-101	4.8	34	475	402	367	78	49.9	66	4.7
Al-130 observed	6.3	46	433	559	468	94	55.5	64	5.0
Al-130 calculated	6.6	47	400	540	487	101	60.2	69	4.8

High Zr/Nb group

basalt (Al-124) to basalt (Al-128)

	SiO_2	TiO_2	Al_2O_3	FeO	MnO	MgO	CaO	Na_2O	K_2O	P_2O_5
Al-124	48.61	2.85	15.82	11.66	0.17	6.14	10.07	3.16	0.86	0.46
Al-128	49.71	2.68	15.67	11.34	0.17	5.61	9.18	4.05	1.12	0.46
R	0.13	0.00	-0.03	0.00	-0.01	-0.05	-0.09	-0.34	-0.05	0.09

0.011 Fo_{84} + 0.087 An_{79} + 0.071 Cpx1 + 0.023 Mt1 + 0.004 Ilm1 + 0.806 Al-128 ΣR^2=0.15

	Th	Rb	Sr	Ba	Zr	Nb	La	Y	Zr/Nb
Al-124	2.4	14	444	189	192	32	20.9	34	6.0
Al-128 observed	3.3	20	418	237	227	38	25.4	39	6.0
Al-128 calculated	3.0	17	451	230	233	39	25.5	40	6.0

continued ...

Table 2.5 continued

Dark Slope Crater group

hawaiite (Al-2) to mugearite (Al-6)

	SiO_2	TiO_2	Al_2O_3	FeO	MnO	MgO	CaO	Na_2O	K_2O	P_2O_5
Al-2	49.14	2.76	15.94	11.74	0.18	5.27	8.24	3.97	1.84	0.92
Al-6	52.67	1.85	16.89	9.50	0.18	3.47	6.21	5.25	2.72	1.26
R	0.02	0.00	0.01	0.00	-0.05	-0.01	-0.01	-0.09	0.04	0.01

0.046 Fo_{76} + 0.163 An_{65} + 0.096 Cpx3 + 0.031 Mt6 + 0.019 Ilm1+ 0.002 Ap + 0.644 Al-2 $\Sigma R^2 = 0.02$

	Th	Rb	Sr	Ba	Zr	Nb	La	Y	Zr/Nb
Al-2	5.4	41	782	458	364	72	45.0	37	5.1
Al-6 observed	8.9	66	1105	720	558	110	73.2	46	5.1
Al-6 calculated	8.3	63	800	681	542	108	67.3	51	5.0

Major element analyses recalculated to 100% with all Fe as FeO. Mineral compositions from Harris (1983): Fo_{84}, Fo_{76}, Fo_{63}, and Fo_{41} from Table 3, analysis 1, 5, 2, and 8, respectively; An_{79}, An_{65}, An_{52}, and An_{42} from Table 1, analysis 6, 1, 7, and 3, respectively; Cpx1, Cpx3, Cpx6, and Cpx7 from Table 2, analysis 1, 3, 6, and 7, respectively; Mt1 from Table 6, analysis HDSA5, Mt6 from Table 11; Ilm1 from Table 6, analysis HDSA5; Ap is stoiciometric apatite, $Ca_5P_3O_{12}(OH)$. R is the residual (observed minus calculated oxide concentration in the parent magma) from the least squares model; ΣR^2 is the sum of squares of residuals. Trace element concentrations in daughter magma calculated for Rayleigh crystal fractionation using the phenocryst assemblage and fraction of liquid remaining from the least squares solution and the distribution coefficients in Appendix 1.

Table 2.6. Major element least squares and trace element Rayleigh crystal fractionation models for the liquid line of descent for compositions between different mafic rock groups.

High Zr/Nb group to intermediate Zr/Nb group

basalt (Al-124) to basalt (Al-28)

	SiO_2	TiO_2	Al_2O_3	FeO	MnO	MgO	CaO	Na_2O	K_2O	P_2O_5
Al-124	48.61	2.85	15.82	11.66	0.17	6.14	10.07	3.16	0.86	0.46
Al-28	47.94	3.43	15.20	12.56	0.20	5.24	9.63	3.74	1.21	0.85
R	0.20	-0.22	-0.08	0.06	-0.03	-0.09	-0.13	-0.28	-0.19	-0.28

$0.028\ Fo_{84} + 0.083\ An_{79} + 0.029\ Cpx1 + 0.003\ Mt1 + 0.865\ Al\text{-}128$ $\Sigma R^2 = 0.31$

	Th	Rb	Sr	Ba	Zr	Nb	La	Y	Zr/Nb
Al-124	2.4	14	444	189	192	32	20.9	34	6.0
Al-28 observed	2.7	23	469	262	230	48	30.0	42	4.8
Al-28 calculated	2.8	16	432	215	220	37	23.9	38	5.9

High Zr/Nb group to low Zr/Nb group

basalt (Al-124) to hawaiite (Al-60)

	SiO_2	TiO_2	Al_2O_3	FeO	MnO	MgO	CaO	Na_2O	K_2O	P_2O_5
Al-124	48.61	2.85	15.82	11.66	0.17	6.14	10.07	3.16	0.86	0.46
Al-60	48.59	3.69	14.87	12.20	0.21	4.97	9.24	3.77	1.43	1.03
R	0.08	0.15	-0.01	-0.03	-0.09	-0.01	-0.06	-0.17	-0.16	-0.24

$0.061\ Fo_{83} + 0.192\ An_{85} + 0.062\ Cpx7 + 0.012\ Mt4 + 0.677\ Al\text{-}60$ $\Sigma R^2 = 0.15$

	Th	Rb	Sr	Ba	Zr	Nb	La	Y	Zr/Nb
Al-124	2.4	14	444	189	192	32	20.9	34	6.0
Al-60 observed	4.1	27	551	379	235	58	35.3	40	4.1
Al-60 calculated	3.5	21	411	266	277	47	30.1	47	5.9

High Zr/Nb group to Dark Slope Crater group

basalt (Al-124) to hawaiite (Al-2)

	SiO_2	TiO_2	Al_2O_3	FeO	MnO	MgO	CaO	Na_2O	K_2O	P_2O_5
Al-124	48.61	2.85	15.82	11.66	0.17	6.14	10.07	3.16	0.86	0.46
Al-2	47.94	3.43	15.20	12.56	0.20	5.24	9.63	3.74	1.21	0.85
R	0.17	0.13	-0.07	-0.02	0.01	-0.06	-0.12	-0.11	-0.53	-0.23

$0.005\ Fo_{76} + 0.103\ An_{79} + 0.118\ Cpx5 + 0.030\ Mt2 + 0.751\ Al\text{-}124$ $\Sigma R^2 = 0.42$

	Th	Rb	Sr	Ba	Zr	Nb	La	Y	Zr/Nb
Al-124	2.4	14	444	189	192	32	20.9	34	6.0
Al-2 observed	5.4	41	782	458	364	72	45.0	37	5.1
Al-2 calculated	3.2	19	463	246	247	42	27.2	41	5.9

See footnote to Table 2.5. Additional mineral compositions in this table from Harris (1983): Cpx5 from Table 2, analysis 5; Mt2 and Mt4 from Table 6, analysis H7(5) and H95(7), respectively.

Table 2.7. Sr, Nd, Pb, and O isotopic compositions of mafic rocks from Ascension Island.

		SiO_2	$^{87}Sr/^{86}Sr$	ε_{Sr}	$^{143}Nd/^{144}Nd$	ε_{Nd}	$^{206}Pb/^{204}Pb$	$^{207}Pb/^{204}Pb$	$^{208}Pb/^{204}Pb$	$\delta^{18}O$ WR	$\delta^{18}O$ fsp
High Zr/Nb basalt											
AI-40	flow	47.55	0.702892 ± 10	-25.7	0.512992 ± 9	+6.91	–	–	–	–	–
AI-107	flow	48.55	0.702811 ± 10	-26.8	0.513028 ± 12	+7.61	19.566	15.605	39.106	+6.12	–
AI-128	flow	49.09	0.702814 ± 11	-26.8	0.513060 ± 8	+8.23	19.451	15.599	39.014	+7.83	+5.87
AI-14	lapilli	49.27	0.703035 ± 11	-23.6	0.513036 ± 7	+7.76	–	–	–	+7.22	–
AI-172	lapilli	49.64	0.702912 ± 9	-25.4	0.513006 ± 7	+7.18	19.421	15.616	39.017	+6.81	–
AI-64	flow	50.58	0.702766 ± 12	-27.4	0.513066 ± 8	+8.35	19.389	15.626	39.027	+6.26	–
Low Zr/Nb hawaiite											
AI-212	flow	47.34	0.702921 ± 11	-25.2	0.512972 ± 9	+6.52	–	–	–	–	–
AI-157	flow	47.69	0.702929 ± 9	-25.1	0.512969 ± 12	+6.46	19.630	15.622	39.140	+6.79	–
AI-60	flow	47.94	0.703130 ± 14	-22.3	0.512971 ± 11	+6.50	–	–	–	+7.07	–
Intermediate Zr/Nb basalt to benmoreite											
AI-28	flow	47.28	0.702942 ± 11	-24.9	0.513008 ± 7	+7.22	19.740	15.685	39.370	+6.86	–
AI-100	flow	47.53	0.702831 ± 15	-26.5	0.513018 ± 10	+7.41	19.482	15.607	39.062	+6.37	+6.79
AI-159b	flow	48.09	0.702766 ± 9	-27.4	0.513013 ± 9	+7.32	19.445	15.594	39.000	+6.76	–
AI-182	flow	48.28	0.702791 ± 9	-27.1	0.513015 ± 7	+7.35	–	–	–	–	–
AI-132	flow	48.53	0.702790 ± 10	-27.1	0.513038 ± 9	+7.80	19.580	15.620	39.160	+7.41	+5.92
AI-72	flow	48.54	0.702951 ± 9	-24.8	0.512960 ± 12	+6.28	19.658	15.641	39.290	+7.21	–
AI-123	lapilli	48.87	0.702941 ± 9	-25.0	0.513040 ± 7	+7.84	19.446	15.623	39.008	+7.41	–
AI-274	scoria block	49.40	0.703263 ± 10	-20.4	0.513011 ± 8	+7.28	–	–	–	–	–
AI-24	flow	49.82	0.702845 ± 14	-26.3	0.512978 ± 9	+6.63	–	–	–	+5.03	–
AI-166	flow	50.88	0.703011 ± 11	-24.0	0.513028 ± 7	+7.61	19.610	15.629	39.178	+5.66	–
AI-139	lapilli	51.01	0.702861 ± 11	-26.1	0.513015 ± 22	+7.35	19.517	15.609	39.060	+6.18	–
AI-143	lapilli	51.90	0.702945 ± 10	-24.9	0.513004 ± 7	+7.14	19.564	15.617	39.160	+7.84	–
AI-165	flow	55.29	0.702844 ± 9	-26.3	0.513016 ± 11	+7.37	19.516	15.603	39.054	+6.48	–
AI-130	flow	55.31	0.702838 ± 9	-26.4	0.513021 ± 8	+7.47	19.602	15.605	39.133	+6.08	–
AI-122	lapilli	55.59	0.702836 ± 10	-26.5	0.513024 ± 7	+7.53	19.587	15.605	39.107	+6.80	–
AI-176	flow	57.30	0.702861 ± 10	-26.1	0.513006 ± 14	+7.18	19.605	15.625	39.202	+5.60	–
AI-137	flow	60.06	0.702798 ± 10	-27.0	0.512982 ± 7	+6.71	19.496	15.639	39.141	+7.05	–
Broken Tooth mugearite and benmoreite											
AI-87	flow	54.75	0.702859 ± 10	-26.1	0.513077 ± 11	+8.56	19.599	15.605	39.128	+7.48	–
AI-76	flow	60.05	0.702868 ± 10	-26.0	0.513091 ± 12	+8.84	19.593	15.588	39.085	+7.39	–
AI-187e	xenolith	61.74	0.702860 ± 10	-26.1	0.513020 ± 9	+7.45	–	–	–	+5.73	–
Dark Slope Crater hawaiite and mugearite											
AI-154	flow	48.33	0.703024 ± 10	-23.8	0.512974 ± 10	+6.55	19.850	15.649	39.443	+5.67	–
AI-2	bomb	48.51	0.703106 ± 10	-22.6	0.512967 ± 8	+6.42	19.863	15.665	39.496	+5.65	–
AI-6	flow	52.12	0.703130 ± 11	-22.3	0.512918 ± 12	+5.46	19.840	15.667	39.497	+6.02	–
AI-298	flow	52.26	0.703107 ± 9	-22.6	0.512951 ± 10	+6.11	–	–	–	–	–

CHAPTER III

Submitted to Journal of Petrology (in review)

Felsic oceanic island magmatism: Origin of high $^{87}Sr/^{86}Sr$ evolved volcanic and plutonic rocks from Ascension Island, South Atlantic Ocean

Running head: *Geochemistry of Ascension Island felsic rocks*

Kar, A.[1,2]
School of Geology and Geophysics
University of Oklahoma
Norman, OK 73019, USA

Weaver, B.
School of Geology and Geophysics
University of Oklahoma
Norman, OK 73019, USA

Davidson, J.
Department of Earth and Space Sciences
University of California Los Angeles
Los Angeles, CA 90095, USA

Colucci, M.
Department of Geology
Southern Methodist University
Dallas, TX 75275, USA

[1] Department of Mathematics and Physics
Fort Valley State University
Fort Valley, GA 31030, USA

[2] Corresponding Author
Telephone: (912) 825 6844
FAX: (912) 825 6618
email: kara@mail.fvsc.peachnet.edu

ABSTRACT

The first phase of felsic magmatism on Ascension Island, in the form of trachyte and rhyolite domes, coulees, lava flows, and pyroclastic deposits, created the central and eastern parts of the island between about 1 and 0.56 Ma ago. The geochemical characteristics of the felsic rocks are largely consistent with an origin by fractional crystallization of high Zr/Nb mafic magmas as evidenced by identical $^{143}Nd/^{144}Nd$ and similar Pb isotopic ratios. The high Zr/Nb basalt flows constitute one of the four distinct basalt and hawaiite suites identified from Ascension based on trace element characteristics. Syenite, monzonite, and granite xenoliths associated with the felsic magmatism are interpreted as cumulate rocks from, and intrusive equivalents of, fractionating felsic magmas. Internal (mineral) isochrons for two granite xenoliths give ages of 0.92 and 1.22 Ma, with initial $^{87}Sr/^{86}Sr > 0.705$. Most of the felsic volcanic rocks and granite are also characterized by high $^{87}Sr/^{86}Sr$ (> 0.706) compared to mafic rocks ($^{87}Sr/^{86}Sr < 0.703$), although $^{143}Nd/^{144}Nd$ of the felsic rocks is similar to that of the low $^{87}Sr/^{86}Sr$ mafic lavas that constitute most of the areal exposure of the island. Such high $^{87}Sr/^{86}Sr$ and high $^{143}Nd/^{144}Nd$ signatures do not correspond to known suboceanic mantle reservoirs. The elevated $^{87}Sr/^{86}Sr$ suggests interaction of the felsic rocks with geothermal fluids derived from seawater which likely took place under subsolidus conditions. Fluids with high Sr contents have been recovered from fractures in a deep (3126 m) geothermal well. In addition, evidence for the involvement of a high $^{87}Sr/^{86}Sr$ component during magmatic differentiation, however, is also provided by the high initial $^{87}Sr/^{86}Sr$ of the granitic xenoliths, and of high $^{87}Sr/^{86}Sr$ (> 0.704) in some of the feldspar phenocrysts separated from felsic rocks. $\delta^{18}O$ ranges of +5.5 to +8.1‰ (whole rock) and +5.5 to +7.2‰ (feldspar) in the felsic rocks also indicate the involvement of a high

$\delta^{18}O$ component, and suggest that hydrothermally-altered pre-existing volcanic basement may have been cannibalized during differentiation of the felsic magmas.

Felsic Magmatism / Fractional Crystallization / Oxygen Isotopes ($\delta^{18}O$) / Radiogenic Isotopes / Rock-Magma Interaction

INTRODUCTION

Felsic volcanism on ocean islands is typically interpreted as the product of fractional crystallization of mafic magmas derived from hotspot-related plume sources (e.g., Le Roex, 1985; Storey et al., 1989). Closed system fractionation processes do not modify incompatible element and isotopic ratios unless carried to extreme. These systematics therefore provide a "window" into the geochemical characteristics of the mantle source region(s). Nevertheless, extreme care is necessary in understanding processes that can modify trace element and isotopic ratios, particularly in highly evolved felsic rocks. Extremely low Sr contents in some felsic magmas may result in the compromise of Sr isotopic systematics by shallow level crustal and post-magmatic alteration processes. This may potentially occur by subsolidus interaction with fluids, incorporation of fluids into the magma, or assimilation of hydrothermally altered crust. The involvement of fluids at any of these stages may also affect oxygen isotope compositions. Sr-O coupled signatures can provide information on isotopic equilibrium of crystallizing mineral phases and the magma, or disequilibrium between a phenocryst and the matrix and post-magmatic modification. Pb-Nd ratios are not significantly disturbed by post magmatic alteration processes as seawater contains insignificant amounts of radiogenic Pb or Nd relative to the high concentrations in the evolved magmas.

Ascension Island (7°56'S, 14°22'W) in the South Atlantic Ocean, is a hotspot-related intra-plate volcanic island. Trachyte and rhyolite compose approximately 14% of

surface exposures (Nielson & Sibbett, 1996) and pyroclastic (scoria and pumice) deposits make up about 43% of the island's total areal extent (Atkins et al., 1964; Harris, 1983). Also present are plutonic (granite, syenite, and monzonite) xenoliths which represent fractionation products of felsic volcanic rocks. Most of the felsic volcanic rocks and plutonic xenoliths have high initial $^{87}Sr/^{86}Sr$ compared to the mafic rocks on the island. The present study is directed to understand the petrogenesis of the felsic (>60% SiO_2) rocks and the cause of high $^{87}Sr/^{86}Sr$ in these felsic volcanic and plutonic rocks from Ascension Island. A more detailed consideration of the interactions involved during differentiation will be presented elsewhere.

GENERAL GEOLOGY OF ASCENSION ISLAND

Ascension Island is a composite volcano with in excess of fifty scoria cones scattered over the island. The exposed volcanic rocks comprise transitional to mildly alkaline basalt-hawaiite-mugearite-benmoreite-trachyte-rhyolite series lava flows, trachytic domes, scoria cones, and pyroclastic deposits (Fig. 3.1). Prior to this study, the pyroclastic deposits have been largely uncharacterized. In this study we geochemically and petrogenetically characterize the voluminous pumice deposits, trachyte domes, felsic lava flows, and plutonic and volcanic xenoliths.

There are two distinctive felsic eruptive centers on the island, the central felsic complex and the eastern felsic complex. The central felsic complex is comprised of the Middleton Ridge felsic center and Green Mountain (Fig. 3.1). Middleton Ridge is composed primarily of trachyte, pumice, and some rhyolite and rhyolitic obsidian. The highest peak on the island, Green Mountain (859 m), is made up of massive, thick pyroclastic (mostly pumice) deposits with the southwestern flanks mostly constituted of trachyte. The eastern felsic complex is made up of numerous trachyte flows and lava

domes (Fig. 3.1). A voluminous trachyte flow originated from Devil's Cauldron and flowed northward and eastward. Devil's Cauldron is interpreted to be an explosion crater with the trachyte dome of Weather Post adjacent. Southeast of Devil's Cauldron and Weather Post is the trachytic flow dome of White Horse, to the east of which is the comenditic coulee of Little White Hill (Fig. 3.1). At the extreme eastern end of the island, South East Head is constituted of trachyte. In the southeastern part of Ascension small trachyte bodies occur at Round Hill, Cocoanut Bay, Ragged Hill, and Pillar Bay (Fig. 3.1). Trachyte from Ragged Hill and Cocoanut Bay contains unusually high modal abundance of alkali feldspar phenocrysts. In the western part of the island trachyte is found locally at Devil's Riding School, Daly's Crags, and Cross Hill (Fig. 3.1). Rhyolitic compositions are relatively rare, being restricted to the rhyolite flow on Middleton Ridge in the central felsic complex, Little White Hill, and a flow in the cliff section to the north of White Horse in the eastern felsic complex.

Plutonic and Volcanic Xenoliths

Felsic plutonic xenoliths (monzonite, syenite, and granite) and volcanic xenoliths (trachyte and rhyolite) occur mainly in pyroclastic deposits on the western flanks of Green Mountain. The granite, syenite, and monzonite xenoliths have been described in great detail by Roedder & Coombs (1967), Harris & Bell (1982), Harris et al. (1982), Harris (1983), Sheppard & Harris (1985), and Harris & Sheppard (1987). The granite xenoliths from Five Mile Post vary in size from a few cm to 25-30 cm in length and generally are fine grained with a few which are coarser grained. Monzonite xenoliths occur on Middleton Ridge and syenite xenoliths in the flows from Broken Tooth (Harris, 1983). Trachytic and rhyolitic xenoliths from close to Five Mile Post vary vastly in size and generally have a schistose texture.

Ages of evolved rocks on Ascension Island

A limited number of age dates (K-Ar) for Ascension trachyte, rhyolite, and pumice exist in the literature (Harris et al., 1982, Nielson and Sibbett, 1996); we have added four new Ar-Ar age dates on feldspar phenocrysts. There is a distinct clustering of ages among the exposed rocks on the island (Fig. 3.2) with the higher SiO_2 rocks being significantly older (range from 1.2 to 0.56 Ma) than the mafic volcanic rocks (range from 0.47 to 0.12 Ma, with a basaltic dike from Middleton Ridge dated at 0.80 Ma).

The first phase of felsic volcanism occurred in the central part of the island. A rhyolite east of Middleton Ridge is dated at 0.99±0.02 Ma; this is overlain by a trachyte flow with an age of 0.82±0.02 Ma and this flow is overlain by a trachyte dome closely associated with a trachyte lava flow dated at 0.65±0.02 (Nielson & Sibbett, 1996). From field and age relationships we suggest that the build up of the Middleton Ridge felsic center started around 1 Ma ago and continued until 0.65 Ma ago.

Felsic magmatism next occurred:

1) west of Middleton Ridge, where the Devil's Riding School trachyte is dated at 0.66±0.02 and is overlain by pumice with an age of 0.61±0.02 Ma;
2) east of Middleton Ridge, where build up of Green Mountain started around 0.65±0.02 Ma and ended around 0.56±0.06 Ma; and,
3) in the eastern felsic complex where there is only one age date for this region, the trachyte dome of Weather Post being dated at 0.67±0.02 Ma. The lack of age dates from the eastern felsic complex makes it difficult to conclude its relationship with the Middleton Ridge felsic center. The eastern felsic complex may be contemporaneous, if not slightly younger than, the Middleton Ridge center.

These age dates suggest areal exposure of the central and the eastern parts of the island was built up over a period of half a million years, from 1 Ma to 0.56 Ma. Nielson

& Sibbett (1996) suggest that, since the oldest dated rocks in both the felsic complexes are rhyolite, with time silica content decreased with eruption of trachyte from a magma chamber that initially tapped rhyolite from the top of the chamber with the chamber being active for > 0.4 Ma.

SAMPLING AND ANALYTICAL TECHNIQUES

For details on sampling techniques and analytical procedure for major and trace element analyses obtained at the University of Oklahoma refer to Weaver et al. (1996), for radiogenic isotope analysis performed at University of California, Los Angeles to Davidson et al. (1993), and for oxygen isotope analysis performed at Southern Methodist University to Borthwick & Harmon (1982). Representative data are presented in Tables 3.1 and 3.2.

PETROGRAPHY

Trachytic rocks vary from being aphyric to very sparsely phyric to strongly phyric and are mostly massive although some are slightly vesicular. The most abundant phenocryst phase is alkali feldspar, with olivine, clinopyroxene, and titanomagnetite forming the other phenocryst or microphenocryst phases. Weaver et al. (1996) reported trachyte that from Ragged Hill and Cocoanut Bay has unusually high contents of alkali feldspar phenocrysts (25 to 35%). The sizes of the phenocrysts varies: feldspar phenocrysts are up to 2 mm, olivine up to 1.5 mm, and titanomagnetite and clinopyroxene are up to 0.5 mm and occur as rare clusters. Plagioclase phenocrysts are rare and tabular in shape, and range up to 2.5 mm. Some trachytic rocks contain small (0.5 mm) rounded crystals of amphibole with reaction rims. Overall the groundmass in the trachyte is fine grained with plagioclase laths ranging between 0.1 and 0.2 mm, and rarely up to 1 mm and exhibiting a patchy, weak flow alignment.

Rhyolitic rocks mostly are aphyric to sparsely phyric and massive in general; microphenocrysts are alkali feldspar.

DISCUSSION

Whole Rock Geochemistry

Major Element Geochemistry

Ascension rocks are transitional to mildly alkaline and are a continuous fractionation series of alkali basalt-hawaiite-mugearite-benmoreite, to the highly fractionated products of trachyte and rhyolite (Weaver et al. 1996; Kar et al., Mafic MS). For felsic rock compositions (> 60 wt% SiO_2; Table 3.1) with increase in SiO_2, Al_2O_3 constantly decreases due to crystallization of feldspar, Fe_2O_3 decreases as a consequence of olivine, clinopyroxene, and titanomagnetite crystallization, K_2O increases but becomes buffered between 65 and 70 wt% SiO_2 probably with crystallization of alkali feldspar, and Na_2O shows a slight decrease at high (> 65 wt%) SiO_2 content with crystallization of alkali feldspar (Fig. 3.3). Most of the pumice samples have moderate to extreme depletion in Na_2O and, in general, a lower abundance of K_2O compared to the similarly differentiated lava flows and domes (Fig. 3.3) which is interpreted as an alteration effect (Weaver et al., 1996).

Trace Element Geochemistry

For Ascension felsic rocks with an increase in SiO_2 there is a wide variation in large low-valence cations with Ba and Sr both decreasing as a result of plagioclase and alkali feldspar crystallization. On the other hand Rb contents increase continuously with SiO_2. The same trend is observed when the low-valence cations are plotted against Zr. Weaver et al. (1996) observed that trachyte from Ragged Hill and Cocoanut Bay has high Ba and K_2O with respect to Zr compared to the rest of the Ascension suite and

interpreted this as due to accumulation of alkali feldspar (Fig. 3.4), as evidenced by the high phenocryst content. Large variation in trace element ratios, for example, Zr/Nb and Zr/Y in the felsic rocks as compared to the mafic volcanic rocks is likely due to the crystallization of alkali amphibole and zirconium- and rare-earth-rich accessory phases found in the intermediate and granitic plutonic xenoliths (Harris, 1983, Weaver et al., 1996). Rhyolite compositions have high SiO_2, Rb, Zr, and Y contents but in more evolved rhyolite compositions Zr/Nb and Zr/Y are lower than in the trachyte flows, probably due to fractionation of a zirconium silicate accessory phase (Weaver et al., 1996).

Weaver et al. (1996) and Kar et al. (Mafic MS) show that Ascension mafic rocks have a wide variation in Zr/Nb, from 4.0 to 6.0. There are four distinct basalt and hawaiite suites - (1) in the southwestern part of the island hawaiite flows and scoria have Zr/Nb of 4.1, (2) in the southern and the southeastern part of the island basalt flows and scoria have Zr/Nb of 5.6 to 6.1, (3) for the rest of the island basalt and hawaiite flows and scoria have Zr/Nb of 4.7 to 5.4, and (4) hawaiite and mugearite flows from Dark Slope Crater have intermediate Zr/Nb (4.9 to 5.4) but are distinguished by high Ni and Sr relative to other trace elements. Borehole data suggest that older Ascension mafic flows have higher Zr/Nb of up to 7.7 (Kar et al., 1995).

The felsic volcanic rocks from Ascension (both surface and those from the boreholes) have a range of Zr/Nb between 4.6 and 9.4 (Fig. 3.4), although the majority of the trachyte and rhyolite samples have Zr/Nb within the range of the high Zr/Nb mafic flows (6.0 to 7.7). The highest Zr/Nb felsic rocks are in the central part of the island: Devil's Riding School trachyte (Zr/Nb = 9.1 to 9.4), Middleton Ridge rhyolite (Zr/Nb = 7.0 to 8.6), and one trachyte from the eastern part of the island (Zr/Nb = 8.7)

(Fig. 3.4). All the borehole felsic rocks have Zr/Nb ranging between 5.8 and 7.4, with one exception, a trachyte with Zr/Nb of 9.1.

In the plutonic rocks Zr/Nb is extremely variable (Fig. 3.4): 4.0 to 13.4 in syenite, 4.0 to 8.6 in monzonite, and 5.1 to 9.0 in granite. Trachyte xenoliths have Zr/Nb (6.0 to 9.2) similar to the surface felsic volcanic rocks. The trends in Zr/Nb *vs.* SiO_2 (Fig. 3.4) show that, with increasing SiO_2, Zr/Nb first increases and then decreases. K/Nb shows a continuous decrease from the plutonic xenoliths (syenite and monzonite) at low SiO_2 to the surface flows and volcanic xenoliths to the granite xenoliths at high SiO_2.

The age relationship of the felsic and mafic rocks, their geographical distribution on the island, and their geochemistry, enable determination of which mafic magma type - high Zr/Nb, low Zr/Nb, intermediate Zr/Nb, or Dark Slope Crater - was parental to the felsic magmas on Ascension Island.

A deep (3126 m) geothermal exploration well records much of the history of the formation of the island (Nielson & Stiger, 1996). Below 1966 m, the sequence is largely mafic and the felsic rocks mostly occur above 887 m depth. Nielson & Stiger (1996) suggest that felsic volcanism is relatively recent in the growth of the volcanic edifice, although felsic rocks are the oldest exposed rocks on the island. Overlapping with the end of felsic volcanism, or starting very shortly thereafter, high Zr/Nb basaltic lavas were erupted in the southeastern part of the island. The low Zr/Nb and Dark Slope Crater mafic flows are younger than the felsic rocks and are extremely limited in spatial distribution and volume; it is therefore difficult to appeal to these magma types having produced through fractionation the voluminous felsic magmas erupted on Ascension. Although of substantial volume, the intermediate Zr/Nb basalt to benmoreite flows are the most recent eruptive products and are highly unlikely to represent magmas parental to the much earlier felsic volcanism.

The majority of trachyte and rhyolite samples have Zr/Nb within the range of the high Zr/Nb mafic rocks (5.6 to 7.7). Since incompatible element ratios do not change with low to moderate degrees of fractionation, the majority of the felsic magmas are considered to be crystal fractionation products of high Zr/Nb mafic magmas. Higher (> 7.7) Zr/Nb in the felsic rocks is the result of greater degrees of crystal fractionation involving the removal of a cumulate assemblage with low Zr/Nb as represented by some of the syenite and monzonite xenoliths (Fig. 3.4). Therefore, from the geographical distribution, age, and behavior of incompatible element ratios of the felsic and high Zr/Nb mafic volcanic rocks it is highly likely that a genetic link between these two types of magma exists. No intermediate products of high Zr/Nb affinity have been found, suggesting that intermediate magmas either encountered shallow low pressure cotectics such that copious mineral precipitation drove compositions rapidly from basalt to felsic over a small temperature range, or that intermediate composition magmas encountered a density maximum in the liquid line of descent inhibiting eruption.

The REE patterns of Ascension mafic and felsic volcanic rocks have variable degrees of LREE enrichment with respect to HREE (Kar et al., Mafic MS) although the LREE are uniformly strongly enriched compared to the HREE. Continuous crystal fractionation involving olivine, plagioclase, clinopyroxene, and magnetite (Harris, 1983) increases the total REE content of the more evolved magmas but does not produce strong inter-element fractionation. The characteristic REE pattern of the basaltic rocks is maintained in the more evolved rocks (Fig. 3.5A) although the absolute abundance has increased and substantial feldspar fractionation has produced a negative Eu anomaly. Rhyolitic compositions have a higher total abundance of REE and a larger negative Eu anomaly compared to trachyte (Fig. 3.5B).

When the average trachyte is normalized to average high and intermediate Zr/Nb mafic compositions (Fig. 3.5C, D) the MREE are strongly depleted relative to the LREE and HREE. If intermediate Zr/Nb mafic magmas were parental to trachyte magmas then $D_{LREE} > D_{HREE}$ is required (Fig. 3.5D), which is unlikely given the fractionating phenocryst assemblage (Harris, 1983). On the other hand fractionation from a high Zr/Nb parent (Fig. 3.5C) would require $D_{LREE} < D_{HREE}$ which is more probable and supports derivation of felsic magmas from high Zr/Nb parental mafic magmas.

Isotopic Data

For the most part, trachyte and rhyolite flows and pumice are isotopically similar to the mafic rocks, especially the high Zr/Nb mafic rocks (Table 3.2, Fig. 3.6). However, the most evolved trachyte and rhyolite samples have low Sr contents, high Rb/Sr, and very high Sr isotope ratios (Table 3.2). Undoubtedly, the high $^{87}Sr/^{86}Sr$ is in part due to in situ decay, and those samples for which we have age data can be corrected for this effect (Fig. 3.6). A maximum age correction of 1.0 Ma (consistent with K-Ar and Ar-Ar age dates) brings the initial $^{87}Sr/^{86}Sr$ down to the range between 0.702301 and 0.706548. Given an initial $^{87}Sr/^{86}Sr$ similar to the mafic rocks (0.7028 to 0.7030), ages in excess of 7 Ma are required for some samples to account for the high $^{87}Sr/^{86}Sr$. This is more than the maximum possible age of the rocks since the volcanic edifice sits on 5- to 6-Ma-old oceanic lithosphere.

Although many of the differentiated rocks typically are characterized by high $^{87}Sr/^{86}Sr$ (> 0.706), $^{143}Nd/^{144}Nd$ is similar to the mafic lavas that constitute most of the areal exposure of the island (Fig. 3.6). Such high $^{87}Sr/^{86}Sr$ and high $^{143}Nd/^{144}Nd$ signatures do not correspond to known suboceanic mantle reservoirs. Therefore, we infer that radiogenic Sr was added through crustal or hydrothermal processes. Assimilation of oceanic sediment (Harris et al., 1982) is precluded by the lack of

variation in $\delta^{18}O$, Pb-isotopic compositions, and $^{143}Nd/^{144}Nd$ (Weis et al., 1987). One possible explanation for high $^{87}Sr/^{86}Sr$ is interaction of either the magma or the felsic rocks with seawater, or assimilation of seawater-altered crust (Weis et al., 1987). This possibility might be consistent with the general $^{87}Sr/^{86}Sr$-SiO_2 correlation if the more felsic rocks are more glassy and more susceptible to hydration. Oxygen isotope data for three pumice samples, two trachytic and one rhyolitic, have whole rock $\delta^{18}O$ values greater than +13 (Table 3.2); these pumice samples are severely depleted in Na_2O (except one) and have very high water loss on heating (H_2O-) as the result of post-magmatic alteration (Weaver et al., 1996). These samples have high age corrected whole rock initial $^{87}Sr/^{86}Sr$ (> 0.706; Table 3.2). Age-corrected feldspar $^{87}Sr/^{86}Sr$ for one pumice sample (AI-44) is much lower than the whole rock (0.7043); the apparent isotopic disequilibrium is indicative of post-crystallization alteration. Cousens et al. (1993) show that Rb, Sr, and O can be mobilized in felsic rocks during post-eruptive processes although Pb-Nd isotopic systematics are not disturbed, and they stress that extreme caution should be exercised when using Sr and O signatures as indicators of mantle derived products. Leaching of the felsic volcanic rocks mobilises a radiogenic Sr component, which is interpreted to be of secondary origin. Alteration is confirmed by analyses of feldspar phenocrysts that typically have significantly lower $^{87}Sr/^{86}Sr$, with the feldspar-whole rock difference in $^{87}Sr/^{86}Sr$ too great to be explained by *in situ* decay. Similar effects are reported by Bohrson and Reid (1997, and this volume) for peralkaline felsic rocks of Socorro Island, Mexico. The susceptibility of these rocks to secondary alteration of $^{87}Sr/^{86}Sr$ is enhanced by their low Sr contents. Nevertheless, secondary alteration cannot be the only process responsible for the high $^{87}Sr/^{86}Sr$ ratios of some of the felsic rocks, as some of the feldspars and residues from leaching still have $^{87}Sr/^{86}Sr$ greater than the range of the basalts.

Two granite xenoliths (Table 3.2) yield internal isochrons (Fig. 3.7) with ages of 0.94 Ma and 1.22 Ma, respectively, and with initial $^{87}Sr/^{86}Sr$ (Fig. 3.7) of 0.705756 and 0.706067, respectively; $^{143}Nd/^{144}Nd$ in one of the xenoliths is similar to the felsic extrusive rocks (Table 3.2). Sheppard & Harris (1985) suggested that some granite xenoliths with high $^{87}Sr/^{86}Sr$ compared to the 0.7029 initial ratio of basalt (Harris et al., 1983) are either significantly older (up to 4.5 Ma) than the volcanic rocks or the granite magma was contaminated with radiogenic Sr from sea water, oceanic crust, or sediment. The isochron ages preclude the former interpretation and implicates high magmatic $^{87}Sr/^{86}Sr$ for at least some of the felsic rocks. The high $^{87}Sr/^{86}Sr$ of the granite xenoliths may characterize potential contaminants capable of increasing the $^{87}Sr/^{86}Sr$ of the differentiated felsic magmas, but this begs the question of how the granitic rocks acquired high $^{87}Sr/^{86}Sr$ in the first place. The low Sr content of the granitic rocks limits the leverage that they will have on Sr isotope ratios of contaminated liquids, unless 1) contamination involves already differentiated (low Sr) liquids rather than basalt, perhaps at the upper reaches of the magma chamber or/and 2) the assimilant is a high Sr feldspar accumulate or residue rather than bulk granite.

In the absence of continental crust, the most plausible origin for a high $^{87}Sr/^{86}Sr$ signature is seawater ($^{87}Sr/^{86}Sr = 0.709$), which may interact directly with felsic magma, with solidified rock, or provide a high $^{87}Sr/^{86}Sr$ contaminant by interacting with the basement lithologies through which felsic magmas ascend. Weis et al. (1987) reject the seawater contamination hypothesis for higher $^{87}Sr/^{86}Sr$ on the basis of lack of petrographic evidence for high- or low-temperature seawater interaction (without mentioning whether this interaction is with magma or rock). Assimilation of seawater-altered oceanic crust (or older altered mafic rocks in the volcanic edifice) by the magma in the late stages of the differentiation process may effect increases in $^{87}Sr/^{86}Sr$ (Weis

et al., 1987) but requires considerable accompanying feldspar fractionation to elevate Rb/Sr. The model proposed by Weis et al. (1987) postulates that addition of less than 1% of high-temperature (> 400°C) altered oceanic crust (with 100 ppm Sr and $^{87}Sr/^{86}Sr$ = 0.709) could account for the high $^{87}Sr/^{86}Sr$ in felsic rocks with very low Sr content.

Grant et al. (1976) propose for lavas from St. Helena that oceanic crust is not involved in raising $^{87}Sr/^{86}Sr$ as the oceanic crust is enriched in both ^{87}Sr and ^{18}O whereas St. Helena volcanic rocks are enriched in ^{87}Sr but depleted in ^{18}O ($\delta^{18}O$ ranges between +6.3 and +10.1‰). Basalt and gabbro, together with trachyte and syenite, in general have $\delta^{18}O$ ranging from +5.5 to +7.4‰ (Faure, 1986). Kyser & O'Neil (1984) report that fresh MORB have very consistent stable isotope composition ($\delta^{18}O$ ranging from +5.5 to +6.0‰) and Eiler et al. (1996) report that unaltered OIB whole rocks and glasses have $\delta^{18}O$ of +4.6 to +7.5‰. Our oxygen isotope data correspond with that of Sheppard & Harris (1985) and $\delta^{18}O$ values increase with increase in SiO_2 content (Fig. 3.8). However, our data also show a considerable spread in $\delta^{18}O$ values at a given degree of differentiation (Fig. 3.8). The high Zr/Nb basalt presumed parental to the felsic rocks have $\delta^{18}O$ values of +5.7 to +7.8‰, whereas whole rock $\delta^{18}O$ for trachyte and rhyolite varies between +5.5 and +8.1‰. The similarities in the ranges of $\delta^{18}O$ further substantiates a genetic link between the high Zr/Nb mafic rocks and the felsic rocks. Given the observed mineral assemblages, fractionation from basalt to rhyolite cannot elevate $\delta^{18}O$ values much more than 0.6‰ (Sheppard and Harris, 1985; Taylor & Sheppard, 1986). Therefore the relatively large range in $\delta^{18}O$, extending to values significantly higher than the nominal +5.5 to +6.0‰ that appears to characterize the mantle, argues for interaction with water at low temperatures. The large range in $\delta^{18}O$ reported for the basaltic rocks suggests that some of these effects may be inherited

from earlier stages of differentiation. In pumice samples $\delta^{18}O$ ranges from +6.4 to +16.8‰ (Fig. 3.8), but the extremely high $\delta^{18}O$ (> +10‰) are not a magmatic signature but a post-magmatic alteration effect. Eiler et al. (1996) report that low $\delta^{18}O$ in olivine from basalt (+4.5 to +5.0‰) is associated with a depleted mantle source whereas high $\delta^{18}O$ (+5.4 to +6.1‰) is associated with an enriched source; the low values are suggestive of hydrothermally altered Pacific lower oceanic crust whereas high values are indicative of incorporation of recycled sediment and/or oceanic crust in their sources. On the other hand, Hoernle et al. (1996) show crustal contamination is inconsistent with their model since at least 30% bulk assimilation of crust is required to generate isotopic variations and mantle $\delta^{18}O$ values (+5.7 to + 6.1‰ for feldspar) for Gran Canaria. For Ascension Island, Weis et al. (1987) model that the addition of small amount (< 1%) of oceanic crust with $\delta^{18}O$ of +3‰ to mafic magma sufficient to influence $^{87}Sr/^{86}Sr$ would shift $\delta^{18}O$ values of the rocks by 0.02‰ which is below detection limits. Eiler et al. (1996) do not report a value for the amount of oceanic crust added and hence it is difficult to assess if there is involvement of a crustal component. Ascension basalt and hawaiite whole rock $\delta^{18}O$ values range from +5.7 to +7.8‰ and feldspar separates from +5.5 to +6.8‰, values somewhat higher than the olivine values from Hawaii but perhaps suggestive of derivation from a similarly enriched mantle source.

As an alternative to the model of Weis et al. (1987), we propose that the high $^{87}Sr/^{86}Sr$ in the felsic rocks of Ascension is generated by interaction of the felsic rocks with geothermal fluids derived from seawater, similar to fluids encountered in fractures of the deep (3126 m) geothermal well (Ascension #1 well) (Adams, 1996). The geothermal system below Ascension is hosted by faults and fractures (Nielson & Stiger, 1996), and two significant zones of fluid entry were encountered in Ascension #1, one at 2475 to 2604 m depth and the other at 2889 to 2957 m depth, and both these fluids

were derived from seawater with Sr content varying between 0.1 and 112 ppm (water sample collected during drilling), and between 9.7 and 202 ppm (water sample collected after drilling was completed); the $\delta^{18}O$ of the geothermal and meteoric waters measured ranged from -14.9 to +3.4‰ (Adams, 1996). West & Leeman (1987) report that the Holua trachyte (Hawaii) whole rock has an unusually radiogenic initial $^{87}Sr/^{86}Sr$ ratio (0.70426) which contrasts strongly with the ratio measured on fresh feldspar phenocrysts (0.70367) and propose prolonged interaction of the trachyte magma with migrating ground waters that had experienced mixing with seawater. The highest $^{87}Sr/^{86}Sr$ values recorded on Ascension are 0.708917 for a rhyolite and 0.709250 for the felsic component of a granite sample. Leachates from trachyte samples also record high $^{87}Sr/^{86}Sr$ (approaching that of seawater; up to 0.7086; unpublished data) whereas feldspar phenocrysts from trachyte have $^{87}Sr/^{86}Sr$ between 0.702896 and 0.703797 and $\delta^{18}O$ between +6.3 and +7.8‰. The elevated $^{87}Sr/^{86}Sr$ of the felsic plutonic and volcanic rocks on Ascension Island suggests interaction of the felsic rocks with geothermal fluids derived from seawater. This likely took place under subsolidus conditions, since feldspar-whole rock pairs are not in Sr isotopic equilibrium, and leaching experiments can be shown to remove a high Sr, high $^{87}Sr/^{86}Sr$ component from the whole rock powders.

We therefore concur with previous workers in recognizing the modification of isotope characteristics in evolved ocean island magmas, and suggest that they cannot be carelessly used to elucidate the mantle sources of ocean islands.

CONCLUSIONS

1) The felsic (>60% SiO_2) rocks from the central and eastern parts of Ascension island are the oldest; a rhyolite dated at 0.99±0.02 Ma (Nielson & Sibbett, 1996) from the

central part of the island representing the evidence of first phase of felsic volcanism. Felsic volcanism continued until at least 0.56±0.06 Ma with build up of the central and eastern parts of the island and was closely followed by the eruption of high Zr/Nb basalt lavas.

2) The geochemical characteristics of the felsic rocks are largely consistent with an origin by fractionation of high Zr/Nb magmas as evidenced by similar trace element ratios and Nd and Pb isotopic ratios.

3) Trace element and isotopic compositions indicate that syenite, monzonite, and granite xenoliths found on Ascension are cumulates from felsic magmas that also produced the felsic volcanic rocks. Internal Rb-Sr isochrons for two granite xenoliths yield ages of 0.92 and 1.22 Ma, respectively.

4) $\delta^{18}O$ in felsic rocks are slightly higher compared to the high Zr/Nb parent magmas which is a result of fractionation combined with some open system interaction with fluids.

5) Fluids recovered from a deep geothermal well drilled on Ascension show the presence of seawater-derived geothermal fluids with Sr content as high as 202 ppm; interaction of these fluids with felsic rocks may generate high $^{87}Sr/^{86}Sr$ under subsolidus conditions as evidenced by leaching experiments and recorded in many of the whole rock samples.

6) In addition, the involvement of a high $^{87}Sr/^{86}Sr$ component during magmatic differentiation is evidenced by high initial $^{87}Sr/^{86}Sr$ from the internal isochrons of the two granite xenoliths which have high initial $^{87}Sr/^{86}Sr$ (> 0.705); $^{143}Nd/^{144}Nd$ and $\delta^{18}O$ in the granite are similar to the mafic extrusive rocks. Some feldspar phenocrysts from the felsic volcanic rocks also have high $^{87}Sr/^{86}Sr$ (> 0.704); $\delta^{18}O$ ranges of +5.5 to +8.1‰ (whole rock) and +5.5 to +7.2‰ (feldspar) in the felsic rocks also indicate

the involvement of a high $\delta^{18}O$ component, and suggest that hydrothermally altered pre-existing volcanic basement may have been cannibalized during differentiation of the felsic magmas.

REFERENCES

Adams, M.C., 1996. Chemistry of fluids from Ascension #1, a deep geothermal well on Ascension Island, South Atlantic Ocean. Geothermics 25: 561-579.

Atkins, F.B., Baker, P.E. & Smith, D.G.W., 1964. Oxford expedition to Ascension Island. Nature 204: 722-724.

Bohrson, W.A., & Reid, M.R., (in press) Genesis of silicic peralkaline volcanic rocks in an ocean island setting by crustal melting and open system processes; Socorro Island, Mexico. Journal of Petrology.

Borthwick, J., & Harmon, R.S., 1982. A note regarding ClF_3 as an alternative to BrF_5 for oxygen isotope analyses. Geochimica et Cosmochimica Acta 46: 1665-1668.

Cousens, B.L., Spera, F.J., & Dobson, P.F., 1993. Post-eruptive alteration of felsic ignimbrites and lavas, Gran Canaria, Canary Islands: Strontium, neodymium, lead, and oxygen isotopic evidence. Geochimica et Cosmochimica Acta 57: 631-640.

Davidson, J.P., Boghossian, N.D., & Wilson, B.M., 1993. The Geochemistry of the Igneous Rock Suite of St. Martin, Northern Lesser Antilles. Journal of Petrology 34: 839-866.

Eiler, J.M., Farley, K.A., Valley, J.W., Hofmann, A.W., & Stopler, E.M., 1996. Oxygen isotope constraints on the sources of Hawaiian volcanism. Earth and Planetary Science Letters 144: 453-468.

Faure, G., 1986. Principles of Isotope Geology. John Wiley and Sons.

Grant, N.K., Powell, J.L., Burkholder, F.R., Walther, J.V., & Coleman, M.L., 1976. The isotopic composition of strontium and oxygen in lavas from St. Helena, South Atlantic. Earth and Planetary Science Letters 31: 209-223.

Harris, C., 1983. The petrology of lavas and associated plutonic inclusions of Ascension Island. Journal of Petrology 24: 424-470.

Harris, C., 1985. Guano-derived rare earth-rich phosphate amygdales in gabbroic inclusions from Ascension Island. Earth and Planetary Science Letters 72: 141-148.

Harris, C., & Bell, J.D., 1982. Natural partial melting of syenite blocks from Ascension Island. Contributions to Mineralogy and Petrology 79: 107-113.

Harris, C., Bell, J.D., & Atkins, F.B., 1982. Isotopic composition of lead and strontium in lavas and coarse-grained blocks from Ascension Island, South Atlantic. Earth and Planetary Science Letters 60: 79-85.

Harris, C., & Sheppard, S.M.F., 1987. Magma and fluid evolution in the lavas and associated granite xenoliths of Ascension Island. In: Fitton, J.G., & Upton, B.G.J. (eds.) Alkaline Igneous Rocks, Geological Society of London Special Publication 30: 269-272.

Hoernle, K., Hansteen, T., & Schimincke, H-U., 1996. The composition of oceanic crust beneath Gran Canaria, Canary Islands: Implications for crustal contamination of ocean island magmas and upper mantle composition. American Geophysical Union Chapman Conference, Tenerife, Canary Islands abstracts with programs.

Kar, A., Weaver., B., Davidson, J., & Colucci, M., 1996. Petrogenesis of mafic volcanic rocks from Ascension Island. American Geophysical Union Fall Meeting abstracts with programs. Vol. 76, No. 46: F698.

Kar, A., Weaver., B., Davidson, J., & Colucci, M., (Mafic MS). Small scale mantle heterogeneities: Evidence from transitional to mildly alkaline volcanic rocks from Ascension Island , South Atlantic Ocean. Journal of Petrology.

Kar, A., Weaver., B., Davidson, J., & Nielson, D., 1995. Geochemical characteristics of borehole samples recovered from Ascension Island, South Atlantic Ocean. Geological Society of America abstracts with programs 27, 6.

Kyser, T.K., & O'Neil, J.R., 1984. Hydrogen isotope systematics of submarine basalts. Geochimica. et Cosmochimica. Acta 48: 2123-2133.

Le Bas, M.J., Le Maitre, R.W., Streckeisen, A., & Zanelttiu, B., 1986. A chemical classification of volcanic rocks based on the total alkali-silica diagrams. Journal of Petrology 27: 745-750.

Le Roex, A.L., 1985. Geochemistry, mineralogy and magmatic evolution of the basaltic and trachytic lavas from Gough Island, South Atlantic. Journal of Petrology 26: 149-186.

Nakamura, N., 1974. Determination of REE, Ba, Fe, Mg, Na and K in carbonaceous and ordinary chondrites. Geochimica et Cosmochimica Acta 38: 757-775.

Nielson, D.L., & Sibbett, B.S., 1996. Geology of Ascension Island, South Atlantic Ocean. Geothermics 25: 427-448.

Nielson, D.L., & Stiger, S.G., 1996. Drilling and evaluation of Ascension #1, a geothermal exploration well on Ascension Island, South Atlantic Ocean. Geothermics 25: 543-560.

Roedder, E., & Coombs, D.S., 1967. Immiscibility in granitic melts indicated by fluid inclusions in ejected granite blocks of Ascension Island. Journal of Petrology 8: 417-451.

Sheppard, S.M.F., & Harris, C., 1985. Hydrogen and oxygen isotope geochemistry of Ascension Island lavas and granites: variation with crystal fractionation and interaction with seawater. Contributions to Mineralogy and Petrology 91: 74-81.

Storey, M., Wolff, J.A., Norry, M.J. and Marriner, G.F., 1989. Origin of hybrid lavas from Agua de Pau volcano, Sao Miguel, Azores; in: Magmatism in the Ocean Basins, eds. Saunders, A.D. and Norry, M.J., Geological Society of London Special Publication 42: 161-180.

Taylor, H.P., & Sheppard, S.M.F., 1986. Igneous Rocks: I. Processes of isotopic fractionation and isotope systematics. In: Valley, J.W., Taylor, H.P., and O'Neil, J.R. (eds.) Stable isotopes in high temperature geological processes, Reviews in Mineralogy 16: 227-271.

Weaver, B., Kar, A., Davidson., J., & Colucci, M., 1996. Geochemical characteristics of volcanic rocks from Ascension Island, South Atlantic Ocean. Geothermics 25: 449-470.

Weis, D., 1983. Pb isotopes in Ascension Island rocks: Oceanic origin for the gabbroic to granitic plutonic xenoliths. Earth and Planetary Science Letters 62: 273-282.

Weis, D., Demaiffe, D., Cauet, S., & Javoy, M., 1987. Sr, Nd, O and H isotopic ratios in Ascension Island lavas and plutonic inclusions; cogenetic origin. Earth and Planetary Science Letters 82: 255-268.

West, H.B., & Leeman, W.P., 1987. Isotopic evolution of lavas from Haleakala Crater, Hawaii. Earth and Planetary Science Letters 84: 211-225.

ACKNOWLEDGMENTS

This paper is a part of a Ph.D. dissertation by Aditya Kar. The project was funded through NSF grant EAR-9204079. Frank Ramos and Pete Holden are thanked for their assistance with Sr isotope determinations. We have benefited from discussions with Wendy Bohrson.

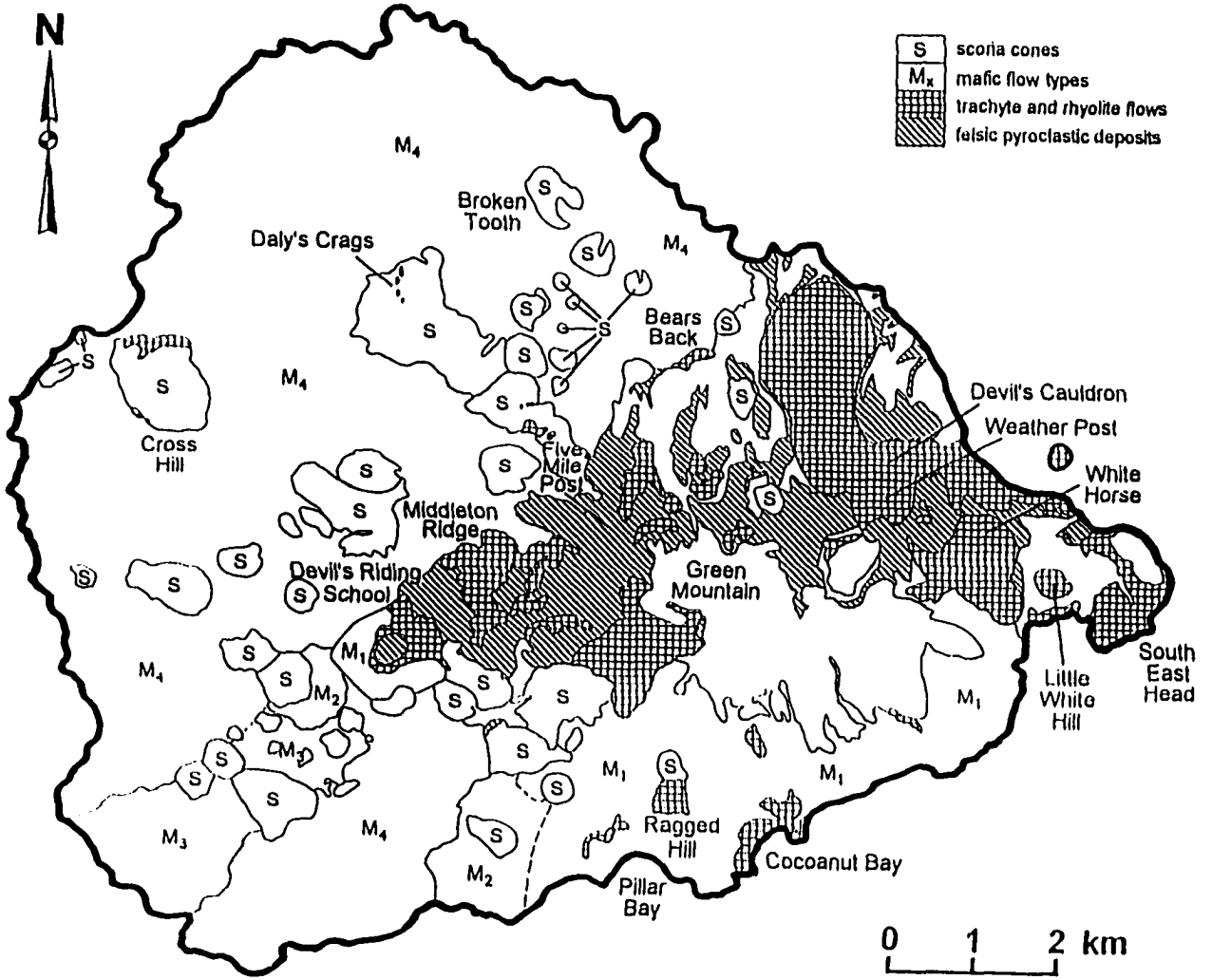

Figure 3.1. Simplified geological map of Ascension Island highlighting the distribution of felsic rock types. Mafic lava flow types are: M_1 high Zr/Nb basalt; M_2 Dark Slope Crater hawaiite and mugearite; M_3 low Zr/Nb hawaiite; M_4 intermediate Zr/Nb basalt to benmoreite. For a more detailed geological map see Kar et al. (Mafic MS).

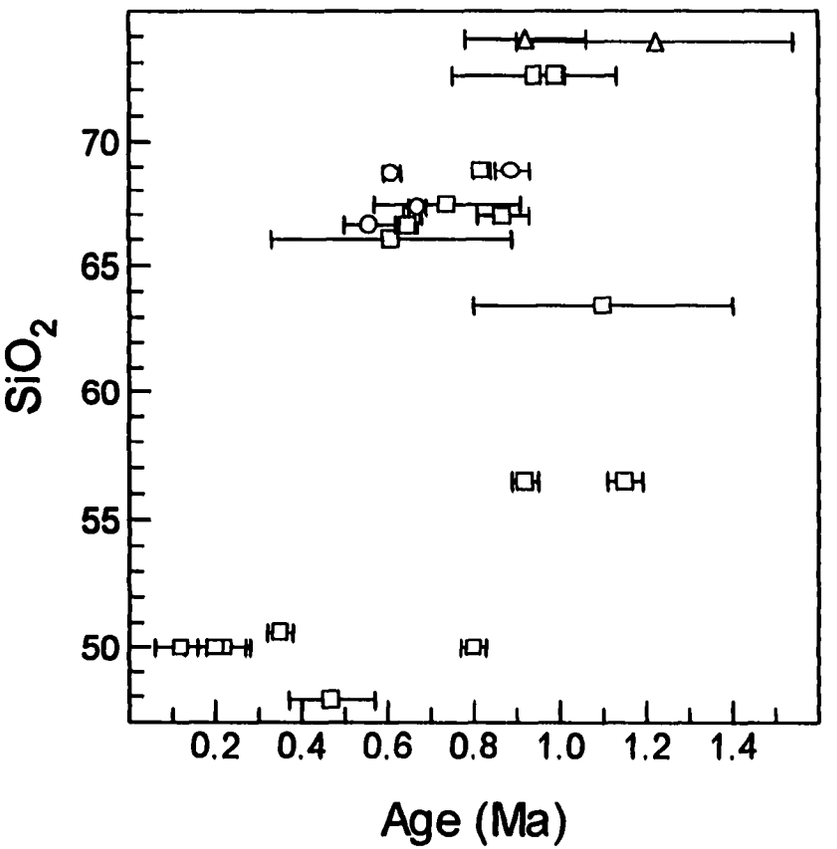

Figure 3.2. Variation in SiO_2 (wt%) *vs.* age (Ma) for mafic and felsic rocks from Ascension Island. Whole rock K-Ar age dates (□) are from Harris et al. (1982) and Nielson & Sibbett (1996) [note that for the Bears Back and Daly's Crags trachyte bodies the ages from Nielson and Sibbett are preferred to those from Harris et al.]; Ar-Ar feldspar age dates (O) are from this study (Middleton Ridge trachyte 0.89±0.04 Ma; Weather Post trachyte 0.67±0.02 Ma; pumice in Devil's Riding School 0.61±0.02 Ma; trachyte NNE of Mountain Red Hill 0.56±0.06 Ma); Rb-Sr isochron dates for granite xenoliths (Δ) are from this study (see Fig. 3.7).

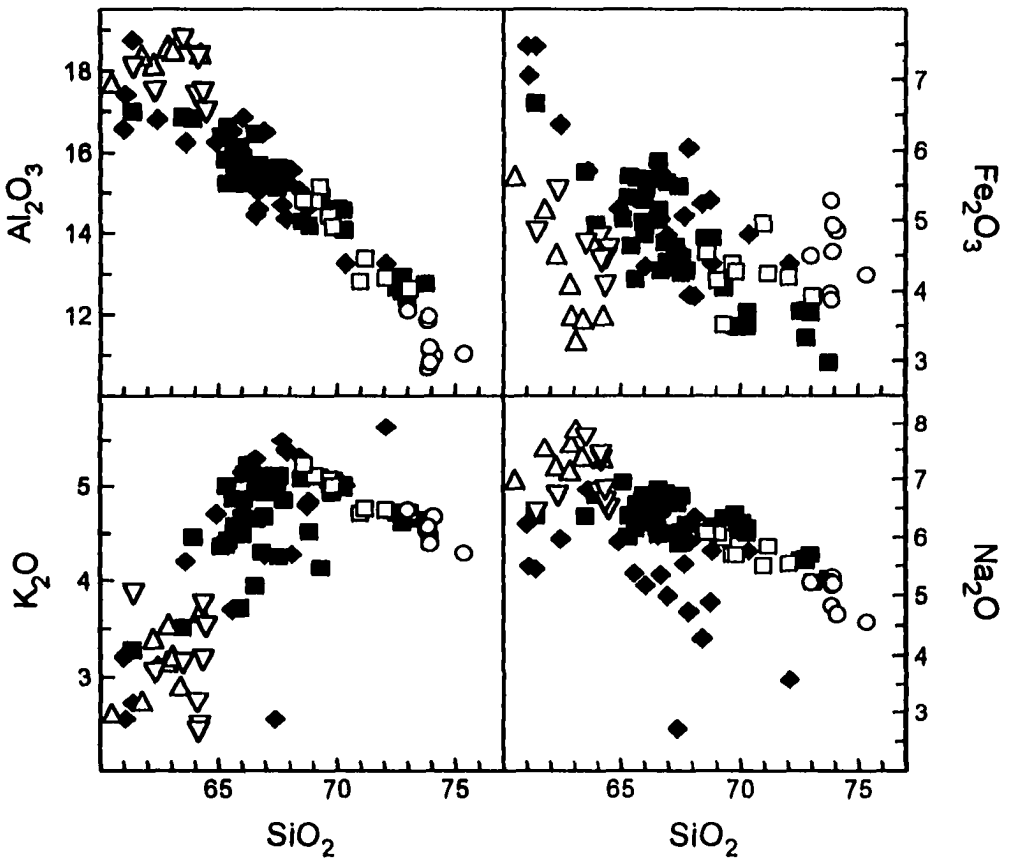

Figure 3.3. Variation in SiO_2 *vs.* Al_2O_3, Fe_2O_3, K_2O, and Na_2O (all in wt%) for felsic rocks from Ascension Island. Symbols plotted denote the following: Δ syenite xenoliths from Broken Tooth; ∇ monzonite xenoliths from Middleton Ridge; O granite xenoliths from Five Mile Post; □ trachyte and rhyolite xenoliths from Green Mountain; ■ trachyte and rhyolite flows; ◆ trachyte and rhyolite pumice.

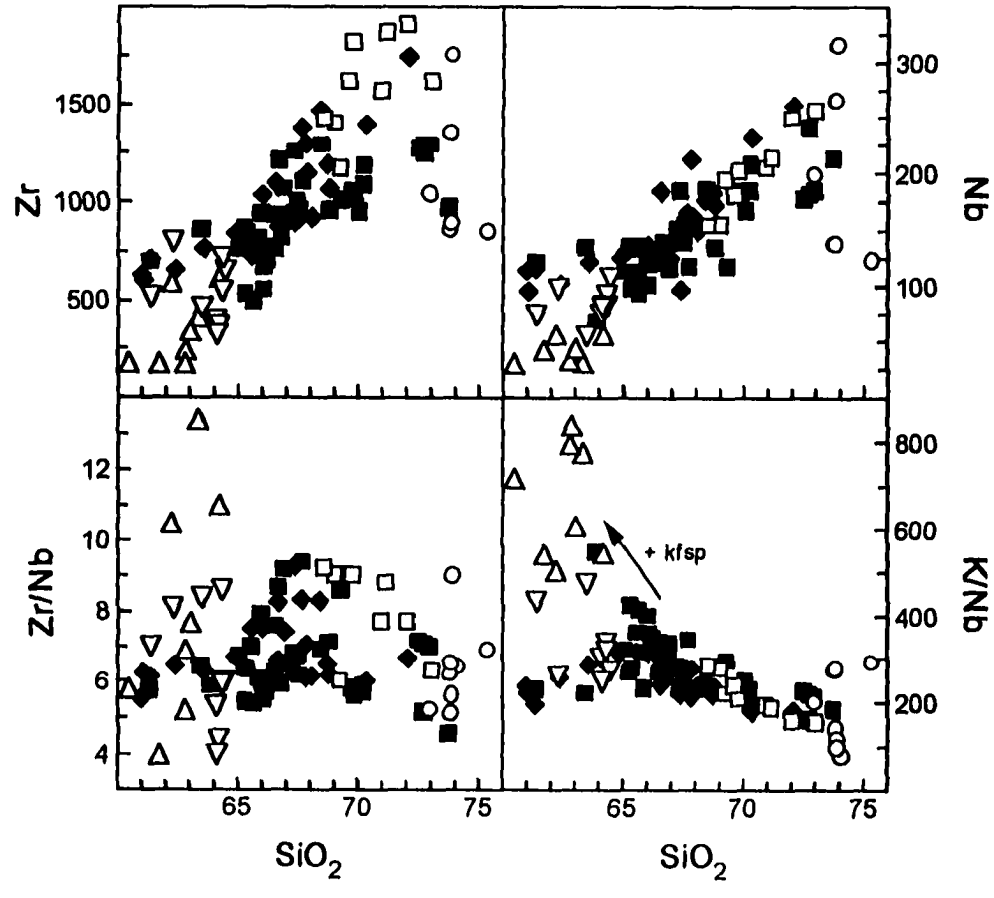

Figure 3.4. Variation in Zr (ppm), Nb (ppm), Zr/Nb, and K/Nb *vs.* SiO_2 (wt%) for felsic rocks from Ascension Island. Symbols as defined for Fig. 3.3.

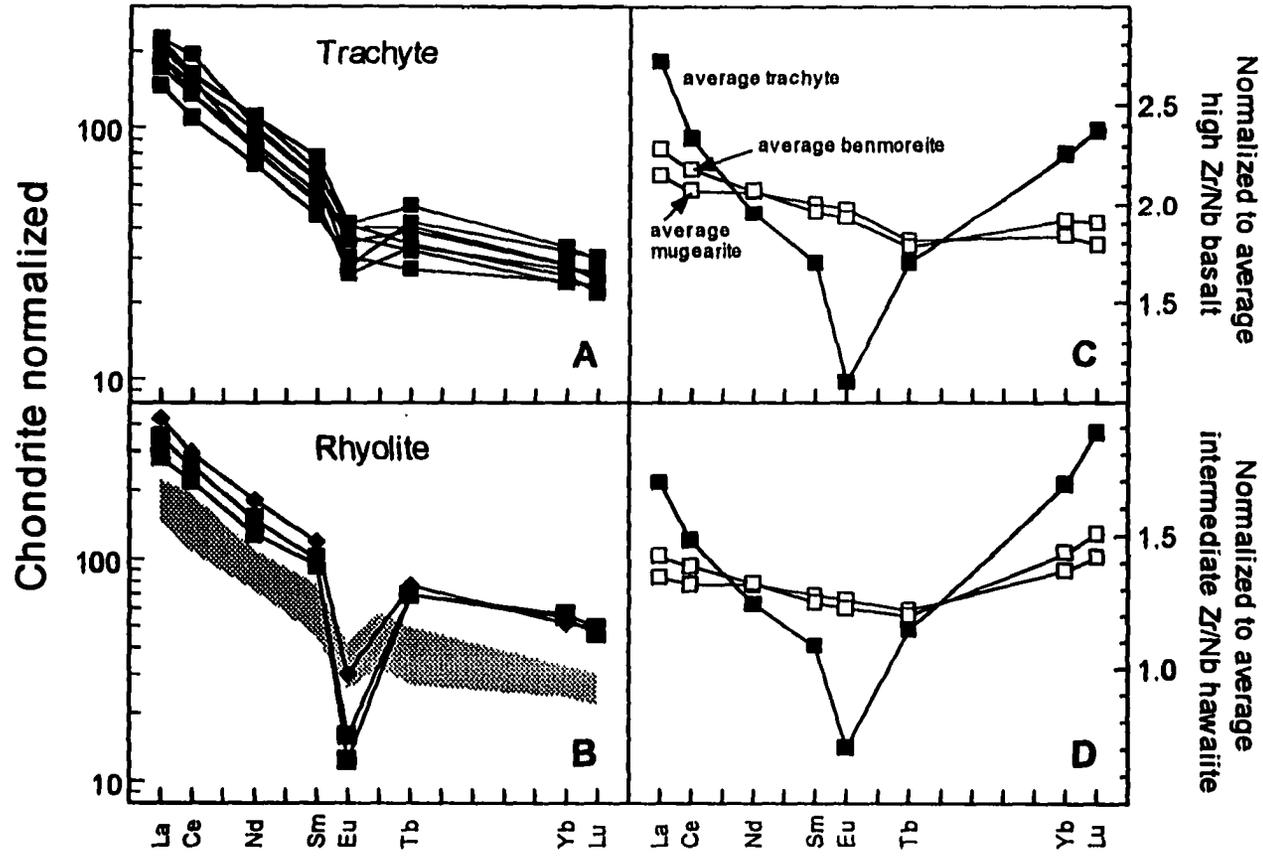

Figure 3.5. Rare earth element patterns (normalized to chondrite values of Nakamura, 1974) for **A** trachyte and **B** rhyolite samples from Ascension Island (note, the REE patterns for the feldspar phyric trachyte of Ragged Hill and Cocoanut Bay are not shown). In **B** the shaded field shows the range of patterns for the trachyte samples. In **C** and **D** the REE patterns for average trachyte, benmoreite, and mugearite have been normalized to the REE patterns of average high Zr/Nb basalt and average intermediate Zr/Nb hawaiite, respectively.

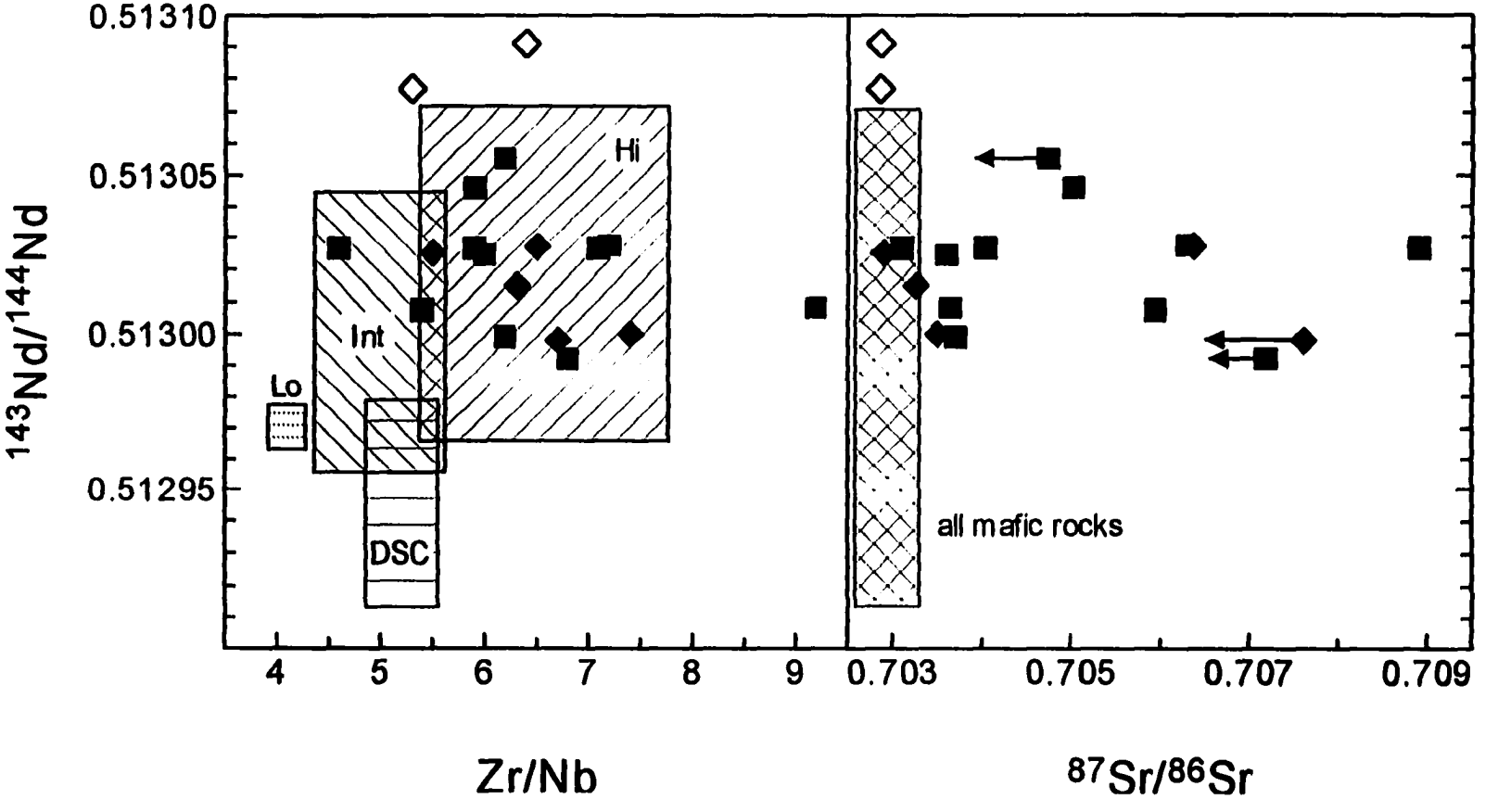

Figure 3.6. Variation in Zr/Nb *vs.* $^{143}Nd/^{144}Nd$ and in $^{87}Sr/^{86}Sr$ *vs.* $^{143}Nd/^{144}Nd$ for Ascension Island mafic and felsic rocks. Symbols as in Fig. 3.3, plus ◇ Broken Tooth mugearite and benmoreite flows. Fields on Zr/Nb *vs.* $^{143}Nd/^{144}Nd$ plot show range of compositions of high Zr/Nb basalt (Hi), low Zr/Nb hawaiite (Lo), intermediate Zr/Nb basalt to benmoreite (Int), and Dark Slope Crater hawaiite and mugearite (DSC). For some high $^{87}Sr/^{86}Sr$, high $^{87}Rb/^{86}Sr$ felsic samples the magnitude of decrease of the ratio on age correction to 1 Ma is shown by an arrow.

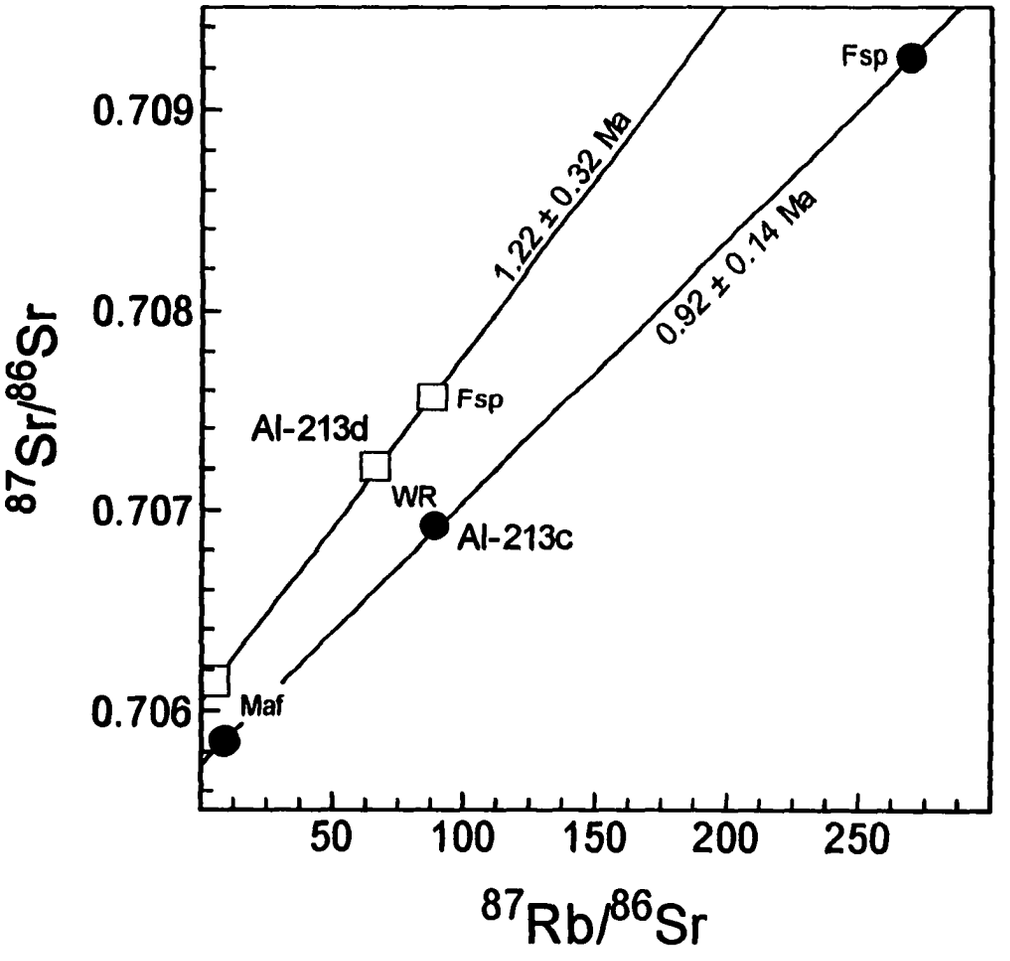

Figure 3.7. Internal Rb-Sr isochrons for two granite xenoliths from Five Mile Post, Ascension Island. The felsic mineral fraction comprises mainly alkali feldspar and the mafic fraction is predominantly amphibole. Note that initial $^{87}Sr/^{86}Sr$ is high for both samples.

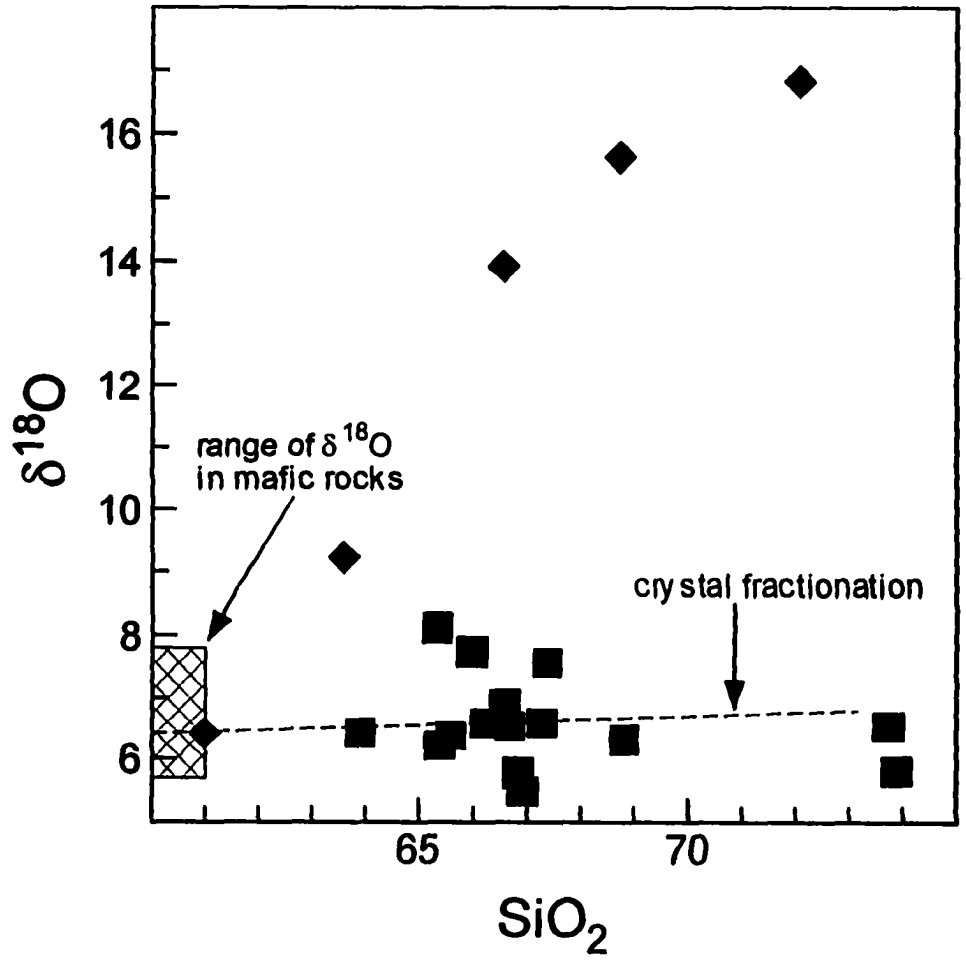

Figure 3.8. Variation in SiO_2 (wt%) *vs.* $\delta^{18}O$ for mafic and felsic volcanic and plutonic rocks from Ascension Island. Symbols as in Fig. 3.3. The range of $\delta^{18}O$ in mafic rocks and the fractionation trend from Sheppard & Harris (1985) are shown.

Table 3.1. Representative chemical analyses of felsic rocks from Ascension Island.

	Trachyte				Rhyolite		Pumice				Granite	Syenite
	Al-111	Al-109	Al-96	Al-91	Al-95	Al-177	Al-120	Al-146	Al-174	Al-42	Al-213c	Al-187e
SiO_2	63.91	65.35	68.82	67.39	69.32	73.75	63.59	66.68	67.38	72.07	73.90	61.74
TiO_2	0.65	0.47	0.40	0.35	0.29	0.14	0.52	0.45	0.52	0.23	0.19	0.72
Al_2O_3	16.81	15.23	14.18	15.60	14.89	12.76	16.25	15.03	20.38	13.26	11.18	18.38
Fe_2O_3	4.93	5.63	4.75	4.32	4.04	2.97	5.71	5.02	4.58	4.38	4.55	5.16
MnO	0.12	0.16	0.19	0.13	0.17	0.08	0.19	0.16	0.22	0.12	0.16	0.14
MgO	0.44	0.05	0.22	0.09	0.07	0.02	0.60	0.41	0.41	0.25	<0.05	0.41
CaO	1.62	0.76	0.68	0.40	0.73	0.32	2.00	1.46	1.14	0.42	0.18	2.93
Na_2O	6.72	6.36	6.18	6.57	6.33	5.28	6.82	5.35	2.71	3.58	5.30	7.55
K_2O	4.46	5.00	4.52	5.10	4.13	4.65	4.20	5.13	2.54	5.66	4.49	2.74
P_2O_5	0.34	0.99	0.06	0.05	0.03	0.03	0.12	0.31	0.12	0.03	0.05	0.23
H_2O-	0.27	0.42	0.29	0.47	0.23	0.12	1.16	2.77	5.98	2.35	0.07	0.15
LOI	0.95	0.58	–0.08	0.25	0.14	0.36	4.67	2.72	7.69	5.25	0.22	0.33
Ni	<2	<2	<2	2	<2	<2	2	2	2	2	<2	<2
Cr	2.0	2.1	1.7	3.2	nd	0.9	1.9	7.1	3.9	3.1	nd	nd
Sc	13.2	14.0	9.6	5.7	nd	1.4	10.3	7.4	7.4	1.7	1	10
V	19	6	5	4	3	5	5	13	9	6	19	7
Zn	71	110	167	155	148	189	149	160	311	256	150	82
Ga	28	30	34	33	30	35	28	31	25	35	38	27
Rb	63	69	87	109	82	161	75	102	73	188	157	28
Sr	184	24	10	7	15	1	114	47	74	7	5	278
Ba	1304	1153	516	219	886	24	868	220	799	21	32	1668
Th	6.40	7.61	11.1	14.3	nd	19.4	8.85	11.9	8.02	25.1	17	2
Pb	3	3	7	7	8	11	5	6	4	14	8	4
Zr	398	532	954	1248	1003	968	766	1074	899	1743	1752	170
Hf	7.88	10.5	20.1	22.3	nd	23.8	13.6	19.8	15.4	33.4	nd	nd
Nb	68	98	134	184	117	212	122	130	97	261	315	42
Ta	4.59	5.83	8.06	10.4	nd	13.6	6.87	7.63	5.47	15.6	nd	nd
La	40.3	45.3	71.9	73.2	nd	91.9	62.6	72.8	100	139	269*	33*
Ce	83.2	94.5	139	165	nd	189	128	142	142	254	479*	61*
Nd	37.2	46.7	68.6	63.0	nd	81.0	59.8	67.1	100	113	289*	28*
Sm	8.10	10.2	15.6	12.9	nd	19.1	12.5	14.6	21.9	24.2	nd	nd
Eu	3.51	3.17	3.20	2.15	nd	1.21	3.61	2.10	5.59	2.31	nd	nd
Tb	1.32	1.64	2.55	2.18	nd	3.59	1.94	2.33	3.64	3.95	nd	nd
Yb	3.72	4.96	7.25	6.99	nd	11.9	5.96	7.81	11.0	11.2	nd	nd
Lu	0.51	0.69	1.00	1.02	nd	1.56	0.84	1.11	1.53	1.66	nd	nd
Y	45	56	85	84	91	137	69	87	151	148	242	27
$Na_2O + K_2O$	11.18	11.36	10.70	11.67	10.46	9.93	11.02	10.48	5.25	9.24	9.79	10.29
Na_2O/K_2O	1.51	1.27	1.37	1.29	1.53	1.14	1.62	1.04	1.07	0.63	1.18	2.76
Zr/Nb	5.9	5.4	7.1	6.8	8.6	4.6	6.3	8.3	9.3	6.7	5.6	4.0
La/Nb	0.59	0.46	0.54	0.40	–	0.43	0.51	0.56	1.03	0.53	0.85	0.79
Rb/Nb	0.93	0.70	0.65	0.59	0.70	0.76	0.61	0.78	0.75	0.72	0.50	0.67
K/Nb	544	424	280	230	293	182	285	328	217	180	118	542
Th/Nb	0.094	0.078	0.083	0.078	–	0.092	0.073	0.092	0.083	0.096	–	–
Zr/Y	8.8	9.5	11.2	14.9	11.0	7.1	11.1	12.3	6.0	11.8	7.2	6.3
Ce_N/Yb_N	5.7	4.8	4.9	6.0	–	4.0	5.5	4.6	3.3	5.8	–	–

Table 3.2. Sr, Nd, Pb, and O isotopic data for felsic rocks from Ascension Island.

		SiO_2	$^{87}Sr/^{86}Sr$	Rb ppm	Sr ppm	$^{87}Rb/^{86}Sr$	$^{87}Sr/^{86}Sr_i$	ε_{Sr}	$^{143}Nd/^{144}Nd$	ε_{Nd}	$^{206}Pb/^{204}Pb$	$^{207}Pb/^{204}Pb$	$^{208}Pb/^{204}Pb$	$d^{18}O$ WR
Trachyte and rhyolite														
Al-111		63.91	0.705038 ± 9	63	184	0.9904	0.705024	+4.6	0.513046 ± 13	+7.96	19.665	15.668	39.332	+6.41
Al-79		66.00	0.703605 ± 10	79	29	7.879	0.703493	−17.1	0.513024 ± 10	+7.53	19.669	15.615	39.232	+7.73
Al-41		66.93	0.703651 ± 9	88	15	16.97	0.703410	−18.3	0.513008 ± 8	+7.22	19.587	15.606	39.031	+5.47
Al-175		66.84	0.703117 ± 8	94	24	11.33	0.702956	−24.7	0.513026 ± 9	+7.57	19.669	15.624	39.194	+5.76
Al-91		67.39	0.707188 ± 11	109	7	45.05	0.706548	+26.2	0.512992 ± 6	+6.91	19.746	15.644	39.339	+7.56
Al-109		65.35	0.705950 ± 11	69	24	8.317	0.705832	+16.1	0.513007 ± 9	+7.20	19.568	15.602	39.122	+8.11
Al-67		67.28	0.703715 ± 10	117	7	48.34	0.703029	−23.7	0.512999 ± 10	+7.04	19.693	15.636	39.264	+6.57
Al-103		66.58	0.704755 ± 11	81	4	58.57	0.703923	−11.0	0.513055 ± 11	+8.13	19.503	15.633	39.132	+6.91
Al-96		68.82	0.704053 ± 9	87	10	25.16	0.703696	−14.2	0.513026 ± 8	+7.57	19.626	15.630	39.236	+6.30
Al-94		72.53	0.706306 ± 14	126	*1*	*364.5*	–	–	0.513027 ± 8	+7.59	–	–	–	–
Al-177		73.75	0.708917 ± 11	161	*1*	*465.9*	–	–	0.513026 ± 7	+7.57	19.516	15.622	39.116	+6.52
Pumice														
Al-120		63.59	0.703255 ± 9	75	114	1.903	0.703228	−20.9	0.513015 ± 8	+7.35	19.617	15.609	39.125	+9.23
Al-121		60.99	0.702898 ± 10	64	270	0.6855	0.702888	−25.7	0.513025 ± 18	+7.55	19.569	15.608	39.118	+6.41
Al-44		68.72	0.706368 ± 15	115	16	20.79	0.706073	+19.5	0.513027 ± 9	+7.59	19.713	15.666	39.368	+15.6
Al-43		66.95	0.703498 ± 10	83	67	3.583	0.703447	−17.8	0.513000 ± 9	+7.06	–	–	–	–
Al-42		72.07	0.707603 ± 10	188	7	77.71	0.706500	+25.6	0.512998 ± 8	+7.02	19.687	15.650	39.330	+16.8
Granite														
Al-213c	WR	73.90	0.706920 ± 11	152.7	4.96	89.07	0.705756	+15.0	–	–	–	–	–	+5.80
	Felsic minerals		0.709250 ± 10	109.9	1.18	269.5	0.705729	+14.6	–	–	–	–	–	–
	Mafic minerals		0.705850 ± 10	27.7	8.51	9.403	0.705727	+14.6	–	–	–	–	–	–
Al-213d	WR	73.83	0.707210 ± 10	86.7	3.80	66.00	0.706067	+19.4	0.512998 ± 8	+7.02	–	–	–	–
	Felsic minerals		0.707560 ± 16	53.2	1.75	87.87	0.706038	+19.0	–	–	–	–	–	–
	Mafic minerals		0.706140 ± 10	14.4	7.41	5.610	0.706043	+19.1	–	–	–	–	–	–

Table 3.1 Footnote:

Al-111 Cocoanut Bay trachyte; Al-109 Ragged Hill trachyte; Al-96 Middleton Ridge trachyte flow; Al-91 Daly's Crags trachyte; Al-95 Middleton Ridge rhyolite flow; Al-177 Little White Hill rhyolite flow dome; Al-120 trachyte pumice from Hummock Point; Al-146 trachyte pumice from NASA Road; Al-174 trachyte pumice from Green Mountain Road; Al-42 rhyolite pumice from Devil's Riding School; Al-213c granite xenolith from Five Mile Post; Al-187e syenite xenolith from Broken Tooth flow.

Major element oxides are recalculated to sum to 100% on an anhydrous basis. H_2O- is weight loss after drying for 12 hours at 110°C. LOI is weight loss after ignition at 950°C for 1 hour (oxidation of Fe^{2+} to Fe^{3+} in near-anhydrous samples results in weight gain, expressed as negative LOI). Trace elements are in parts per million; Ni, V, Zn, Ga, Rb, Sr, Ba, Pb, Zr, Nb, and Y determined by XRF, other trace elements determined by INAA except *La, Ce, Nd determined by XRF. nd - not determined.

Table 3.2 Footnote:

Sr, Nd, and Pb isotope ratios determined at UCLA. Initial $^{87}Sr/^{86}Sr$ for trachyte, rhyolite, and pumice samples was calculated using an age of 1 Ma which likely results in over-correction for some samples (see Fig. 2). For the granite samples the isochron age (0.92 Ma for Al-213c and 1.22 Ma for Al-213d) was used for age correction. O isotope compositions were determined at SMU.

Rb and Sr abundance determined by XRF at OU except for granite samples for which Rb and Sr were determined by isotope dilution at UCLA. For Al-94 and Al-177 the determined Sr abundance is at the detection limit of the XRF technique and there may be significant error in calculated $^{87}Rb/^{86}Sr$.

CHAPTER IV

To be submitted to Earth and Planetary Science Letters

Geochemical characteristics of borehole samples recovered from Ascension Island, South Atlantic Ocean

Kar, A.[1,2]

School of Geology and Geophysics
University of Oklahoma
Norman, OK 73019, USA

Weaver, B.

School of Geology and Geophysics
University of Oklahoma
Norman, OK 73019, USA

Davidson, J.

Department of Earth and Space Sciences
University of California Los Angeles
Los Angeles, CA 90095, USA

Neilson, D.

Earth Sciences and Resource Institute
Department of Civil and Environmental Engineering
University of Utah
Salt Lake City, UT 84112, USA

[1] Department of Mathematics and Physics
Fort Valley State University
Fort Valley, GA 31030, USA

[2] Corresponding Author
Telephone: (912) 825 6844
FAX: (912) 825 6618
email: kara@mail.fvsc.peachnet.edu

ABSTRACT

Exposed volcanic rocks on Ascension Island comprise a basalt to trachyte and rhyolite suite with a high proportion of pyroclastic deposits (43%) relative to lava flows (57%). Compositional variations in mafic (basalt and hawaiite) lava flows and scoria reveal four distinct magma types which are best discriminated by Zr/Nb and isotopic (Sr, Nd, Pb) composition.

Seven holes drilled for geothermal prospecting (GH1 to GH6 and LDTGH) recovered almost continuous core and penetrated the volcanic pile to a maximum depth of 200 m below sea level. The volcanic rocks recovered from the boreholes were formed subaerially, suggesting substantial subsidence of the Ascension volcanic edifice. Overall, the relative proportion of pyroclastic deposits (mafic to silicic) to lava flows in the cores is similar to that of the exposed volcanic rocks although there are large variations between boreholes.

A shallow hole (GH3, bottom depth at approximately sea-level) in the southwestern part of the island reveals that low Zr/Nb (4.1) hawaiite flows overlie intermediate Zr/Nb (5.5) hawaiite flows which overlie hawaiite and mugearite flows of Dark Slope Crater (intermediate Zr/Nb but high Sr and Ni relative to Zr), relationships inferred from the surface geology. In the other six boreholes the mafic (basalt and hawaiite) lava flows do not display any systematic variation in geochemical characteristics with depth, most of the flows being of the intermediate Zr/Nb (~5) type. However, basalt and hawaiite flows from the deepest levels of three boreholes to the east and north of Devil's Riding School have higher Zr/Nb (7.4 to 7.7 in GH1 at 10 to -6 m relative to sea-level; 6.8 to 7.1 in GH6 at -122 to -194 m relative to sea-level; 6.6 in LDTGH at -113 to -142 m relative to sea-level) than any of the surface basalt or hawaiite lava flows (maximum Zr/Nb of 6.1).

Geochemical data for flows from the boreholes shows that there are no simple temporal relationships between the different mafic magma types erupted on Ascension Island. However, some boreholes may have penetrated close to the base of the slightly more alkaline flows which likely overlie an earlier, more tholeiitic, shield phase of magmatism on Ascension.

INTRODUCTION

Ascension Island, situated at 7°56'S and 14°22'W in the South Atlantic Ocean, is a hotspot-related volcanic island. It is located 80 km west of the Mid Atlantic Ridge and 50 km south of Ascension Fracture Zone on oceanic crust which is 5 to 6 million years old. The volcanic edifice covers about 2000 km^2 of the ocean floor and rises about 2700 m from the ocean floor with a little less than 860 m of the island exposed above sea level (Brozena, 1986). The areal exposure of the island is about 98 km^2.

Compositional variations in mafic (basalt and hawaiite) lava flows and scoria reveal four distinct magma types which are best discriminated by trace element and isotopic (Sr, Nd, and Pb) compositions (Kar et al., Mafic MS). Incompatible element ratios and radiogenic isotopic systematics of Ascension also establish that large-scale chemical heterogeneities occur in the mantle under the South Atlantic Ocean and small-scale heterogeneities occur on a single-island basis (Kar et al., Mafic MS). Well established data now exist on the surface geology, mineralogy, geochemistry and ages of the volcanic and plutonic rocks, and also on the fluids associated with magmatism (Atkins et al., 1964; Roedder & Coombs, 1967; Harris & Bell, 1982; Harris et al., 1982; Harris, 1983; Weis, 1983; Harris, 1985; Sheppard & Harris, 1985; Harris & Sheppard, 1987; Weis et al., 1987; Adams, 1996; Nielson & Sibbett, 1996; Nielson & Stiger, 1996; Weaver et al., 1996; Kar et al., Felsic MS; Kar et al., Mafic MS). Geological data also

exists on the large volcanic edifice of Ascension Island (Nielson & Sibbett, 1996). Seven boreholes drilled for geothermal prospecting recovered almost continuous core and penetrated the volcanic pile to a maximum depth of 200 m below sea-level (Neilson & Sibbett, 1996; Kar et al., 1995). This paper is aimed at understanding the geochemical nature of the subsurface of Ascension Island from borehole studies.

SURFACE GEOLOGY OF ASCENSION ISLAND

Ascension is a composite volcano and the exposed volcanic rocks comprise transitional to mildly alkaline basalt-hawaiite-mugearite-benmoreite-trachyte-rhyolite series lava flows, trachyte domes and flows, scoria cones, and pyroclastic deposits. Pyroclastic (pumice and scoria) deposits make up about 43% of the island's total areal extent (Harris, 1983). Other than pyroclastic deposits and the trachyte, most of the island is covered by lava flows. The Ascension mafic flows and scoria have a significant range in Zr/Nb, from 4.0 to 6.0 (see below). There are four distinct mafic rock types that are identified based on trace element variations (Fig. 4.1):

(1) High Zr/Nb basalt

Basalt lava flows (SiO_2 47.6 to 50.6 wt%) from the southeastern part of the island and extensive basaltic lapilli deposits on Green Mountain have relatively low Zr (160 to 248 ppm) but high Zr/Nb (5.6 to 6.1). Only three scoria cones, in the southwestern and northern parts of the island, have high Zr/Nb.

(2) Low Zr/Nb hawaiite

Localized hawaiite lava flows in the southwestern part of the island (Fig. 4.1) have a restricted range of compositional variation (SiO_2 47.3 to 47.9 wt%; Zr 235 to 259 ppm) and have low Zr/Nb (4.1). These flows originated from a number of small scoria cones.

(3) Intermediate Zr/Nb basalt-hawaiite-mugearite-benmoreite

Most of the western and northern parts of Ascension Island (Fig. 4.1) are covered by basalt to benmoreite lava flows (SiO_2 47.25 to 60.95 wt%) with a wide range in Zr (140 to 610 ppm) and intermediate Zr/Nb (4.5 to 5.6). Most of the scoria cones on the island are of intermediate Zr/Nb composition.

Basalt and hawaiite

Basalt and hawaiite flows and scoria have 47.3 to 51.6 wt% SiO_2, 140 to 387 ppm Zr, and a range in Zr/Nb of 4.6 to 5.6 although Zr/Nb < 4.8 or Zr/Nb > 5.2 is rare.

Mugearite and benmoreite

Mugearite flows and scoria have 50.2 to 55.3 wt% SiO_2, 333 to 470 ppm Zr, and Zr/Nb of 4.7 to 5.9 whereas benmoreite flows and scoria have 54.7 to 61.0 wt% SiO_2, 429 to 610 ppm Zr, and Zr/Nb of 4.9 to 6.0.

(4) Dark Slope Crater hawaiite-mugearite

Hawaiite and mugearite flows (SiO_2 48.2 to 52.1 wt%) originating from Dark Slope Crater have intermediate Zr/Nb (4.9 to 5.2) but have high Ni (28 to 52 ppm) and Sr (596 to 902 ppm) relative to Zr (318 to 558 ppm) compared to other intermediate Zr/Nb hawaiite flows and scoria (Ni < 20 ppm and Sr < 540 ppm at equivalent Zr content).

Felsic Rocks

There are two distinctive felsic eruptive centers on the island, the central felsic complex and the eastern felsic complex. The central felsic complex is comprised of the Middleton Ridge felsic center and Green Mountain (Fig. 4.1). Middleton Ridge is composed primarily of trachyte, pumice, and some rhyolite and rhyolitic obsidian. The eastern felsic complex is made up of numerous trachyte flows and lava domes (Fig. 4.1).

SAMPLING AND ANALYTICAL TECHNIQUES

Samples were taken from the core stored at the University of Utah Research Institute, Salt Lake City. For details of the sample preparation technique and analytical procedure for major and trace element analyses obtained at the University of Oklahoma refer to Weaver et al. (1996) and for radiogenic isotope analysis performed at University of California, Los Angeles refer to Davidson et al. (1993).

BOREHOLE STRATIGRAPHY AND GEOCHEMISTRY

Seven boreholes (GH1 to GH6 and LDTGH; Fig. 4.1) were drilled for geothermal exploration on Ascension Island (Neilson & Sibbett, 1996). Boreholes GH5, GH1, LDTGH, and GH6 lie on a north-south line stretching a distance of about 3 km (Fig. 4.1). In addition to these seven boreholes, a deep exploration well (Ascension #1) was drilled at the location of LDTGH to a depth of 3125 m but was not cored.

The overall proportions of rock types in the boreholes are similar to the surface exposure, with a high percentage of silicic flows and pyroclastic deposits (Fig. 4.2). Boreholes GH3, GH4, and GH5 penetrated mostly mafic flows whereas GH6, LDTGH, GH1, and GH2 penetrated significant thicknesses of silicic rocks (Fig. 4.2). The rocks recovered from the seven boreholes (even the rocks recovered from below sea level) have evidence of being erupted subaerially, implying subsidence of the volcanic edifice by at least 200 m while surface eruptions continued (Neilson & Sibbett, 1996). The deep exploration well (Ascension #1) was the only well that penetrated hyaloclastite layers. The presence of hyaloclastite layers topped by subaerial basalt flows indicates that the island has undergone at least three phases of emergence and subsidence (Neilson & Stiger, 1996). More active phases of volcanism leading to the emergence of the island above sea level were followed by more quiescent phases and subsidence of

the volcanic edifice below sea level due to loading of the oceanic lithosphere. There has been 1.5 to 2 km of subsidence since the onset of hyaloclastite formation (Neilson & Stiger, 1996). A detailed description of the boreholes follows.

GH1, McTurk's Culvert and RAF Base

GH1 was drilled to the southeast of Lady Hill and adjacent to the New Mountain Road (Fig. 4.1). Fig. 4.2 shows the stratigraphy of the rocks cored. The surface exposure in this area is a mugearite flow (AI-178). GH1 was drilled to a total depth of 177.7 m (top of the hole at +171.6 m rsl [relative to sea level], bottom of the hole at –6.1 m rsl) and predominantly penetrated pyroclastic deposits (mafic and silicic) and a silicic flow with mafic flows only in the upper and lower parts of the hole (Fig. 4.3).

The two mafic flows cored in the interval 146.3 to 135.6 m rsl (GH1-1 and GH1-2, separated by a soil horizon at 139.6 m rsl) are non-vesicular, aphyric (rare plagioclase + olivine + titanomagnetite phenocrysts) hawaiite of intermediate Zr/Nb (5.1 and 5.2) with high P/Zr (17.2 and 19.8). The silicic flow cored in the interval 77.1 to 36.0 m rsl is compositionally equivalent (UURI data) to the rhyolite flow exposed on Middleton Ridge and also cored in GH6 and LDTGH. The mafic dyke(?) cored in the interval 32.3 to 28.6 m rsl is extensively altered and was not sampled. The mafic flows cored from 9.8 m rsl to the bottom of the hole (GH1-3 to GH1-5) are sparsely to highly vesicular, highly-phyric (plagioclase > olivine + clinopyroxene) basalt which have Zr/Nb (7.4 to 7.7) much higher than any of the surface flows (maximum Zr/Nb 6.2). P/Zr is low (9.7 to 10.3), similar to the surface high Zr/Nb flows.

GH2, east rim of Cricket Valley

GH2 was drilled on the eastern rim of Cricket Valley (Fig. 4.1) and the stratigraphy of the rocks cored are shown in Fig. 4.2. The surface exposure in this area is of

volcanic breccia. GH2 was drilled to a total depth of 533.4 m (top of the hole at +478.5 m rsl, bottom of the hole at –54.9 m rsl) and penetrated a sequence dominated by mafic and silicic pyroclastic deposits and silicic flows with mafic flows only in the upper and lower parts of the hole (Fig. 4.4).

The mafic flow cored in the interval 447.4 to 436.1 m rsl was not sampled. The mafic flow cored in the interval 423.0 to 317.0 m rsl was sampled from the central (GH2-1) and lower (GH2-2) parts of the unit; this is the flow exposed in the walls of Cricket Valley sampled as AI-64 and AI-65 from the upper part of the unit. This flow is remarkably uniform in composition considering its unusual thickness (106 m); it is a high Zr/Nb basalt with SiO_2 varying only between 50.58 and 51.33 wt% and MgO only between 4.99 and 5.30 wt%; an unusual feature of this flow is the elevated Rb/Nb (0.67 to 0.72; range 0.40 to 0.68 in other high Zr/Nb flows). Beneath this very thick flow, in the interval 312.4 to 303.5 m rsl (GH2-3), is a sparsely vesicular, sparsely phyric (plagioclase + olivine + titanomagnetite phenocrysts) mugearite of intermediate Zr/Nb (5.1).

Three trachyte flows are present; a flow with a faulted lower contact between 277.3 and 264.5 m rsl (GH2-4) and two thick flows between 185.6 to 124.9 m rsl (GH2-5) and 123.7 to 87.7 m rsl (GH2-6) with an intervening volcaniclastic layer.

The mafic flow (dyke?) cored in the interval 82.3 to 79.2 m rsl and the mafic flow cored in the interval 79.2 to 65.8 m rsl (GH2-7, GH2-8) are sparsely vesicular and non-vesicular, respectively, aphyric (rare plagioclase + olivine + titanomagnetite microphenocrysts or phenocrysts) mugearite which are chemically very similar. The mafic flows and dykes(?) cored in the interval 62.1 to 33.2 m rsl (GH2-9 to GH2-11) are non-vesicular, aphyric (rare plagioclase + olivine ± clinopyroxene ± titanomagnetite microphenocrysts or phenocrysts) mugearite which are more evolved (55.0 to 56.9 wt%

SiO_2, 459 to 530 ppm Zr) than the overlying mugearite flows (GH2-7 and GH2-8; 52.4 to 53.2 wt% SiO_2, 390 to 398 ppm Zr). The mafic flow cored in the interval 3.6 to -5.5 m rsl (GH2-12) is a non-vesicular, aphyric (rare plagioclase + titanomagnetite microphenocrysts) hawaiite of intermediate Zr/Nb (5.5) and high P/Zr (17.1).

A rhyolite flow is present in the bottom of the hole (-16.2 to -54.9 m rsl; GH2-13).

GH3, north of Booby Hill

GH3 was drilled just to the north of Booby Hill (Fig. 4.1) and the stratigraphy within the hole is shown in Fig. 4.2. This hole is an area where a number of geochemically distinct magma types were erupted. The scoria cones of Cotar Hill [Cone 43], Horse Shoe Crater [Cone 33], and nearby unnamed cones (Cone 36, Cone 37) erupted hawaiite magma with low Zr/Nb (4.0 to 4.1). Dark Slope Crater [Cone 32] erupted magma ranging in composition from hawaiite to mugearite that is of intermediate Zr/Nb (4.9 to 5.2) but, compared to other intermediate Zr/Nb flows, has high Sr and Ni relative to Zr.

GH3 penetrated to a total depth of 62.8 m (top of the hole at +64.6 m rsl, bottom of the hole at –1.8 m rsl) through a sequence entirely composed of mafic lava flows with intervening flow breccia (Fig. 4.5).

The two flows cored in the interval 59.1 to 50.9 m rsl (GH3-1 and GH3-2) are aphyric (rare plagioclase + clinopyroxene + titanomagnetite ± olivine microphenocrysts or phenocrysts) hawaiite of low Zr/Nb (4.1 and 4.2).

The two flows cored in the interval 45.4 to 32.3 m rsl (GH3-3 and GH3-4) are aphyric hawaiite of intermediate Zr/Nb (5.5) and moderate P/Zr (13.6 and 14.2), the lower of the two flows is slightly more evolved. These flows are not similar in composition to any exposed flows or scoria cones in this area.

The flows cored in the interval 26.8 to 5.5 m rsl (GH3-5 to GH3-8) are aphyric to sparsely phyric (olivine ± plagioclase microphenocrysts or phenocrysts) hawaiite and mugearite of Dark Slope Crater (distinctive high Sr and Ni relative to Zr) and are increasingly evolved downhole.

The flow cored in the bottom 1.2 m of the hole is extensively altered and was not sampled, and may be a substantially older flow than those above it.

In the South West Bay cliff sections, low Zr/Nb flows directly overlie Dark Slope Crater flows, without the intervening intermediate Zr/Nb flows found in GH3.

GH4, near Bear's Back

GH4 was drilled to the southwest of Bear's Back (Fig. 4.1) and the stratigraphy within the hole is shown in Fig. 4.2. The surface exposure in this area is of pyroclastic deposits. GH4 was drilled to a total depth of 220.4 m (top of the hole at +178.6 m rsl, bottom of the hole at –41.8 m rsl) and mostly penetrated mafic flows and intervening flow breccia, although the uppermost 35.1 m comprises pyroclastic deposits (Fig. 4.6).

The two flows cored in the intervals 143.5 to 135.6 m rsl and 124.7 to 100.0 m rsl (GH4-1 and GH4-2) are non-vesicular, aphyric (rare plagioclase + titanomagnetite ± olivine ± clinopyroxene phenocrysts) benmoreite and trachyte.

The flow cored in the interval 94.5 m to 89.0 m rsl (GH4-3) is a sparsely vesicular, sparsely phyric (plagioclase + olivine phenocrysts) basalt of high Zr/Nb (6.4; slightly higher Zr/Nb than any of the surface flows) and with low P/Zr (8.3).

The flows cored in the interval 66.1 to -31.1 m rsl (GH4-4 to GH4-8) are non-vesicular, aphyric (plagioclase + olivine + titanomagnetite microphenocrysts or phenocrysts) hawaiite of intermediate Zr/Nb (5.3 to 5.5) and moderate P/Zr (12.9 to 14.1); these flows have distinctive high Sr (650 to 660 ppm) and are compositionally

very similar to those exposed on Bear's Back, implying approximately 120 m uplift of the flows in the formation of Bear's Back.

GH5, old Mountain Road

GH5 was drilled to the south-southeast of Sisters Peak, adjacent to the Old Mountain Road (Fig. 4.1) and the stratigraphy within the hole is shown in Fig. 4.2. The surface exposure in this area is of a basalt flow sampled as AI-167. GH5 was drilled to a depth of 271.9 m (top of the hole at +157.0 m rsl, bottom of the hole at –114.9 m rsl) and mostly penetrated mafic pyroclastic deposits and mafic flows (Fig. 4.7).

The three flows cored in the interval 149.4 to 119.8 m rsl (GH5-1 to GH5-3) are non-vesicular, sparsely phyric (plagioclase + olivine + titanomagnetite phenocrysts) hawaiite of intermediate Zr/Nb (4.9 to 5.1) and high P/Zr (18.9 to 19.6); they are compositionally very similar to surface flow AI-167.

The two flows cored in the interval 111.3 to 104.9 m rsl (GH5-4 and GH5-5) are non-vesicular and aphyric (rare plagioclase or titanomagnetite phenocrysts) mugearite of intermediate Zr/Nb (5.4) and low P/Zr (10.3).

The thin flow cored in the interval 70.1 to 68.0 m (GH5-6) is a non-vesicular, aphyric (rare plagioclase + titanomagnetite + resorbed amphibole phenocrysts or microphenocrysts) benmoreite flow.

The two flows cored in the interval 42.7 to 19.2 m rsl (GH5-7 and GH5-8) are non-vesicular, highly phyric (plagioclase + olivine clinopyroxene titanomagnetite phenocrysts or microphenocrysts) basalt of high Zr/Nb (5.7) and low P/Zr (10.5 and 10.8).

The dyke(?) cored in the interval -10.0 to -76.2 m rsl (GH5-9) is a non-vesicular, sparsely phyric (alkali feldspar + clinopyroxene + titanomagnetite phenocrysts or

microphenocrysts) trachyte which is unusual in having low Zr, Nb, and Sr for the SiO_2 compared to surface felsic flows.

GH6, Devil's Riding School

GH6 was drilled to the east of Devil's Riding School adjacent to the NASA Road (Fig. 4.1) and the stratigraphy within the hole is shown in Fig. 4.2. The surface exposure in this area is of pyroclastic deposits. GH6 was drilled to a depth of 394.4 m (top of the hole at +189.0 m rsl, bottom of the hole at –205.4 m rsl) and mostly penetrated pyroclastic deposits and silicic flows in the upper part of the hole and mafic flows in the lower part of the hole (Fig. 4.8).

The trachyte flow cored in the interval 186.9 to 164.6 m rsl (GH6-1) is non-vesicular and sparsely phyric (K-feldspar + clinopyroxene phenocrysts or microphenocrysts) and is the same flow as exposed on the northern and northeastern flanks of Devil's Riding School.

The rhyolite flow cored in the interval 72.6 to 42.1 m rsl is compositionally equivalent to the Middleton Ridge rhyolite (UURI data).

The mafic flows cored in the interval -121.6 to -193.8 m rsl (GH6-2 to GH6-4) are non-vesicular to moderately vesicular, aphyric to sparsely-phyric (plagioclase + olivine + titanomagnetite phenocrysts or microphenocrysts) hawaiite and basalt of high Zr/Nb (6.8 to 7.1). GH6-2 is more evolved (hawaiite with 51.3 wt% SiO_2 and 293 ppm Zr) and has moderate P/Zr (14.7), whereas GH6-3 and GH6-4 are less evolved (basalt with 48.3 and 48.5 wt% SiO_2 and 242 and 245 ppm Zr) and have low to moderate P/Zr (11.8 and 13.5)

The mafic flow cored in the interval -193.8 to -203.6 m rsl (GH6-5) is a moderately vesicular, highly-phyric (plagioclase >> titanomagnetite + olivine phenocrysts or

microphenocrysts) basalt flow of high Zr/Nb (6.2) and low P/Zr (10.6). This flow is compositionally similar to those exposed on the flanks of Devil's Riding School.

LDTGH, west of Middleton Ridge

LDTGH was drilled to the west of Middleton Ridge and approximately 750 m north-northwest of the site of GH6 and 500 m south-southeast of the site of GH1 (Fig. 4.1) and the stratigraphy within the hole is shown in Fig. 4.2. The surface exposure in this area is of pyroclastic deposits. LDTGH was drilled to a depth of 339.9 m (top of the hole at +174.7 m rsl, bottom of the hole at –165.2 m rsl) and mostly penetrated silicic pyroclastic deposits and flows with mafic flows only in the lower part of the hole (Fig. 4.9).

The trachyte flow cored in the interval 138.7 to 101.9 m rsl (not sampled; UURI data) is the same flow as exposed on Middleton Ridge and also found in GH1 and GH6 (Fig. 4.2).

The mafic flow cored in the interval -113.3 to -142.0 m rsl (LDT-1) is non-vesicular, aphyric (no phenocrysts or microphenocrysts) hawaiite of high Zr/Nb (6.6) and moderate P/Zr (14.9).

The flow cored in the interval -147.5 to -165.2 m rsl (LDT-2) is a non-vesicular, aphyric (rare plagioclase + olivine + titanomagnetite phenocrysts or microphenocrysts) trachyte. The low alkalis are due to alteration.

DISCUSSION

The first phase of felsic volcanism occurred in the central part of the Ascension Island. The Middleton Ridge Rhyolite identified from boreholes GH1, LDTGH, and GH6 is dated at 0.99±0.02 Ma; this is overlain by a trachyte flow with an age of 0.82±0.02 Ma and this flow is overlain by a trachyte dome closely associated with a trachyte lava

flow dated at 0.65±0.02 (Nielson & Sibbett, 1996). From field and age relationships Kar et al. (Felsic MS) suggest that the build up of the Middleton Ridge felsic center started around 1 Ma ago and continued until 0.65 Ma ago. In the eastern felsic complex, where there is only one age date, the trachyte dome of Weather Post is dated at 0.67±0.02 Ma. The eastern felsic complex may be contemporaneous, if not slightly younger than, the Middleton Ridge center (Kar et al., Felsic MS). These age dates suggest areal exposure of the central and the eastern parts of the island was built up over a period of half a million years, from 1 Ma to 0.56 Ma. Borehole GH2 was drilled on the eastern rim of Cricket Valley to a total depth of 533.4 m and penetrated a sequence dominated by mafic and silicic pyroclastic deposits and silicic flows with mafic flows only in the upper and lower parts of the hole (Fig. 4.2). GH5, GH1, and LDTGH also contain evidence of significant amount of felsic volcanism. Occurrence of felsic rocks throughout GH2 indicate that the eastern felsic complex was active over a long period of time.

Surface mafic flows show a range of Zr/Nb ranging between 4.1 to 6.0 whereas mafic samples recovered from deeper parts of the boreholes have slightly higher Zr/Nb (maximum 7.7) as compared to the surface flows (Fig. 4.10; Table 4.1).

Borehole GH1 is located about 1.5 km south of borehole GH5 (Fig. 4.1). The two mafic flows cored in the interval 146.3 to 135.6 m rsl in GH1 and the three flows cored in the interval 149.4 to 119.8 m rsl in GH5 are compositionally very similar to each other (hawaiite with Zr/Nb of 4.9 to 5.2 and high P/Zr of 17.2 to 19.8). These flows also are similar to the surface flow (AI-167; Table 4.1) exposed in the same general area as borehole GH5. Hence these flows can be traced over a kilometer in the subsurface and this is the only instance where mafic flows can be correlated between boreholes. In borehole GH1 the hawaiite flow overlies the Middleton Ridge rhyolite which has an age of 0.99 Ma (Nielson & Sibbett, 1996). The correlation of the flows in GH1 and GH5

gives an upper limit of borehole GH5 at less than 0.99 Ma which is not a well constrained age and necessitates more age dating for the volcanic rocks to well define the phases of magmatism on Ascension Island.

The 106-m-thick high Zr/Nb basalt flow from GH2 is remarkably uniform in composition considering its unusual thickness; there is no flow breccia in the entire 106 m interval and no evidence of significant chemical variation that would result from crystal settling in a lava lake. An unusual feature of this flow is the elevated Rb/Nb with respect to the other high Zr/Nb flows. These flows contain numerous felsic inclusions and hence indicate that the mafic magma was perhaps contaminated during their ascent through felsic rocks as evidenced by the presence of latter rocks in the lower portions of borehole GH2.

In borehole GH3 (Fig. 4.5) low Zr/Nb hawaiite flows overlie intermediate Zr/Nb hawaiite flows which overlie Dark Slope Crater hawaiite and mugearite flows. The flow cored in the bottom of this hole is heavily altered and may be a significantly older flow. In all the other six boreholes (except GH3) the basalt and hawaiite flows do not display any systematic variation in geochemical characteristics with depth, most of the flows being of intermediate Zr/Nb (~5.0) type. Basalt and hawaiite flows from the deeper levels of three boreholes, however, have high Zr/Nb (7.4 to 7.7 in GH1 at 10 to -6m rsl; 6.8 to 7.1 in GH6 at -122 to -194 m rsl; 6.6 in LDTGH at -113 to -142, rsl) than any of the surface flows (maximum Zr/Nb of 6.1). This suggests that there may have been temporal evolution from eruption of high Zr/Nb lavas earlier in the growth of the volcanic edifice to the eruption of the lower, and more variable, Zr/Nb lavas in more recent times.

P/Zr is high in the low Zr/Nb flows and extremely variable in intermediate Zr/Nb basalt, hawaiite, and some mugearite flows as compared with the high Zr/Nb and the

Dark Slope Crater flows (Table 4.1), and is consistent with observations from the surface flows (Kar et al., 1995). However, in borehole GH6 P/Zr shows a noticeable increase within the magmas of the high Zr/Nb group from a depth of –200 m (rsl) to a depth –130m (rsl); P/Zr is 10.6 at the bottom of the borehole (-200 rsl) and increases continuously to 14.7 at a depth of -130 m rsl. In boreholes GH1, GH3, GH5, and GH6 the flows at the top of the boreholes have higher P/Zr than the flows deeper in the holes. In borehole GH2 a sequence of mugearite flows have decreasing SiO_2 and increasing P/Zr (Fig. 4.4) suggesting that lavas were tapped from a stratified magma chamber. In borehole GH6 there is a trend from low P/Zr (10.6) in the lower part of the borehole to higher P/Zr (14.7) in the upper part of the borehole (Fig. 4.8). In borehole GH3 (Fig. 4.5) the Dark Slope Crater type flows occur lowest in the stratigraphic column followed sequentially up the column by intermediate Zr/Nb group and low Zr/Nb group flows. Overall, the SiO_2 content decreases up the stratigraphic column within a particular mafic group; within the Dark Slope Crater group a definite trend of decrease in SiO_2 (mugearite to hawaiite) is noted, again suggesting perhaps the magmas were erupted from a stratified magma chamber. However, between the mafic groups the P/Zr content increases up the stratigraphic column. In all of the boreholes the mafic flows below ~50 m rsl (except for one flow at ~0 m rsl in GH2) have P/Zr < 15 (closer to normal value) whereas above 50 m rsl the mafic flows are anomalously enriched in P. This indicates that the later magmas have been contaminated with phosphorous.

Kar et al. (Phosphorous MS) show that apatite has crystallized out of mafic magmas (SiO_2 > 50 wt%) as evidenced by rapid decrease in P_2O_5 in the more evolved (SiO_2 between 55 to 60 wt%) mafic rocks of Ascension. High Zr/Nb group flows are the oldest mafic rocks exposed. Dark Slope Crater magmas were erupted next, followed by the low Zr/Nb mafic magmas. The youngest mafic magmas are the intermediate Zr/Nb

group ranging from basalt to benmoreite (Kar et al., Mafic MS). The geochemical characteristics of the felsic rocks are largely consistent with an origin by fractional crystallization of high Zr/Nb mafic magmas as evidenced by identical $^{143}Nd/^{144}Nd$ and similar Pb isotopic ratios (Felsic MS). Fractionation to very evolved compositions is a relatively late feature of the volcanic edifice on Ascension Island (Nielson & Sibbett, 1996; Kar et al., Mafic MS). Hence the earlier magmas (e.g., high Zr/Nb) which are also low (normal) in P content did not interact with apatite-rich cumulate rocks. However, certain later mafic magmas (e.g., low Zr/Nb and certain intermediate Zr/Nb) experienced significant resorption of apatite-rich cumulate bodies during magmatism. Resorption of these apatite-rich cumulates in the later mafic magmas could perhaps have raised the P content of the later low Zr/Nb and certain intermediate Zr/Nb mafic magmas that have anomalously high P content.

For the surface mafic volcanic rocks, $^{87}Sr/^{86}Sr$ ranges from 0.702766 to 0.703263 and $^{143}Nd/^{144}Nd$ ranges from 0.512918 to 0.513066. Flows from Dark Slope Crater have the lowest $^{143}Nd/^{144}Nd$ (0.512918 to 0.512974), although there is some overlap with the low Zr/Nb flows ($^{143}Nd/^{144}Nd$ range from 0.512969 to 0.512972), and the high Zr/Nb flows have the highest $^{143}Nd/^{144}Nd$ (0.512992 to 0.513066). The intermediate Zr/Nb flows have a range of $^{143}Nd/^{144}Nd$ from 0.512960 to 0.513040 (Fig. 4.11). Two borehole basalt and hawaiite flows with intermediate Zr/Nb (GH2-12, Zr/Nb 5.5; GH5-7, Zr/Nb 5.7) have $^{143}Nd/^{144}Nd$ of 0.513003 to 0.512971, values within the range of the surface intermediate Zr/Nb flows (Fig. 4.11). Four borehole basalt and hawaiite flows with high Zr/Nb (GH4-3, Zr/Nb 6.4; LDT-1, Zr/Nb 6.6; GH6-3, Zr/Nb 6.9, GH1-3, Zr/Nb 7.6) have $^{143}Nd/^{144}Nd$ of 0.513009 to 0.513047, values within the range of the surface high Zr/Nb flows (Fig. 4.11). This suggests that the older high Zr/Nb flows were produced by greater degrees of melting of the same source which produced the younger, surface

high Zr/Nb flows. Overall, there are few systematic geochemical variations with depth in the boreholes. The low Zr/Nb and Dark Slope Crater magma types have been erupted only very locally and perhaps only during the most recent phases of activity. There may, therefore, be smaller degrees of melting and a greater diversity in magma compositions during the waning phases of magmatism on Ascension Island.

CONCLUSIONS

1) The overall proportions of rock types in the boreholes are similar to the surface exposure, with a high percentage of silicic flows and pyroclastic deposits.
2) Boreholes GH5, GH1, LDTGH, and GH6 lie on a north-south line stretching a distance of about 3 km. Only one correlation could be established between the borehole flows other than the Middleton Ridge rhyolite which has been traced over three boreholes from GH1 through GH6 (Neilson & Sibbett, 1996); hawaiite flows in borehole GH1 can be correlated with flows in borehole GH5, over a kilometer and half away.
3) The mafic flow in the upper part of GH2 is remarkably uniform in composition over a thickness of >100 m with no flow breccia in the entire interval and no evidence of significant chemical variation but has a high content of felsic inclusions . This is a high Zr/Nb flow however the incompatible element ratio (e.g. Rb/Nb) is different from other high Zr/Nb flows indicating contamination of the mafic magmas by felsic rocks during the ascent of these mafic magmas.
4) In borehole GH2 a sequence of mugearite magma have decreasing SiO_2 with decreasing depth and in borehole GH3 a sequence of hawaiite-mugearite magma have decreasing SiO_2 with decreasing depth, suggesting magmas were tapped from a stratified magma chamber.

5) P/Zr is higher in the low Zr/Nb and extremely variable in the intermediate Zr/Nb basalt, hawaiite, and some mugearite as compared with the high Zr/Nb and the Dark Slope Crater flows and is consistent with observations from the surface flows. However, in borehole GH6 high Zr/Nb magmas at the base of the borehole a noticeable increase in P/Zr from the bottom to the top. In borehole GH3 low Zr/Nb hawaiite flows overlie intermediate Zr/Nb hawaiite flows which overlie four Dark Slope Crater hawaiite and mugearite flows. P/Zr in the low Zr/Nb is high and in the Dark Slope Crater group low, indicating the later magmas have been contaminated with apatite-rich cumulate xenoliths.

6) In all the boreholes, except GH3, the basalt and hawaiite flows do not display any systematic variation in geochemical characteristics with depth, most of the flows being of intermediate Zr/Nb (~5.0) type. Basalt and hawaiite flows from the deeper levels of three boreholes, however, have high Zr/Nb (maximum Zr/Nb 7.7) than any of the surface flows (maximum Zr/Nb of 6.1), but have similar $^{143}Nd/^{144}Nd$, implying a decreasing degree of melting of a common source with time in the production of the high Zr/Nb magma type. The low Zr/Nb and Dark Slope Crater magma types have been erupted only very locally and perhaps only during the most recent phases of activity. This suggests that there may have been a temporal change from eruption of high Zr/Nb lavas earlier in the growth of the volcanic edifice to the eruption of the lower, and more variable, Zr/Nb lavas in more recent times. There may, therefore, be smaller degrees of melting and a greater diversity in magma compositions during the waning phases of magmatism on Ascension Island.

ACKNOWLEDGMENTS

This paper is a part of a Ph.D. dissertation by Aditya Kar. The project was supported by NSF grant EAR-9204079.

REFERENCES

Adams, M.C., 1996. Chemistry of fluids from Ascension #1, a deep geothermal well on Ascension Island, South Atlantic Ocean. Geothermics 25: 561-579.

Atkins, F.B., Baker, P.E., & Smith, D.G.W., 1964. Oxford expedition to Ascension Island. Nature 204: 722-724.

Brozena, J.M., 1986. Temporal and spatial variability of seafloor spreading processes in the northern South Atlantic. Journal of Geophysical Research 91: 497-510.

Davidson, J.P., Boghossian, N.D., & Wilson, B.M., 1993. The Geochemistry of the Igneous Rock Suite of St. Martin, Northern Lesser Antilles. Journal of Petrology 34: 839-866.

Harris, C., 1983. The petrology of lavas and associated plutonic inclusions of Ascension Island. Journal of Petrology 24: 424-470.

Harris, C., 1985. Guano-derived rare earth-rich phosphate amygdales in gabbroic inclusions from Ascension Island. Earth and Planetary Science Letters 72: 141-148.

Harris, C., & Bell, J.D., 1982. Natural partial melting of syenite blocks from Ascension Island. Contributions to Mineralogy and Petrology 79: 107-113.

Harris, C., Bell, J.D., & Atkins, F.B., 1982. Isotopic composition of lead and strontium in lavas and coarse-grained blocks from Ascension Island, South Atlantic. Earth and Planetary Science Letters 60: 79-85.

Harris, C., & Sheppard, S.M.F., 1987. Magma and fluid evolution in the lavas and associated granite xenoliths of Ascension Island. In: Fitton, J.G., & Upton, B.G.J. (eds.) Alkaline Igneous Rocks, Geological Society of London Special Publication 30: 269-272.

Kar, A., Weaver, B.L., Davidson, J.P., & Nielson, D., 1995. Geochemical characteristics of borehole samples recovered from Ascension Island, South Atlantic Ocean. GSA Abstracts with Programs 27 no. 6: A-254.

Kar, A., Weaver, B., Davidson, J., & Colucci, M., (Felsic MS). Felsic oceanic island magmatism: Origin of high $^{87}Sr/^{86}Sr$ evolved volcanic and plutonic rocks from Ascension Island, South Atlantic Ocean. Journal of Petrology (in review).

Kar, A., Weaver, B., Davidson, J., & Colucci, M., (Mafic MS). Small-scale mantle heterogeneities: Evidence from transitional to mildly alkaline volcanic rocks from Ascension Island, South Atlantic Ocean.

Kar, A., Weaver, B., & Davidson, J., (Phosphorous MS). Anomalous phosphorous behavior in OIB basalt and hawaiite from Ascension Island, South Atlantic Ocean: Evidence of apatite resorption during low pressure crystal fractionation.

Nielson, D.L., & Sibbett, B.S., 1996. Geology of Ascension Island, South Atlantic Ocean. Geothermics 25: 427-448. Roedder, E., & Coombs, D.S., 1967. Immiscibility in granitic melts indicated by fluid inclusions in ejected granite blocks of Ascension Island. Journal of Petrology 8: 417-451.

Nielson, D.L., & Stiger, S.G., 1996. Drilling and evaluation of Ascension #1, a geothermal exploration well on Ascension Island, South Atlantic Ocean. Geothermics 25: 543-560.

Roedder, E., & Coombs, D.S., 1967. Immiscibility in granitic melts indicated by fluid inclusions in ejected granite blocks of Ascension Island. Journal of Petrology 8: 417-451.

Sheppard, S.M.F., & Harris, C., 1985. Magma and fluid evolution in the lavas and associated granite xenoliths of Ascension Island. Alkaline Igneous Rocks (Fitton, J.G.

and Upton, B.G.J. ed.), Geological Society of London Special Publication 30: 269-272.

Weaver, B.L., Kar, A., Davidson, J.P., and Colucci, M., 1996. Geochemical characteristics of volcanic rocks from Ascension Island, South Atlantic Ocean. Geothermics 25: 449-470.

Weis, D., 1983. Pb isotopes in Ascension Island rocks: Oceanic origin for the gabbroic to granitic plutonic xenoliths. Earth and Planetary Science Letters 62: 273-282.

Weis, D., Demaiffe, D., Cauet, S., & Javoy, M., 1987. Sr, Nd, O and H isotopic ratios in Ascension Island lavas and plutonic inclusions; cogenetic origin. Earth and Planetary Science Letters 82: 255-268.

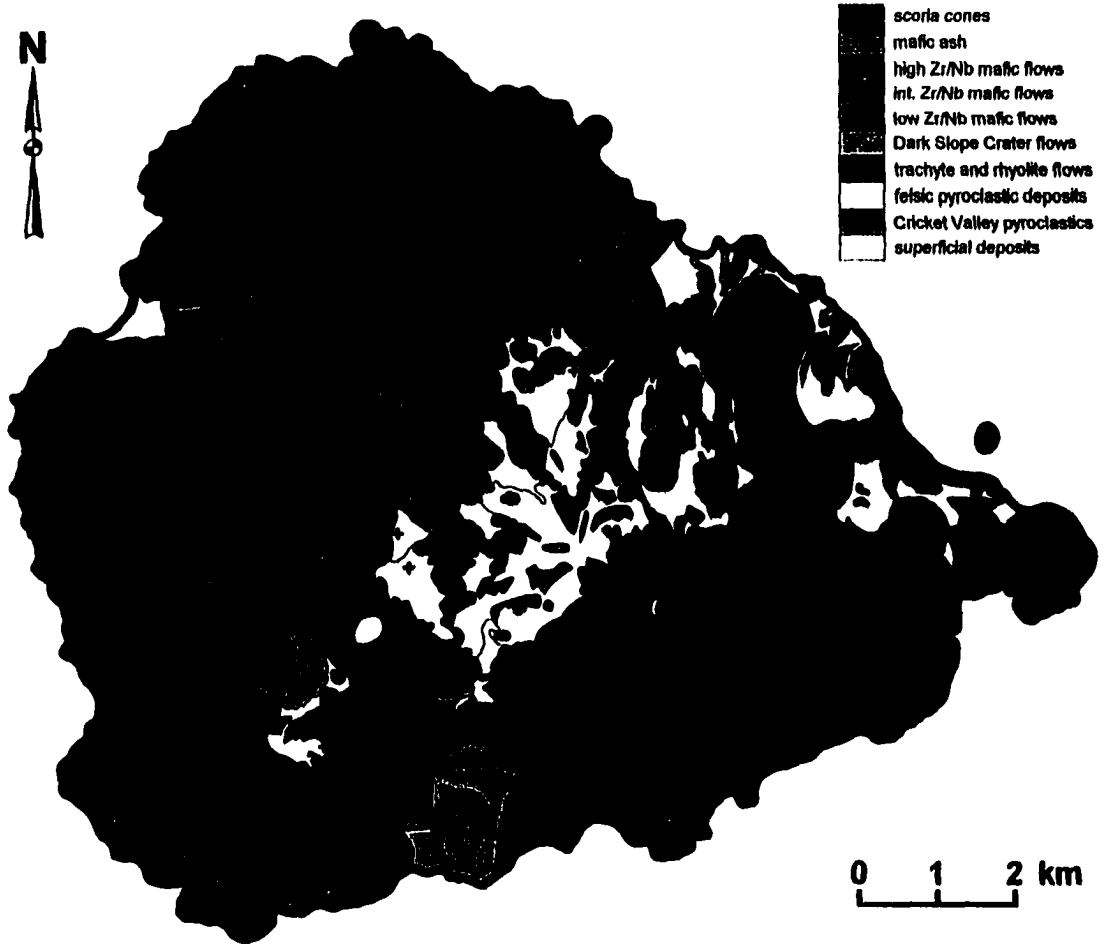

Figure 4.1. Geological map of Ascension Island, somewhat modified from Nielson and Sibbett (1996). The four geochemically distinct mafic flow types (high Zr/Nb, intermediate Zr/Nb, low Zr/Nb, Dark Slope Crater) are identified and the compositions of selected flows are indicated as: B basalt, H hawaiite, M mugearite, Be benmoreite. The locations of the seven boreholes, GH1 to GH6 and LDTGH, are shown.

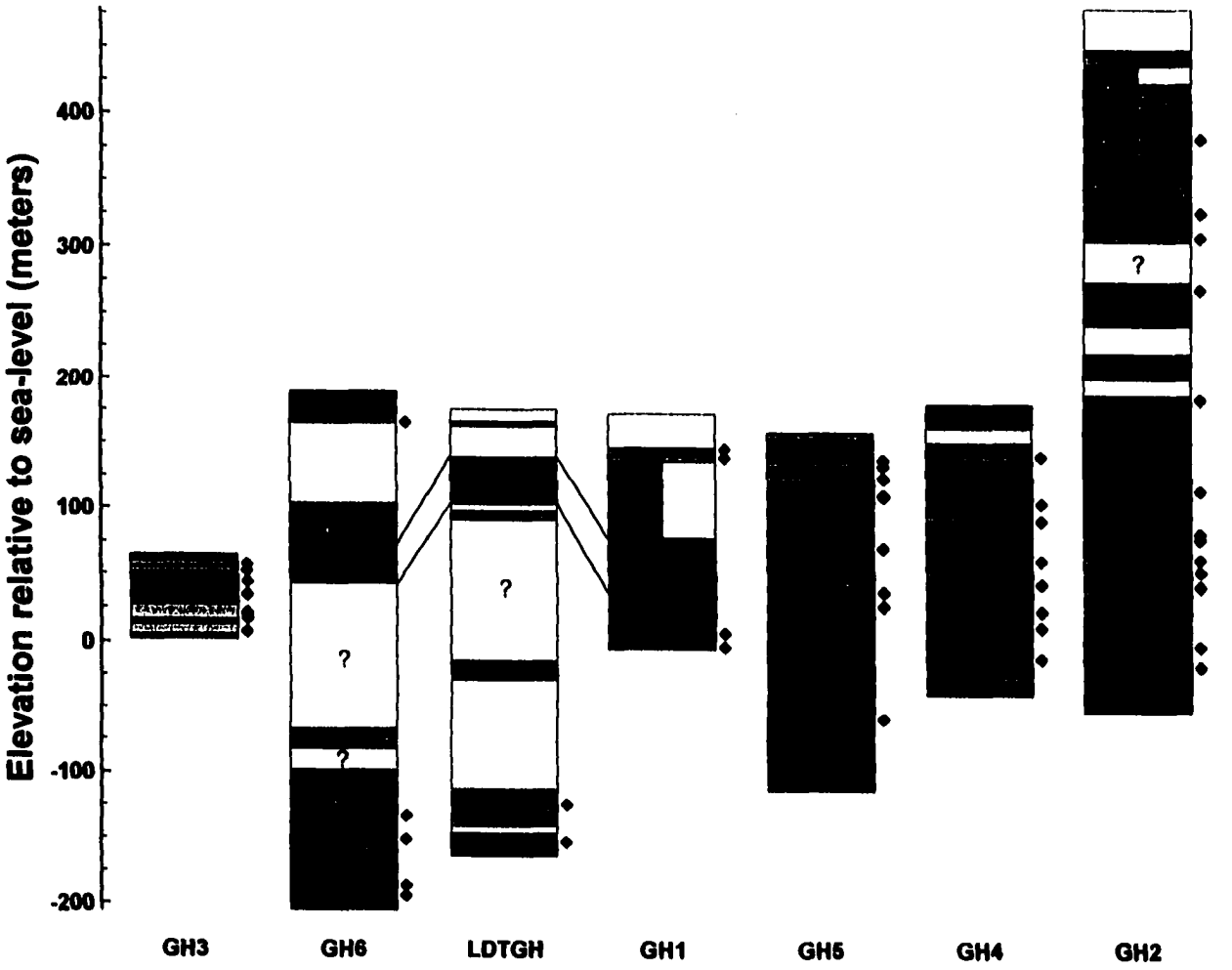

Figure 4.2. Stratigraphy within the seven shallow boreholes on Ascension Island. ◆ indicates a sample taken for geochemical analysis in this study. DRS is the Devil's Riding School trachyte flow; MRR is the Middleton Ridge rhyolite flow. NR is a triconed interval with no recovery.

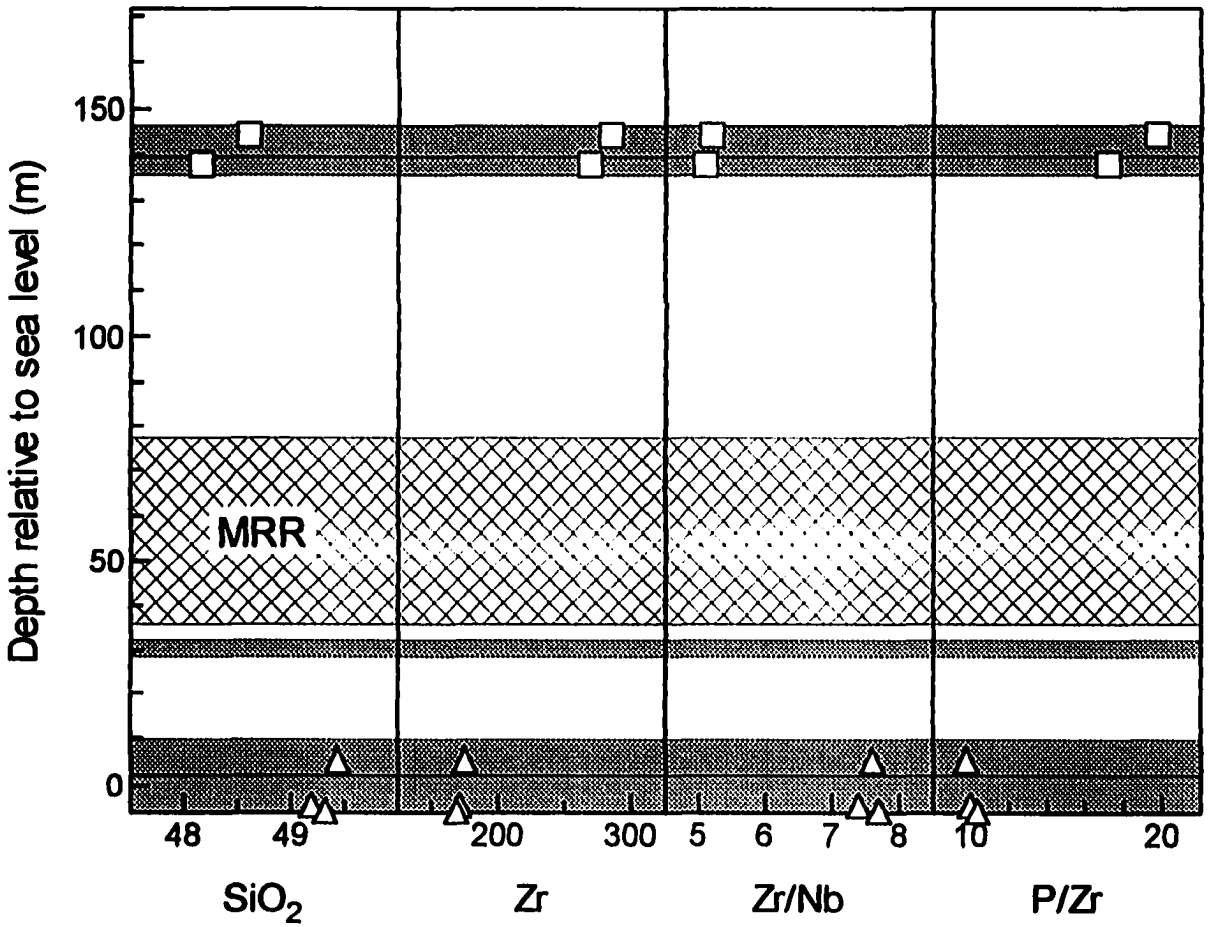

Figure 4.3. Geochemical stratigraphy within borehole GH1. Symbols indicate composition of samples: Δ high Zr/Nb basalt, □ intermediate Zr/Nb hawaiite. MRR is the Middleton Ridge rhyolite flow.

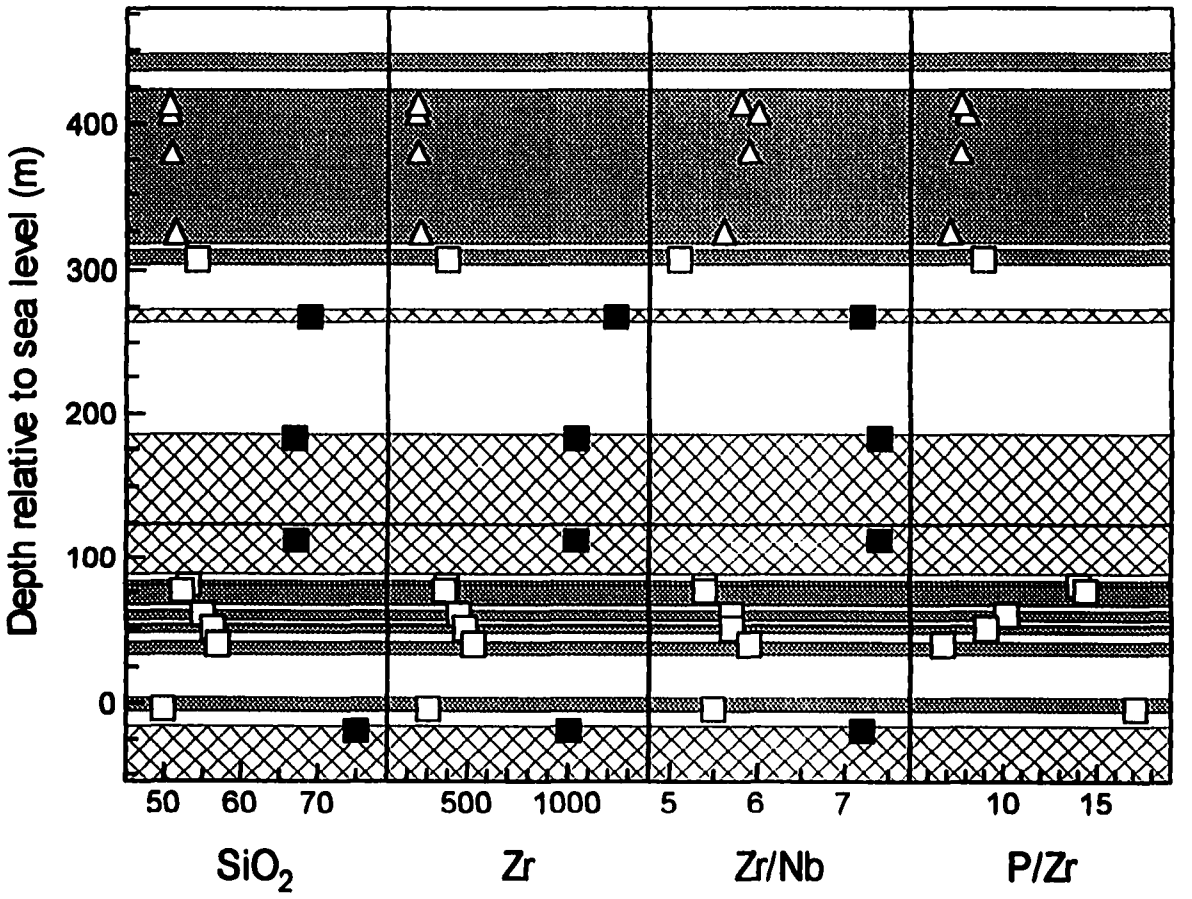

Figure 4.4. Geochemical stratigraphy within borehole GH2. Symbols indicate composition of samples: △ high Zr/Nb basalt, □ intermediate Zr/Nb hawaiite and mugearite, ■ trachyte and rhyolite. The two stratigraphically highest samples of the thick basalt flow between 423.0 and 317.0 m rsl were taken from the exposure of this flow in the walls of Cricket Valley.

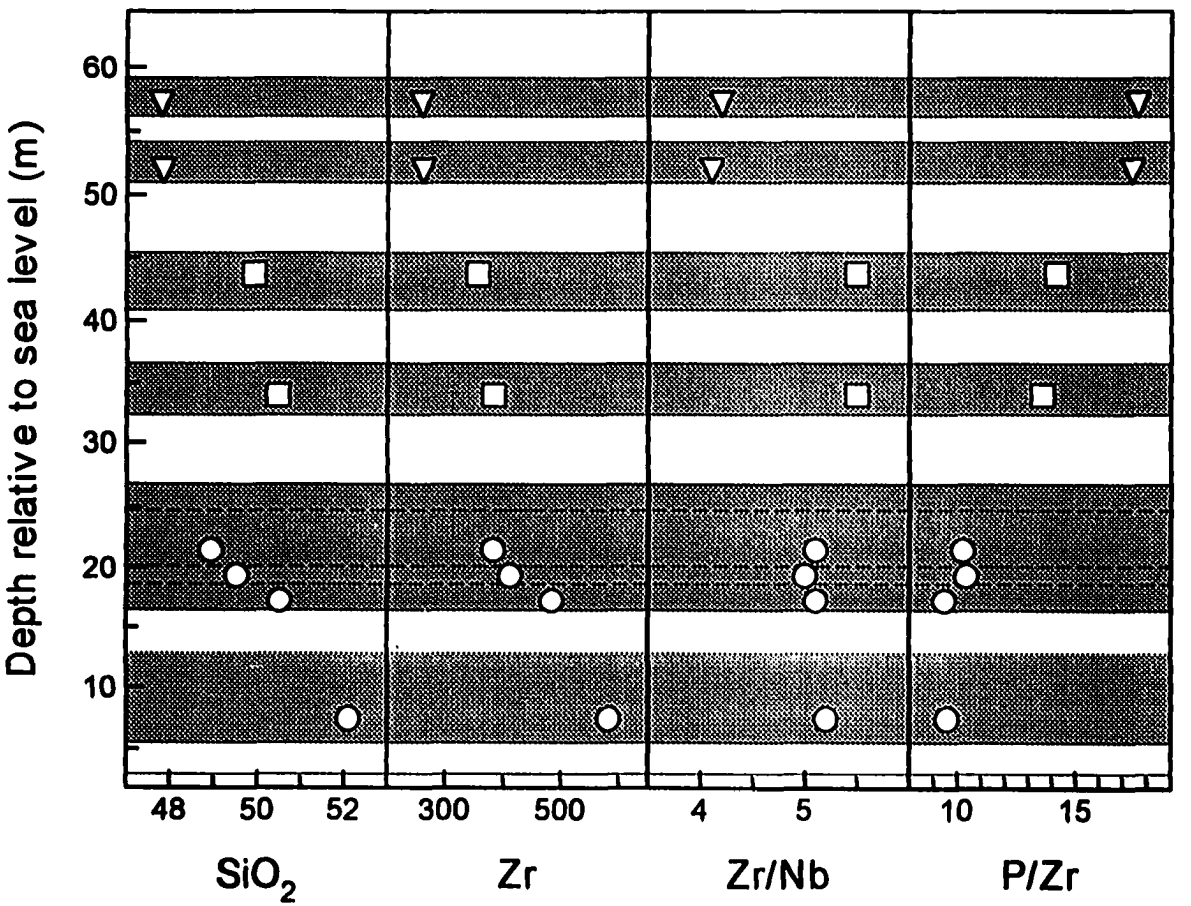

Figure 4.5. Geochemical stratigraphy within borehole GH3. Symbols indicate composition of samples: ▽ low Zr/Nb hawaiite, □ intermediate Zr/Nb hawaiite, O Dark Slope Crater hawaiite and mugearite.

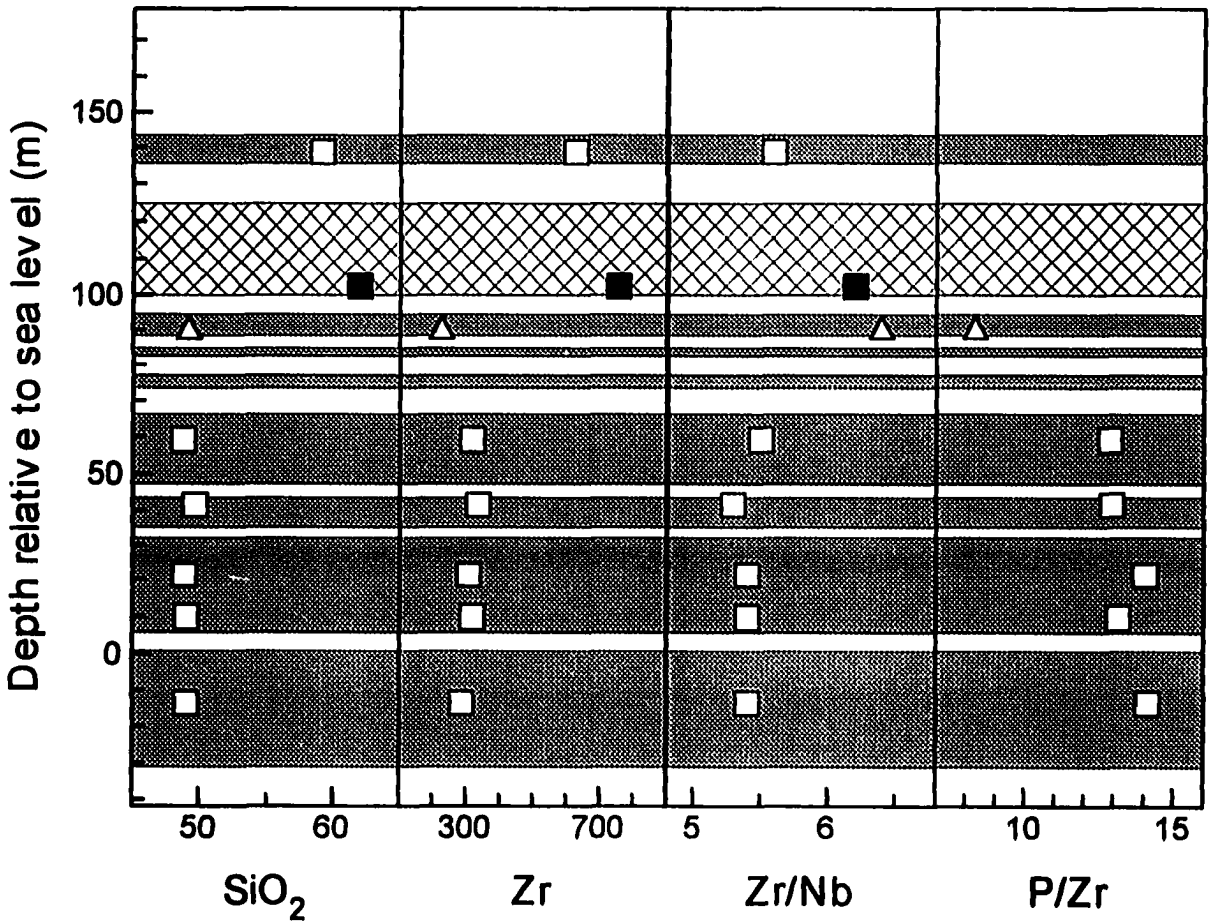

Figure 4.6. Geochemical stratigraphy within borehole GH4. Symbols indicate composition of samples: Δ high Zr/Nb basalt, □ intermediate Zr/Nb hawaiite, ■ trachyte.

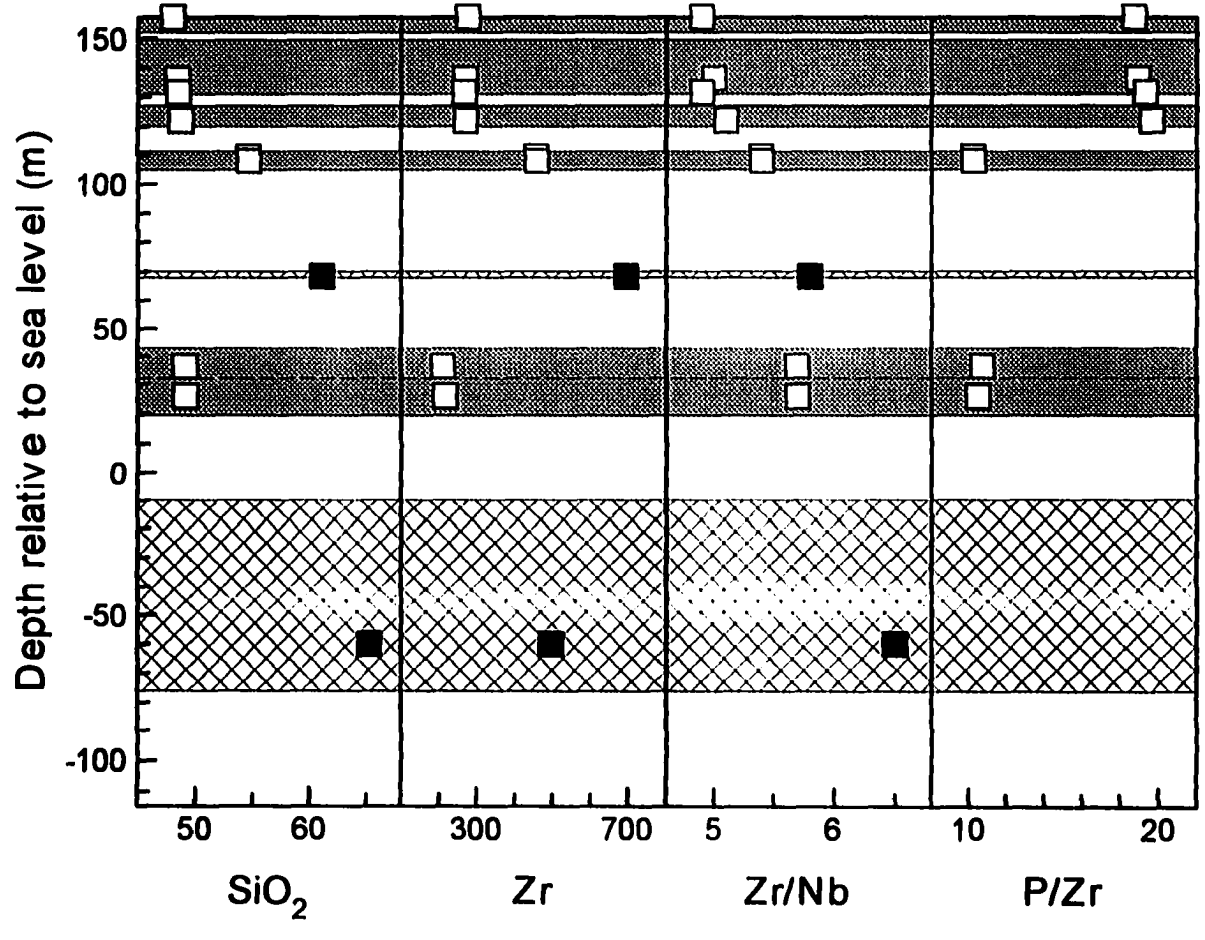

Figure 4.7. Geochemical stratigraphy within borehole GH5. Symbols indicate composition of samples: □ intermediate Zr/Nb hawaiite and mugearite, ■ trachyte. The flow in the top of the hole was sampled at the surface as sample AI-167.

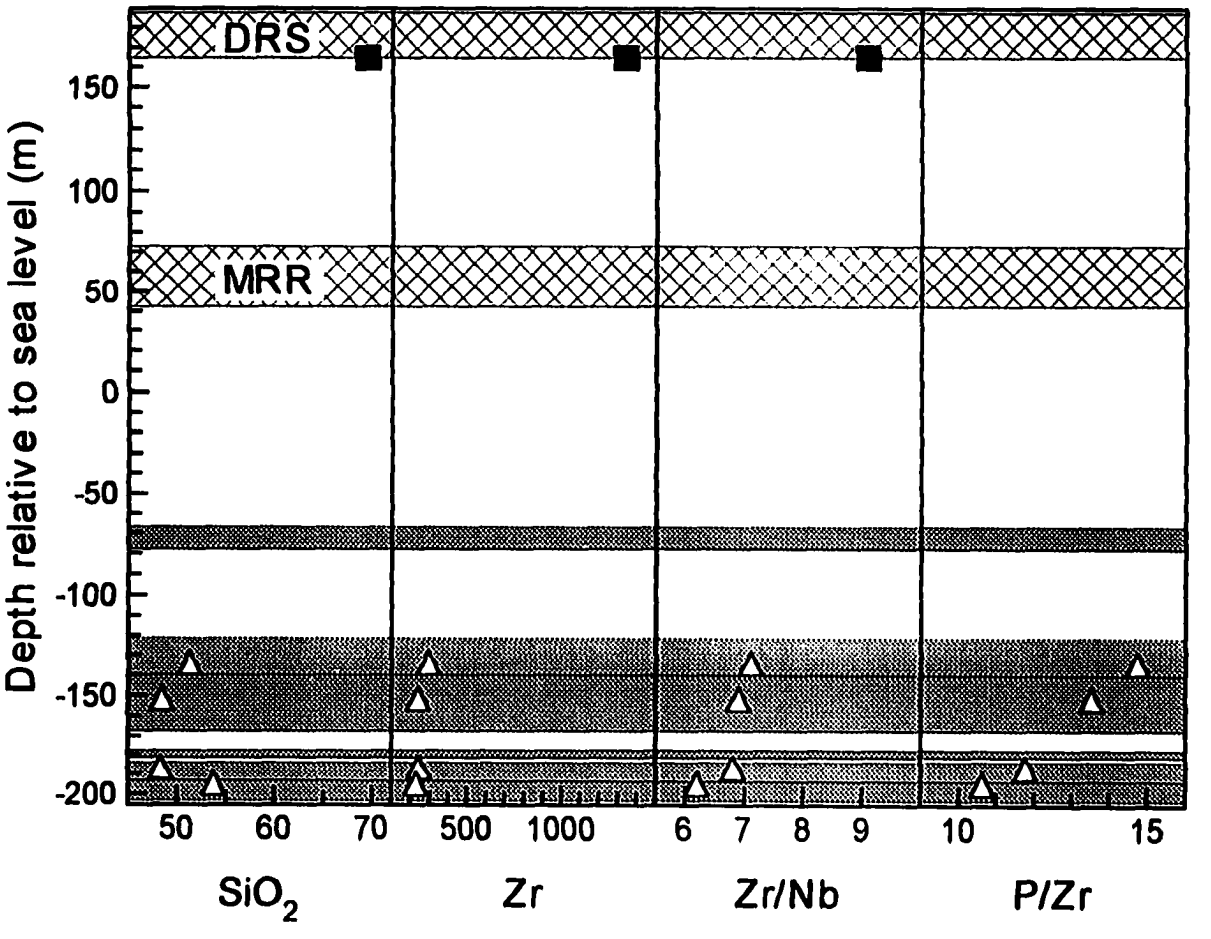

Figure 4.8. Geochemical stratigraphy within borehole GH6. Symbols indicate composition of samples: △ high Zr/Nb basalt, ■ trachyte. DRS is the Devil's Riding School trachyte flow, MRR is the Middleton Ridge rhyolite flow.

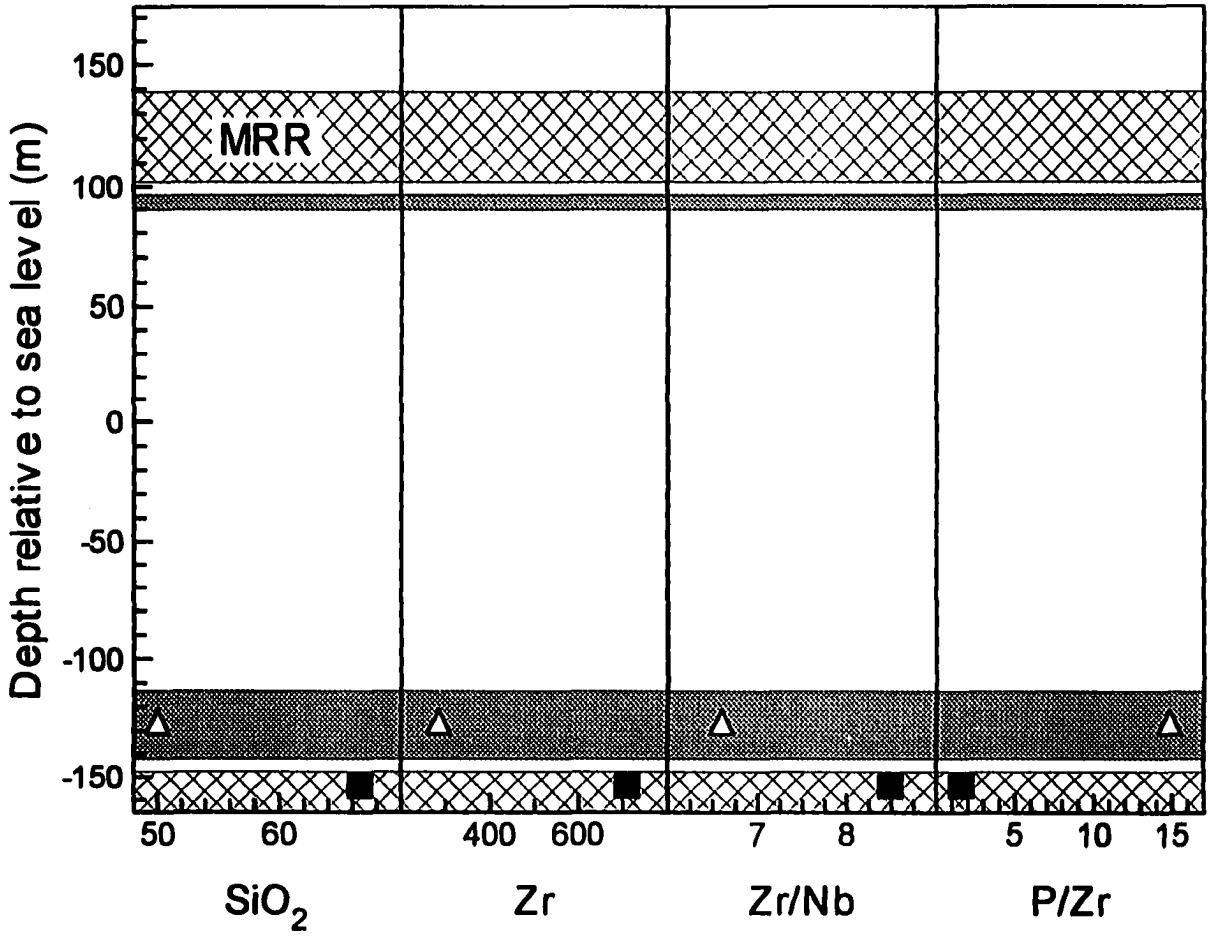

Figure 4.9. Geochemical stratigraphy within borehole LDTGH. Symbols indicate composition of samples: Δ high Zr/Nb basalt, ■ trachyte. MRR is the Middleton Ridge rhyolite flow.

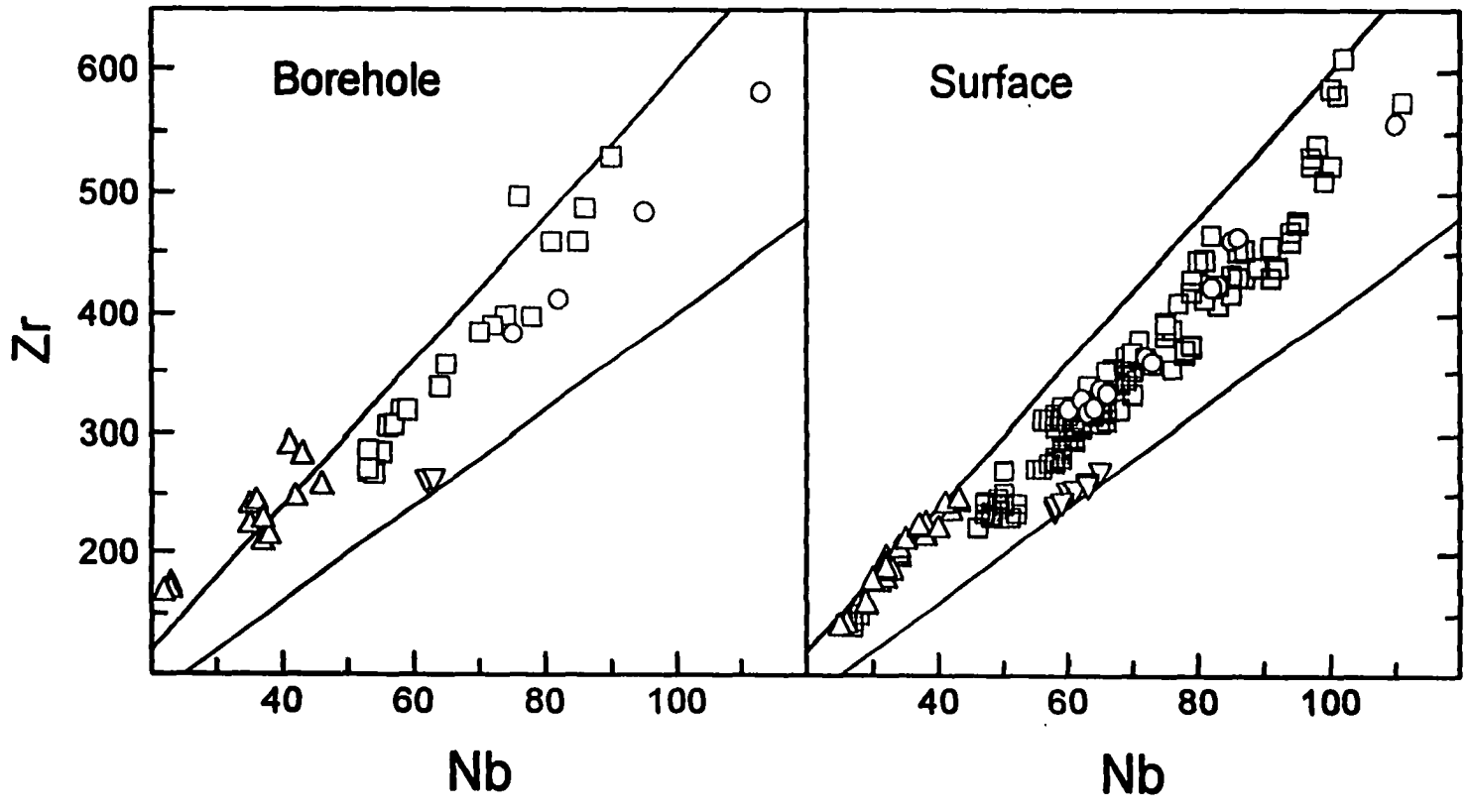

Figure 4.10. Variation in Zr *vs.* Nb (both in *ppm*) for basalt to benmoreite volcanic rocks from the boreholes and the surface of Ascension Island. △ high Zr/Nb basalt; □ intermediate Zr/Nb basalt to benmoreite; ▽ low Zr/Nb hawaiite; O Dark Slope Crater hawaiite and mugearite. The low Zr/Nb and Dark Slope Crater flows were only found in borehole GH3. High Zr/Nb flows were found in boreholes GH1, GH2, GH4, GH6, and LDTGH, generally in the deeper levels of the holes. Intermediate Zr/Nb flows were found in boreholes GH1 to GH5.

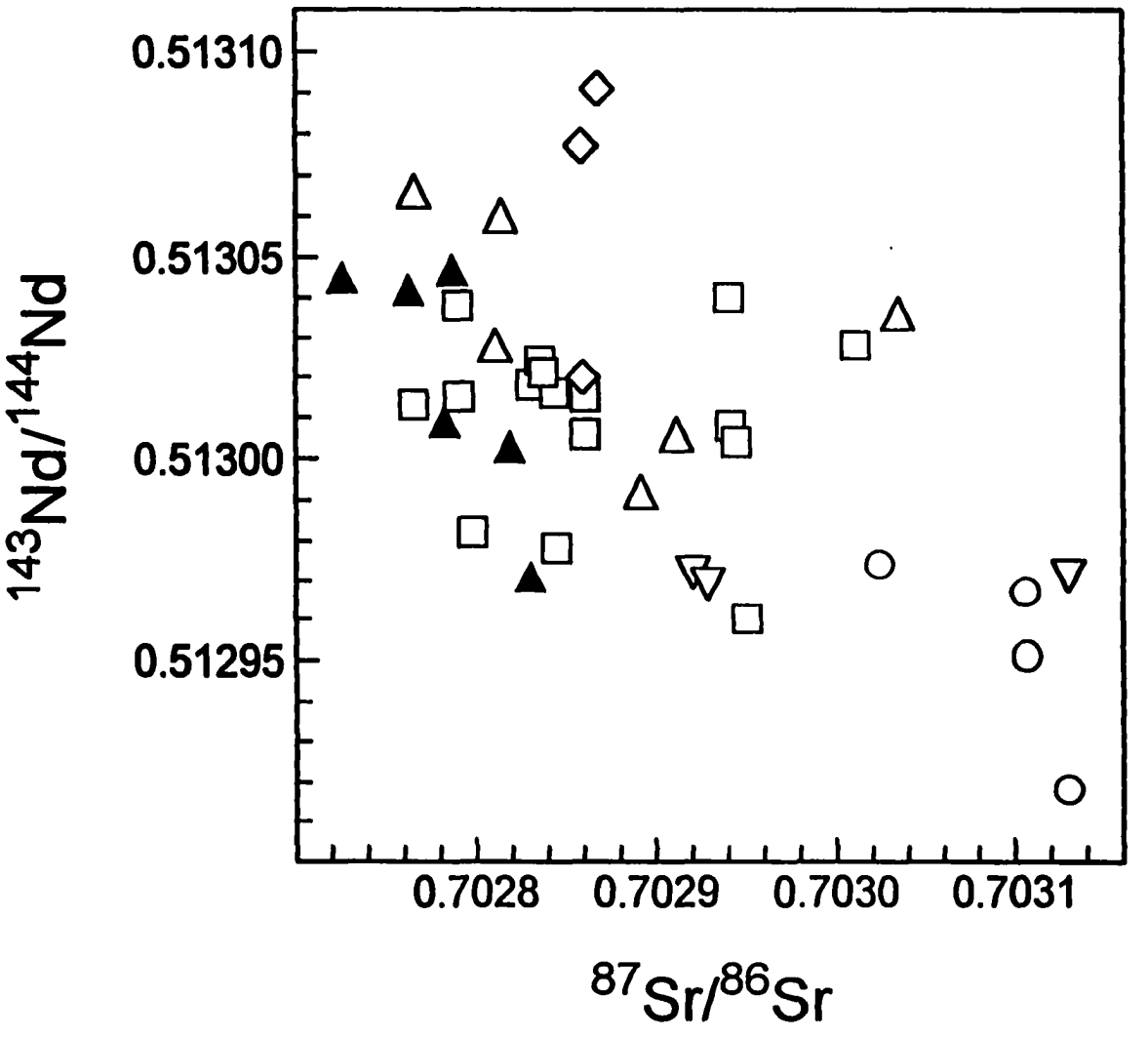

Figure 4.11. Variation in $^{143}Nd/^{144}Nd$ *vs.* $^{87}Sr/^{86}Sr$ for basalt to benmoreite volcanic rocks from the boreholes and the surface of Ascension Island. Symbols as in Fig. 4.10 except that ▲ represents the composition of the borehole samples.

Table 1. Representative chemical analyses of basalt to benmoreite surface and subsurface lava flows from Ascension Island.

	GH1		GH2						GH3		
	GH1-1	GH1-3	GH2-2	AI-64	GH2-3	GH2-7	GH2-11	GH2-12	GH3-1	AI-60	GH3-3
	H	B	B	B	M	M	Be	H	H	H	H
Depth	144.3	5.6	325.0		306.3	79.7	39.9	-4.1	57.1		43.7
SiO_2	48.61	49.43	51.33	50.58	54.24	53.23	56.94	49.92	47.79	47.94	49.93
TiO_2	3.51	2.46	2.48	2.52	2.29	2.61	1.87	3.30	3.74	3.64	3.06
Al_2O_3	14.32	16.09	15.49	15.61	15.70	15.34	15.85	15.06	15.06	14.67	15.11
Fe_2O_3	14.19	12.20	11.89	11.98	10.92	11.64	9.40	13.01	13.40	13.37	12.79
MnO	-	-	-	0.17	-	-	-	-	-	0.21	-
MgO	4.47	4.87	5.15	5.23	3.21	2.74	1.95	3.46	4.71	4.90	4.35
CaO	8.56	10.78	8.29	8.56	6.45	6.60	5.38	8.62	8.78	9.12	7.84
Na_2O	3.71	3.02	3.51	3.61	4.53	4.72	5.46	4.09	3.88	3.71	4.17
K_2O	1.34	0.76	1.44	1.29	1.85	1.84	2.33	1.34	1.59	1.41	1.59
P_2O_5	1.29	0.39	0.42	0.45	0.81	1.28	0.82	1.20	1.05	1.02	1.16
H_2O-	0.19	0.99	0.22	0.31	0.30	1.25	0.65	1.33	0.16	0.41	0.10
LOI	-0.63	0.70	-0.38	-0.40	0.13	0.67	0.39	0.73	-0.82	0.54	-0.79
Ni	3	45	34	34	5	<2	<2	6	4	12	14
Zn	102	80	90	87	146	139	148	114	97	132	115
Ga	28	21	25	26	27	26	27	25	25	24	26
Rb	29	13	33	28	38	38	50	29	36	27	34
Sr	497	403	385	414	459	476	425	505	582	551	590
Th	4	2	4	4	4	6	5	4	4	4	5
Pb	<2	<2	<2	<2	<2	2	3	<2	<2	<2	<2
Zr	285	175	249	244	259	398	530	306	260	235	356
Nb	55	23	42	41	46	74	90	56	62	58	65
Y	55	33	41	41	63	60	64	48	42	40	49
Zr/Nb	5.2	7.6	5.6	6.0	5.1	5.4	5.9	5.5	4.2	4.1	5.5
Rb/Nb	0.53	0.57	0.72	0.68	0.49	0.51	0.56	0.52	0.58	0.47	0.52
K/Nb	202	274	258	261	196	209	213	197	212	202	199
P/Zr	19.8	9.7	7.1	8.0	8.9	14.0	6.8	17.1	17.6	18.9	14.2
Zr/Y	5.2	5.3	8.9	6.0	6.3	6.6	8.3	6.4	6.2	5.9	7.3

B basalt; H hawaiite; M mugearite; Be benmoreite. Depth is the sample location within the borehole in metres relative to sea level.

Major element oxides are recalculated to sum to 100% on an anhydrous basis. H_2O- is weight loss after drying for 12 hours at 110°C. LOI is weight loss after ignition at 950°C for 1 hour (oxidation of Fe^{2+} to Fe^{3+} in near-anhydrous samples results in weight gain, expressed as negative LOI). Trace elements are in parts per million and were determined by XRF.

Table 1 continued

	GH3		GH4		GH5				GH6	LDTGH
	GH3-8	Al-6	GH4-3	GH4-8	GH5-3	Al-167	GH5-5	GH5-7	GH6-3	LDT-1
	M	M	B	H	H	B	M	B	B	H
Depth	7.4		89.2	-13.7	122.0		108.0	36.0	-151.5	-125.7
SiO_2	52.10	52.12	49.19	49.05	48.75	48.07	54.64	49.15	48.46	49.98
TiO_2	1.77	1.83	2.54	3.25	3.52	3.63	2.18	2.25	3.77	3.52
Al_2O_3	16.98	16.71	15.30	15.65	14.37	14.32	15.63	17.78	14.05	14.81
Fe_2O_3	10.18	10.44	12.99	12.82	14.01	14.14	10.52	10.60	14.96	12.84
MnO	-	0.18	-	-	-	0.22	-	-	-	-
MgO	3.44	3.43	5.66	4.37	4.56	4.70	3.10	5.59	4.08	3.61
CaO	5.97	6.15	9.43	8.46	8.45	8.92	6.14	9.83	9.45	8.89
Na_2O	5.47	5.20	3.50	4.00	3.80	3.60	4.71	3.22	3.35	4.04
K_2O	2.81	2.69	0.96	1.47	1.32	1.21	2.00	1.06	1.13	1.34
P_2O_5	1.28	1.25	0.43	0.93	1.22	1.19	1.08	0.52	0.75	0.97
H_2O-	0.23	0.53	0.20	0.34	0.15	0.41	0.20	0.75	2.01	1.39
LOI	-0.27	0.28	-0.32	-0.20	-0.69	-0.26	-0.32	0.67	2.06	1.44
Ni	32	31	34	8	4	11	4	66	11	6
Zn	144	154	93	110	101	128	131	103	90	105
Ga	29	30	23	26	27	26	28	23	23	26
Rb	75	66	16	31	28	24	40	22	18	30
Sr	1172	1105	457	650	485	473	471	503	403	449
Th	9	9	2	<2	3	3	5	3	<2	4
Pb	4	<2	2	<2	3	2	2	2	<2	<2
Zr	583	558	225	287	271	277	459	211	242	285
Nb	113	110	35	53	53	57	85	37	35	37
Y	44	46	34	42	54	53	69	30	46	49
Zr/Nb	5.2	5.1	6.4	5.4	5.1	4.9	5.4	5.7	6.9	6.6
Rb/Nb	0.66	0.60	0.46	0.58	0.53	0.42	0.47	0.59	0.51	0.70
K/Nb	204	203	228	230	207	176	195	238	268	255
P/Zr	9.6	9.8	8.3	14.1	19.6	18.7	10.3	10.8	13.5	14.9
Zr/Y	13.3	12.1	6.6	6.8	5.0	5.2	6.7	7.0	5.3	5.8

Table 2. Sr and Nd isotopic data for subsurface rocks from Ascension Island.

		Zr/Nb	$\frac{^{87}Sr}{^{86}Sr}$	ε_{Sr}	$\frac{^{143}Nd}{^{144}Nd}$	ε_{Nd}
GH1-3	basalt	7.6	0.702726 ± 9	–28.0	0.513045 ± 9	+7.94
GH2-12	hawaiite	5.5	0.702819 ±11	–26.7	0.513003 ±19	+7.12
GH4-3	basalt	6.4	0.702783 ±11	–27.2	0.513009 ± 9	+7.24
GH5-7	basalt	5.7	0.702830 ±11	–26.5	0.512971 ± 8	+6.50
GH6-3	basalt	6.9	0.702763 ±11	–27.5	0.513042 ± 9	+7.88
LDT-1	hawaiite	6.6	0.702787 ±10	–27.1	0.513047 ±11	+7.98

Chapter V

To be submitted to Journal of Geophysical Research

Anomalous phosphorous behavior in OIB basalt and hawaiite from Ascension Island, South Atlantic Ocean: evidence of apatite resorption during low pressure crystal fractionation

Kar, A.[1,2]

School of Geology and Geophysics
University of Oklahoma
Norman, OK 73019, USA

Weaver, B.

School of Geology and Geophysics
University of Oklahoma
Norman, OK 73019, USA

Davidson, J.

Department of Earth and Space Sciences
University of California Los Angeles
Los Angeles, CA 90095, USA

[1] Department of Mathematics and Physics
Fort Valley State University
Fort Valley, GA 31030, USA

[2] Corresponding Author
Telephone: (912) 825 6844
FAX: (912) 825 6618
email: kara@mail.fvsc.peachnet.edu

ABSTRACT

The volcanic rocks of Ascension Island comprise a transitional to mildly alkaline basalt-trachyte suite. Compositional variations in mafic (basalt and hawaiite) lava flows and scoria define four magma types discriminated by Zr/Nb and isotopic (Sr, Nd, Pb) characteristics: (1) in the southwestern part of the island hawaiite flows and scoria have Zr/Nb of 4.1, (2) in the southern and the southeastern part of the island basalt and hawaiite flows and scoria have Zr/Nb of 5.6 to 6.1, (3) for the rest of the island basalt and hawaiite flows and scoria have Zr/Nb of 4.7 to 5.4, and (4) hawaiite and mugearite flows from Dark Slope Crater have intermediate Zr/Nb (4.9 to 5.4) but are distinguished by high Ni and Sr relative to other trace elements. The high Zr/Nb magmas are the oldest mafic rocks exposed, Dark Slope Crater magmas were erupted next, followed by the low Zr/Nb magmas. The youngest magmas are the intermediate Zr/Nb magmas. Basalt and hawaiite compositions show an extreme variation in P/Zr of 7.7 to 23.8. P/Zr ranges from 7.7 to 12.3 in the high Zr/Nb group; 16.6 to 19.0 in the low Zr/Nb group, and 8.1 to 23.8 in the intermediate Zr/Nb group. The high Zr/Nb and DSC groups have low (normal) P/Zr whereas the younger flows (low Zr/Nb and, particularly, the intermediate Zr/Nb flows) have anomalously high P/Zr suggesting that the later mafic magmas were enriched in P. Tholeiitic and mildly to moderately alkaline rocks from oceanic islands typically have P/Zr close to, or only slightly above, the silicate earth value of 8.6. No mantle processes can so strongly fractionate P/Zr. A number of possible explanations exist for the high phosphorous in certain Ascension mafic rocks: 1) contamination of samples by guano, which is abundant on many of the lava flow surfaces; 2) supergene processes, 3) variable P/Zr in the magma source region; 4) accumulation in magmas of apatite phenocrysts or microphenocrysts; or 5) resorption by magmas of apatite, perhaps during passage of magma through apatite-rich

cumulate bodies. All these factors are evaluated to individually account for the high P behavior in the mafic magmas.

INTRODUCTION

Far from the "geochemical madness" associated with crustal contamination and assimilation of magmas in continental settings, oceanic magmatism is ideal for investigating the characteristics of the mantle source region for hotspot-related magmas. These hotspot magmas are least contaminated during ascent from their mantle source through the thin oceanic lithosphere to the surface. However, recent investigations have shown that in oceanic settings, contamination of magmas by oceanic crust (Thirlwall, 1996; Eiler et al, 1996; Garcia et al., 1996; Lassiter and Hauri, 1996; Hofmann, 1996; Castellana and Wolff, 1992) and contamination of later products of ocean island magmatism by assimilation of earlier products of magmatism (Bohrson and Reid, 1995; Freundt and Schmincke, 1995) can alter the geochemical signature of oceanic magmas by open system processes.

The volcanic rocks exposed on Ascension Island (7°56'S, 14°22'W; Fig. 5.1) in the South Atlantic Ocean comprise a transitional to mildly alkaline basalt-trachyte suite. Compositional variations in mafic (basalt and hawaiite) lava flows and scoria define four magma types discriminated by Zr/Nb and isotopic (Sr, Nd, Pb) composition (Kar et al, 1996). Basalt and hawaiite compositions have unusual and extreme variation in P/Zr. Lava flows of the older groups have normal P/Zr (7.7 to 12.9) whereas the younger flows have highly variable P/Zr (8.1 to 24.0), with many flows having anomalously high P/Zr (>15), suggesting that later mafic magmas were enriched in P while the early magmas were unaffected. Tholeiitic and mildly to moderately alkaline rocks from oceanic islands typically have P/Zr close to the silicate earth value of 8.5. No mantle

processes can so strongly fractionate P/Zr. So what factors contribute to making P/Zr so variable? An in-depth investigation is presented in this paper.

GENERAL GEOLOGY AND PETROGRAPHY OF ASCENSION ISLAND VOLCANIC ROCKS

Lava flows ranging in composition from basalt to trachyte comprise 57% (Harris, 1983) of the exposed surface on Ascension Island (Fig. 5.2). Pyroclastic (scoria and pumice) deposits, including more than fifty scoria cones (Table 5.1, Fig. 5.3), cover the remainder (43%) of the island. The surface distribution of the scoria cones (Fig. 5.3) shows that in the northern part of the island all of the basalt and hawaiite scoria cones except one have P/Zr > 12, but cones with P/Zr of 12 to 16 and P/Zr > 16 are found in close proximity to one another (Fig. 5.3). In the southern and southwestern parts of the island both low P/Zr (<12) and high P/Zr (>12) scoria cones are also found in close proximity to one another (Fig. 5.3).

Four distinct mafic rock types are identified (Kar et al., 1995). 1) High Zr/Nb basalt flows from the southeastern part of the island (Fig. 5.2) and extensive basaltic lapilli deposits on Green Mountain are sparsely to moderately phyric with a phenocryst and microphenocryst assemblage of plagioclase + olivine + titanomagnetite ± clinopyroxene, 2) low Zr/Nb hawaiite flows erupted locally in the southwestern part of the island (Fig. 5.2) are aphyric with rare plagioclase phenocrysts, 3) hawaiite and mugearite flows erupted locally from Dark Slope Crater in the southwestern part of the island (Fig. 5.2) are aphyric (rare olivine microphenocrysts), and 4) most of the western and northern parts of Ascension Island are covered by basalt to benmoreite lava flows of intermediate Zr/Nb (Fig. 5.2). Basalt flows are typically sparsely phyric and contain plagioclase + olivine phenocrysts. Hawaiite flows mostly are aphyric and contain rare

microphenocrysts of plagioclase + olivine + clinopyroxene + titanomagnetite. The mugearite flows are aphyric to moderately phyric and contain variable proportions of plagioclase + titanomagnetite + olivine phenocrysts and microphenocrysts. The benmoreite flows are aphyric with a microphenocryst assemblage of plagioclase + olivine + titanomagnetite. All of the flows from Broken Tooth are petrographically distinctive in that they contain xenocrysts derived by disaggregation of entrained syenite inclusions.

Trachytic rocks vary from being aphyric to strongly phyric with most abundant phenocryst phase being alkali feldspar, with olivine + clinopyroxene + titanomagnetite forming the other phenocryst or microphenocryst phases. Rhyolitic rocks mostly are aphyric to sparsely phyric and have alkali feldspar microphenocrysts.

SAMPLING AND ANALYTICAL TECHNIQUES

For details of sampling techniques and the analytical procedure for major and trace element geochemistry performed at the University of Oklahoma refer to Weaver et al. (1996) and for radiogenic isotope analysis performed at UCLA to Davidson et al. (1993).

MAJOR ELEMENT GEOCHEMISTRY

Representative chemical analyses of the various mafic rock types showing the range of phosphorous content are presented in Table 5.2. The Ascension volcanic rocks are a transitional to mildly alkaline fractionation series from basalt through hawaiite, mugearite, and benmoreite, to the highly fractionated products of trachyte and rhyolite (Kar et al., Felsic MS). MgO, Fe_2O_3, CaO, and TiO_2 decrease with increasing SiO_2 over the entire compositional range as a consequence of olivine, clinopyroxene, feldspar, and titanomagnetite crystallization and is consistent with crystal fractionation

from basalt to trachyte and rhyolite (Harris, 1983; Kar et al. Mafic and Felsic MSs). Al_2O_3 and Na_2O increase with increasing SiO_2 from basalt to benmoreite, but then decrease with increasing SiO_2 in trachyte and rhyolite compositions due to alkali feldspar crystallization. K_2O increases over entire range of SiO_2 composition.

Overall, P_2O_5 initially increases with increasing SiO_2 to ~50 wt% but then decreases (Fig. 5.4) with onset of apatite crystallization. There are, however, peculiarities in the behavior of P_2O_5. P_2O_5 is low (0.40 to 0.69 wt%) in the high Zr/Nb basalt group and moderately low (0.78 to 0.99 wt%) in Dark Slope Crater hawaiite flows. P_2O_5 is higher (0.92 to 1.12 wt%) in the low Zr/Nb hawaiite group and extremely variable (0.50 to 1.69 wt%) in the intermediate Zr/Nb group basalt and hawaiite (Fig. 5.4). In intermediate Zr/Nb group mugearite and benmoreite flows, P_2O_5 consistently decreases to ~0.40 wt% (Fig. 5.4) with onset of apatite crystallization. In trachyte, P_2O_5 is low (0.99 to 0.06 wt%) and in rhyolite is extremely low (0.01 to 0.03 wt%).

A subset of the intermediate Zr/Nb group flows in the south-southeastern part of the island (except Upper Valley Crater flows) have between 0.5 to 1.0 wt% P_2O_5 and 50 to 55 wt% SiO_2 (Fig. 5.4). These flows do not conform to the trend of initially increasing and then decreasing P_2O_5 with increasing SiO_2 as described above but have a gradual increase in P_2O_5 (from < 0.50 wt% to ~1.0 wt%) over a wide SiO_2 range (~49 to 55 wt%).

TRACE ELEMENT GEOCHEMISTRY

There are significant differences in P/Zr between the four mafic groups identified (Fig. 5.5 and Fig. 5.6): 1) the high Zr/Nb basalt group has low P/Zr (7.7 to 12.9), 2) the low Zr/Nb hawaiite group has strong enrichment in P relative to other incompatible elements and elevated P/Zr (16.8 to 19.0), 3) the Dark Slope Crater hawaiite flows

have moderately low P/Zr (11.0 to 13.0; lower in mugearite due to apatite fractionation), and 4) the intermediate Zr/Nb basalt and hawaiite flows have highly variable P/Zr ranging from 8.1 to 24.0.

In the high Zr/Nb and Dark Slope Crater groups incompatible element normalized patterns are typical for OIB with pronounced enrichment in Nb and Ta relative to other highly incompatible elements (Fig. 5.7). However, in the low Zr/Nb group, and in the intermediate Zr/Nb basalt and hawaiite with high P/Zr, there is a pronounced P "spike" in the incompatible element normalized patterns (Fig. 5.7).

DISCUSSION

The primordial mantle has P/Zr of 8.5 and N-MORB has average P/Zr lower (7.5) than the primordial mantle value (Table 5.3) reflecting derivation from a depleted source. Basaltic rocks from Hawaii (as represented by Mauna Kea) also have lower average P/Zr (7.5) than the primordial mantle (Table 5.3). In contrast, alkaline rocks from South Atlantic Ocean islands (St. Helena, Tristan da Cunha, Gough) have average P/Zr which is slightly greater than the primordial mantle value (Table 5.3) due to derivation from an enriched source and/or low degrees of melting with $D_P < D_{Zr}$. However, P/Zr in excess of 12 is extremely rare in OIB and found only in undersaturated magmas which represent lower degrees of melting, such as basanite from Tristan da Cunha (Table 5.3). Ascension Island basalt and hawaiite compositions are remarkable in that they have, over a moderate range of Zr (150 to 350 ppm), extremely variable P_2O_5 with many of the mafic rocks having $P_2O_5 > 1.0$ wt% and up to 1.7 wt% (Fig. 5.4). In rocks of similar Zr concentration, P_2O_5 varies by as much as 0.9 wt%. This variation in P_2O_5 is also manifested by highly variable P/Zr, which ranges from 7 to as high as 24 (Table 5.3; Fig. 5.5). Ascension high Zr/Nb and Dark Slope

Crater mafic rocks have normal P/Zr (Table 5.3). Ascension low Zr/Nb and intermediate Zr/Nb basalt and hawaiite flows with P/Zr > 12 are anomalously enriched in P (Table 5.3).

No mantle processes can so strongly fractionate P/Zr unless residual apatite is present during partial melt generation in the mantle. Rosenbaum et al. (1995) report high phosphorous (P_2O_5 ~26 wt.%) interstitial glass from alkali basalt hosted spinel lherzolite xenolith from the Massif Central with enriched REE (La ~50 ppm; Yb ~2ppm). The Massif Central alkali basalt and basanite with anomously high phosphorous abundance are attributed to interaction rising partial melts from the asthenosphere with the high phosphorous rich melts within the lithosphere (Rosenbaum et al., 1995). Experimental studies (Watson, 1980) show that depression of the upper mantle solidus to ~1100°C in the presence of H_2O results in apatite-saturated melts containing only 1-2 wt% P_2O_5 (at 50 wt% SiO_2) rather than the 3-4% required at 1250°C. If H_2O-bearing source regions do produce magmas at 1100°C, then residual apatite could occur in greater abundance and to higher degrees of melting than is possible in dry source regions (Watson, 1980). However, since the mantle contains much less than the chondritic abundance of phosphorous, there is no reasonable way in which basic magmas could be formed in the presence of greater amounts of residual apatite (Watson, 1980). The factors that contribute to making P/Zr so variable in Ascension mafic rocks are evaluated in the following section.

A number of possible explanations exist for the high phosphorous content of certain Ascension mafic rocks: 1) contamination of samples by guano, which is abundant on many of the lava flow surfaces; 2) enrichment in P due to supergene processes, 3) variable P/Zr in the magma source region; 4) accumulation in magmas of apatite phenocrysts or microphenocrysts; or 5) resorption by magmas of apatite,

perhaps during passage of magma through apatite-rich cumulate bodies.

Direct contamination of samples by guano (~40 wt% P_2O_5) is extremely unlikely. Guano contaminated flow surfaces were carefully avoided during sampling. Where multiple samples were taken from a single vent, P/Zr is consistent for guano-covered and guano-free flows and scoria. Also, a leaching experiment on a high P/Zr flow sample showed the P_2O_5 to be non-leachable and therefore primary magmatic. Harris (1985) suggested that the secondary REE-rich phosphate found in some gabbro xenoliths was deposited from a low-T aqueous fluid that had dissolved guano. We do not see how such a process could contaminate large volumes of rock or magma. It is possible such fluids may have circulated to depth where they may have interacted with, and contaminated, mafic magma, perhaps also triggering eruption. It is highly questionable, however, whether it is realistic to invoke sufficient volumes of fluid to elevate P_2O_5 by 0.5 to 1.0 wt% in magma (the range of P_2O_5 observed in basalt and hawaiite of the intermediate Zr/Nb group), and there is no systematic disturbance of $\delta^{18}O$ in the basalt samples as would be expected with low-temperature alteration.

Involvement of guano is also discounted for high-phosphorus basalt flows containing abnormally high REE and Y concentrations from French Polynesia based on Nd isotopic systematics (Cotten et al., 1994). Rather, the source of this enrichment is considered to be from mobilization of REE and Y as phosphate complexes by meteoric water from older basalt flows. Anomalously high REE, Y, and Ba together with high P is also documented from several Hawaiian islands, e.g. Kahoolawe (Fodor et al., 1992) and Oahu (Roden et al., 1994); this enrichment is attributed to weathering of basalt leading to soil formation with dissolution of primary igneous minerals liberating REE-Y±Ba which complex with PO_4, SO_4, and F in meteoric fluids and are precipitated as secondary phosphates or adhere to clays in the basalt flows (Bohrson & Reid, 1995).

On Ascension, there is evidence of anomalous enrichment of REE, Y and Ba in mafic clasts occurring in trachyte (Kar et al., Mafic_Clast MS) which probably were enriched by meteoric fluids. However, the anomalous (low to high) behavior of P in the mafic rocks are primary igneous characteristics as there are no systematic disturbances of Sr, Nd, Pb, and O isotope ratios in the mafic rocks with high P.

In the intermediate Zr/Nb group basalt and hawaiite compositions, P/Zr broadly increases with Y/Zr suggesting that apatite may be the cause of P enrichment in the high P/Zr rocks (Fig. 5.6). The Y content of the mafic rocks varies between 31 to 68 ppm. Harris (1983) reports that apatite occurs as a common fine-grained inclusion in silicate minerals in monzogabbroic xenoliths, and that large, cumulus apatite occurs in plutonic inclusions from Middleton Ridge, Crystal Bay, Pillar Bay, NASA Road, and Green Mountain. Apatite also occurs as very fine needles in certain P_2O_5-rich volcanic rocks but is not identified in trachytic and comenditic rocks (Harris, 1983). Our study shows that apatite is absent in all types of basalt and hawaiite flows but occurs as apatite needles in mugearite and benmoreite flows. Evolved rocks have very low P_2O_5 contents and lack any evidence of apatite and hence have experienced significant apatite crystallization.

Phosphorus, an incompatible element during much of the crystallization history of basaltic magma, can reach concentrations of several weight percent before saturation of phosphate minerals occurs (Toplis et al., 1994). Leeman et al. (1976) report 2 to 3 wt% P_2O_5 concentration in natural basic magma. Experimental studies (Watson, 1980) show that solubility of apatite in basic magmas is extremely high (3 to 4 wt% dissolved P_2O_5 is required for saturation at 1250°C) and that even small degrees of melting will result in apatite consumption; i.e., residual apatite in magma source regions is uncommon. For Ascension lavas, the mafic rocks of the high Zr/Nb, low Zr/Nb, and

Dark Slope Crater groups are undersaturated in apatite and show a slight increase in P_2O_5 for a narrow range (47 to 50 wt%) in SiO_2 within the individual groups (Fig. 5.4). The compositional range in intermediate Zr/Nb group (basalt to benmoreite) shows that apatite saturation occurs at ~50 wt% SiO_2 (Fig. 5.4); P_2O_5 initially increases to 1.5 wt% (maximum 1.69 wt%) until it reaches saturation at ~50 wt% SiO_2 and then decreases rapidly subparallel to the apatite-saturation isotherms (Fig 4; Watson, 1980) for SiO_2 > 50 wt%. The P_2O_5 increase in the intermediate Zr/Nb group to abnormally high concentrations for a certain SiO_2 content does not signify a "normal" crystal fractionation trend but a build-up of P_2O_5 in the undersaturated mafic magma. The subset of intermediate Zr/Nb mafic flows (as described in the major element chemistry section) erupted on the southern and southeastern parts of the island do not indicate "normal" crystal fractionation trend involving apatite either (small increase in P_2O_5 for a large increase in SiO_2). Magma mixing calculations between an intermediate Zr/Nb hawaiite (AI-265; SiO_2 48.43 wt%) with low P_2O_5 (0.62 wt%) and an intermediate Zr/Nb mugearite (AI-112; SiO_2 54.43 wt%) with low P_2O_5 (0.77 wt%) to produce an intermediate Zr/Nb mugearite (AI-255; SiO_2 52.29 wt%) low P_2O_5 (0.67 wt%) do not yield a good major element least squares residual and match for incompatible trace elements and hence low P_2O_5 content may be interpreted as a source characteristic for this subset of mafic flows.

Freundt and Schmincke (1995) show for Gran Canaria Island that both P_2O_5 and Y increase for mafic magmas and then P_2O_5 decreases for compositions above 55% SiO_2. The source of enrichment in P_2O_5 is attributed to apatite-rich cumulates or xenoliths. Apatite occurs in gabbroic and silicic inclusions from Socorro Island. Assimilation of apatite accumulated during previous stages of magmatism on Socorro produced enrichment of P_2O_5, Ba, and light and middle rare earth elements in the later

basalt flows (Bohrson & Reid, 1995).

On Ascension we find no such apatite-rich cumulates or xenoliths or xenocrysts but that does not preclude the presence of apatite-rich cumulate bodies; it might just be an artifact of sampling. and probably indicates that assimilated xenoliths were disaggregated, apatite resorbed, and remaining xenocrysts completely separated from magma prior to eruption. Also, the surface distribution of high P/Zr vents might be expected to map out the distribution of apatite-rich cumulate bodies in the subsurface if there was a systematic distribution of the occurrence of these cumulate bodies. However, the spatial distribution of high P/Zr scoria cones (Fig. 5.3) apparently is random. In the northern part of the island basalt and hawaiite scoria cones with P/Zr between 12 and 16 and P/Zr >16 are found in close proximity to one another and in the southern and southwestern parts of the island low P/Zr (< 12) and high P/Zr (> 12) scoria cones are found in close proximity to one another. However, two adjacent vents might erupt magma from magma chambers at different depths - one magma chamber might be in contact with a cumulate body whereas the other might not.

Evidence of apatite in Ascension Island rocks

Apatite has crystallized out of mafic magmas (SiO_2 > 50 wt%) as evidenced by rapid decrease in P_2O_5 in the more evolved (SiO_2 between 55 to 60 wt%) mafic rocks of Ascension. This apatite could have been resorbed by the mafic magmas (undersaturated in P_2O_5) during later stages of mafic magmatism on Ascension. In general, accumulation of approximately 2.5% apatite (containing 42 wt% P_2O_5) in basaltic magma will raise the whole rock P_2O_5 content by approximately 1 wt%. A simple mass-balance calculation for Ascension mafic rocks involving a high Zr/Nb magma (with average 0.50 wt% P_2O_5) and apatite to generate the highest P_2O_5 content (1.69 wt%) in the intermediate Zr/Nb magma would require a magma:apatite ratio of

97:3. A least squares model (Table X) shows that generation of a benmoreitic intermediate Zr/Nb magma (0.84 wt% P_2O_5) from a parental mugearitic intermediate Zr/Nb magma (1.45 wt% P_2O_5) (Kar et al., Mafic MS) requires crystallization of 1.9 wt% apatite. A similar calculation with Broken Tooth mugearite (0.98 wt% P_2O_5) fractionating to benmoreite (0.67 wt% P_2O_5) requires crystallization of 1.3 wt% apatite (Table 4).

Two hawaiite flows having very similar major element chemistry (SiO_2 49.76 wt% in both; MgO 4.47 wt% in AI-89 and 4.15 wt% in AI-30) and most trace element chemistry (Zr 309 ppm in AI-89 and 318 ppm in AI-30) represent having undergone similar degree of fractionation. Normalization of the REE in a high P/Zr intermediate Zr/Nb hawaiite flow (AI-30) to a moderate P/Zr intermediate Zr/Nb hawaiite flow (AI-89) produces a middle rare earth enriched (MREE) pattern (Fig. 5.8) consistent with apatite resorption. Incompatible elements of the high P/Zr hawaiite (AI-30) when normalized to the moderate P/Zr (AI-89) (Fig. 5.8) shows an extreme enrichement in P (1.6 times) together with Y (~1.2 times) in the high P/Zr flow with respect to the moderate P/Zr flow again indicating involvement of apatite in the high P/Zr flows. Hence direct and indirect evidence of cumulus apatite is present on Ascension Island.

The high Zr/Nb mafic magmas are the oldest mafic rocks exposed, Dark Slope Crater magmas were erupted next, followed by the low Zr/Nb mafic magmas. The youngest mafic magmas are the intermediate Zr/Nb group ranging from basalt to benmoreite (Kar et al., Mafic MS). The geochemical characteristics of the felsic rocks are largely consistent with an origin by fractional crystallization of high Zr/Nb mafic magmas as evidenced by identical $^{143}Nd/^{144}Nd$ and similar Pb isotopic ratios (Felsic MS). Fractionation to very evolved compositions being a relatively late feature of the volcanic edifice on Ascension Island (Nielson & Sibbett, 1996; Kar et al., Mafic MS). Hence the earlier magmas (e.g., high Zr/Nb) which are also low (normal) in P content

did not interact with apatite-rich cumulate rocks. However, certain later mafic magmas (e.g. low Zr/Nb and certain intermediate Zr/Nb) experienced significant resorption of apatite-rich cumulate bodies during magmatism. Resorption of this apatite-rich cumulates in the later mafic magmas could perhaps have raised the P content of the later low Zr/Nb and certain intermediate Zr/Nb mafic magmas that have anomalously high P content.

CONCLUSIONS

1) Normal P abundance occurs in the earlier formed mafic magmas (e.g. high Zr/Nb and Dark Slope Crater groups) whereas high P in later mafic magmas (e.g low Zr/Nb and certain intermediate Zr/Nb groups).
2) Direct contamination of samples by guano (~40 wt% P_2O_5) are discounted as a leaching experiment on a high P/Zr flow sample showed the P_2O_5 to be non-leachable and therefore primary magmatic. Supergene processes are also discounted as there is no systematic disturbance of $\delta^{18}O$ in the basalt samples as would be expected with low-temperature alteration.
3) There is direct and indirect evidences of presence of apatite-rich cumulate bodies in the volcanic edifice. Apatite crystallizes out of mafic magmas (SiO_2 > 50 wt%) as evidenced by rapid decrease in P_2O_5 in the more evolved (SiO_2 between 55 to 60 wt%) mafic rocks of Ascension. Kar et al. (Mafic MS) show by least squares model that generation of a benmoreitic intermediate Zr/Nb magma (0.84 wt% P_2O_5) from a parental mugearitic intermediate Zr/Nb magma (1.45 wt% P_2O_5) requires crystallization of 1.9 wt% apatite. In general, accumulation of approximately 2.5% apatite (containing 42 wt% P_2O_5) in basaltic magma will raise the whole rock P_2O_5 content by approximately 1 wt%. A simple mass-balance calculation for Ascension

mafic rocks involving a high Zr/Nb magma (with average 0.50 wt% P_2O_5) and apatite to generate the highest P_2O_5 content (1.69 wt%) in the intermediate Zr/Nb magma would require a magma:apatite ratio of 97:3. Normalization of the REE in a high P/Zr intermediate Zr/Nb hawaiite flow (AI-30) to a moderate P/Zr intermediate Zr/Nb hawaiite flow (AI-89) both of which have undergone similar degrees of fractionation produces a middle rare earth enriched (MREE) pattern consistent with apatite resorption. Incompatible elements of the high P/Zr hawaiite (AI-30) when normalized to the moderate P/Zr (AI-89) shows an extreme enrichement in P (1.6 times) together with Y (~1.2 times) in the high P/Zr flow with respect to the moderate P/Zr flow again indicating involvement of apatite in the high P/Zr flows. Hence direct and indirect evidence of cumulus apatite is present on Ascension Island.

4) Earlier mafic magmas (e.g., high Zr/Nb) low (normal) in P/Zr content did not interact with apatite-rich cumulate rocks. However, later mafic magmas (e.g. low Zr/Nb and certain intermediate Zr/Nb) experienced significant resorption of apatite-rich cumulate bodies during magmatism.

5) Assimilation of apatite-rich cumulate rocks and resorption of apatite may account for high P/Zr. None of the flows with high P/Zr, however, contain xenoliths or xenocrysts, and this would require that xenoliths were disaggregated, apatite resorbed by mafic magmas (undersaturated in P_2O_5), and remaining xenocrysts completely separated from magma prior to eruption.

ACKNOWLEDGEMENTS

This paper is a part of a Ph.D. dissertation by Aditya Kar. The project was supported by NSF grant EAR-9204079.

REFERENCES

Bohrson, W.A., and Reid, M.R., 1995. Petrogenesis of alkaline basalts from Socorro Island, Mexico: Trace element evidence for contamination of ocean island basalt in the shallow ocean crust. Journal of Geophysical Research, 100, B12, 24: 555-576.

Castellana, B., and Wolff, J.A., 1992. Open system evolution of phonolitic magma, Brava, Cape Verde (abstract), Eos Transactions, AGU, 73 (43), Fall Meeting Supplement, 654.

Cliff, R.A., Baker, P.E., and Mateer, N.J. 1991. Geochemistry of Inaccessible Island volcanics. Chemical Geology 92: 251-260.

Cotten, J., Le Dez, A., Bau, M., Caroff, M., Maury, R.C., Dulski, P., Fourcade, S., Bohn, M., & Brousse, R., 1995. Origin of anomalous rare-earth element and yttrium enrichments in subaerially exposed basalts: Evidence from French Polynesia. Chemical Geology 119: 115-138.

Davidson, J.P., Boghossian, N.D., & Wilson, B.M., 1993. The Geochemistry of the Igneous Rock Suite of St. Martin, Northern Lesser Antilles. Journal of Petrology 34: 839-866.

Eiler, J.M., Farley, K.A., Valley, J.W., Hofmann, A.W., & Stopler, E.M., 1996. Oxygen isotope constraints on the sources of Hawaiian volcanism. Earth and Planetary Science Letters 144: 453-468.

Fodor, R.V., Frey, F.A., Bauer, G.R., & Clague, D.A., 1992. Ages, rare-earth element enrichment, and petrogenesis of tholeiitic and alkalic basalts from Kahoolawe Island, Hawaii. Contributions to Mineralogy and Petrology 110: 442-462.

Freundt, A., and Schmincke, H-U. (1995) Petrogenesis of rhyolite-trachyte-basalt composite ignimbrite P1, Gran Canaria, Canary Islands. Journal of Geophysical Research, 100, B1, 455-474.

Frey, F., Wise, W.S., Garcia, M.O., West, H., Kwon, S.-T., & Kennedy, A. 1990. Evolution of Mauna Kea Volcano, Hawaii: Petrologic and geochemical contsraints on postshield volcanism. Journal of Geophysical Research, 95, B2, 1271-1300.

Frey, F., Garcia, M.O., Wise, W.S., Kennedy, A., Gurriet, P., & Albarede, F. 1991. The evolution of Mauna Kea Volcano, Hawaii: Petrogenesis of tholeiitic and alkalic basalts. Journal of Geophysical Research, 96, B9, 14,347-14,375.

Garcia, M.O., Pietruszka, A.J., Ito, E., & Eiler, J.M., 1996. Oxygen isotopes reveal a history of crustal contamination for lavas from the ongoing Puu Oo eruption of Kilauea Volcano, Hawaii. American Geophysical Union Chapman Conference, Tenerife, Canary Islands abstracts with programs.

Harris, C., 1983. The petrology of lavas and associated plutonic inclusions of Ascension Island. Journal of Petrology 24: 424-470.

Harris, C., 1985. Guano-derived rare earth-rich phosphate amygdales in gabbroic inclusions from Ascension Island. Earth and Planetary Science Letters 72: 141-148.

Harrison, T.M., and Watson, B.E. (1984) The behavior of apatite during crustal anatexis: Equilibrium and kinetic considerations. Geochim. Cosmochim. Acta, 48, 1467-1477.

Hofmann, A.W., 1996. A geochemist's view of mantle dynamics. American Geophysical Union Chapman Conference, Tenerife, Canary Islands abstracts with programs.

Kar, A., Weaver, B.L., Davidson, J.P., & Nielson, D., 1995. Geochemical characteristics of borehole samples recovered from Ascension Island, South Atlantic Ocean. GSA Abstracts with Programs 27 no. 6: A-254.

Kar, A., Weaver., B., Davidson, J., & Colucci, M., 1996. Petrogenesis of mafic volcanic rocks from Ascension Island. American Geophysical Union Fall Meeting abstracts with programs. Vol. 76, No. 46: F698.

Kar, A., Weaver, B., Davidson, J., & Colucci, M., (Felsic MS). Felsic oceanic island magmatism: Origin of high $^{87}Sr/^{86}Sr$ evolved volcanic and plutonic rocks from Ascension Island, South Atlantic Ocean. Journal of Petrology (in review).

Kar, A., Weaver, B., Davidson, J., & Colucci, M., (Mafic MS). Small-scale mantle heterogeneities: Evidence from transitional to mildly alkaline volcanic rocks from Ascension Island, South Atlantic Ocean.

Kar, A., Weaver, B., & Davidson, J., (Mafic Clast MS). Mafic clasts with unusual REE patterns in felsic volcanic rocks: Evidence of subsolidus alteration of mafic rocks from Ascension Island, South Atlantic Ocean.

Lassiter, J.C., & Hauri, E.H., 1996. Local crustal assimilation by Hawaiian lavas or ancient recycled crust in the Hawaiian Plume? Os-Isotope contraints for ^{18}O enriched and depleted lavas. American Geophysical Union Chapman Conference, Tenerife, Canary Islands abstracts with programs.

Leeman, W.P., Vitaliano, C.J., Prinz, M., 1976. Evolved lavas from the Snake River plain, Craters of the Moon National Monument, Idaho. Contributions to Mineralogy and Petrology 56: 35-60.

le Roex, A.L., 1985. Geochemistry, mineralogy and magmatic evolution of the basaltic and trachytic lavas from Gough Island, South Atlantic. Journal of Petrology 26: 149-186.

le Roex, A.P., Cliff, R.A., & Adir, B.J.I. 1990. Tristan da Cunha, South Atlantic: Geochemistry and petrogenesis of a basanite-phonolite lava series. Journal of Petrology 27: 779-812.

McDonough, W.F., & Sun, S., -S., 1995. The composition of the Earth. Chemical Geology 120: 223-253.

Nakamura, N., 1974. Determination of REE, Ba, Fe, Mg, Na and K in carbonaceous and ordinary chondrites. Geochimica et Cosmochimica Acta 38: 757-775.

Nielson, D.L., 1996. Introduction to geothermal exploration on Ascension Island, South Atlantic Ocean. Geothermics 25: 419-425.

Nielson, D.L., & Sibbett, B.S., 1996. Geology of Ascension Island, South Atlantic Ocean. Geothermics 25: 427-448.

Roden, M.F., Frey, F.A., and Clague, D.A., 1994. Geochemistry of tholeiitic and alkalic lavas from the Koolau Range, Oahu, Hawaii: implications for Hawaiian volcanism. Earth and Planetary Science Letters 69: 141-158.

Rosenbaum, J.M., Wilson, M., Condliffe, E., & Morris, G.A., 1995. Mobile phosphorous in the Massif Central mantle. EOS, 76, No. 46: F642.

Thirwall, M.F., 1996. The identification and potential significance of crustal contamination in ocean island volcanics. American Geophysical Union Chapman Conference, Tenerife, Canary Islands abstracts with programs.

Toplis, M.J., Libourel, G., & Carroll, M.R., 1994. The role of phosphorus in crystallization processes of basalt: An experimental study. Geochimica et Cosmochimica Acta 58: 797-810.

Watson, E.B., 1980. Apatite and phosphorus in mantle source regions: an experimental study of apatite/melt equilibria at pressures to 25 kbar. Earth and Planetary Science Letters 51: 322-335.

Weaver, B.L., Kar, A., & Davidson, J.P., 1995. Unusual behaviour of phosphorus in mafic lavas from Ascension Island, South Atlantic Ocean. EOS 76 no. 46: F698.

Weaver, B.L., Kar, A., Davidson, J.P., and Colucci, M., 1996. Geochemical characteristics of volcanic rocks from Ascension Island, South Atlantic Ocean. Geothermics 25: 449-470.

Weaver, B.L., Tarney, J., & Saunders, A.D., 1985. Geochemistry and mineralogy of basalts recovered from the Central North Atlantic. In Bougault, H., Cande, S.C., et al., Init. Repts. DSDP, 82: Washington (US Govt. Priniting Office): 395-419.

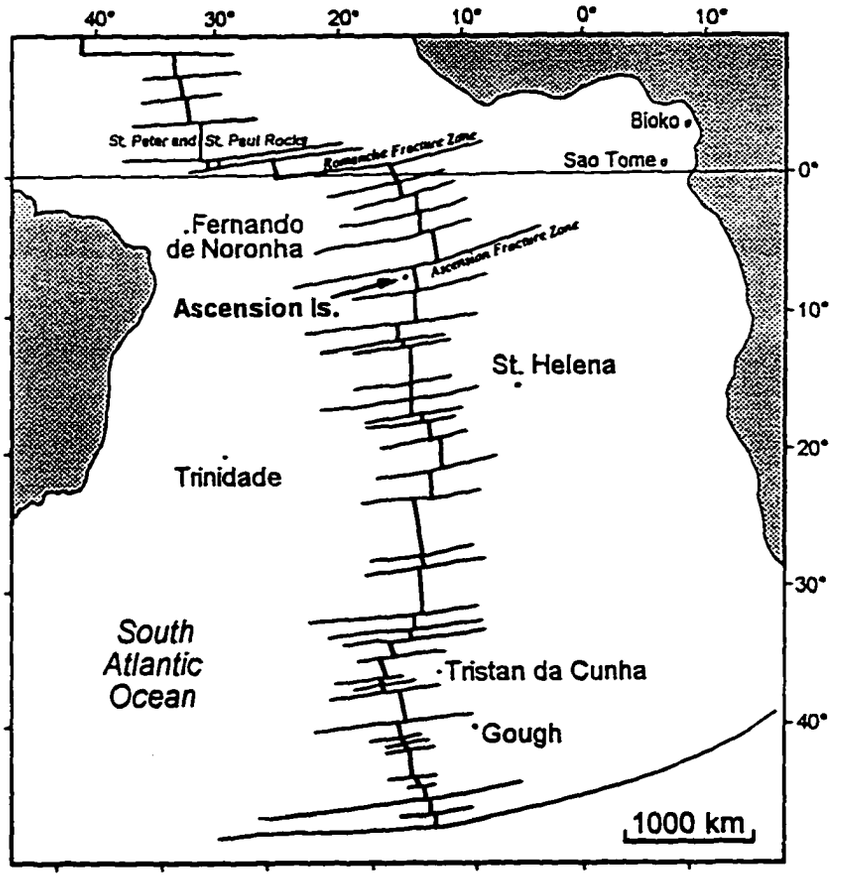

Figure 5.1. Map of part of the South Atlantic Ocean showing the locations of oceanic islands, the axis of the Mid-Atlantic Ridge, and major transform faults and fracture zones. After Nielson (1996).

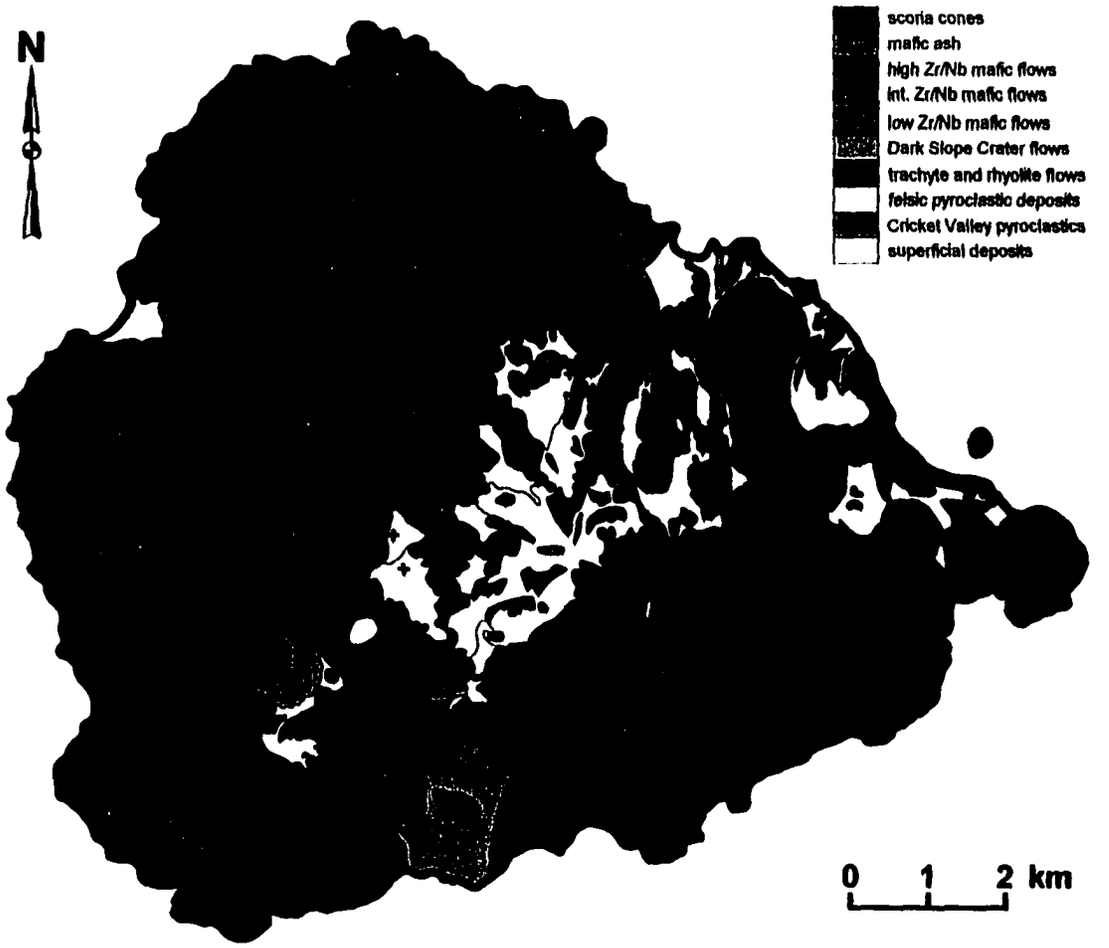

Figure 5.2. Geological map of Ascension Island, somewhat modified from Nielson and Sibbett (1996). The four geochemically distinct mafic flow types (high Zr/Nb, intermediate Zr/Nb, low Zr/Nb, and Dark Slope Crater) are identified and the compositions of selected flows are indicated as: **B** basalt, **H** hawaiite, **M** mugearite, **Be** benmoreite.

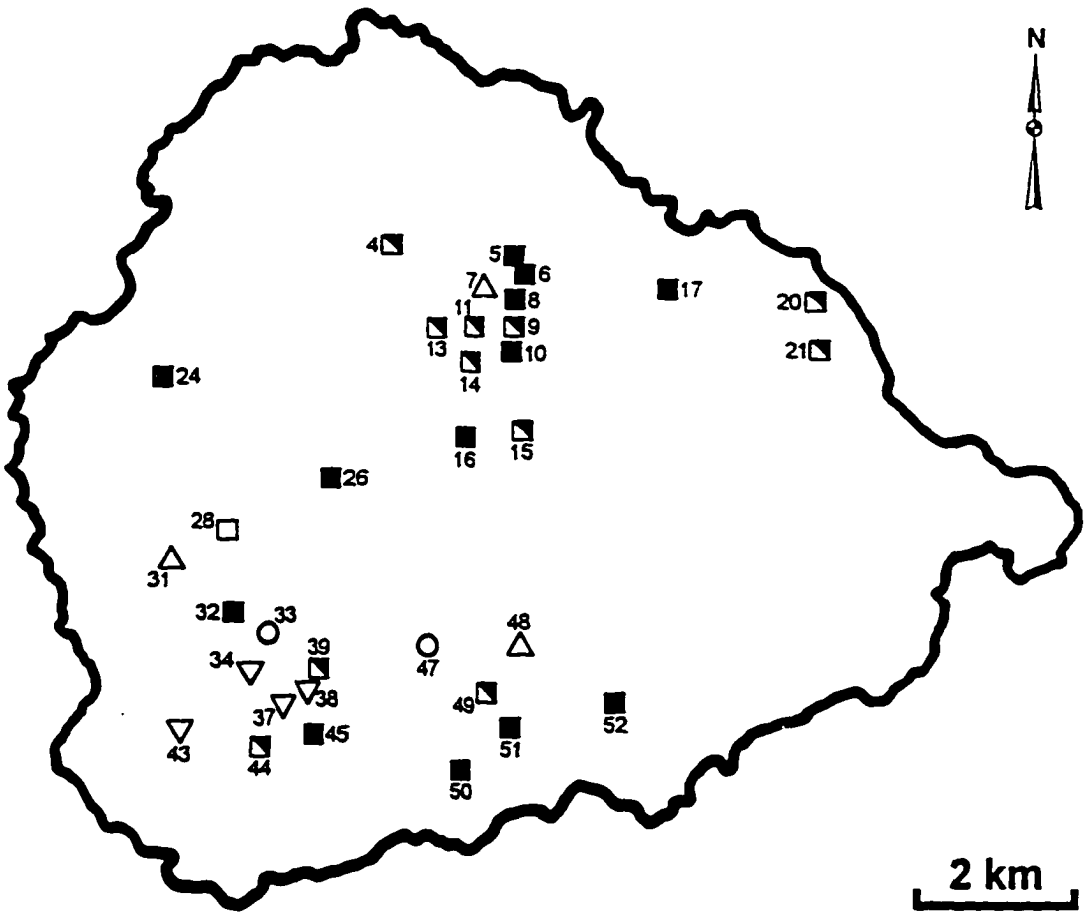

Figure 5.3. Location and composition of basalt and hawaiite scoria cones on Ascension Island. △ high Zr/Nb, P/Zr < 12; ▽ low Zr/Nb, P/Zr > 16; intermediate Zr/Nb, □ P/Zr < 12, ◪ 12 < P/Zr < 16 ; ■ P/Zr > 16; O Dark Slope Crater, P/Zr < 12.

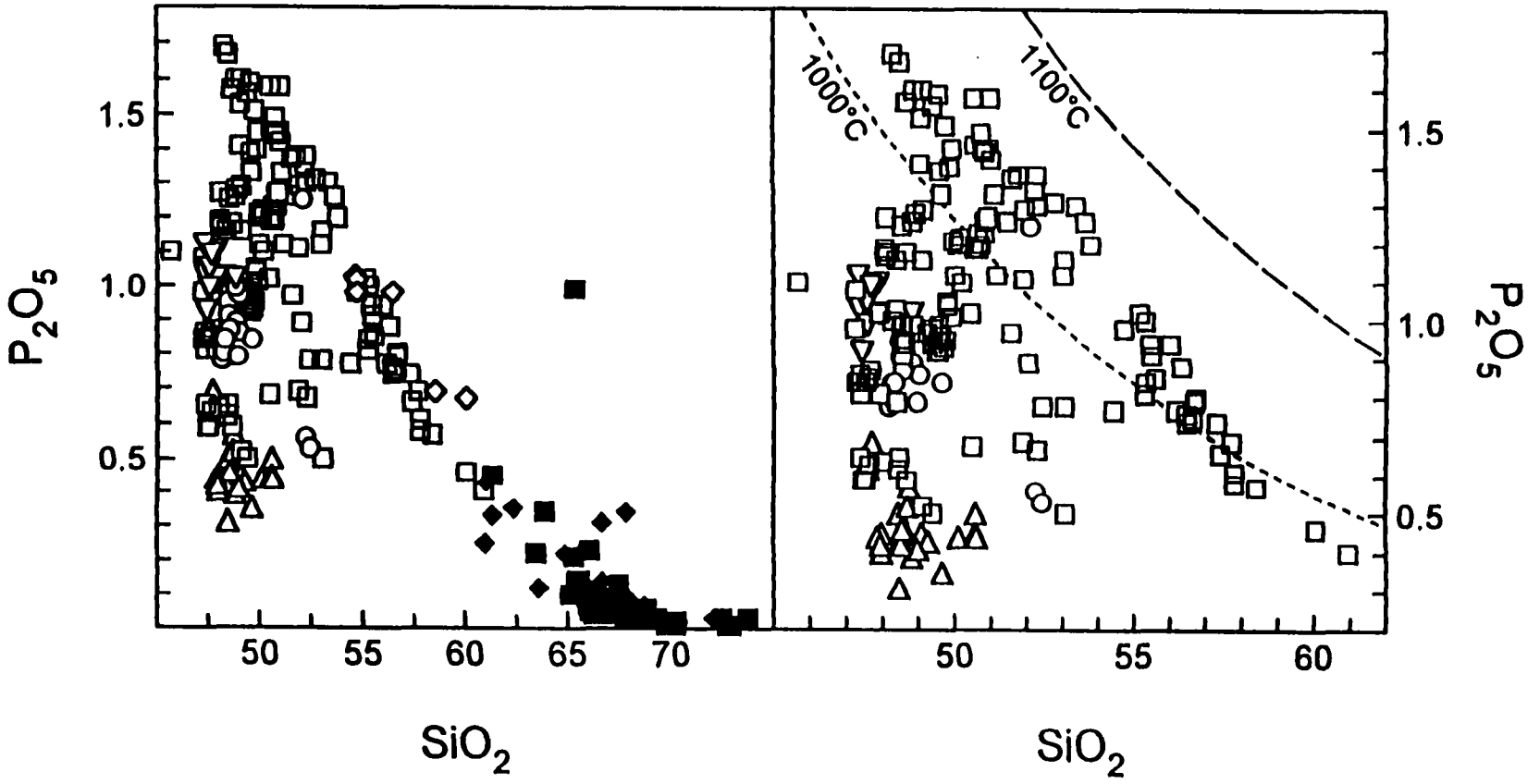

Figure 5.4. Variation in P_2O_5 *vs.* SiO_2 for volcanic rocks from Ascension Island. *A)* basalt to rhyolite lava flows and pyroclastic deposits, and *B)* basalt to benmoreite flows and scoria with apatite saturation curves for temperatures of 1000°C and 1100°C from Harrison and Watson (1984). Symbols denote: △ high Zr/Nb basalt; □ intermediate Zr/Nb basalt to benmoreite; ▽ low Zr/Nb hawaiite; O Dark Slope Crater hawaiite and mugearite; ◇ Broken Tooth mugearite and benmoreite; ◆ trachyte and rhyolite pumice; ■ trachyte and rhyolite flows and flow domes.

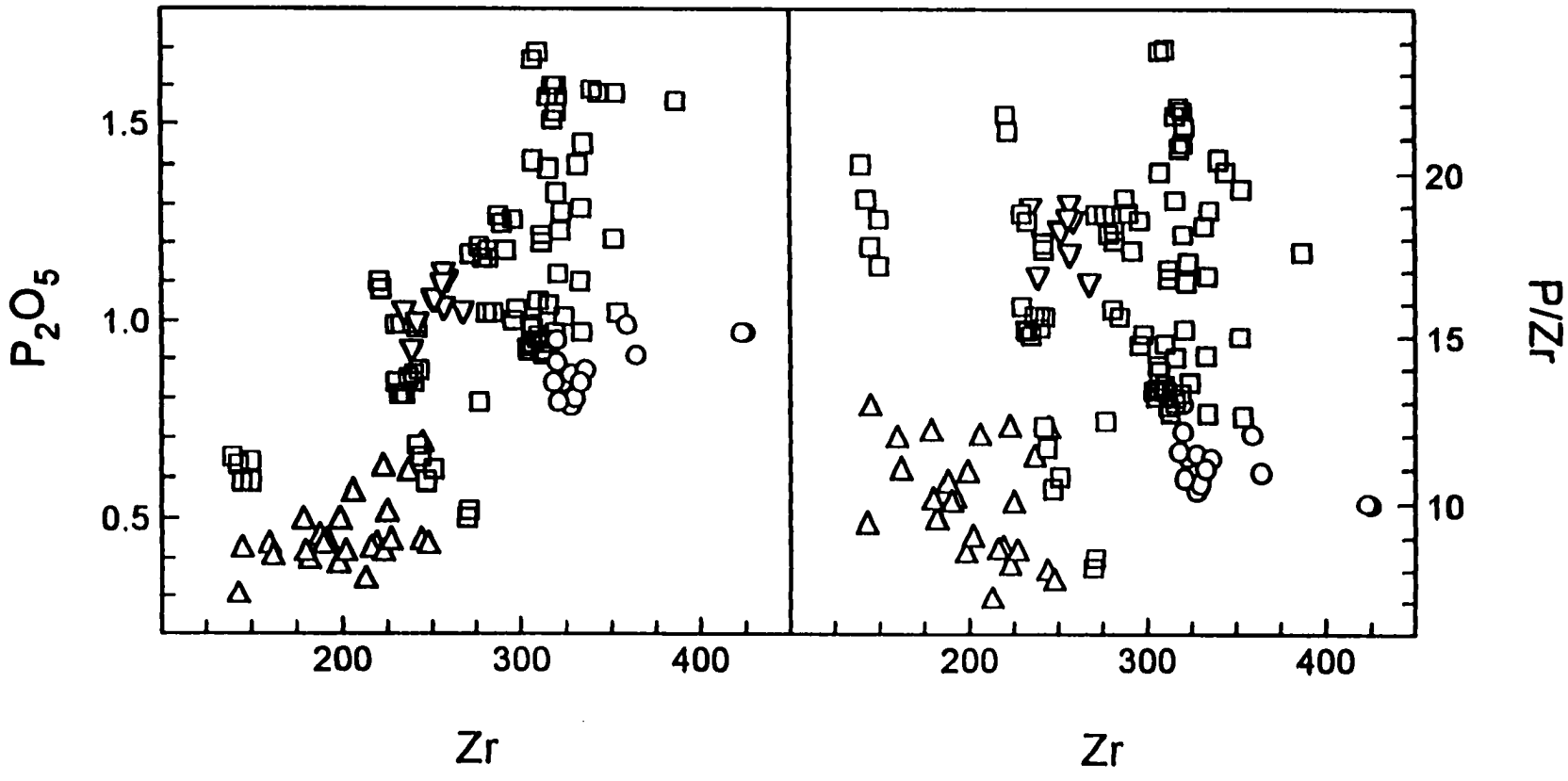

Figure 5.5. Variation in *A)* P_2O_5 *vs.* Zr and *B)* P/Zr *vs.* Zr for basalt and hawaiite rocks from Ascension Island. Symbols as in Fig. 5.4.

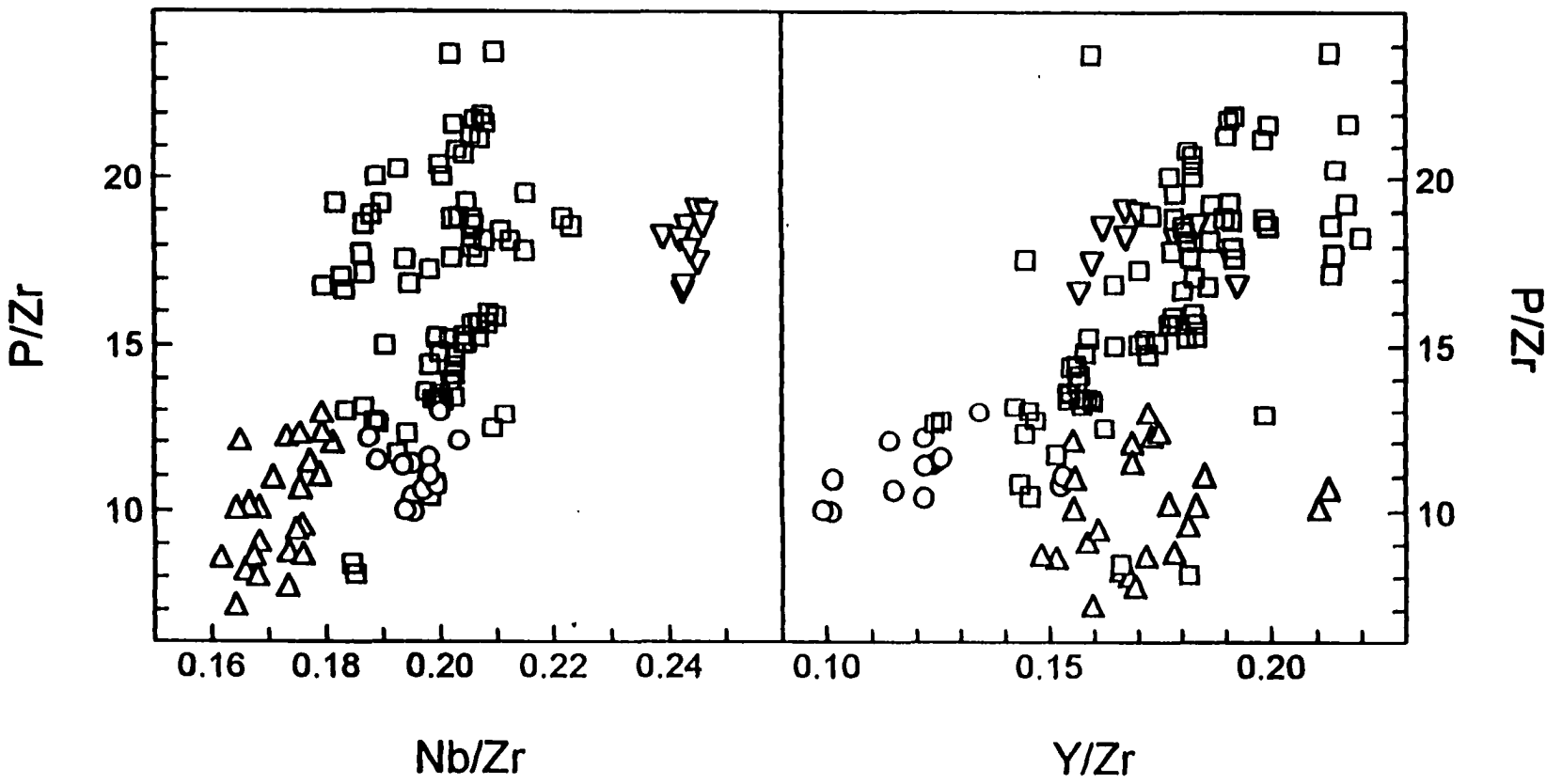

Figure 5.6. Variation in *A)* P/Zr *vs.* Nb/Zr and *B)* P/Zr *vs.* Y/Zr for basalt and hawaiite rocks from Ascension Island. Symbols as in Fig. 5.4.

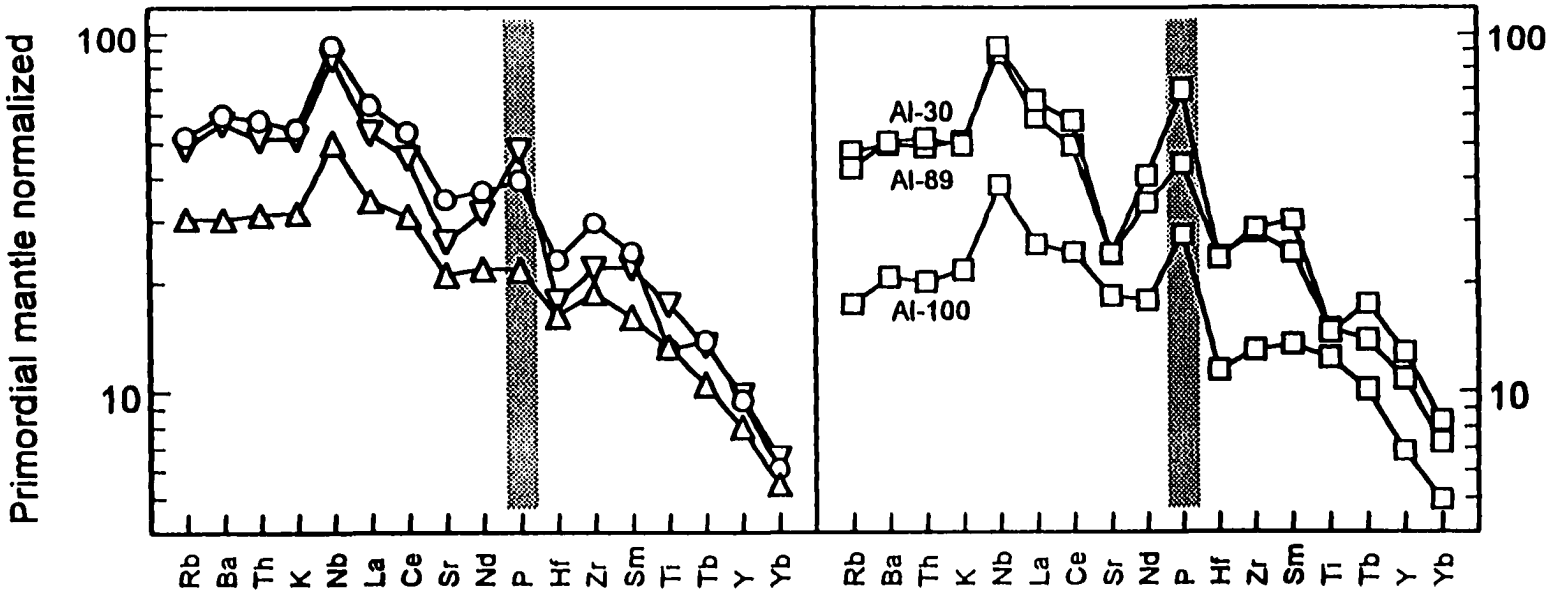

Figure 5.7. Incompatible element patterns (normalized to primordial mantle values of McDonough & Sun, 1995) for mafic rocks from Ascension Island. *A)* Patterns for average high Zr/Nb basalt (Δ), average low Zr/Nb hawaiite (∇), and average Dark Slope Crater hawaiite (O). P is normal in the high Zr/Nb basalt but strongly enriched in the low Zr/Nb hawaiite. *B)* Patterns for three intermediate Zr/Nb samples with variable P enrichment; basalt Al-100 has P/Zr of 17.8, hawaiite Al-89 has P/Zr of 13.4, and hawaiite Al-30 has P/Zr of 20.7.

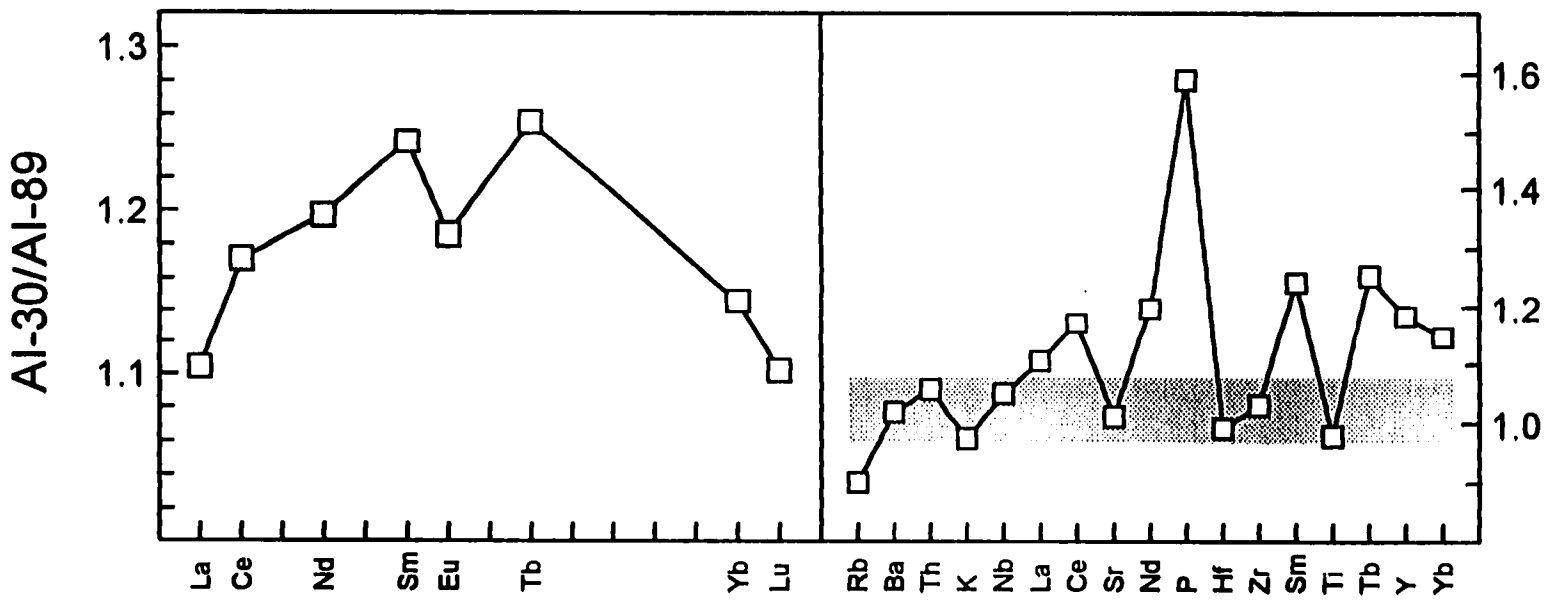

Figure 5.8. Trace element characteristics of intermediate Zr/Nb, high P/Zr hawaiite Al-30 compared to intermediate Zr/Nb, moderate P/Zr hawaiite Al-89. *A)* Rare earth element pattern (normalized to chondrite values of Nakamura, 1974). *B)* Incompatible element pattern (normalized to primordial mantle values of McDonough & Sun, 1995).

Table 5.1. Location and chemical characteristics of Ascension Island scoria cones.

Cone No.	Name	Grid Reference	Composition	P/Zr
1	Broken Tooth	703258	Mugearite to benmoreite	11.4-5.7
2	Hollow Tooth	709251	Benmoreite	8.8,9.2
3	unnamed	714247	Benmoreite	2.9,3.4
4	unnamed	689248	Mugearite	14.8
5	unnamed	704247	Hawaiite (intermediate Zr/Nb)	16.7
6	unnamed	706245	Hawaiite (intermediate Zr/Nb)	17.1
7	Sisters Red Hill	700244	Basalt (high Zr/Nb)	10.1
8	unnamed	704242	Hawaiite (intermediate Zr/Nb)	22.0
9	Street Crater	705238	Hawaiite (intermediate Zr/Nb)	12.9
10	Butt Crater	704235	Hawaiite (intermediate Zr/Nb)	23.8,24.0
11	Perfect Crater	699239	Hawaiite (intermediate Zr/Nb)	13.4
12	unnamed	687241	not known	
13	Sisters Peak	693239	Hawaiite (intermediate Zr/Nb)	13.2-15.2
14	unnamed	699234	Hawaiite (intermediate Zr/Nb)	13.4
15	Thistle Hill	705225	Mugearite	14.0
16	Travellers Hill	697225	Hawaiite (intermediate Zr/Nb)	17.6,18.1
17	Lower Valley Crater	724243	Basalt (intermediate Zr/Nb)	18.8
18	Upper Valley Crater	726234	Mugearite	7.0,8.0
19	unnamed	730221	not known	
20	unnamed	743241	Hawaiite (intermediate Zr/Nb)	15.8
21	unnamed	744233	Hawaiite (intermediate Zr/Nb)	14.7
22	Fort Thornton	647240	Benmoreite	7.7
23	Fort Hayes	645236	Benmoreite	9.0
24	Cross Hill	658233	Basalt (intermediate Zr/Nb)	21.2-22.9
25	unnamed	682222	not known	
26	Lady Hill	681219	Hawaiite (intermediate Zr/Nb)	18.1
27	unnamed	674218	Benmoreite	6.9
28	unnamed	667213	Hawaiite (intermediate Zr/Nb)	8.1,8.4
29	Table Crater	674209	Mugearite	11.2
30	Cat Hill	648211	Benmoreite	7.7,9.7
31	South West Bay Red Hill	660209	Basalt (high Zr/Nb)	9.5-12.9
32	Command Hill	668202	Basalt (intermediate Zr/Nb)	17.2-20.3
33	Dark Slope Crater	672199	Hawaiite to mugearite (DSC-type)	10.0-13.0
34	Horse Shoe Crater	670193	Hawaiite (low Zr/Nb)	19.0
35	unnamed	666193	not known	
36	unnamed	670190	not known	
37	unnamed	674190	Hawaiite (low Zr/Nb)	17.5
38	unnamed	678192	Hawaiite (low Zr/Nb)	18.5
39	unnamed	679195	Hawaiite (intermediate Zr/Nb)	12.6
40	unnamed	684196	Mugearite	14.1,14.6
41	unnamed	681192	not known	
42	Round Hill	664190	not known	
43	Cotar Hill	661187	Hawaiite (low Zr/Nb)	16.8,18.9
44	South Gannet Hill	671185	Basalt (intermediate Zr/Nb)	15.2-15.9
45	Booby Hill	678186	Hawaiite (intermediate Zr/Nb)	19.0
46	Spoon Crater	696198	not known	
47	unnamed	694197	Hawaiite (DSC-type)	11.4,12.1
48	Mountain Red Hill	705197	Basalt (high Zr/Nb)	10.2
49	unnamed	701192	Mugearite	16.4
50	South Red Crater	697181	Hawaiite (intermediate Zr/Nb)	19.2
51	Green Top Crater	705187	Hawaiite (intermediate Zr/Nb)	18.9
52	South East Crater	717190	Hawaiite (intermediate Zr/Nb)	20.0
53	Coast Red Nipple	741188	not known	
54	Round Hill	752193	not known	
55	Crater Cliff	758202	not known	
56	unnamed	763212	not known	

Cone number has been assigned arbitrarily. Scoria cone names and grid references are from the 1:25,000 Ascension Island topographic map, series G 892, edition 4-GSGS, 1992.

Table 5.2. Representative chemical analyses of basalt to benmoreite lava flows from Ascension Island. **Footnote for this table is on next page.

	High Zr/Nb			Low Zr/Nb		Intermediate Zr/Nb					Dark Slope Crater	
	Al-107 B	Al-37 B	Al-64 B	Al-60 H	Al-157 H	Al-100 B	Al-89 H	Al-30 H	Al-171 M	Al-176 Be	Al-2 H	Al-6 M
SiO_2	48.55	47.59	50.58	47.94	47.69	47.53	49.76	49.76	53.39	57.30	48.51	52.12
TiO_2	3.00	2.98	2.52	3.64	3.83	2.67	3.22	3.15	2.19	1.52	2.72	1.83
Al_2O_3	15.28	15.43	15.61	14.67	15.54	15.80	15.40	14.83	15.41	16.64	15.73	16.71
Fe_2O_3	13.48	13.43	11.98	13.37	13.84	12.78	12.83	12.65	10.79	8.31	12.88	10.44
MnO	0.16	0.18	0.17	0.21	0.20	0.17	0.22	0.22	0.24	0.23	0.18	0.18
MgO	5.33	5.55	5.23	4.90	3.88	6.65	4.47	4.15	3.27	2.30	5.20	3.43
CaO	9.46	9.74	8.56	9.12	8.32	10.35	8.15	8.17	7.44	4.85	8.13	6.15
Na_2O	3.34	3.42	3.61	3.72	3.96	2.81	3.48	4.08	4.31	5.55	3.92	5.20
K_2O	0.94	1.06	1.29	1.41	1.65	0.65	1.52	1.48	1.66	2.56	1.82	2.69
P_2O_5	0.46	0.62	0.45	1.02	1.09	0.59	0.95	1.51	1.30	0.74	0.91	1.25
H_2O-	0.42	0.31	0.31	0.41	0.70	0.33	0.18	0.68	1.16	0.17	0.72	0.53
LOI	0.18	-0.20	-0.40	0.54	0.61	-0.44	-0.86	0.44	0.46	0.13	0.18	0.28
Ni	39	48	34	12	13	97	14	10	8	5	52	31
Cr	28	54	27	2.6	1.8	156	6.9	1.9	2.0	2.0	52	12
Sc	33.5	28.1	28.9	27.9	28.8	30.0	24.0	19.2	20.6	13.7	21.7	13.1
V	304	248	201	294	287	248	218	176	83	44	221	90
Zn	93	101	87	132	140	92	122	128	147	139	131	154
Ga	26	24	26	24	24	23	26	25	27	28	25	30
Rb	18	19	28	27	32	11	30	27	32	56	41	66
Sr	436	551	414	551	533	385	502	507	479	431	782	1105
Ba	201	259	289	379	395	144	345	351	374	584	458	720
Th	2.33	2.94	3.69	4.06	4.67	1.70	4.13	4.36	4.58	6.56	5.44	8.93
Pb	<2	<2	<2	<2	2	<2	3	2	<2	2	3	<2
Zr	188	237	244	235	256	145	309	318	364	530	364	558
Hf	4.88	5.72	5.96	5.36	5.67	3.51	7.27	7.20	7.87	11.3	7.83	11.6
Nb	33	42	41	58	63	27	62	65	69	97	72	110
Ta	2.27	3.09	3.03	3.85	4.06	2.02	4.12	4.58	4.27	5.77	4.64	7.35
La	23.3	28.5	29.9	35.3	37.3	17.5	40.4	44.6	44.0	56.4	45.0	73.2
Ce	53.4	65.7	65.5	75.2	83.1	42.9	87.1	102	104	118	97.2	158
Nd	31.4	34.7	32.7	39.3	46.0	24.0	45.7	54.7	56.8	62.7	48.2	67.0
Sm	7.36	8.34	8.13	8.98	10.6	5.95	10.7	13.3	13.3	13.6	10.3	14.3
Eu	2.44	2.87	2.67	3.12	3.54	2.20	3.72	4.41	4.62	4.30	3.30	4.75
Tb	1.08	1.21	1.23	1.30	1.50	1.09	1.49	1.87	1.84	2.04	1.57	1.90
Yb	2.90	2.73	3.16	2.88	3.38	2.43	3.56	4.08	4.65	4.84	2.58	3.23
Lu	0.36	0.34	0.47	0.38	0.45	0.29	0.49	0.54	0.59	0.66	0.34	0.38
Y	40	40	41	40	47	31	49	58	64	63	37	46
P/Zr	10.7	11.4	8.0	18.9	18.6	17.8	13.4	20.7	15.6	6.1	10.9	9.8
Zr/Nb	5.7	5.6	6.0	4.1	4.1	5.4	5.0	4.9	5.3	5.5	5.1	5.1
Ba/Nb	6.1	6.2	7.0	6.5	6.3	5.3	5.6	5.4	5.4	6.0	6.4	6.5
Rb/Nb	0.55	0.45	0.68	0.47	0.51	0.41	0.48	0.42	0.46	0.58	0.57	0.60
K/Nb	236	210	261	202	217	200	204	189	200	219	210	203
Th/Nb	0.071	0.070	0.090	0.070	0.074	0.063	0.65	0.69	0.64	0.068	0.076	0.081
La/Nb	0.71	0.68	0.73	0.61	0.59	0.65	0.067	0.067	0.066	0.58	0.63	0.67
Zr/Y	4.7	5.9	6.0	5.9	5.4	4.7	6.3	5.5	5.7	8.4	9.8	12.1
Ce_N/Yb_N	4.7	6.1	5.3	6.6	6.3	4.5	6.2	6.4	5.7	6.2	9.6	12.4

Table 5.3. Comparison of P/Zr in the primordial mantle, Ascension Island volcanic rocks, and volcanic rocks from other oceanic islands.

		P/Zr	
		Average	**Range**
Primordial mantle		8.5	
N-MORB		7.5	6.6-9.1
Hawaii (Mauna Kea)		7.5	5.0-10.6
Ascension	High Zr/Nb	10.0	7.2-12.3
	Intermediate Zr/Nb	16.3	8.1-23.8
	Low Zr/Nb	18.2	16.8-19.0
	Dark Slope Crater	11.0	10.0-13.0
Saint Helena	Basalt	11.3	8.4-14.4
Tristan da Cunha	Basalt	9.8	7.9-11.8
	Basanite	12.3	9.1-16.5
Inaccessible	Basalt	11.7	8.4-13.7
Gough	Basalt	8.9	7.7-10.1

The primordial mantle P/Zr value is from McDonough and Sun (1995); data for N-MORB is for samples with Zr/Nb > 20 from DSDP Leg 82, Weaver et al. (1985); data for Mauna Kea, Hawaii, is from West et al. (1988) and Frey et al. (1990, 1991); data for St. Helena is from Weaver (unpublished); data for Tristan da Cunha is from Le Roex et al. (1990); data for Inaccessible Island is from Cliff et al. (1991); data for Gough Island is from Le Roex (1985).

**Table 5.2 Footnote:

B basalt; H hawaiite; M mugearite; Be benmoreite.
AI-107 flow in Grazing Valley; AI-37 flow on south flank of Devil's Riding School; AI-64 flow exposed in walls of Cricket Valley; AI-60 flow lobe from Cotar Hill; AI-157 flow in cliff section at South West Bay; AI-100 flow from Command Hill; AI-89 flow from breach in northeast flank of Sisters Complex; AI-30 flow east of South Gannet Hill; AI-171 flow adjacent to English Bay Road; AI-176 fissure flow on Letterbox; AI-2 bomb from northwest flank of Dark Slope Crater; AI-6 flow on southeast flank of Dark Slope Crater.
Major element oxides are recalculated to sum to 100% on an anhydrous basis. H_2O- is weight loss after drying for 12 hours at 110°C. LOI is weight loss after ignition at 950°C for 1 hour (oxidation of Fe^{2+} to Fe^{3+} in near-anhydrous samples results in weight gain, expressed as negative LOI). Trace elements are in parts per million; Ni, V, Zn, Ga, Rb, Sr, Ba, Pb, Zr, Nb, and Y determined by XRF, other trace elements determined by INAA.

CHAPTER VI

To be submitted to Geochimica et Cosmochimica Acta

Mafic clasts with unusual REE patterns in felsic volcanic rocks: evidence of subsolidus alteration of mafic rocks from Ascension island, South Atlantic Ocean

Kar, A.[1,2]
School of Geology and Geophysics
University of Oklahoma
Norman, OK 73019, USA

Weaver, B.
School of Geology and Geophysics
University of Oklahoma
Norman, OK 73019, USA

Davidson, J.
Department of Earth and Space Sciences
University of California Los Angeles
Los Angeles, CA 90095, USA

Colucci, M.
Department of Geology
Southern Methodist University
Dallas, TX 75275, USA

[1] Department of Mathematics and Physics
Fort Valley State University
Fort Valley, GA 31030, USA

[2] Corresponding Author
Telephone: (912) 825 6844
FAX: (912) 825 6618
email: kara@mail.fvsc.peachnet.edu

ABSTRACT

Mafic clasts are common in the felsic volcanic rocks of Ascension Island. The clasts are geochemically heterogeneous with compositions varying from basalt to hawaiite, mugearite, and benmoreite. The clasts are found in trachyte of both the central and eastern felsic complexes. These clasts have extremely high abundance and anomalous distributions of rare-earth elements (REE) and yttrium (Y), whereas other incompatible trace element concentrations and O, Sr, Nd, and Pb isotopic ratios do not differ from those of mafic (basalt to benmoreite) flows. REE and Y enrichment in the clasts with respect to the mafic flows is a post-magmatic alteration feature. This is supported by negative Ce anomalies in these mafic clasts, since decoupling of Ce from the other REE is restricted to oxidizing, low-temperature, aqueous environments. Similar Nd isotopic ratios between the clasts and the mafic flows preclude the possibility that additional REE and Y are derived from marine sediment or guano, but rather suggest an origin from mafic flows within the volcanic pile.

INTRODUCTION

Incompatible trace element abundance and patterns, particularly those of the rare earth elements (REE), have traditionally been used in igneous petrogenesis as indicators of processes relating to crystal fractionation, partial melting, and characteristics of mantle source regions of ocean island basalt (OIB) suites. However, unusual features of REE patterns, e.g. negative Ce anomalies, have been reported from basalt (island arc and OIB) and even from mantle peridotite (Neal & Taylor, 1989). Cotten et al. (1995) summarize the cause of such REE-enriched patterns as 1) source characteristics, e.g. contribution of subducted pelagic sediment, 2) peculiarities of the slab dehydration/mantle metasomatism processes involving percolation through the upper

mantle of unusual (H_2O + CO_2 + Cl) REE-bearing high temperature metasomatic fluids, and 3) regional scale low-temperature (<250°C) hydrothermal alteration. REE mobilization and precipitation processes are documented from laterite profiles and weathering profiles of basaltic sequences (petrographically fresh or nearly fresh), where they had lead to the development of Ce anomalies (Cotten et al., 1995). The purpose of this paper is to document the geochemical characteristics of the unusual REE and Y occurrences and to discuss the possible origin for such enrichment in mafic clasts from Ascension Island, South Atlantic Ocean.

GENERAL GEOLOGY OF ASCENSION ISLAND

The majority of Ascension Island, situated at 7°56'S and 14°22'W, is covered by mafic and felsic lava flows and pyroclastic deposits. Data for subsurface lava flows from seven boreholes (Neilson & Stiger, 1996), which penetrated the volcanic pile to a maximum depth of ~200 m below sea-level, indicate that high Zr/Nb mafic volcanism (Kar et al., 1995) occurred first on the island. There are two distinct felsic eruptive centers on the island, the central felsic complex and the eastern felsic complex. Age dates suggest that areal exposure of the central and the eastern parts of the island was built up over a period of half a million years, from 1 Ma to 0.56 Ma (Neilson & Sibbett, 1996; Kar et al., Felsic MS). Following the felsic volcanism, or shortly thereafter, mafic volcanism occurred in the following sequence - 1) high Zr/Nb basalt was erupted (now exposed at the surface together with older flows in the subsurface), 2) localized eruption of Dark Slope Crater type hawaiite and mugearite, 3) localized eruption of low Zr/Nb hawaiite, and 4) widespread eruption of intermediate Zr/Nb lava ranging in composition from basalt to benmoreite. Mafic clasts ranging in composition from basalt

to benmoreite occur in trachyte flows and domes of both the central and eastern felsic complexes.

Mafic clasts in felsic volcanic rocks

In the central felsic complex mafic clasts are found in the trachyte of Middleton Ridge and Devil's Riding School (Fig. 6.1). Middleton Ridge is composed primarily of trachyte, pumice, and some rhyolite and rhyolitic obsidian. The mafic clasts (three were collected) are mugearite and benmoreite in composition. Four more mafic clasts were collected from a trachyte flow on the east side of Devil's Riding School. These clasts had a pinkish tinge and are of basalt and hawaiite composition.

The eastern felsic complex is characterized by a voluminous trachyte flow that originated from Devil's Cauldron and flowed northward and eastward. Devil's Cauldron is interpreted to be an explosion crater with the trachyte dome of Weather Post adjacent (Fig. 6.1). A mafic clast, 50 × 30 cm was collected from the trachyte at Weather Post. This clast is extremely porphyritic and vesiculated, with large phenocrysts of plagioclase (2 to 3 cm) together with olivine and pyroxene phenocrysts. In the southeastern part of Ascension small trachyte bodies occur at Round Hill, Cocoanut Bay, Ragged Hill, and Pillar Bay (Fig. 6.1). Trachyte from Ragged Hill and Cocoanut Bay contains an unusually high modal abundance of alkali feldspar phenocrysts. Two mafic clasts sampled from the Ragged Hill trachyte have clast sizes of 20 × 40 cm and 30 × 70 cm. These clasts are vesiculated and porphyritic with clots of plagioclase phenocrysts. The mugearite clasts appear quite fresh compared to the host trachyte. From the Cocoanut Bay trachyte five more clasts collected have compositions ranging from hawaiite to mugearite. The clast size varied from 5 × 15 cm to 30 × 50 cm and the clasts showed evidence of crenulated margins. These clasts are

characterized by having spherical-to-oval vesicles with secondary minerals filling the vesicles. Also present were small phenocrysts of olivine, plagioclase, and pyroxene. The contact of the more massive clast (30 × 50 cm; AI-235c) shows evidence of quenching; the contact of the host trachyte with the clast is much finer grained as compared to elsewhere in the host trachyte body.

SAMPLING AND ANALYTICAL TECHNIQUES

For details on sampling techniques and analytical procedure for major and trace element analyses obtained at the University of Oklahoma refer to Weaver et al. (1996), for radiogenic isotope analysis performed at University of California, Los Angeles to Davidson et al. (1993), and for oxygen isotope analysis performed at Southern Methodist University to Borthwick & Harmon (1982).

PETROGRAPHY

Aphyric basalt clasts, massive to vesiculated from Devils Riding School trachyte have a mineral assemblage of plagioclase, olivine, clinopyroxene, and titano-magnetite, with different clasts showing moderate to well developed flow alignment of the plagioclase laths and sporadic occurrence of plagioclase (up to ~2 mm) ± olivine microphenocrysts.

The hawaiite clast from Devils Riding School is more fine grained as compared to the basalt clasts with plagioclase (sporadic microphenocrysts) dominating the mineralogy together with clinopyroxene, titano-magnetite, and olivine. However, vesiculated hawaiite clasts from Cocoanut Bay are coarser grained (comparable in size to Devils Riding School basalt clasts) and similar in mineralogy to the Devils Riding School hawaiite clast with plagioclase as the dominant mineral phase with additional olivine, titano-magnetite, and clinopyroxene but containing a significant amount of fine apatite needles.

Mugearite clasts from Cocoanut Bay trachyte are extremely similar petrographically to the hawaiite clasts from the same area; the mineralogy is mostly plagioclase together with titano-magnetite, clinopyroxene, and olivine. In contrast, the mugearite clast from Weather Post trachyte is much more fine grained however, containing a significant proportion of microphenocrysts of euhedral plagioclase, together with olivine, and clinopyroxene. A glomerocrystic assemblage of plagioclase, olivine, clinopyroxene, and titanomagnetite is also present. The groundmass is constituted mostly of plagioclase, clinopyroxene, titanomagnetite, and olivine. The Ragged Hill mugearite clasts are vesiculated, the groundmass minerals being coarser compared to the Weather Post clast. Randomly oriented plagioclase, clinopyroxene, olivine, and titanomagnetite form the groundmass and microphenocryst assemblage. Also present in the groundmass are very fine-grained apatite needles. In contrast, the fine-grained groundmass of the mugearite clast from Middleton Ridge has an appearance of "quenched" texture. It also contains microphenocrysts of euhedral plagioclase (3 to 5 mm) + clinopyroxene ± olivine ± titano-magnetite, with glomerocrysts of clinopyroxene and titano-magnetite.

The benmoreite clasts from Middleton Ridge have the same "quenched" groundmass as observed in the mugearite. They are vesiculated with large (up to ~5 mm) euhedral phenocrysts of plagioclase ± clinopyroxene (up to 2 mm).

WHOLE ROCK GEOCHEMISTRY

Major Element Geochemistry

Ascension Island lava flows and pyroclastic deposits are transitional to mildly alkaline and are a continuous fractionation series of basalt-hawaiite-mugearite-benmoreite, to the highly fractionated products of trachyte and rhyolite (Kar et al., Felsic MS). The major element variations from basalt to trachyte conform to those

expected from crystal fractionation of the observed phenocryst phases from a basalt parent magma. MgO, Fe_2O_3, CaO, and TiO_2 decrease with increasing SiO_2 over the entire compositional range as a consequence of olivine, clinopyroxene, feldspar, and titanomagnetite crystallization. Al_2O_3 and Na_2O increase with increasing SiO_2 from basalt to benmoreite, but then decrease with increasing SiO_2 in trachyte and rhyolite compositions with alkali feldspar crystallization setting in. P_2O_5 initially increases with increasing SiO_2, but then decreases with the onset of apatite crystallization. K_2O increases over entire range of SiO_2 composition. Most of the pumice samples have moderate to extreme depletion in Na_2O and, in general, a lower abundance of K_2O compared to the similarly differentiated lava flows and domes which is interpreted as an alteration effect (Weaver et al., 1996).

The mafic clasts in trachyte have the same compositional range (47.49 to 55.15 wt% SiO_2) from basalt to hawaiite, mugearite, and benmoreite with the majority of the clasts collected having a mugearitic composition (Table 6.1). The overall behavior of the major elements is similar to that described above but the absolute abundance is variable. Basalt clasts (Zr/Nb of 6.0 and 6.8) have in general, higher TiO_2, Fe_2O_3, MgO, P_2O_5, and $Na_2O + K_2O$ with respect to other high Zr/Nb surface or subsurface flows. Hawaiite-mugearite-benmoreite clasts (Zr/Nb of 4.3 to 5.1) have higher TiO_2, Fe_2O_3, P_2O_5, and much higher $Na_2O + K_2O$ with respect to intermediate Zr/Nb surface and subsurface flows.

Trace Element Geochemistry

Ascension Island mafic lava flows and pyroclastic deposits have been subdivided into four distinct genetically identifiable groups largely based on trace element and isotopic characteristics (Kar et al., 1996): 1) high Zr/Nb (5.6 to 6.1) basalt; 2) Dark Slope Crater type (Zr/Nb of 4.9 to 5.4) hawaiite; 3) low Zr/Nb (4.1) hawaiite; 4)

intermediate Zr/Nb (4.7 to 5.4) basalt - hawaiite - mugearite - benmoreite. Data for subsurface flows from the boreholes suggests that older Ascension mafic flows have higher Zr/Nb of up to 7.7 (Kar et al., 1995). The mafic clasts analyzed have the characteristics of high Zr/Nb basalt (Table 6.1) and intermediate Zr/Nb hawaiite - mugearite - benmoreite (Table 6.1).

Trace element abundances (except REE and Y) in the mafic clasts (high Zr/Nb basalt and intermediate Zr/Nb hawaiite; Table 6.1) are very similar to the surface and subsurface mafic flows; the clasts have similar Rb, Sr, Ba, Zr, and Nb contents. Y content is comparable in the basalt clast to the flows whereas in the hawaiite clasts Y contents are extremely variable (45 to 628 ppm) as compared to hawaiite flows (35 to 66 ppm Y). Trace element behavior is extremely anomalous in the intermediate Zr/Nb mugearite and benmoreite clasts. In the clasts of intermediate Zr/Nb mugearite and benmoreite composition Rb is low and Sr is high (Table 6.1) with respect to the flows; Ba is anomalously high (Table 6.1) as compared to the other mugearite and benmoreite flows and is more comparable to the host trachyte and rhyolite. For Ascension felsic rocks with an increase in SiO_2 there is a wide variation in large low-valence cations with Ba and Sr both decreasing as a result of plagioclase and alkali feldspar crystallization whereas Rb contents increase continuously with SiO_2 (Kar et al., Felsic MS). Weaver et al. (1996) observed that trachyte from Ragged Hill and Cocoanut Bay, host to the hawaiite and mugearite clasts, has high Ba and K_2O with respect to Zr compared to the rest of the Ascension suite and interpreted this as due to accumulation of alkali feldspar, as evidenced by the high phenocryst content. Large variation in trace element ratios (e.g. Zr/Nb and Zr/Y) in the felsic rocks as compared to the mafic volcanic rocks is also reported (Weaver et al., 1996). Rhyolite compositions have high SiO_2, Rb, Zr, and Y contents but in more evolved rhyolite compositions Zr/Nb and Zr/Y are lower than

in the trachyte flows, probably due to fractionation of a zirconium silicate accessory phase (Weaver et al., 1996). REE and Y behavior in the mafic clasts deserves special mention.

The Cocoanut Bay clasts have consistently low Zr/Nb ranging from 4.3 to 4.7 for the five clasts (Table 6.1). These clasts do not conform well to any surface intermediate Zr/Nb mafic flows.

The REE patterns of Ascension mafic and felsic flows have variable degrees of LREE enrichment with respect to HREE (Kar et al., Mafic & Felsic MS) although the LREE are uniformly strongly enriched compared to the HREE. The total REE abundance of the more evolved magmas increases with respect to the more mafic magmas with continuous crystal fractionation involving olivine, plagioclase, clinopyroxene, and titano-magnetite (Harris, 1983) but does not produce strong inter-element fractionation. The characteristic REE pattern of the basaltic rocks is maintained in the more evolved rocks although the absolute abundance has increased and substantial feldspar fractionation has produced a negative Eu anomaly (Kar et al., Felsic MS). Rhyolitic compositions have a higher total abundance of REE and a larger negative Eu anomaly compared to trachyte (Kar et al., Felsic MS).

The REE pattern for Middleton Ridge trachyte (AI-96) is slightly enriched as compared to the other volcanic rocks (Fig. 6.2). This trachyte is host to the benmoreite clasts (e.g., AI-97). The same general pattern is maintained in the REE pattern of the clast (except Ce, which is depleted relative to the other LREE) although the absolute abundance is ~5 times enriched (Fig. 6.2) with respect to the host trachyte. Total REE abundance is however, highly variable between the mafic clasts (Table 6.1).

Incompatible element behavior is variable as compared to other samples - 1) large-ion lithophile elements (LILE), e.g. Th, K, and Sr, behave similarly however, the clast

being slightly enriched in Rb but highly enriched in Ba (Fig. 6.2); 2) high field strength elements (HSFE), e.g. Nb, P, and Ti, behave similarly to Zr and Hf, being slightly depleted in the clast (Fig. 6.2).

Radiogenic and Stable Isotopes

Nd isotope data for the four Ascension Island mafic groups recognized from trace element data (Kar et al., Mafic MS) show that the high Zr/Nb group has $^{143}Nd/^{144}Nd$ of 0.512992 to 0.513066 whereas $^{143}Nd/^{144}Nd$ is lower in the low Zr/Nb group (0.512969 to 0.512972) and, particularly, the Dark Slope Crater group (0.512918 to 0.512974). The intermediate Zr/Nb group mostly has $^{143}Nd/^{144}Nd$ within the range of the high Zr/Nb group. Ascension mafic rocks have a general trend of slightly increasing $^{87}Sr/^{86}Sr$ with decreasing $^{143}Nd/^{144}Nd$ although the range in $^{87}Sr/^{86}Sr$ is not large; the Dark Slope Crater group has the highest $^{87}Sr/^{86}Sr$. Sr isotope compositions of the high and intermediate Zr/Nb groups largely overlap, and the low Zr/Nb group has $^{87}Sr/^{86}Sr$ at the upper end of the range of the high and intermediate Zr/Nb groups, with 0.702766 to 0.703263 and $^{143}Nd/^{144}Nd$ ranging from 0.512918 to 0.513066. Mafic clasts have radiogenic (Sr, Nd, and Pb) isotopic ratios within the range of the mafic flows analyzed from Ascension (Table 6.1). The geochemical characteristics of the felsic rocks are largely consistent with an origin by fractionation of high Zr/Nb mafic magmas as evidenced by similar trace element ratios and Nd and Pb isotopic ratios (Kar et al., Mafic MS).

There is a significant range in $\delta^{18}O$ in the mafic rocks. The low Zr/Nb group has $\delta^{18}O$ ranging from +6.5 to +7.1‰, the high Zr/Nb group has $\delta^{18}O$ from +5.7 to +7.8‰, the intermediate Zr/Nb group has $\delta^{18}O$ between +5.0 and +7.8‰, and the Dark Slope Crater group has $\delta^{18}O$ between +6.8 to +7.5‰ (Kar et al., Felsic MS). The one mafic

clast analyzed for $\delta^{18}O$ has a whole rock value (Table 6.1) within the range of the intermediate Zr/Nb group.

DISCUSSION

Enrichment in REE linked to incipient weathering of basalt flows from Hawaii (Fodor et al., 1987) and Australia (Price et al., 1991) is also characterized by negative Ce anomalies. The most likely explanation is that REE enrichment is associated with the percolation into fresh or almost fresh basalt flows of aqueous solutions enriched in REE, and possibly in other incompatible elements, that originate from the interaction of surface waters with upper portions of basaltic flows under tropical conditions (Cotten et al., 1995).

Cotten et al. (1995) show that addition of ~0.3 wt% REE-Y-phosphate (e.g., rhabdophane) to nearly fresh basalt results in the observed anomalies. Nd isotopic ratios reveal that the additional Nd, and presumably the other REE, is derived from a source isotopically similar to the local basalt flows, which excludes a seawater, marine sediment, or guano origin. The most likely source is thus the overlying basalt flows from which REE and Y were mobilized by interaction with meteoric waters.

Could the high REE in the mafic clasts from Ascension Island be due to interaction with the host trachyte magma? The possibility of inheriting the REE from the host trachyte is negligible as the REE enrichment is different in different clasts. The three mafic clasts from Middleton Ridge have highly variable REE abundance. Also, the REE enrichment in the mafic clasts is commonly much greater than in the host trachyte (Fig. 6.2).

Seawater derived geothermal fluids have been proposed as the cause of high $^{87}Sr/^{86}Sr$ (>0.706) in felsic rocks (trachyte and pumice) from Ascension Island under

subsolidus conditions (Kar et al., Felsic MS). High $^{87}Sr/^{86}Sr$ in pumice is also consistent with high $\delta^{18}O$ (> +10‰) in pumice samples. The effects of extreme hydration and alteration of pumice are reported by Weaver et al. (1996). Compared to an average of six trachyte flow samples with 66.0 to 68.8 wt% SiO_2, a highly hydrated pumice sample (e.g., Al-174) is severely depleted in Na_2O and K_2O, somewhat depleted in SiO_2 and Fe_2O_3, slightly to moderately enriched in TiO_2, Al_2O_3, CaO, and P_2O_5, and strongly enriched in MgO. TiO_2 and Al_2O_3 probably were immobile, their apparent increase being due to loss of other elements. The mafic clasts are enriched in total alkali content with respect to surface and subsurface mafic volcanic rocks indicating mobilization of Na_2O and K_2O.

There are also marked alteration effects on trace element abundance in the pumice samples, most notable being the strong enrichment in Sr (by a factor of five), Y, and the rare earth elements (but excluding Ce, with Eu being more enriched than the other REE), significant enrichment in Ba, U, and Cs, and significant depletion in Rb, Th, and Pb (Fig. 6.3). Elements such as Zr and Nb are immobile in hydrous fluids, and the apparent depletion in Nb relative to Zr (Fig. 6.3) likely is a consequence of igneous fractionation, there being a substantial range in Zr/Nb (4.6 to 9.4) in the trachyte and rhyolite flows (Weaver et al., 1996). Similar trace element behavior is found in the mafic clasts. Trace element abundances (except REE and Y) in the mafic clasts (high Zr/Nb basalt and intermediate Zr/Nb hawaiite; Table 6.1) are very similar to the surface and subsurface mafic flows; the clasts have similar Rb, Sr, Ba, Zr, and Nb contents. The Y content is comparable in the basalt clast to the flows whereas in the hawaiite clasts Y contents are extremely variable (45 to 628 ppm) as compared to hawaiite flows (35 to 66 ppm Y). Trace element behavior is extremely anomalous in the intermediate Zr/Nb mugearite and benmoreite clasts. In the intermediate Zr/Nb clasts of mugearite and

benmoreite composition Rb is low and Sr is high (Table 6.1) with respect to the flows; Ba is anomalously high (Table 6.1) as compared to the other mugearite and benmoreite flows and is more comparable to the host trachyte and rhyolite.

The REE pattern of the altered pumice sample is enriched relative to the unaltered trachyte (Fig. 6.3) and this enrichment is also reflected in incompatible element ratios (Fig. 6.3). The altered pumice generally have a negative Ce anomaly indicating post magmatic alteration. The mafic clasts have a similar enrichment and a Ce depletion (Fig. 6.2), but the total abundance of REE is much higher in the clasts with respect to the pumice. Enrichment in major element abundance, particularly total alkalis, in the clasts suggest mobilization of the alkali elements and certain incompatible elements such as Sr and Ba.

The radiogenic and stable (Sr, Nd, Pb, and O) isotopic ratios in the mafic clasts, however, are within the range of mafic flows (Table 6.1) whereas there are significant differences (enrichment) reported in the Sr and O isotopic ratios of pumice samples (Kar et al., Felsic MS). Could this mean then there is a decoupling in major and trace element abundance and isotopic ratios in the mafic clasts? No primary or secondary processes can produce such decoupling where major and trace element abundance is altered and isotopic ratios are undisturbed. The Ascension volcanic edifice hosts numerous faults and fractures (Neilson & Stiger, 1996). The geothermal fluids circulating within the volcanic edifice have been suggested to account for the high $^{87}Sr/^{86}Sr$ (>0.706) in felsic rocks (trachyte and pumice). The high but variable REE contents of the mafic clasts perhaps suggest that these geothermal fluids could have mobilized the REE and Y as phosphate complexes from mafic rocks. If geothermal fluids were the cause of increasing Sr and O in the trachyte, the mafic clasts would carry a similar signature and the if the geothermal fluids were carrying the REE and Y in

solution then the host trachyte would be enriched in these incompatible elements. None of these are observed in the mafic clasts or in the trachyte.

As suggested by Cotton et al. (1995) only a fraction of a weight percent of a REE-Y phosphate mineral such as rhabdophane can significantly enrich the REE and Y content of fresh basalt. Anomalously high REE and Y contents in subaerially exposed basalt flows from French Polynesia have been suggested as percolation into fresh or almost fresh basalt of aqueous solutions enriched in REE and possibly other incompatible elements and originate from the interaction of surface waters with the upper portions of basaltic flows under tropical conditions (Cotton et al., 1995). Enrichment in REE has been attributed to incipient alteration of basalt from Hawaii and Australia (Fodor et al., 1992; Price et al., 1991). In the case of Ascension alteration of pyroclastic deposits (pumice) by meteoric water is also perhaps responsible for enrichment of REE in the mafic clasts. These meteoric fluids could have altered the exposed pyroclastic deposits that cover majority of the island and felsic volcanic rocks and penetrated through the pyroclastic cover and faults and fractures and interacted with the mafic rocks under subsolidus conditions thus enriching the mafic rocks in REE and Y. The isotopic ratios of Sr and O were not significantly disturbed from a mass balance point of view. Later felsic volcanism brought these clasts to the surface as mafic xenoliths.

Mafic clasts have a general oblong shape and are uniformly smooth and rounded. The felsic volcanism that brought the clasts to the surface could not have mechanically abraded them in to such shapes. Hence the rocks the clasts were derived must have been abraded by mechanical weathering. Evidence of such weathering exist in a deep geothermal hole (Ascension #1) drilled to a depth of 3126 m that shows evidence of hydrothermal alteration of the volcanic rocks (Nielson & Stiger, 1996). The rocks

recovered from boreholes have evidence of being erupted subaerially, implying a subsidence of 200 m while surface eruption continued (Kar et al., 1995). Ascension #1 penetrated the hyaloclastite layers. The presence of hyaloclastite layers topped by subaerial basalt flows indicate that the island has undergone at least three phases of emergence and subsidence in the past. There has been 1.5 to 2 kilometers of subsidence since the onset of hyaloclastite formations (Nielson & Stiger, 1996). Two significant zones of fluid entry were reported from Ascension #1 well, the shallow entry zone (2500 m depth) being derivative of seawater and the deep (2957 m), a geothermal fluid derived from seawater (Adams, 1996). Hence the rock-water (meteoric) interaction occurred above 2500 m. Most probably upper parts of the mafic flows were subjected to the most mechanical weathering and interaction with meteoric water thus creating the oblong shapes of the mafic clasts and inheriting the unusual REE and Y abundance in the mafic rocks.

Felsic volcanic rocks on Ascension Island likely originated by fractionation of high Zr/Nb mafic magmas as evidenced by similar trace element and Nd and Pb isotopic ratios (Kar et al., Felsic MS). Incorporation of high Zr/Nb basalt clasts in the Devil's Riding School trachyte further substantiates this finding. However, intermediate Zr/Nb mafic (basalt to benmoreite) flows are proposed to be the youngest phase of volcanism on Ascension (Kar et al., Mafic MS). Mafic clasts of intermediate Zr/Nb composition, notably those occurring in the Middleton Ridge trachyte (0.82 Ma, Neilson & Sibbett, 1996) suggest intermediate Zr/Nb mafic volcanism to be substantially older than recognized before.

CONCLUSIONS

1) High Zr/Nb basalt clasts and intermediate Zr/Nb hawaiite-mugearite-benmoreite clasts occurring as xenoliths in the trachyte have anomalously high REE and Y abundance. The enrichment occurred under subsolidus conditions by interaction of mafic rocks with meteoric water circulating through the volcanic edifice.
2) This secondary enrichment of REE is supported by negative Ce anomaly in the clasts, since decoupling of Ce from the other REE is restricted to oxidizing, low-T aqueous environments.
3) The possibility of inheriting the REE from the host trachyte is not likely as the REE enrichment is different in different clasts. The three mafic clasts from Middleton Ridge have highly variable REE abundance. Also, the REE enrichment in the mafic clasts is commonly much greater than in the host trachyte. Similar Nd isotopic ratios between the clasts and the mafic flows conclude that additional REE and Y are not derived from marine sediments or guano, but rather suggest an origin from the mafic rocks.
4) Alteration of REE in pyroclastic deposits (pumice) by meteoric water is also perhaps responsible for enrichment of REE in the mafic clasts. These meteoric fluids could have altered the exposed pyroclastic deposits that cover the majority of the island and felsic volcanic rocks and penetrated through the pyroclastic cover via faults and fractures and interacted with the mafic rocks under subsolidus conditions thus enriching the mafic rocks in REE and Y. The isotopic ratios of Sr and O were not significantly disturbed from mass balance point of view. Later felsic volcanism brought these clasts to the surface as mafic xenoliths.
5) Mafic clasts have a general oblong shape and are uniformly smooth and rounded. The felsic volcanism that brought the clasts to the surface could not have

mechanically abraded them into such shapes. Hence the rocks the clasts were derived must have been abraded by mechanical weathering.

6) Rock-water (meteoric) interaction occurred above 2500 m based on the fact that two significant entry zones of fluid derived from seawater are reported from a deep borehole (Ascension #1). Most probably upper parts of the mafic flows were subjected to mechanical weathering and interaction with meteoric water thus creating the rounded shapes of the mafic clasts and inheriting the unusual REE and Y abundance in the mafic rocks.

7) Incorporation of high Zr/Nb basalt clasts in the Devil's Riding School trachyte further substantiates that felsic magmas are derived from crystal fractionation of high Zr/Nb mafic magmas. Mafic clasts of intermediate Zr/Nb composition, notably those occurring in the Middleton Ridge trachyte (0.82 Ma), suggest intermediate Zr/Nb mafic volcanism to be substantially older than previously recognized.

REFERENCES

Adams, M.C., 1996. Chemistry of fluids from Ascension #1, a deep geothermal well on Ascension Island, South Atlantic Ocean. Geothermics 25: 561-579.

Atkins, F.B., Baker, P.E. & Smith, D.G.W., 1964. Oxford expedition to Ascension Island. Nature 204: 722-724.

Borthwick, J., & Harmon, R.S., 1982. A note regarding ClF_3 as an alternative to BrF_5 for oxygen isotope analyses. Geochimica et Cosmochimica Acta 46: 1665-1668.

Cotten, J., Le Dez, A., Bau, M., Caroff, M., Maury, R.C., Dulski, P., Fourcade, S., Bohn, M., & Brousse, R., 1995. Origin of anomalous rare-earth element and yttrium enrichments in subaerially exposed basalts: Evidence from French Polynesia. Chemical Geology 119: 115-138.

Davidson, J.P., Boghossian, N.D., & Wilson, B.M., 1993. The Geochemistry of the Igneous Rock Suite of St. Martin, Northern Lesser Antilles. Journal of Petrology 34: 839-866.

Fodor, R.V., Bauer, G.R., Jacobs, R.S., & Bornhorst, T.J., 1987. Kahoolawe Island, Hawaii: tholeiitic, alkalic, and unusual hydrothermal (?) "enrichment" characteristics. J. Volcanol. Geotherm. Res. 31: 171-176.

Fodor, R.V., Frey, F.A., Bauer, G.R., & Clague, D.A., 1992. Ages, rare-earth element enrichment, and petrogenesis of tholeiitic and alkalic basalts from Kahoolawe Island, Hawaii. Contributions to Mineralogy and Petrology 110: 442-462.

Harris, C., 1983. The petrology of lavas and associated plutonic inclusions of Ascension Island. Journal of Petrology 24: 424-470.

Kar, A., Weaver., B., Davidson, J., & Colucci, M., 1996. Petrogenesis of mafic volcanic rocks from Ascension Island. American Geophysical Union Fall Meeting abstracts with programs.

Kar, A., Weaver., B., Davidson, J., & Colucci, M., (this volume). Small scale mantle heterogeneities: Evidence from transitional to mildly alkaline volcanic rocks from Ascension Island , South Atlantic Ocean. Journal of Petrology.

Kar, A., Weaver., B., Davidson, J., & Nielson, D., 1995. Geochemical characteristics of borehole samples recovered from Ascension Island, South Atlantic Ocean. Geological Society of America abstracts with programs 27, 6.

Kar, A., Weaver, B., Davidson, J., & Colucci, M., (Felsic MS). Felsic oceanic island magmatism: Origin of high $^{87}Sr/^{86}Sr$ evolved volcanic and plutonic rocks from Ascension Island, South Atlantic Ocean. Journal of Petrology (in review).

McDonough, W.F., & Sun, S., -S., 1995. The composition of the Earth. Chemical Geology 120: 223-253.

Nakamura, N., 1974. Determination of REE, Ba, Fe, Mg, Na and K in carbonaceous and ordinary chondrites. Geochimica et Cosmochimica Acta 38: 757-775.

Neal, C.R., & Taylor, L.A., 1989. A negative Ce anomaly in a peridotite xenolith: evidence for crustal recycling into the mantle or mantle metasomatism? Geochimica et Cosmochimica Acta 53: 1035-1040.

Nielson, D.L., & Sibbett, B.S., 1996. Geology of Ascension Island, South Atlantic Ocean. Geothermics 25: 427-448.

Nielson, D.L., & Stiger, S.G., 1996. Drilling and evaluation of Ascension #1, a geothermal exploration well on Ascension Island, South Atlantic Ocean. Geothermics 25: 543-560.

Price, R.C., Gray, C.M., Wilson, R.E., Frey, F.A., and Taylor, S.R., 1991. The effects of weathering on rare-earth element, Y and Ba abundances in Tertiary basalts from southeastern Australia. Chemical Geology 93: 245-265.

Weaver, B., Kar, A., Davidson., J., & Colucci, M., 1996. Geochemical characteristics of volcanic rocks from Ascension Island, South Atlantic Ocean. Geothermics 25: 449-470.

ACKNOWLEDGMENTS

This paper is a part of a Ph.D. dissertation by Aditya Kar. The project was funded through NSF grant EAR-9204079.

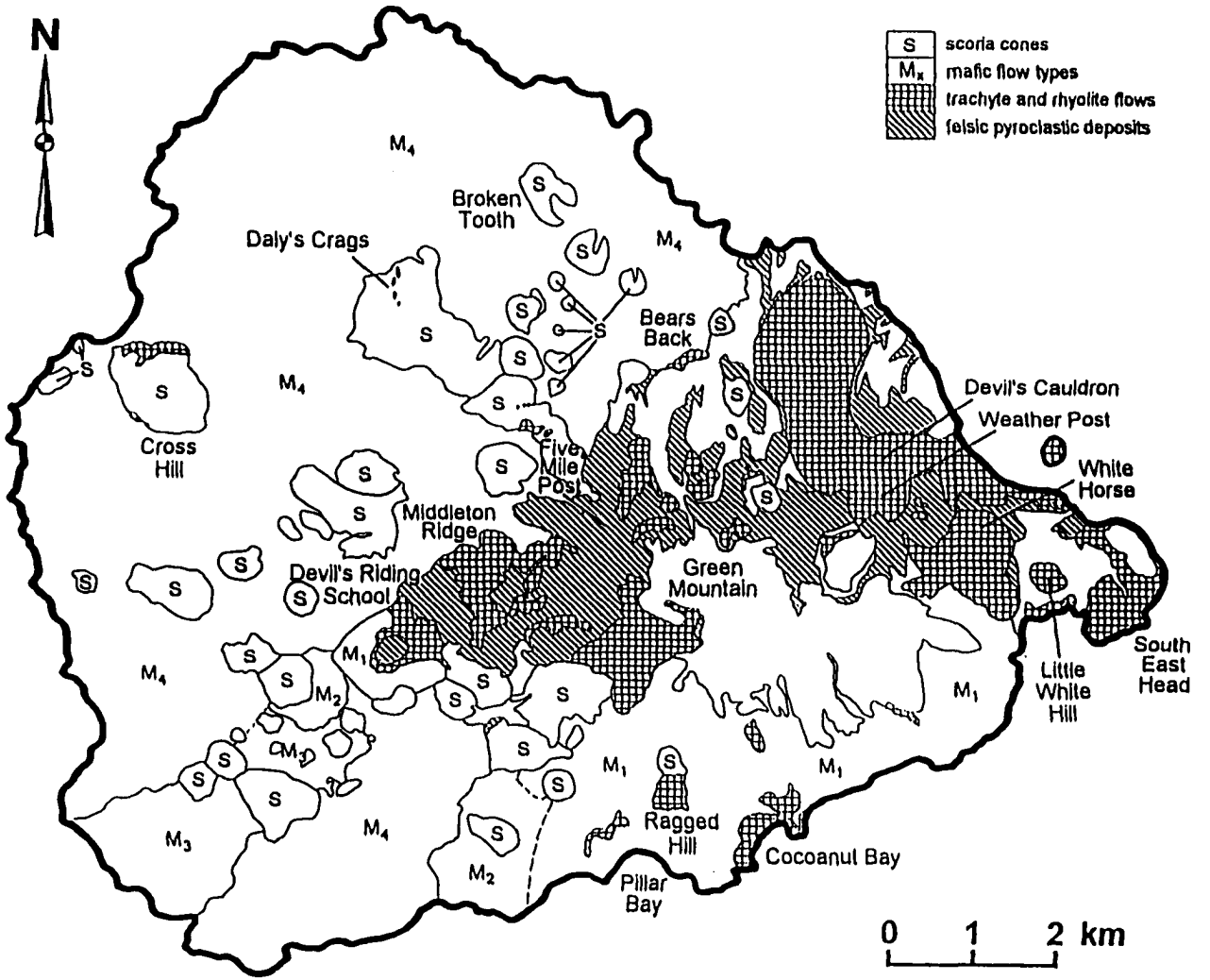

Figure 6.1. Simplified geological map of Ascension Island highlighting the distribution of felsic rocks.

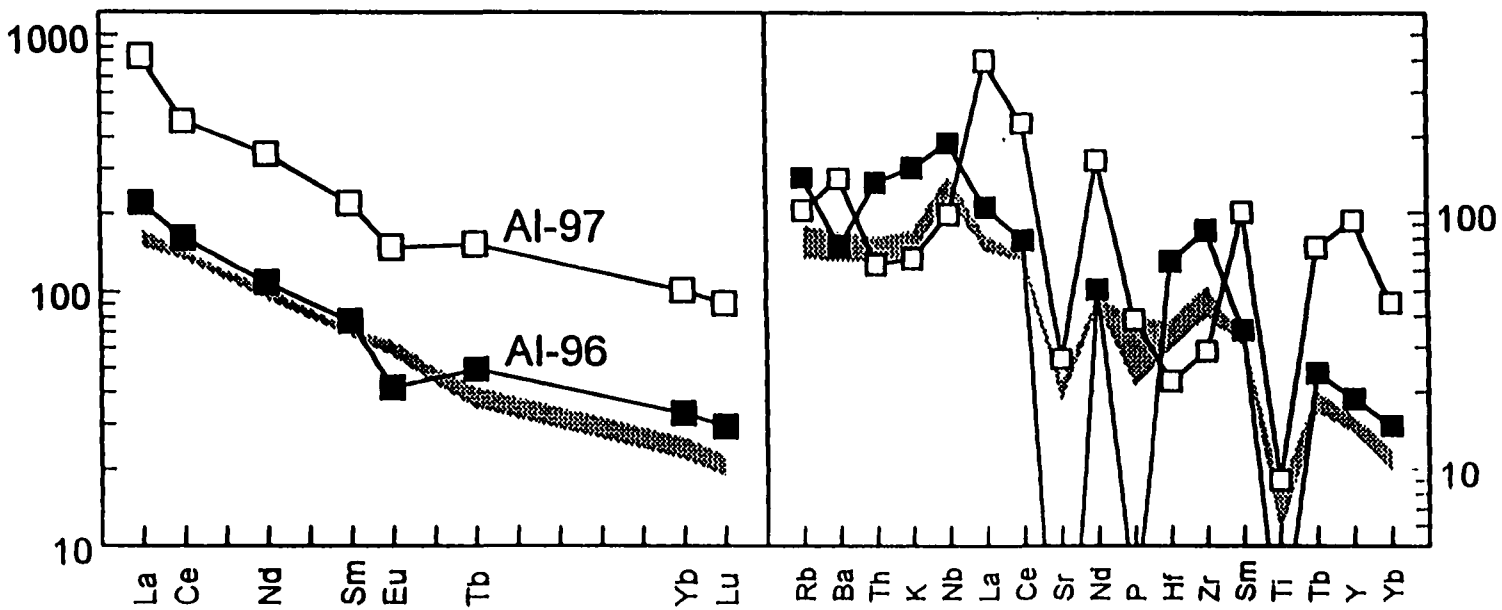

Figure 6.22. Rare earth element patterns (normalized to chondrite values of Nakamura, 1974) and incompatible element patterns (normalized to primordial mantle values of McDonough and Sun, 1995) for Middleton Ridge trachyte sample Al-96 and benmoreite clast Al-97.

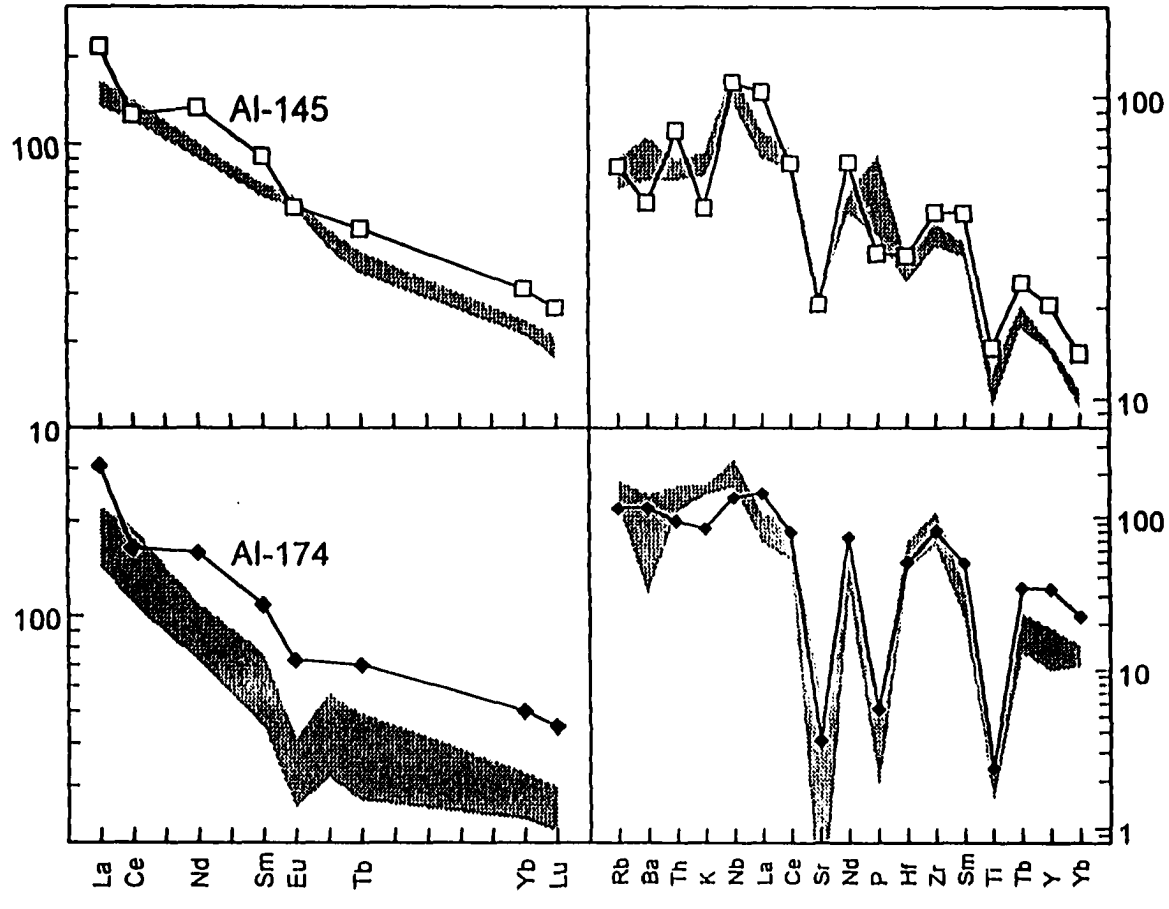

Figure 6.3. Rare earth element patterns (normalized to chondrite values of Nakamura, 1974) and incompatible element patterns (normalized to primordial mantle values of McDonough and Sun, 1995) of altered mugearite lapilli Al-145 and altered pumice Al-174.

Table 6.1. Representative chemical analyses of basalt to benmoreite clasts in trachyte from Ascension Island, South Atlantic Ocean.

	High Zr/Nb			Intermediate Zr/Nb							
	AI-224	AI-226	AI-227	AI-235c	AI-235a	AI-235e	AI-234a	AI-240	AI-250b	AI-250a	AI-97
	DRS B	DRS B	DRS H	CB H	CB M	CB M	RH M	WP M	MR M	MR Be	MR Be
SiO_2	47.57	47.49	49.19	49.12	54.57	49.89	51.40	54.45	54.22	54.96	55.15
TiO_2	3.86	2.91	3.60	3.55	2.28	2.98	2.36	1.94	1.94	1.93	1.96
Al_2O_3	13.97	15.78	17.21	15.78	16.09	15.14	16.47	17.03	17.59	17.84	17.89
Fe_2O_3	15.65	13.23	13.83	13.13	10.08	12.36	11.03	8.96	8.78	8.84	9.00
MnO	-	0.18	0.25	-	-	-	0.25	-	0.18	0.16	0.18
MgO	4.70	5.39	2.68	3.13	2.21	3.47	3.67	3.54	2.40	2.05	1.82
CaO	9.10	9.89	6.24	7.67	4.94	7.05	8.47	6.65	6.38	5.46	5.21
Na_2O	3.39	3.48	4.10	4.57	5.49	4.99	4.56	4.90	5.92	6.06	5.94
K_2O	0.94	1.05	1.77	1.91	2.76	2.39	1.29	2.02	1.77	1.84	2.01
P_2O_5	0.82	0.60	1.13	1.14	1.58	1.73	0.50	0.51	0.82	0.84	0.84
H_2O-	0.35	0.34	1.99	0.62	0.80	0.79	0.26	0.21	0.65	1.56	1.35
LOI	-0.39	-0.02	2.24	0.82	1.02	1.07	0.35	0.17	0.66	0.79	0.85
Ni	17	46	70	8	7	6	24	31	25	52	39
Sc	-	27*	24*	-	-	-	26*	-	19*	20*	19.7
V	-	248	223	-	-	-	204	-	103	90	87
Zn	227	186	523	99	119	220	107	148	403	665	497
Ga	28	25	27	25	25	25	25	26	26	28	27
Rb	18	22	36	33	39	39	19	40	40	34	65
Sr	440	552	406	552	498	536	405	411	598	586	565
Ba	-	275	354	-	-	-	1303	-	761	823	947
Th	3*	3*	3*	6*	6*	5*	2*	4*	6*	3*	5.38
Pb	<2	3	2	8	3	40	<2	6	2	3	<2
Zr	217	238	287	278	317	332	188	357	316	324	323
Hf	-	-	-	-	-	-	-	-	-	-	6.78
Nb	32	40	60	63	68	77	36	71	62	71	70
Ta	-	-	-	-	-	-	-	-	-	-	3.94
La	-	46*	857*	-	-	-	32*	-	100*	528*	273
Ce	-	79*	1207*	-	-	-	59*	-	113*	466*	400
Nd	-	56*	635*	-	-	-	32*	-	96*	404*	216
Sm	-	-	-	-	-	-	-	-	-	-	44.5
Eu	-	-	-	-	-	-	-	-	-	-	11.4
Tb	-	-	-	-	-	-	-	-	-	-	7.92
Yb	-	-	-	-	-	-	-	-	-	-	22.1
Lu	-	-	-	-	-	-	-	-	-	-	3.06
Y	70	64	628	48	67	61	36	221	187	648	422
Zr/Nb	6.8	6.0	4.8	4.4	4.7	4.3	5.2	5.0	5.1	4.6	4.6
Ba/Nb	-	6.9	5.9	-	-	-	36.2	-	12.3	11.6	13.5
Rb/Nb	0.56	0.55	0.60	0.52	0.57	0.51	0.53	0.56	0.65	0.48	0.93
K/Nb	244	218	245	252	337	258	297	236	237	215	238
La/Nb	-	1.15	14.3	-	-	-	0.89	-	1.61	7.44	4.20
P/Zr	16.5	11.0	17.2	17.9	21.8	22.7	11.6	6.2	11.3	11.3	11.3
Zr/Y	3.1	3.7	0.5	5.8	4.7	5.4	5.2	1.6	1.7	0.5	0.8
$^{87}Sr/^{86}Sr$	-	-	-	-	-	-	-	-	-	-	0.702983

Table 6.1 continued

	High Zr/Nb			Intermediate Zr/Nb							
	Al-224	Al-226	Al-227	Al-235c	Al-235a	Al-235e	Al-234a	Al-240	Al-250b	Al-250a	Al-97
	DRS	DRS	DRS	CB	CB	CB	RH	WP	MR	MR	MR
	B	B	H	H	M	M	M	M	M	Be	Be
$^{143}Nd/^{144}Nd$	-	-	-	-	-	-	-	-	-	-	0.512987
$^{206}Pb/^{204}Pb$	-	-	-	-	-	-	-	-	-	-	19.624
$^{207}Pb/^{204}Pb$	-	-	-	-	-	-	-	-	-	-	15.622
$^{208}Pb/^{204}Pb$	-	-	-	-	-	-	-	-	-	-	39.209
$\delta^{18}O$	-	-	-	-	-	-	-	-	-	-	6.85

B basalt; H hawaiite; M mugearite; Be benmoreite.
Sample Location: DRS = Devil's Riding School; CB = Cocoanut Bay; RH = Ragged Hill; WP = Weather Post; MR = Middleton Ridge.

Major element oxides are recalculated to sum to 100% on an anhydrous basis. H_2O- is weight loss after drying for 12 hours at 110°C. LOI is weight loss after ignition at 950°C for 1 hour (oxidation of Fe^{2+} to Fe^{3+} in near-anhydrous samples results in weight gain, expressed as negative LOI). Trace elements are in parts per million; Ni, V, Zn, Ga, Rb, Sr, Ba, Pb, Zr, Nb, and Y determined by XRF, other trace elements determined by INAA, or by XRF if indicated by *.

CHAPTER VII

CONCLUSIONS

1) The felsic (>60% SiO_2) rocks from the central and eastern parts of Ascension island are the oldest; a rhyolite dated at 0.99±0.02 Ma (Nielson & Sibbett, 1996) from the central part of the island representing the evidence of first phase of felsic volcanism. Felsic volcanism continued until at least 0.56±0.06 Ma with build up of the central and eastern parts of the island and was closely followed by the eruption of high Zr/Nb basalt lavas.

2) The geochemical characteristics of the felsic rocks are largely consistent with an origin by fractionation of high Zr/Nb magmas as evidenced by similar trace element ratios and Nd and Pb isotopic ratios.

3) Trace element and isotopic compositions indicate that syenite, monzonite, and granite xenoliths found on Ascension are cumulates from felsic magmas that also produced the felsic volcanic rocks. Internal Rb-Sr isochrons for two granite xenoliths yield ages of 0.92 and 1.22 Ma, respectively.

4) $\delta^{18}O$ in felsic rocks are slightly higher compared to the high Zr/Nb parent magmas which is a result of fractionation combined with some open system interaction with fluids.

5) Fluids recovered from a deep geothermal well drilled on Ascension show the presence of seawater-derived geothermal fluids with Sr content as high as 202 ppm; interaction of these fluids with felsic rocks may generate high $^{87}Sr/^{86}Sr$ under subsolidus conditions as evidenced by leaching experiments and recorded in many of the whole rock samples.

6) In addition, the involvement of a high $^{87}Sr/^{86}Sr$ component during magmatic differentiation is evidenced by high initial $^{87}Sr/^{86}Sr$ from the internal isochrons of the two granite xenoliths which have high initial $^{87}Sr/^{86}Sr$ (> 0.705); $^{143}Nd/^{144}Nd$ and $\delta^{18}O$ in the granite are similar to the mafic extrusive rocks. Some feldspar phenocrysts from

the felsic volcanic rocks also have high $^{87}Sr/^{86}Sr$ (> 0.704); $\delta^{18}O$ ranges of +5.5 to +8.1‰ (whole rock) and +5.5 to +7.2‰ (feldspar) in the felsic rocks also indicate the involvement of a high $\delta^{18}O$ component, and suggest that hydrothermally altered pre-existing volcanic basement may have been cannibalized during differentiation of the felsic magmas.

7) Based on trace element characteristics, four distinct groups of mafic rocks are identified on Ascension Island: a low Zr/Nb hawaiite group, a high Zr/Nb basalt group, an intermediate Zr/Nb basalt to benmoreite group, and, a subset of the intermediate Zr/Nb group, the Dark Slope Crater hawaiite and mugearite group.

8) Crystal fractionation controls the chemical variation within each group, but cannot account for the chemical differences between the groups.

9) There are significant differences in the Sr, Nd, and Pb isotopic compositions of some of the groups. Lava flows from Dark Slope Crater have the lowest $^{143}Nd/^{144}Nd$ and the highest $^{87}Sr/^{86}Sr$ and $^{206}Pb/^{204}Pb$. The low Zr/Nb group has similar $^{143}Nd/^{144}Nd$ to the Dark Slope Crater group, but lower $^{87}Sr/^{86}Sr$ and $^{206}Pb/^{204}Pb$. The high Zr/Nb and intermediate Zr/Nb groups have generally similar Sr-Nd-Pb systematics, with higher $^{143}Nd/^{144}Nd$ and lower $^{87}Sr/^{86}Sr$ and $^{206}Pb/^{204}Pb$ than the Dark Slope Crater and low Zr/Nb groups. These relationships can be explained by mixing between three mantle components, one depleted component and two distinct enriched components.

10). The similarity of Sr, Nd, and Pb isotopic compositions between the younger intermediate Zr/Nb group and the older high Zr/Nb group, and the presence in the subsurface of flows with higher Zr/Nb but similar $^{143}Nd/^{144}Nd$, implies that the degree of partial melting of the same overall mantle source has decreased over time.

11) In $^{208}Pb/^{204}Pb$ - $^{206}Pb/^{204}Pb$ space the Ascension volcanic rocks are displaced to the right of the NHRL and define two mixing trends, one to a HIMU component with the

composition of the St. Helena HIMU source, the other also a HIMU component but with higher $^{208}Pb/^{204}Pb$ relative to $^{206}Pb/^{204}Pb$ than the St. Helena source.

12) The St. Helena HIMU component represents the composition of the hotspot which has mixed with the depleted upper mantle to varying degrees to produce the magmas of the high Zr/Nb, intermediate Zr/Nb, and low Zr/Nb groups. The second HIMU component is only represented in the volumetrically minor Dark Slope Crater group, and this may represent a local enriched lithospheric source.

APPENDIX 1

X-RAY FLUORESCENCE (XRF) ANALYSIS

XRF is a quantitative analytical technique for the determination of element concentrations in a wide variety of sample types. It is a precise and sensitive technique with detection limits of down to the part per million (ppm) concentration level; it is also a fairly rapid technique with simple sample preparation and is non-destructive. Major and trace elements were analyzed using a Rigaku SMAX 3080 XRF spectrometer at the University of Oklahoma.

Preparation of samples for Major and Trace Element Analysis

1) Wherever possible, fresh, unaltered samples were taken from the field. Rocks were intially broken down into small chips in the field, and weathered, fractured surfaces, and any vesicle fillings were removed. In the case of scoriaceous lava flows with small vesicles it was not always possible to ensure that the vesicle filling or lining was removed. Cinders and blocks from the scoria cones are almost invariably oxidized, although fresh scoria was sampled wherever possible.

2) Scoria samples were ultrasonically cleaned and washed in distilled water prior to breaking them down further.

3) A jaw-crusher was used to break down the rock chips collected from the field and between crushing different samples the jaws of the crusher was thoroughly cleaned with alcohol.

4) Finally, the fine rock chips were made into powders for chemical analysis using an agate shatterbox. Again, extreme care was taken to clean the shatterbox. First all mafic samples were made into powder followed by all felsic samples. Also between

successive sample preparation the shatterbox was cleaned thoroughly, first with tap water and air-dried, and then with alcohol before preparing the next sample to prevent any contamination between the samples.

5) Major Element: Rock powders were first dried overnight at 110°C and the water loss (H_2O-) was determined. The dried powder was then ignited in an oven for an one (1) hour at 950°C and weighed again to determine the weight loss (or gain) on ignition (LOI). The dried, ignited powders were mixed with a lanthanum-doped lithium tetraborate/lithium carbonate flux (Spectroflux 105) with a rock to flux in the ratio of 1:5. The mixture was mixed thoroughly in a Pt crucible and then melted over a gas flame. Once melted it was quickly casted into a glass fusion bead.

6) Trace Element: 4.5 g of bulk rock powder was weighed and pressed lightly into a disc. On this disc boric acid powder was poured and then subjected to 5 (?) pressure for about one minute. The boric acid powder solidifies under pressure and a powder pellet is thus prepared for analysis.

Principles of X-Ray Fluorescence

An x-ray source is used to bombard the sample and produce fluorescence of the elements in the sample; the secondary x-ray beam from the sample is a mixture of scattered primary tube x-rays plus characteristic K and L series lines emitted by elements within the sample.

The polychromatic secondary x-ray spectrum can be dispersed into its component wavelegths using a diffracting crystal, and the intensity of individual characteristic x-ray lines measured by a detector.

Calibration of analyte characteristic x-ray line intensity against analyte concentration for standards of know chemical composition allows quantification of element abundance in unknown samples. Also, to ensure maximum sensitivity and lowest detection limit in the determination of a particular analyte, maximum signal strength (e.g., characteristic x-ray line intensity) is obtained by selecting the appropriate combination of machine components.

Analytical Procedure

The major elements analyzed included SiO_2, TiO_2, Al_2O_3, Fe_2O_3, MnO, MgO, CaO, Na_2O, K_2O, and P_2O_5 and the trace elements analyzed were Ba, Ce, Co, Cr, Cu, La, Mn, Nb, Ni, Pb, Rb, Sc, Sr, Th, V, Y, Zn, and Zr.

Choice of x-ray tube:

A Rh anode x-ray tube produces good excitation for most elements to be analyzed (K series tube lines excite good fluorescence of trace elements with analytical lines in the range 0.65 to 1.7Å; the trace elements analyzed were Cu, Nb, Ni, Pb, Rb, Sr, Th, Y, Zn, and Zr. L series tube lines excite good fluorescence of major elements).

In conjuction to Rh tube, a W anode x-ray tube produces enhanced excitation of elements of interest which are not well excited by the Rh tube. L series tube lines produce good excitation of trace elements with analytical lines in the range of 1.8 to 3.1Å and included the elements Ba, Ce, Cr, La, Mn, Nd, Sc, and V.

Tube Conditions:

Rh anode x-ray tube:

40 kV, 65 mA for major element analysis (Table 1)

60 kV, 40 mA for trace element analysis (Table 2)

W anode x-ray tube:

60 kV, 45 mA for trace element analysis (Table 3)

Choice of analyte line:

Kα, the most intense line is used. However, L series line (preferably Lα) is used even with a loss of sensitivity and precision due to machine conditions, K series lines becoming increasing close together. So, L series lines are used for analysis of elements with Z > 50, e.g., Ba, LREE, Pb, Th, U, with a Rh tube.

Choice of crystal-collimator combination:

For peaks with no nearby lines of other elements a combination (e.g., LiF(200) + coarse collimator) is used where resolution is not required to give the maximum intensity.

For peaks with nearby lines of other elements a combination (e.g., LiF(220) + fine collimator) is used which gives improved resolution to avoid potential interferences but accepting a loss of intensity.

For peaks with unresovable line overlap a combination (e.g., LiF(200) + coarse collimator) is used which does not produce high resolution, thereby stabilizing the line overlap correction that is applied. Overlap corrections applied for Sr Kβ on Zr Kα and Rb Kβ on Y Kα; correction factors are determined from spiked samples. Corrections are also applied for spectral contamination of Pb, Zn, Cu, and Ni.

Choice of detector:

Flow detector s used for low atomic number elements (Z=11 to 25), and the scintillation detector for moderate to high atomic number elements (Z > 25).

Pulse Height Analysis:

Pulse height analysis windows are chosen carefully for each analyte line, so as to include all counts arising from x-ray photons of the analyte but to exclude counts due to n>1 diffraction from the crystal and crystal fluorescence.

Matrix effects:

Matrix effects which are very significant in XRF analysis was accounted for by dilution and fusion of the sample in a flux as described in sample preparation method. Small residual matrix effects were removed by application of alpha coefficient corrections. Ideally, the major element oxides should sum to 100% by this technique, and reported major element analyses (Tables in the text and Appendix IV) have been normalized to 100%; original totals were in the range of 99-101%. For trace elements determined using the Rh anode x-ray tube, mass absorption corrections were applied internally using the intensity of the Rh Kα Compton scatter peak (Harvey and Atkin, 1982). For trace elements determined by the W anode x-ray tube, matrix corrections were applied using mass absorption coefficients calculated from the major element composition.

Calibrations and standard:

Major and trace element calibrations were constructed using a wide range of international standards, and instrumental drift was monitored by use of an internal standard.

Table 1: Rh Tube Major Element Conditions

Analytical conditions:

Rh anode tube operated at 40 kV, 65 mA.

		Crystal	Det	Slit	PHA	Peak	Backgrounds		Time
Si	**Kα**	PET(001)	F	C	10-30	109.10	106.25	-	40
Ti	**Kα**	LIF(200)	F	F	10-30	86.18	-	89.00	40
Al	**Kα**	PET(001)	F	C	10-30	144.95	143.40	-	40
Fe	**Kα**	LIF(200)	F	F	10-30	57.55	56.30	-	20
Mg	**Kα**	TAP(001)	F	F	10-30	45.24	43.15	47.20	100
Ca	**Kα**	PET(001)	F	F	10-30	45.13	44.00	-	40
Na	**Kα**	TAP(001)	F	F	10-30	55.22	53.40	57.80	100
K	**Kα**	PET(001)	F	F	10-30	50.62	49.20	-	40
P	**Kα**	Ge(111)	F	F	10-30	140.95	132.00	143.90	100

Table 2: Rh Tube Trace Element Conditions

Analytical conditions:

Rh anode tube operated at 60 kV, 45 mA.

		Crystal	Det	Slit	PHA	Peak	Background		Time
Rh	K Co	LIF(200)	S	F	7-35	18.44	-	-	20
Ni	Kα	LIF(220)	F	C	7-30	71.28	70.10	72.80	100
Co	Kα	LIF(220)	F	F	7-30	77.85	77.25	78.60	100
Cu	Kα	LIF(220)	F	C	7-30	65.55	62.75	68.50	100
Zn	Kα	LIF(200)	S	F	7-35	41.78	41.20	42.60	100
Ga	Kα	LIF(200)	F	F	7-30	39.95	38.35	39.60	100
Rb	Kα	LIF(200)	S	F	7-35	26.60	25.75	27.00	100
Sr	Kα	LIF(200)	S	F	7-35	25.13	24.50	25.75	100
Th	$L\alpha_1$	LIF(200)	S	F	7-35	27.46	27.00	28.60	200
Pb	$L\beta_1$	LIF(200)	S	F	7-35	28.25	27.00	28.60	200
U	$L\alpha_1$	LIF(200)	S	F	7-35	26.14	25.75	27.00	200
Zr	Kα*	LIF(200)	S	F	7-35	22.54	21.73	23.10	100
Nb	Kα	LIF(200)	S	F	7-35	21.38	20.98	21.73	200
Y	Kα*	LIF(200)	S	F	7-35	23.75	23.10	24.50	100

*Overlap corrections applied for Sr Kβ on Zr Kα; Rb Kβ on Y Kα. Correction factors determined from spiked samples.
Rh Kα Compton peak used as an internal standard for all analytes.
Corrections applied for spectral contamination of Pb, Zn, Cu, and Ni.

Table 3: W Tube Trace Element Conditions

Analytical conditions:

W anode tube operated at 60 kV, 45 mA.

		Crystal	Det	Slit	PHA	Peak	Background		Time
W	**$L\beta_1$**	LIF(200)	S	C	10-35	37.15	-	37.45	40
Fe	**Kβ**	LIF(220)	F	F	7-25	76.18	74.20	-	20
Ca	**Kβ**	LIF(200)	F	F	7-30	100.25	96.25	-	40
Ti	**Kα**	LIF(200)	F	F	7-30	86.21	84.50	88.50	40
Mn	**Kα**	LIF(200)	F	F	7-30	63.03	61.95	64.70	40
Cr	**Kα***	LIF(200)	F	C	7-30	69.40	67.00	71.00	100
V	**Kα***	LIF(220)	F	F	7-30	123.18	121.25	126.00	100
Sc	**Kα***	LIF(200)	F	F	7-30	97.78	96.25	-	100
Ba	**$L\alpha_1$***	LIF(200)	F	F	7-30	87.22	84.50	88.50	200
La	**$L\alpha_1$***	LIF(200)	F	C	7-30	83.02	82.05	84.00	200
Ce	**$L\beta_1$**	LIF(220)	F	F	7-30	111.65	110.75	113.75	200
Nd	**$L\alpha_1$**	LIF(220)	F	F	7-30	112.70	110.75	113.75	200

*Overlap corrections applied for Ti Kβ on V Kα; V Kβ on Cr Kα; Ti Kα on Ba Lα; Ti Kα on La Lα; Ca Kβ on Sc Kα. Correction factors determined from spiked samples.
Correction applied for spectral contamination of Cr.

Table 4: Lower Limit of Detection for XRF Trace Elements

Rh tube elements

Elcement	*Standard*	*2σ LLD (ppm)*
Ni	AGV-1	1.6
Cu	AGV-1	1.6
Zn	SY-2	1.7
Rb	SY-2	1.0
Sr	SY-2	1.0
Zr	SY-2	0.8
Nb	SY-2	0.5
Y	SY-2	0.7
Pb	SY-2	1.5
Th	SY-2	1.6
U	NIM-G	1.3
Ga	DR-N	1.3
Co	DR-N	3.3

W tube elements

Element	*Standard*	*2σ LLD (ppm)*
Cr	BHVO-1	0.9
V	JB-2	1.6
Sc	BHVO-1	1.4
Ba	GS-N	2.5
La	AGV-1	1.9
Ce	AGV-1	3.2
Nd	AGV-1	2.7

INSTRUMENTATION NEUTRON ACTIVATION ANALYSIS (INAA)

Principles of INAA (Potts, 1987)

Samples 'activated' by irradiation with neutrons (usually in a nuclear reactor), makes specific isotopes become radioactive by neutron capture-type nuclear reactions. After removal from the reactor, samples are allowed to decay ('cool') to permit unwanted short-lived activity to diminish. Gamma-ray spectra from activated samples are then measured using solid-state germanium gamma-ray detectors, usually over the energy range 60 to 1600 KeV. Specific isotopes may be identified by their gamma-rays of characteristic energy and quantitative determinations are made by comparing the areas of these photopeaks with those in the spectrum of a standard sample, irradiated and counted under identical conditions.

INAA involves the irradiation and analysis of rock powders that undergo no chemical treatment in the course of the analysis and hence is a non-destructive procedure. The technique is used predominantly for the analysis of specific trace elements down to detection limits in the ppm to ppb range, and is especially sensitive for the rare-earth elements (La, Ce, Nd, Sm, Eu, Tb, Yb, and Lu), Sc, Co, Cr, Cs, Hf, Ta, Th, U, and some other elements.

Sample Preparation

0.25 g of rock powder sealed in polyethylene vials in three (3) sets of groups of eight (8) were irradiated at Georgia Institute of Technology. Out of these twenty-four powders, each set contained two internal standards, NIM-G (granite) and JB-1a (basalt). Approximately one week after irradiation the samples were sent to University

of Oklahoma where counting was done on low energy photon spectrometer (LEPS) detector and coaxial detector and data reduction were performed.

INAA

The gamma rays emitted during the decay of radionuclides in an activated sample are detected by an analyzing crystal (high-purity Ge), assigned an arbitrary energy according to the size of the pulse produced in the detector, and stored in the appropriate channel of a multichannel buffer (MCB). A gamma ray spectrum for a sample is acquired over a period of time in the MCB, but for permanent storage and data analysis the spectrum is saved in the computer memory. Each sample was counted for three (3) hours on a LEPS detector for determination of ^{153}Sm and ^{147}Nd and on a coaxial detector for determination of ^{140}La and ^{177}Lu. Approximately one month after irradiation the samples were counted for 12 hours per sample on both the LEPS and coaxial detectors for determination of ^{141}Ce, ^{152}Eu, ^{160}Tb, ^{169}Yb, $^{233}Pa(Th)$, ^{182}Ta, ^{181}Hf, ^{46}Sc, ^{60}Co, and ^{51}Cr.

Table 1: Data for commonly analyzed radionuclides produced by (n, γ) thermal neutron capture reactions in INAA

Stable nuclide	Isotopic abundance	Cross section	Radio-nuclide	Half-life		Gamma-ray peak (keV)	LLD (ppm)	Prec-ision
^{139}La	99.91	9.0	^{140}La	40.28	h	1596.49	0.5	2.6
^{140}Ce	88.48	0.57	^{141}Ce	32.5	d	145.44	2.1	3.1
^{146}Nd	17.18	1.3	^{147}Nd	10.99	d	91.11	4.6	3.5
^{152}Sm	26.74	206	^{153}Sm	46.7	h	103.18	0.1	2.1
^{151}Eu	47.82	5900	^{152}Eu	13.4	y	121.78	0.05	3.9
^{152}Gd	0.20	1100	^{153}Gd	241.6	d	97.43 103.18	4.6 3.9	11.0
^{159}Tb	100	25.5	^{160}Tb	72.4	d	86.79	0.09	3.9
^{169}Tm	100	103	^{170}Tm	128.6	d	84.25	0.34	5.9
^{168}Yb	0.135	3470	^{169}Yb	32.02	d	63.12	0.14	3.1
^{176}Lu	2.59	1740	^{177}Lu	6.71	d	112.95 208.36	0.14 0.07	1.7
^{180}Hf	35.2	12.6	^{181}Hf	42.39	d	133.02 482.16	0.22 0.17	3.0
^{181}Ta	99.998	21	^{182}Ta	114.5	d	67.75	0.07	4.7
^{232}Th	100	7.4	^{233}Pa	27.0	d	94.67 98.44 311.90	0.9 0.5 0.22	4.3
^{238}U	99.275	2.7	^{239}Np	2.35	d	106.13 228.18 277.60	0.5 1.0 1.9	26.5

Isotopic abundance in percent; **thermal neutron capture cross section** in barns; **half-life** of radionuclide in hours (*h*), days (*d*), or years (*y*); **energy** of analysed gamma-ray photopeak in KeV; **2σ lower limit of detection (LLD)** in ppm; **typical precision** expressed as the coefficient of variation in percent (100 × σ/x).

RADIOGENIC ISOTOPE ANALYSIS

Radiogenic Isotope data was generated at the University of California, Los Angeles using a multicollector VG Sector mass spectrometer.

Sample Preparation:

For isotopic analyses, approximately 30 mg of rock powder was dissolved in an HF-HNO_3 mixture in sealed teflon beakers for more than 6 hours on a hot plate. Sr and REE were separated by standard cation exchange techniques, and Nd subsequently separated from the other REE using HDEP-coated teflon resin. Pb was separated from a separate dissolution using 600 ml anion exchange columns. Total process blanks were approximately 300, 100, and 1000 pg for Sr, Nd, and Pb respectively.

Analytical Procedure (Davidson, Boghossian, & Wilson, 1993):

Sr was run with TaO_2 and phosphoric acid on single Re filaments using a dynamic routine on the multicollector mass spectrometer. $^{87}Sr/^{86}Sr$ ratios were normalized to $^{86}Sr/^{88}Sr = 0.1194$. NBS 987 over the period of analysis was measured as 0.710220 ±10. Pb was run on single Re filaments with silica gel and phosphoric acid, on the same instrument. Mass fractionation was monitored by including at least one (1) NBS 981 standard in each turret of ten (10) samples, and corrected for by normalizing to accepted values of NBS 981. Nd was loaded in dilute HNO_3 on one side of a separable triple Re filament assembly, and run in dynamic mode on the VG Sector 54-30 mass spectrometer at UCLA. $^{143}Nd/^{144}Nd$ ratios were normalized to $^{146}Nd/^{144}Nd = 0.7219$. Analyses of the La Jolla standard gave a value of 0.511851 ± 12.

STABLE ISOTOPE ANALYSIS

Oxygen isotope measurements were made on a Finnegan MAT 251 gas source mass spectrometer at the stable isotope laboratory of Southern Methodist University.

Analytical Procedure (Borthwick & Harmon, 1982):

In normal day-to-day operation, sample size is varied randomly between 2 to 25 mg and reacted with approximately a 7:1 molar excess of reagent. Reactions are carried out for 14 to 16 hours at 600°C for quartz or 650°C for most other minerals and whole-rock powders. At these high temperatures there is some reaction of the nickel tube walls resulting in a normal reaction vessel life of 180 to 200 runs per tube (wall thickness = 0.22 cm). Blank levels are < 1 μmole O_2 per tube and thus no blank corrections are used.

The six tubes in each run set have the gaseous waste of previous reaction removed via a Kbr trap at 80°C and a liquid nitrogen storage trap. The reaction vessels are then heated at 650°C and 10^{-5} Torr for one hour. This eliminates the

APPENDIX 2

Ascension Island samples and locations

Grid references are from the 1:25,000 Ascension Island topographic map, series G 892, edition 4-GSGS, 1992

Al-		Grid ref	Location
1	basalt bomb	667203	Command Hill [C32], north side
2	hawaiite bomb	670200	Dark Slope Crater [C33], northwest flank
3	gabbro xenolith	671198	Dark Slope Crater [C33], southwest rim
4	hawaiite flow	672198	Dark Slope Crater [C33], flow on southeast rim
5	gabbro xenolith	673199	Dark Slope Crater [C33], southeast rim
6	mugearite flow	672198	Dark Slope Crater [C33], southeast flank
7	gabbro xenolith	673199	Dark Slope Crater [C33], southeast rim
8	gabbro xenolith	673199	ditto
9	gabbro xenolith	673199	ditto
10	gabbro xenolith	673199	ditto
11	gabbro xenolith	673199	ditto
12	basalt lapilli	655211	base of west side of South West Bay Red Hill [C31]
13	mugearite flow	655211	base of west side of South West Bay Red Hill [C31]; below Al-12
14	basalt lapilli	655211	base of west side of South West Bay Red Hill [C31]; lapilli from cone
15	trachyte pumice block	714212	weakly welded ash-flow tuff, near Red Lion, Green Mountain
16	lithic (trachyte?) block	714212	weakly welded ash-flow tuff, near Red Lion, Green Mountain
17	trachyte	716218	near Monkey Rock
18	trachyte pumice block	714215	Green Mountain Road
19	benmoreite pumice block	712214	Green Mountain Road
20	trachyte pumice block	709217	Green Mountain Road
21	trachyte pumice block	709217	Green Mountain Road
22	vitrophyre	?	Middleton Ridge
23	trachyte	?	Middleton Ridge
24	hawaiite flow	676238	Sisters, young flow, flow surface east of Al-25
25	hawaiite flow	674238	Sisters, young flow, flow front, One Boat Golf course
26	basalt lapilli	669188	South Gannet Hill [C44] ; base of north flank
27	basalt bomb	673185	ditto ; top of hill
28	basalt flow	674180	~600 m southeast of South Gannet Hill [C44]; flow from breach
29	basalt flow	677181	~800 m east-southeast of South Gannet Hill; older flow than Al-28
30	hawaiite flow	681183	side of runway, west of Sandy Run; older flow than Al-29
31	hawaiite flow	678197	~ 600 m east-southeast of Dark Slope Crater
32	gabbro xenolith	673199	Dark Slope Crater [C33]; southeast rim
33	gabbro xenolith	673199	ditto
34	gabbro xenolith	673199	ditto
35	gabbro xenolith	673199	ditto
36	basalt flow	684206	Devil's Riding School, north side
37	basalt flow	681200	Devil's Riding School, south side of rim
38	hawaiite scoria block	684197	Cone 40, partial scoria cone, south side of Devil's Riding School
39	trachyte pumice	684199	Devil's Riding School, south side; underlying basalt
40	basalt flow	685201	Devil's Riding School, southeast side
41	trachyte flow	687202	Devil's Riding School, east side; overlying Al-40
42	rhyolite pumice	684204	Devil's Riding School, north side of centre ; layer 1 of 6
43	trachyte pumice	684204	ditto ; layer 3 of 6
44	trachyte pumice	684204	ditto ; layer 5 of 6
45	basalt lapilli	683202	Devil's Riding School, south side of centre
46	hawaiite bomb	681219	Lady Hill [C26], top of
47	benmoreite flow	676217	~500 m west-southwest of Lady Hill
48	benmoreite flow	674216	Donkey Plain, ~800 m west-southwest of Lady Hill
49	mugearite flow	674209	Table Crater [C29]
50	mugearite flow	670209	~300 m west-southwest of Table Crater
51	mugearite flow	668211	~500 m west-northwest of Table Crater
52	benmoreite scoria block	645236	Fort Hayes [C23]
53	hawaiite flow	647236	Georgetown, between Forts Hayes and Thornton
54	benmoreite flow (local)	647240	Fort Thornton [C22]; flow from cone
55	mugearite	657239	~700 m north-northwest of Cross Hill
56	hawaiite flow	661249	~400 m north-northeast of Benin City
57	benmoreite flow	659256	Comfortless Cove
58	hawaiite flow	662247	~300 m north-northeast of Benin City ; older than Al-56
59	trachyte	662248	ditto ; underlying Al-58
60	hawaiite flow (local)	657187	~300 m southwest of Cotar Hill [C43]; flow from Cotar Hill
61	hawaiite flow	661183	~400 m south of Cotar Hill; older than Al-60
62	basalt flow	661171	near Mars Bay; South Gannet Hill flow
63	basalt & beach sand		South West Bay; *TS/probe only*

64	basalt flow	735214	Cricket Valley, west side
65	basalt flow	735214	ditto ; above Al-64
66	trachyte	740225	Devil's Cauldron, west rim
67	trachyte	744219	Weather Post, south side
68	block and ash flow	756221	southeast of Powers Peak; *TS sample only*
69	benmoreite flow	769213	Letterbox; small trachyte inclusions *TS sample only*
70	trachyte	765217	northwest of Letterbox
71	benmoreite flow	763218	gully northwest of Letterbox; Devil's Ink Pot flow
72	hawaiite flow	715239	Bears Back, south side
73	benmoreite scoria block	713248	Cone 3, northwest side of Bears Back
74	hawaiite flow	711249	~300 m southeast of Hollow Tooth
75	hawaiite flow	704253	~500 m south of Broken Tooth; flow from Sisters
76	benmoreite flow	704256	Broken Tooth [C1]; flow from breach; older than Al-75
77	benmoreite scoria block	703255	Broken Tooth [C1], south flank
78	mugearite flow	737249	~500 m southeast of North East Point, near Ariane site
79	trachyte	720239	Bears Back, gully at southeast side; underlying basalt
80	mugearite flow	720237	~1.1 km southeast of Bears Back; older than Al-72 and Al-79
81	hawaiite flow (local)	704240	~200 m north of Street Crater; flow from Street Crater [C9]
82	hawaiite flow	702240	~300 m northwest of Street Crater; flow from Sisters
83	trachyte	701233	~1 km southeast Sisters Peak
84	mugearite flow	686271	~200 m north of BBC Station
85	mugearite flow	680272	flow front at southwest end of English Bay
86	mugearite flow	712265	~1.2 km northeast of Broken Tooth; flow from Broken Tooth
87	mugearite flow (local)	705262	~400 m north-northeast of Broken Tooth; flow from Broken Tooth
88	mugearite bomb	709266	~1 km northeast Broken Tooth; from Broken Tooth
89	hawaiite flow	706269	~1 km north-northeast of Broken Tooth; flow from Sisters
90	mugearite lapilli	685248	Daly's Crags; lapilli from Sisters complex mantling the Crags (Al-91)
91	trachyte	685248	Daly's Crags
92	benmoreite flow	684255	flow front on English Bay Road, ~800 m north-northwest of Daly's Crags
93	rhyolite obsidian	692215	Middleton Ridge ; west base
94	rhyolite (flow banded)	693213	ditto ; overlying and associated with obsidian Al-93
95	rhyolite (massive)	696212	ditto ; overlying Al-94
96	trachyte	701212	ditto ; above Al-95
97	benmoreite inclusion	701212	ditto ; inclusion from Al-96
98	trachyte pumice	703211	ditto ; ~3 m air-fall unit above Al-96,-97
99	trachyte	712210	cliff face east of Middleton Ridge (flow 20-30 m thick)
100	basalt flow	665204	~400 m northwest of Command Hill [C32]; flow from this cone
101	mugearite flow	665205	~500 m northwest of Command Hill; flow underlying Al-100
102	basalt flow	658206	~400 m south of South West Bay Red Hill, near RC Grotto, Command Hill flow
103	trachyte	706202	~500 m north-northeast of Mountain Red Hill
104	trachyte	708201	~500 m northeast of Mountain Red Hill
105	trachyte	712199	~700 m east-northeast of Mountain Red Hill
106	basalt flow	710195	~700 m east-southeast of Mountain Red Hill
107	basalt flow (local)	700203	Grazing Valley, ~600 m northwest of Mountain Red Hill
108	hawaiite dyke	691198	unnamed cone [C47] southwest of Spoon Crater
109	trachyte	718187	Ragged Hill dome
110	basalt flow	722182	~600 m southeast of Ragged Hill
111	trachyte	726178	Cocoanut Bay, west end
112	mugearite flow	725178	ditto
113	mugearite lapilli	746234	north-northeast of Devil's Cauldron
114	trachyte pumice	746232	ditto
115	trachyte vitrophyre	746230	ditto ; block in pyroclastic unit
116	trachyte	745229	ditto ; overlying Al-115
117	basalt flow (local)	745240	~900 m south-southeast of Hummock Point; flow from breached Cone 21
118	basalt flow (local)	744243	~500 m south-southeast of Hummock Point; flow from breached Cone 20
119	trachyte	742247	Hummock Point
120	trachyte pumice	738248	~500 m west of Hummock Point ; basal part of 1.1 m graded pyroclastic unit
121	trachyte pumice	738248	ditto ; middle part of graded unit
122	mugearite lapilli	738248	ditto ; top part of graded unit
123	basalt lapilli	738248	ditto ; 25 cm layer above -120 to -122 sequence
124	basalt flow	743195	~900 m northwest of Round Hill
125	basalt flow	745195	~900 m northwest of Round Hill; underlies Al-124
126	trachyte	745196	~800 m northwest of Round Hill; underlies Al-124,-125
127	basalt flow	751196	~400 m north of Round Hill
128	basalt flow	759204	south of Sharp Cliff
129	trachyte	751226	gully to Spire Beach
130	benmoreite flow	751230	cliff section at north end of Spire Beach
131	rhyolite	761222	cliffs directly opposite Boatswain Bird Island

132	basalt flow	764222	ditto ; beneath Al-131
133	trachyte xenoliths (9)	710216	Green Mountain Road ; 1700-1800 feet (133a to i)
134	basalt lapilli	709219	ditto ; ~1300 feet
135	trachyte pumice	708220	ditto ; ~1200 feet; unit directly below Al-134
136	hawaiite flow	722252	flow front at northwest end of North East Bay
137	benmoreite flow	720255	~600 m northwest of North East Bay; from Cone 3
138	basalt flow	659231	Cross Hill [C24], southeastern flank
139	basalt lapilli	674221	Lady Hill [C26], west side of base
140	benmoreite flow	668229	One Boat, opposite petrol station
141	basalt lapilli	654236	Cross Hill [C24], northwest flank
142	mugearite flow	652230	~600 m west-southwest of Cross Hill, close to The Needles
143	mugearite lapilli	695205	NASA Road, ~500 m northwest of Spoon Crater
144	trachyte pumice	695205	ditto ; above Al-143
145	mugearite lapilli	695205	ditto ; above Al-144
146	trachyte pumice	695205	ditto ; above Al-145
147	rhyolite block	740209	Cricket Valley, southern part of rim
148	basalt lapilli	738205	Devils Ashpit
149	basalt flow	702188	~300 m north-west of Green Top Crater
150	hawaiite flow	648191	South West Bay, southern end ; lowermost flow in cliff sequence
151	hawaiite flow	648191	ditto ; above Al-150
152	hawaiite flow	648191	ditto ; above Al-151
153	hawaiite flow	652194	South West Bay, main cliffs ; lowermost flow in cliff sequence
154	hawaiite flow	652194	ditto ; above Al-153
155	hawaiite flow	652194	ditto ; above Al-154
156	hawaiite flow	652194	ditto ; above Al-155
157	hawaiite flow	652194	ditto ; above Al-156
158	basalt flow	648197	Drunk's Hideaway, South West Bay; Command Hill flow, younger than 153-157
159a	hawaiite flow	685236	~900 m west-southwest of Sisters Peak ; young Sisters flow
159b	basalt flow	685236	ditto ; uplifted flow under Sisters flow
160	basalt flow	689235	~500 m southwest of Sisters Peak; uplifted flow
161	hawaiite flow (local)	692233	~600 m south of Sisters Peak; small, young Sisters flow
162	basalt flow	716179	Pillar Bay, east side
163	trachyte	718185	Ragged Hill dome
164	trachyte	716185	ditto
165	mugearite flow	715189	~400 m northwest of Ragged Hill
166	mugearite flow	649221	~1 km north of US Base
167	basalt flow	682229	Old Mountain Road, ~1.4 km east of junction at One Boat
168	benmoreite flow	688263	English Bay Road, ~700 m south-southeast of BBC Station
169	trachyte	734247	North East Bay
170	basalt lapilli	725243	Lower Valley Crater [C17]; overlying pumice Al-181
171	mugearite flow	686258	English Bay Road
172	basalt lapilli	716212	Elliot's Path, directly east of the Red Lion
173	basalt lapilli	711213	Green Mountain Road ; roadcut at ~1850 feet
174	trachyte pumice	711213	ditto ; layer above Al-173 in same roadcut
175	trachyte	752217	White Horse, west side
176	benmoreite flow	770212	Letterbox
177	rhyolite (banded)	763211	Little White Hill, southern side
178	mugearite flow	685214	~700 m southeast of Lady Hill, by New Mountain Road
179	basalt flow	692226	~500 m west of Travellers Hill; flow from Travellers Hill [C16]
180	basalt lapilli	695226	Travellers Hill [C16], northeastern flank
181	trachyte pumice	725243	Lower Valley Crater, underlying mafic lapilli Al-170
182	hawaiite flow	706234	North East Bay Road; flow from Butt Crater [C10]
183	hawaiite flow	674246	English Bay Road, ~300 m south of Pyramid Point Road junction
184	benmoreite flow	645211	~300 m west of Cat Hill; flow from Cat Hill [C30]
185	mugearite lapilli	647212	Cat Hill [C30], north side
186	benmoreite scoria block	708250	Hollow Tooth [C2], southwest side
186a	benmoreite bomb	708250	ditto
187	syenite inclusions (5)	705256	Broken Tooth [C1] benmoreite flow (Al-76); (187a to e)
188	hawaiite flow	705249	immediately north of Cone 5, possibly from breach
189	hawaiite lapilli	705247	Cone 5, north flank
190	trachyte	654231	~600 m west of Cross Hill
191	mugearite lapilli	662232	Cross Hill [C24], east flank
192	mugearite flow	663263	~900 m northeast of Pyramid Point; from flow front(?)
193	mugearite flow	662262	~700 m northeast of Pyramid Point; older flow than Al-192(?)
194	mugearite flow	688249	flow from breached crater (Cone 4) northeast of Daly's Crags
195	basalt lapilli	661189	Cotar Hill [C43], north flank
196	basalt lapilli	662190	Round Hill [C42], west flank
197	basalt lapilli	661186	Cotar Hill [C43], south flank
198	basalt lapilli	653234	Cross Hill [C24], west flank
199	benmoreite flow	648225	Gallows Hill

200	basalt flow	661208	South West Bay Red Hill [C31], southeast flank; slaggy flow on flank
201	basalt lapilli	658208	ditto , south flank
202	hawaiite flow	667198	~500 m southwest of Dark Slope Crater [C33]
203	hawaiite flow	669198	Dark Slope Crater [C33], southwest flank
204	hawaiite flow	669198	ditto ; flow below Al-203
205	hawaiite flow	670199	ditto ; flow above Al-204,-203
206	gabbro xenolith	670199	ditto
207	hawaiite scoria bomb	674190	Cone 37, east flank
208	hawaiite lapilli	677192	Cone 38, west flank
209	hawaiite lapilli	678195	Cone 39, west flank
210	hawaiite lapilli	679186	Booby Hill [C45], west flank
211	hawaiite flow	679192	Cone 38, from breach on east side
212	hawaiite flow	671192	Horse Shoe Crater [C34], from breach on southeast side
213	granite xenoliths (7)	710218	Five Mile Post, Green Mountain Road (213a to g)
214	hawaiite lapilli	703235	Butt Crater [C10], west flank
215	basalt block/bomb	701244	Sisters Red Hill [C7], northeast flank
216	benmoreite flow	714262	~500 m south of Porpoise Point
217	benmoreite bomb	706256	Broken Tooth [C1], in benmoreite flow Al-76
218	hawaiite flow	718257	~1 km northwest of North East Bay
219	mugearite flow	664269	~900 m southwest of North West Point
220	mugearite flow	666270	~700 m southwest of North West Point
221	mugearite flow	690248	~400 m east of Daly's Crags; older flow from Sisters(?)
222	mugearite flow	681255	English Bay Road, ~900 m northwest of Daly's Crags
223	mugearite flow	671274	North West Point
224	mafic inclusion	687204	Devil's Riding School; inclusion in trachyte
225	syenite inclusion	687202	ditto
226	mafic inclusion	686203	ditto
227	mafic inclusion	686202	ditto
228	trachyte	687202	Devil's Riding School, east side; flow below Al-41
229	trachyte pumice	692198	west flank of Spoon Crater ; 5 cm layer
230	basalt lapilli	692198	ditto ; 20 cm layer above Al-229
231	hawaiite lapilli	692198	ditto ; 2 m layer above Al-230
232	hawaiite scoria block	704187	Green Top Crater [C51]
233	basalt massive block	704191	Mountain Red Hill [C48], south flank
234	mafic inclusions (2)	718187	Ragged Hill trachyte (234a,b)
235	mafic inclusions (5)	726179	Cocoanut Bay trachyte (235a to e)
236	hawaiite massive block	718190	South East Crater [C52]
237	basalt lapilli	718191	gully northeast of South East Crater ; ~1m lapilli layer
238	benmoreite pumice	718191	ditto ; ~10 cm layer under Al-237
239	hawaiite flow	743218	Weather Post, south side ; small flow in explosion crater
240	mafic inclusion	743218	ditto ; inclusion in trachyte
241	trachyte	742218	ditto ; air-fall block in pyroclastics
242	trachyte	741219	Weather Post, southeast side
243	trachyte	740219	ditto ; carapace of dome
244	mugearite flow	740218	Cricket Valley; north rim
245	benmoreite flow	740218	ditto ; overlies Al-244
246	basalt flow	740218	ditto ; overlies Al-245
247	hawaiite flow	741224	Devil's Cauldron, south wall; driblet flow within crater
248	rhyolite vitrophyre	741224	ditto ; block in flow Al-248
249	xenoliths (12)	705211	Middleton Ridge; assorted xenoliths, gabbro to granite (249a to l)
250	mafic inclusions (2)	701212	Middleton Ridge trachyte flow (250a,b)
251	hawaiite flow	693269	~600 m east of BBC Station; flow front
252	hawaiite flow	692269	~500 m east of BBC Station; flow under Al-251
253	hawaiite flow	671235	English Bay Road, ~300 m north of One Boat Golf Club
254	mugearite flow	726236	Upper Valley Crater [C18] ; flow from breach in north side
255	mugearite flow	726236	ditto ; blocks within Al-254 flow
256	trachyte pumice	725237	~300 m northwest of Upper Valley Crater; air-fall block
257	hawaiite flow	728245	~400 m northeast of Lower Valley Crater, side of North East Bay Road
258	hawaiite flow	651184	near Met. Station; Cotar Hill flow
259	basalt flow	651186	near Met. Station; Command Hill flow from flow front on Al-258
260	benmoreite dyke	698209	ridge south of Middleton Ridge
261	rhyolite obsidian	698209	ditto ; in trachyte hosting dyke Al-260
262	granite xenolith	698209	ditto ; in trachyte hosting dyke Al-260
263	hawaiite flow	697179	South Red Crater [C50]; flow from breached southern side
264	mugearite flow	698183	~100 m north of South Red Crater; flow wrapping around crater
265	hawaiite flow	765220	northwest of Letterbox, cliff sequence
266	hawaiite flow	765220	ditto ; flow above Al-265
267	mugearite dyke	767218	northwest of Letterbox; cutting pyroclastics and flow sequence (-265,266)
268	trachyte	768218	South East Head, northeast side
269	hawaiite block	693238	Sisters Peak [C13], top
270	hawaiite lapilli	693238	ditto

271	hawaiite flow	697220	~400 m south of Travellers Hill; flow from southeast breach of Cone 16
272	benmoreite scoria block	672218	Cone 27, ~900 m west-scuthwest of Lady Hill
273	hawaiite scoria block	667213	Cone 28, ~800 m northeast of SW Bay Red Hill ; wall of breach to SE
274	basalt scoria block	665213	ditto ; wall of breach to SW
275	mugearite flow	669214	~200 m northeast of Cone 28
276	mugearite flow	670216	~400 m northeast of Cone 28; younger flow than AI-275
277	hawaiite flow	697230	Two Boats Village, north end
278	hawaiite flow	697230	ditto ; flow above AI-277
279	hawaiite scoria block	704242	Cone 8, ~600 m northeast of Perfect Crater
280	hawaiite flow	706241	~300 m northeast of Street Crater
281	hawaiite block	706245	Cone 6, ~900 m northeast of Perfect Crater
282	trachyte	722241	Bears Back, gully east of
283	hawaiite flow	722241	Bears Back, gully east of; flow immediately overlying AI-282
284	hawaiite scoria block	696235	ridge of older cone [C14] ~500 m southeast of Sisters Peak
285	hawaiite block	698239	Perfect Crater [C11], west rim
286	hawaiite flow	700236	~300 m south-southeast of Perfect Crater
287	mugearite lapilli	683196	Cone 40, south of Devil's Riding School
288	hawaiite flow	684194	~800 m south of Devil's Riding School
289	hawaiite flow	694196	~300 m southwest of Spoon Crater
290	hawaiite flow	694195	~400 m south-southwest of Spoon Crater
291	mugearite lapilli	703228	Thistle Hill [C15], northwest flank
292	hawaiite lapilli	700231	road cut North East Bay Road, ~800 m south of Perfect Crater
293	rhyolite pumice	696193	cliff in gully ~600 m south of Spoon Crater
294	trachyte block	696193	ditto ; blocks in pumice unit AI-293
295	hawaiite flow	697195	~800 m west-southwest of Mountain Red Hill
296	mugearite scoria block	699192	~800 m southwest of Mountain Red Hill; northwest rim of old Cone 49
297	hawaiite flow	689174	~1 km southwest of South Red Crater
298	mugearite flow	690175	~0.9 km southwest of South Red Crater; older flow than AI-297
299	hawaiite flow	687179	~0.4 km southeast of end of runway

Borehole samples

GH1 Location: McTurk's Culvert and RAF Base, grid reference 688217.
Top of hole 171.6 m above sea level, depth of hole 177.7 m.

GH1-1	hawaiite flow (intermediate Zr/Nb)	27.3 m depth in hole, +144.3 m relative to sea level
GH1-2	basalt flow (intermediate Zr/Nb)	33.7 m depth in hole, +137.9 m relative to sea level
GH1-3	basalt flow (high Zr/Nb)	166.0 m depth in hole, +5.6 m relative to sea level
GH1-4	basalt flow (high Zr/Nb)	176.0 m depth in hole, -4.4 m relative to sea level
GH1-5	basalt flow (high Zr/Nb)	177.2 m depth in hole, -5.6 m relative to sea level

GH2 Location: East rim of Cricket Valley, grid reference 743213.
Top of hole 478.5 m above sea level, depth of hole 533.4 m.

GH2-1	basalt flow (high Zr/Nb)	97.9 m depth in hole, +380.6 m relative to sea level
GH2-2	basalt flow (high Zr/Nb)	153.5 m depth in hole, +325.0 m relative to sea level
GH2-3	mugearite flow	172.2 m depth in hole, +306.3 m relative to sea level
GH2-4	trachyte flow	210.7 m depth in hole, +267.8 m relative to sea level
GH2-5	trachyte flow	295.9 m depth in hole, +182.6 m relative to sea level
GH2-6	trachyte flow	365.9 m depth in hole, +112.6 m relative to sea level
GH2-7	mugearite dyke/flow	398.8 m depth in hole, +79.7 m relative to sea level
GH2-8	mugearite flow	402.7 m depth in hole, +75.8 m relative to sea level
GH2-9	mugearite dyke/flow	418.9 m depth in hole, +59.6 m relative to sea level
GH2-10	benmoreite dyke/flow	428.1 m depth in hole, +50.4 m relative to sea level
GH2-11	benmoreite dyke/flow	438.6 m depth in hole, +39.9 m relative to sea level
GH2-12	hawaiite flow (intermediate Zr/Nb)	482.6 m depth in hole, -4.1 m relative to sea level
GH2-13	rhyolite flow	497.8 m depth in hole, -19.3 m relative to sea level

GH3 Location: North of Booby Hill, grid reference 678188.
Top of hole 64.6 m above sea level, depth of hole 62.8 m.

GH3-1	hawaiite flow (low Zr/Nb)	7.5 m depth in hole, +57.1 m relative to sea level
GH3-2	hawaiite flow (low Zr/Nb)	12.7 m depth in hole, +51.9 m relative to sea level
GH3-3	hawaiite flow (intermediate Zr/Nb)	20.9 m depth in hole +43.7 m relative to sea level
GH3-4	hawaiite flow (intermediate Zr/Nb)	30.6 m depth in hole, +34.0 m relative to sea level
GH3-5	hawaiite flow (Dark Slope Crater)	43.2 m depth in hole, +21.4 m relative to sea level
GH3-6	hawaiite flow (Dark Slope Crater)	45.3 m depth in hole, +19.3 m relative to sea level
GH3-7	mugearite flow (Dark Slope Crater)	47.4 m depth in hole, +17.2 m relative to sea level
GH3-8	mugearite flow (Dark Slope Crater)	57.2 m depth in hole, +7.4 m relative to sea level

GH4 Location: Near Bears Back, grid reference 711236.
Top of hole 178.6 m above sea level, depth of hole 220.4 m.

GH4-1	benmoreite flow	39.9 m depth in hole, +138.7 m relative to sea level
GH4-2	trachyte flow	76.2 m depth in hole, +102.4 m relative to sea level
GH4-3	basalt flow (high Zr/Nb)	89.4 m depth in hole, +89.2 m relative to sea level
GH4-4	hawaiite flow (intermediate Zr/Nb)	119.5 m depth in hole, +59.1 m relative to sea level
GH4-5	hawaiite dyke/flow (intermediate Zr/Nb)	137.1 m depth in hole, +41.5 m relative to sea level
GH4-6	hawaiite flow (intermediate Zr/Nb)	157.4 m depth in hole, +21.2 m relative to sea level
GH4-7	hawaiite flow (intermediate Zr/Nb)	168.9 m depth in hole, +9.7 m relative to sea level
GH4-8	hawaiite flow (intermediate Zr/Nb)	192.3 m depth in hole, -13.7 m relative to sea level

GH5 Location: Old Mountain Road, grid reference 688228.
Top of hole 157.0 m above sea level, depth of hole 271.9 m.

GH5-1	basalt flow (intermediate Zr/Nb)	20.8 m depth in hole, +136.2 m relative to sea level
GH5-2	basalt flow (intermediate Zr/Nb)	25.4 m depth in hole, +131.6 m relative to sea level
GH5-3	hawaiite flow (intermediate Zr/Nb)	35.0 m depth in hole, +122.0 m relative to sea level
GH5-4	mugearite flow	47.5 m depth in hole, +109.5 m relative to sea level
GH5-5	mugearite flow	49.0 m depth in hole, +108.0 m relative to sea level
GH5-6	trachyte flow	88.7 m depth in hole, +68.3 m relative to sea level
GH5-7	basalt flow ()	121.0 m depth in hole, +36.0 m relative to sea level
GH5-8	basalt flow ()	131.4 m depth in hole, +25.6 m relative to sea level
GH5-9	trachyte dyke/flow	217.1 m depth in hole, -60.1 m relative to sea level

GH6 Location: Devil's Riding School, grid reference 690203.
Top of hole 189.0 m above sea level, depth of hole 394.4 m.

GH6-1	trachyte flow (Devil's Riding School)	24.6 m depth in hole, +164.4 m relative to sea level
GH6-2	hawaiite flow (high Zr/Nb)	322.9 m depth in hole, -133.9 m relative to sea level
GH6-3	basalt dyke/flow (high Zr/Nb)	340.5 m depth in hole, -151.5 m relative to sea level
GH6-4	basalt dyke/flow (high Zr/Nb)	375.9 m depth in hole, -186.9 m relative to sea level
GH6-5	? flow ()	383.9 m depth in hole, -194.9 m relative to sea level

LDTGH Location: West of Middleton Ridge, grid reference 689210.
Top of hole 174.7 m above sea level, depth of hole 339.9 m.

LDT-1	hawaiite flow (high Zr/Nb)	300.4 m depth in hole, -125.7 m relative to sea level
LDT-2	trachyte flow	328.7 m depth in hole, -154.0 m relative to sea level

APPENDIX 3

PETROGRAPHY

The following is a summary description of the petrography of the different mafic and felsic rocks of Ascension Island based on examination of thin sections.

MAFIC ROCKS

Gabbro xenoliths

We collected xenoliths from the Dark Slope Crater and Middleton Ridge. The mineralogy includes clinopyroxene, plagioclase and olivine in different proportions in the different xenoliths with either plagioclase > pyroxene > olivine or pyroxene > plagioclase > olivine. The plagioclase grains to 8 mm, clinopyroxene grains to 6 mm, and olivine grains to 4 mm in size. Some clinopyroxene are twinned and also show development of exsolution lamellae. Olivine grains are mostly altered and fragmented with most of them showing undulose extinction. Subhedral to anhedral plagioclase crystals form the cumulus phase with pyroxene and olivine forming the intercumulus phases where plagioclase > pyroxene > olivine.

High Zr/Nb flows

These flows are sparsely to moderately phyric basalt containing a microphenocryst assemblage of mostly plagioclase and olivine, order varying from flow to flow, together with titanomagnetite and rare patchy clinopyroxene crystals. Some olivine crystals are altered, but with fresh cores. The size of the phenocrysts are about 1 to 1.5 mm occasionally going up to about 3 mm. The groundmass is sparsely to moderately vesicular.

Low Zr/Nb flows

These flows are aphyric in nature and hawaiitic in composition. Rare plagioclase phenocryst

are observed with a size range to 2.5 mm. The groundmass is fine to medium grained with plagioclase laths typically of 0.1-0.2 mm, ranging up to 0.5 mm. Some of the flows are moderately vesicular with small vesicles scattered throughout the groundmass.

Intermediate Zr/Nb flows

The majority of the island is covered by intermediate Zr/Nb flows ranging in composition from basalt, hawaiite, mugearite and benmoreite.

Basalt

Sparsely phyric, slightly to moderately vesicular flows contain plagioclase and olivine phenocrysts. Plagioclase phenocrysts are fairly abundant, in the size range of 2.5 - 3 mm, ranging up to 5 mm. The crystals are mostly euhedral with some that have undergone partial resorption. Olivine microphenocrysts are common, up to 1 mm in size, and rarely forming glomerocrystic clusters with plagioclase phenocrysts. Olivine appear generally fresh except for incipient alteration of rims to iddingsite and the crystals are euhedral, and partly embayed or resorbed. Small, somewhat square opaque minerals forms inclusions in the olivine crystals. Groundmass contain laths of plagioclase up to 0.5 mm and marginally altered olivine; opaque minerals are mostly very small, but range up to 0.2 mm. At places the groundmass contains dark patches which are much less crystalline.

Hawaiite

Mostly aphyric and slightly to moderately vesicular, although some flows are massive, these flows contain rare microphenocrysts of plagioclase ranging to 1 mm, olivine, ranging to less than 1 mm and variably altered, and clinopyroxene ranging to 1.5 mm with the crystals embayed and resorbed. Titanomagnetite microphenocrysts are more common than the other crystal and range up to 0.5 mm. Groundmass is fine grained and containing plagioclase laths typically about 0.1 mm.

Mugearite

These flows are aphyric to moderately phyric and contain variable proportions of feldspar, plagioclase, and titanomagnetite phenocrysts and olivine microphenocrysts and phenocrysts. Feldspar phenocrysts are rare and range to 1.5 mm, olivine microphenocrysts are very rare, range to 0.5 mm and are completely altered. Groundmass is medium grained with feldspar laths up to 0.5 mm with patchy, irregular development of flow alignment.

Benmoreite

Aphyric benmoreite flows varies from massive to high vesicularity with plagioclase up to 1 mm in size forming the rare microphenocrysts. In some flows rare olivine (0.5 mm) and titanomagnetite (less than 1 mm) microphenocrysts are also observed. Groundmass is of variable grain size with plagioclase laths typically 0.2 mm, up to 0.5 mm, and with some development of flow alignment of plagioclase laths. One of the youngest geologic features of the island is the fissure eruption of benmoreite lava on the extreme eastern section of the island (Letterhead). These lavas are moderately phyric and vesicular and contain plagioclase phenocrysts, and clinopyroxene, olivine and titanomagnetite microphenocrysts.

Intermediate Zr/Nb Mugearite and Benmoreite flows from Broken Tooth

Mugearite flows from Broken Tooth on the northern section of the island are sparsely phyric and moderately but variably vesicular. Feldspar and clinopyroxene form the phenocryst assemblage. The benmoreite lavas from the same cone (Broken Tooth) contains feldspar, olivine, and clinopyroxene phenocrysts, and titanomagnetite microphenocrysts. These lavas are phyric and moderately vesicular.

Intermediate Zr/Nb Hawalite and Mugearite flows from Dark Slope Crater

Aphyric and moderately vesicular these hawaiite flows contain rare olivine microphenocrysts which range in size to 1 mm, typically extensively altered, but occasionally with fresh cores.

The groundmass contains plagioclase laths up to 0.2 mm in size, small altered olivine and small opaque minerals.

FELSIC ROCKS

Plutonic and Volcanic Xenoliths

Felsic plutonic xenoliths (monzonite, syenite, and granite) and volcanic xenoliths (trachyte and rhyolite) occur mainly in pyroclastic deposits on the western flanks of Green Mountain. The granite, syenite, and monzonite xenoliths have been described in great detail by Roedder & Coombs (1967), Harris & Bell (1982), Harris et al. (1982), Harris (1983), Sheppard & Harris (1985), and Harris & Sheppard (1987). The granite xenoliths from Five Mile Post vary in size from a few cm to 25-30 cm in length and generally are fine grained with a few which are coarser grained. Monzonite xenoliths occur on Middleton Ridge and syenite xenoliths in the flows from Broken Tooth (Harris, 1983). Trachytic and rhyolitic xenoliths from close to Five Mile Post vary vastly in size and generally have a schistose texture.

Trachyte and Rhyolite

Trachytic rocks vary from being aphyric to very sparsely phyric to strongly phyric and are mostly massive although some are slightly vesicular. The most abundant phenocryst phase is alkali feldspar, with olivine, clinopyroxene, and titanomagnetite forming the other phenocryst or microphenocryst phases. Weaver et al. (1996) reported trachyte that from Ragged Hill and Cocoanut Bay has unusually high contents of alkali feldspar phenocrysts (25 to 35%). The sizes of the phenocrysts varies: feldspar phenocrysts are up to 2 mm, olivine up to 1.5 mm, and titanomagnetite and clinopyroxene are up to 0.5 mm and occur as rare clusters. Plagioclase phenocrysts are rare and tabular in shape, and range up to 2.5 mm. Some trachytic rocks contain small (0.5 mm) rounded crystals of amphibole with reaction rims. Overall the

groundmass in the trachyte is fine grained with plagioclase laths ranging between 0.1 and 0.2 mm, and rarely up to 1 mm and exhibiting a patchy, weak flow alignment.

Rhyolitic rocks mostly are aphyric to sparsely phyric and massive in general; microphenocrysts are alkali feldspar.

APPENDIX 4

Major element, trace element, radiogenic isotope, and stable isotope data

	SiO_2	TiO_2	Al_2O_3	Fe_2O_3	MnO	MgO	CaO	Na_2O	K_2O	P_2O_5	LOI	H_2O-	Cr xrf	Cr inaa	Ni xrf	Co xrf	Co inaa	Cu xrf	Zn xrf	V xrf	Sc xrf	Sc inaa	Ga xrf	Rb xrf	Sr xrf	Ba xrf	Th xrf
	Gabbro xenoliths																										
Al-10	42.05	0.09	7.96	9.83	0.17	34.24	5.02	0.42	0.03	0.19	0.25	0.35	2110		1204	114		47	65	38	4		5	<1	61	28	<2
Al-7	46.31	0.15	13.59	6.49	0.12	19.14	13.22	0.67	0.04	0.27	0.23	0.42	2416		545	71		43	39	86	21		8	<1	130	76	<2
Al-32	48.42	0.23	12.09	5.82		16.65	15.64	0.70	0.03	0.22	0.21	0.16			403	57		60	48				9	<1	122		<2
Al-206	46.90	0.16	15.58	7.00		15.72	13.39	1.05	0.05	0.15	0.39	0.30			482	63		105	37				11	<1	125		<2
Al-3	48.31	0.12	14.44	6.34	0.11	15.20	14.51	0.85	0.02	0.10	0.19	0.37	775		273	61		88	70	144	28		11	<1	87	14	<2
Al-35	47.39	0.15	19.43	5.30		11.30	14.89	1.25	0.05	0.24	0.50	0.35			242	53		58	53				13	1	169		<2
Al-8	50.55	0.29	16.39	4.56	0.09	9.71	16.95	1.26	0.04	0.16	0.86	0.65	1592		153	29		64	46	150	34		12	<1	103	54	<2
Al-5	49.45	0.20	20.43	4.97	0.16	7.93	15.03	1.65	0.05	0.13	0.68	0.70	556		131	39	36.3	55	86	97	21	32.0	15	<1	143	109	<2
Al-9	48.04	0.19	21.03	6.74	0.27	7.61	13.71	2.04	0.06	0.31	0.50	0.57	559		215	52	47.3	70	118	76	11	20.7	15	<1	197	121	<2
Al-33	47.75	0.10	26.38	3.19		5.62	15.17	1.56	0.05	0.18	0.85	0.37			119	22		26	34				15	<1	195		<2
Al-34	47.69	0.10	26.25	2.44		5.87	15.95	1.54	0.05	0.11	0.43	0.24			138	18		33	43				15	<1	196		<2
Al-249h	46.96	0.53	14.00	9.87		13.81	12.78	1.52	0.08	0.45	0.14	0.45			164	84		5	94				13	1	374		<2
Al-249m	47.29	0.71	19.12	7.65		9.99	13.18	1.59	0.11	0.36	1.05	0.77			124	43		21	49				17	2	551		<2
Al-249a	48.57	0.83	20.06	6.57		8.12	13.57	1.73	0.13	0.42	1.37	1.15			91	32		10	47				19	1	511		<2
Al-249f	48.72	0.42	23.76	4.49		5.22	14.60	2.19	0.12	0.48	0.70	0.70			43	27		18	54				19	<1	590		<2
Al-249n	48.48	0.37	25.10	4.25		4.14	14.79	2.30	0.11	0.46	0.54	0.50			37	38		2	64				19	<1	707		<2
	Mafic xenoliths in trachyte																										
Al-224	47.57	3.86	13.97	15.65		4.70	9.10	3.39	0.94	0.82	-0.39	0.35			17	41		17	227				28	18	440		3
Al-226	47.49	2.91	15.78	13.23	0.18	5.39	9.89	3.48	1.05	0.60	-0.02	0.34			46	54		22	186	248	27		25	22	552	275	3
Al-227	49.19	3.60	17.21	13.83	0.25	2.68	6.24	4.10	1.77	1.13	2.24	1.99			70	50		<2	523	223	24		27	36	406	354	3
Al-225	63.45	0.69	18.41	3.88		0.35	1.30	7.45	4.23	0.24	0.53	0.16			5	<2		4	104				27	49	181		4
Al-234a	51.40	2.36	16.47	11.03	0.25	3.67	8.47	4.56	1.29	0.50	0.35	0.26			24	48		34	107	204	26		25	19	405	1303	2
Al-234b	51.24	2.40	16.29	11.23	0.21	3.73	8.47	4.69	1.24	0.50	0.18	0.19			26	53		44	166	215	28		25	21	407	1266	3
Al-235c	49.12	3.55	15.76	13.13		3.13	7.67	4.57	1.91	1.14	0.82	0.62			8	26		18	99				25	33	542		6
Al-235d	50.24	3.31	15.37	12.10		3.89	7.64	4.74	1.64	1.07	0.66	0.42			10	25		11	94				25	19	510		6
Al-235e	49.89	2.98	15.14	12.36		3.47	7.05	4.99	2.39	1.73	1.07	0.79			6	19		19	220				25	39	536		5
Al-235b	52.44	2.87	16.08	11.18		3.31	5.90	5.21	2.11	0.90	1.40	0.91			9	22		11	99				26	27	468		5
Al-235a	54.57	2.28	16.09	10.08		2.21	4.94	5.49	2.76	1.58	1.02	0.80			7	13		21	119				25	39	498		6
Al-240	54.45	1.94	17.03	8.96		3.54	6.65	4.90	2.02	0.51	0.17	0.21			31	20		31	148				26	40	411		4
Al-250b	54.22	1.94	17.59	8.78	0.18	2.40	6.38	5.92	1.77	0.82	0.66	0.65			25	43		18	403	103	19		26	40	598	761	6
Al-250a	54.96	1.93	17.84	8.84	0.16	2.05	5.48	6.06	1.84	0.84	0.79	1.56			52	32		15	665	90	20		28	34	586	823	3
Al-97	55.15	1.96	17.89	9.00	0.18	1.82	5.21	5.94	2.01	0.84	0.85	1.35	12	15.9	39	31	28.6	14	497	87	20	19.7	27	65	565	947	5
	Syenite xenoliths																										
Al-187d	60.47	0.87	17.69	5.64		0.78	3.37	6.99	2.60	1.59	0.60	0.27			4	<2		7	88				26	31	364		4
Al-187e	61.74	0.72	18.38	5.16	0.14	0.41	2.93	7.55	2.74	0.23	0.33	0.15			<2	19		2	82	7	10		27	28	278	1668	2
Al-187c	62.23	0.60	18.16	4.52	0.07	0.30	2.46	7.23	3.40	1.03	0.64	0.23			4	23		7	57	11	11		26	31	263	1513	3
Al-187f	62.82	0.55	18.56	4.10		0.48	2.55	7.15	3.16	0.63	0.47	0.24			4	<2		4	72				26	30	301		3
Al-187a	62.86	0.57	18.62	3.65	0.09	0.38	2.30	7.63	3.54	0.36	0.48	0.13			<2	9		8	51	11	7		27	25	268	1625	2
Al-187g	63.05	0.46	18.50	3.29		0.34	2.54	7.91	3.22	0.69	0.66	0.27			2	<2		4	73				25	24	302		3
Al-187b	63.35	0.47	18.79	3.60		0.35	2.79	7.39	2.90	0.36	0.32	0.15			3	<2		4	62				27	32	371		3
Al-187h	64.21	0.39	18.42	3.65		0.27	1.71	7.36	3.67	0.32	0.51	0.28			3	<2		8	47				29	35	206		5
	Monzonite xenoliths																										
Al-249g	61.39	0.90	18.09	4.83		1.06	2.55	6.43	3.86	0.89	0.43	0.50			8	2		7	83				28	79	311		5
Al-249l	62.31	0.94	17.48	5.43		0.99	2.61	6.72	3.05	0.47	0.30	0.30			4	<2		6	81				28	62	298		5

	SiO_2	TiO_2	Al_2O_3	Fe_2O_3	MnO	MgO	CaO	Na_2O	K_2O	P_2O_5	LOI	H_2O-	Cr xrf	Cr inaa	Ni xrf	Co xrf	Co inaa	Cu xrf	Zn xrf	V xrf	Sc xrf	Sc inaa	Ga xrf	Rb xrf	Sr xrf	Ba xrf	Th xrf
Al-249l	63.50	0.65	18.76	4.67		0.15	1.14	7.75	3.15	0.23	0.38	0.29			3	<2		3	70				29	33	153		2
Al-249b	64.09	0.83	17.36	4.76		0.80	2.48	6.77	2.72	0.19	0.17	0.08			5	<2		4	65				27	52	327		7
Al-249l	64.14	0.72	18.32	4.44		0.52	2.00	7.43	2.40	0.03	0.43	0.20			3	<2		2	76				28	62	311		5
Al-249k	64.17	0.72	18.35	4.42		0.57	1.93	7.33	2.47	0.04	0.49	0.20			5	<2		2	83				28	78	297		5
Al-249d	64.34	0.69	17.47	4.07		0.66	1.95	6.61	3.75	0.46	0.37	0.31			5	<2		4	68				29	86	294		7
Al-249e	64.34	0.73	17.45	4.46		0.63	2.02	6.82	3.18	0.37	0.26	0.26			4	<2		5	72				28	50	223		5
Al-249c	64.46	0.75	16.98	4.59		0.81	2.13	6.48	3.52	0.28	0.29	0.16			5	<2		3	81				29	84	311		6
	Trachyte/rhyolite xenoliths																										
Al-133i	68.58	0.31	14.80	4.53		0.06	0.24	6.07	5.23	0.18	0.34	0.38			7	<2		3	166				36	105	6		13
Al-133g	69.06	0.31	14.78	4.14		0.08	0.32	6.06	5.11	0.14	0.38	0.38			8	<2		4	164				35	103	9		13
Al-133b	69.28	0.31	15.14	3.51		0.14	0.28	5.98	5.10	0.26	0.40	0.31			4	<2		4	126				34	140	19		18
Al-133c	69.66	0.29	14.42	4.38		0.07	0.18	5.69	5.07	0.24	0.53	0.43			8	<2		4	181				37	119	8		16
Al-133f	69.81	0.28	14.15	4.26		0.03	0.28	5.69	5.00	0.50	0.51	0.62			9	2		4	185				36	131	18		19
Al-133a	70.97	0.29	12.81	4.95		0.06	0.35	5.50	4.71	0.36	0.37	0.41			6	<2		5	199				34	135	4		19
Al-133h	71.19	0.25	13.37	4.24		0.04	0.29	5.84	4.76	0.02	0.31	0.12			7	<2		6	220				37	141	3		17
Al-133d	72.06	0.23	12.90	4.19		0.04	0.19	5.54	4.75	0.10	0.18	0.19			7	<2		7	223				37	158	3		20
Al-133e	73.06	0.21	12.64	3.92		0.07	0.12	5.22	4.72	0.04	0.28	0.22			9	<2		5	223				38	171	2		24
	Granite xenoliths																										
Al-262	72.99	0.19	12.11	4.49		<0.05	0.23	5.21	4.75	0.03	0.03	0.05			7	<2		3	231				40	87	3		15
Al-213d	73.83	0.18	11.86	3.95	0.12	<0.05	0.27	5.23	4.53	0.03	0.13	0.09			3	36		4	174	5	2		38	91	4	48	12
Al-213a	73.86	0.24	10.69	5.28	0.24	<0.05	0.31	4.82	4.53	0.03	0.13	0.06			<2	35		3	331	5	5		37	96	6	41	23
Al-213f	73.86	0.18	11.96	3.87	0.11	<0.05	0.25	5.17	4.57	0.03	0.18	0.06			2	18		5	153	4	1		39	88	5	53	12
Al-213c	73.90	0.19	11.18	4.55	0.16	<0.05	0.18	5.30	4.49	0.05	0.22	0.07			<2	33		6	150	19	1		38	157	5	32	17
Al-213g	73.93	0.22	10.82	4.92	0.16	<0.05	0.19	5.19	4.39	0.18	0.37	0.17			2	47		11	160	7	4		40	180	9	43	10
Al-213b	74.10	0.19	10.99	4.85	0.20	<0.05	0.25	4.68	4.68	0.06	0.25	0.10			<2	25		11	247	5	3		39	108	18	45	37
Al-213e	75.35	0.12	11.04	4.22	0.14	<0.05	0.28	4.55	4.29	0.01	0.16	0.04			<2	37		9	171	11	1		37	68	5	38	9
	High Zr/Nb basalt																										
Al-173	48.72	2.16	17.95	10.78	0.15	6.08	10.33	2.68	0.71	0.44	0.37	0.75	126		109	45		60	113	207	26		21	17	531	194	2
Al-230	48.80	2.46	16.02	11.97	0.18	6.01	10.04	3.21	0.92	0.39	-0.55	0.98			48	70		60	93	296	33		20	17	421	262	2
Al-45	50.60	3.05	15.28	13.74	0.17	4.82	7.92	3.00	0.92	0.50	1.83	4.22	24	24.5	37	68	66.1	45	141	250	34	31.7	22	25	400	174	2
Al-148	48.89	2.57	15.90	11.99	0.18	5.98	10.01	3.10	0.96	0.42	-0.41	0.51	28		40	43		59	93	281	32		24	20	427	251	2
Al 237	48.74	2.55	15.67	12.20	0.17	5.85	9.67	3.67	0.91	0.57	0.71	1.93			38	68		52	97	269	32		20	17	407	253	2
Al-172	49.64	2.73	16.08	12.99	0.18	5.65	9.01	2.52	0.85	0.35	1.45	2.15	35	32.2	47	43	41.1	53	105	243	31	28.2	23	20	404	212	2
Al-134	50.11	2.73	15.67	12.77	0.18	5.49	8.80	2.83	0.98	0.44	0.40	1.71	30		43	40		52	106	253	31		24	21	415	213	4
Al-14	49.27	1.88	16.79	10.85	0.15	7.00	10.48	2.44	0.71	0.43	1.01	2.42	151	165	100	41	42.5	85	83	199	28	26.1	18	13	435	171	2
Al-201	48.46	1.86	16.81	10.68	0.16	6.84	11.07	2.98	0.83	0.31	0.65	0.13			93	72		94	83	235	28		20	14	425	157	2
Al-200	48.97	2.03	17.00	10.79	0.15	5.71	11.01	3.09	0.84	0.41	0.12	0.55			75	64		60	99	234	29		21	12	462	211	2
Al-127	48.44	2.42	16.24	11.40	0.16	5.70	10.97	3.29	0.88	0.50	0.17	0.44	63		47	52		51	80	250	29		23	15	448	254	2
Al-124	47.98	2.81	15.61	13.01	0.17	6.06	9.94	3.12	0.85	0.45	-0.24	0.39	36	35.7	50	61	56.0	52	93	278	32	32.0	24	14	444	189	3
Al-149	48.49	2.93	15.16	13.12	0.18	5.70	9.57	3.47	0.95	0.43	-0.18	0.35	26		41	60		64	96	324	31		23	19	472	218	3
Al-110	48.51	2.73	15.77	12.95	0.17	5.71	9.44	3.38	0.92	0.42	-0.24	0.31	35		52	56		38	102	274	32		24	10	420	207	4
Al-128	49.09	2.65	15.48	12.44	0.17	5.54	9.07	4.00	1.11	0.45	-0.65	0.16	31	32.9	38	54	54.6	46	94	246	28	30.0	25	20	418	237	2
Al-162	47.97	3.03	15.08	13.61	0.20	5.77	9.82	3.20	0.92	0.40	-0.06	0.49	29		43	57		55	100	324	32		23	18	435	197	2
Al-107	48.55	3.00	15.28	13.48	0.16	5.33	9.46	3.34	0.94	0.46	0.18	0.42	25	27.9	39	59	59.7	56	93	304	33	33.5	26	18	436	201	2
Al-106	47.86	3.01	15.58	13.70	0.18	5.57	9.83	3.11	0.72	0.44	0.11	0.46	31		42	61		26	100	330	33		24	7	438	203	3
Al-233	47.95	3.02	15.00	13.66	0.19	5.75	9.93	3.29	0.79	0.42	-0.18	0.58			43	65		44	101	394	35		25	12	434	209	2

	SiO_2	TiO_2	Al_2O_3	Fe_2O_3	MnO	MgO	CaO	Na_2O	K_2O	P_2O_5	LOI	H_2O-	Cr xrf	Cr inaa	Ni xrf	Co xrf	Co inaa	Cu xrf	Zn xrf	V xrf	Sc xrf	Sc inaa	Ga xrf	Rb xrf	Sr xrf	Ba xrf	Th xrf
Al-215	48.70	2.53	15.69	12.65	0.19	5.71	9.83	3.30	0.88	0.52	-0.02	0.37			49	65		45	145	270	28		23	17	512	234	3
Al-36	47.71	3.08	15.43	13.60	0.16	5.05	9.60	3.54	1.14	0.69	-0.06	0.35	47		35	56		25	207	249	30		25	24	559	267	3
Al-37	47.59	2.98	15.43	13.43	0.18	5.55	9.74	3.42	1.06	0.62	-0.20	0.31	50	53.7	48	72	69.7	48	101	248	27	28.1	24	19	551	259	2
Al-40	47.55	2.96	15.62	13.22	0.16	5.54	10.03	3.31	0.98	0.63	0.07	0.34	54		47	76		43	119	238	28		24	19	539	243	2
Al-64	50.58	2.52	15.61	11.98	0.17	5.23	8.56	3.61	1.29	0.45	-0.40	0.31	22	26.8	34	46	46.1	38	87	201	25	28.9	26	28	414	289	3
Al-65	50.62	2.57	15.55	12.29	0.17	4.99	8.46	3.57	1.34	0.44	-0.35	0.54	25		36	46		31	89	228	27		26	29	406	276	4
	Low Zr/Nb hawaiite																										
Al-60	47.94	3.64	14.67	13.37	0.21	4.90	9.12	3.72	1.41	1.02	0.54	0.41	3	2.6	12	53	48.8	22	132	294	29	27.9	24	27	551	379	3
Al-61	47.45	3.65	15.14	13.53	0.19	5.14	8.96	3.59	1.43	0.92	-0.72	0.37	7		19	61		25	103	254	23		25	29	572	387	4
Al-152	47.58	3.79	15.32	13.79	0.18	4.20	8.71	3.84	1.60	0.99	0.30	0.64	2	6.0	14	45	47.8	22	103	263	27	28.4	24	33	563	413	4
Al-151	47.58	3.74	15.04	13.54	0.19	4.61	8.80	3.85	1.60	1.05	-0.17	0.51	3		16	55		23	97	239	25		25	35	588	427	4
Al-157	47.69	3.83	15.54	13.84	0.20	3.88	8.32	3.96	1.65	1.09	0.61	0.70	3	1.8	13	57	56.5	13	140	287	28	28.8	24	32	533	395	5
Al-258	47.55	3.78	15.21	13.74	0.20	4.36	8.80	3.74	1.57	1.05	-0.31	0.65			20	49		25	103	303	27		26	26	575	410	5
Al-211	47.88	3.80	15.48	13.61	0.19	3.69	8.60	4.00	1.65	1.10	0.62	0.76			10	51		13	122	322	27		23	34	584	433	5
Al-207	47.37	3.76	15.12	13.48	0.21	4.70	8.85	3.89	1.59	1.03	0.42	0.19			12	55		17	111	321	29		24	34	573	419	5
Al-212	47.34	3.76	15.06	13.57	0.21	4.08	9.13	4.10	1.63	1.12	0.07	0.37			9	48		15	108	324	27		25	33	574	425	4
Al-208	48.84	3.73	15.40	13.42	0.21	4.57	7.96	3.25	1.60	1.02	2.13	1.90			8	68		21	116	278	30		24	38	596	413	5
	Intermediate Zr/Nb basalt and hawaiite																										
Al-1	47.39	2.60	15.85	12.79	0.18	6.65	10.46	2.77	0.66	0.65	0.10	0.30	130	127	85	46	45.9	60	91	283	28	30.1	21	12	386	155	<2
Al-100	47.53	2.67	15.80	12.78	0.17	6.65	10.35	2.81	0.65	0.59	-0.44	0.33	146	156	97	59	57.7	53	92	248	29	30.0	23	11	385	144	<2
Al-102	48.00	2.73	15.45	12.90	0.17	6.46	10.23	2.77	0.65	0.64	-0.04	0.36	153		96	61		57	96	255	29		21	12	381	149	2
Al-158	47.47	2.70	15.67	12.81	0.17	6.86	10.14	2.94	0.65	0.59	-0.49	0.22	153	177	105	61	60.9	59	96	250	25	30.8	21	12	382	152	2
Al-259	47.63	2.64	15.89	12.66	0.17	6.52	10.50	2.78	0.58	0.63	-0.04	0.38			85	60		65	90	269	28		22	10	401	159	<2
Al-170	48.58	2.53	16.12	11.52	0.20	6.13	9.62	3.02	1.29	0.99	0.45	0.81	71		67	35		47	104	191	27		23	25	486	277	2
Al-123	48.87	2.55	16.17	11.42	0.20	5.91	9.59	3.06	1.24	0.99	0.22	0.24	81	83.9	63	33	32.5	49	113	195	25	23.0	21	25	492	288	3
Al-12	47.25	3.60	15.59	14.91	0.22	4.77	8.63	2.92	1.13	0.98	1.41	2.21	35		26	37		28	120	295	30		23	22	448	269	3
Al-26	47.61	3.42	15.09	13.92	0.21	5.22	9.24	3.21	1.23	0.85	0.03	0.42	30		30	40		31	118	303	29		24	25	455	260	4
Al-27	47.40	3.41	15.08	13.99	0.20	5.21	9.28	3.43	1.19	0.81	-0.20	0.17	32		32	39		38	108	303	29		24	23	464	268	2
Al-28	47.28	3.38	14.99	13.76	0.20	5.17	9.50	3.69	1.19	0.84	-0.31	0.30	32	32.7	29	99	91.6	33	108	296	28	27.0	25	23	469	262	3
Al-62	47.38	3.43	15.12	13.93	0.20	5.12	9.13	3.63	1.20	0.86	-0.76	0.30	28		29	61		33	115	291	30		24	21	466	268	2
Al-195	47.92	3.35	15.25	13.86	0.21	5.30	8.99	3.16	1.15	0.81	-0.35	1.15			25	54		35	116	314	30		24	23	454	271	<2
Al-197	47.69	3.44	15.21	13.94	0.22	5.15	8.99	3.24	1.25	0.87	-0.32	0.51			23	71		34	121	327	30		25	25	467	286	2
Al-196	47.93	3.43	15.11	14.10	0.21	5.17	8.97	3.09	1.18	0.81	0.20	1.11			27	49		33	116	309	29		24	24	445	273	3
Al-29	47.54	3.46	14.92	13.99	0.20	5.10	9.14	3.59	1.22	0.84	-0.42	0.29	29		33	85		27	110	301	29		24	22	460	275	3
Al-210	49.69	3.15	15.26	12.56	0.22	4.31	7.84	4.00	1.61	1.36	0.22	0.65			1	26		10	130				23	35	499		4
Al-297	48.93	3.24	14.79	13.20	0.23	4.16	8.19	4.51	1.47	1.28	-0.14	0.27			5	32		4	129	207	21		28	30	513	353	4
Al-299	49.14	3.25	15.21	12.78	0.23	4.19	8.07	4.28	1.56	1.29	-0.40	0.28			12	34		4	132	205	22		27	20	501	395	4
Al-30	49.76	3.15	14.83	12.65	0.22	4.15	8.17	4.08	1.48	1.51	0.44	0.68	4	1.9	10	81	73.1	<1	128	176	25	19.2	25	27	507	351	3
Al-290	49.09	3.17	14.98	12.80	0.25	4.25	8.21	4.15	1.57	1.53	-0.15	0.39			9	34		6	137	207	21		25	28	508	365	3
Al-295	49.58	3.05	15.01	12.53	0.25	4.10	7.97	4.30	1.62	1.59	-0.29	0.37			6	34		2	146	186	21		26	31	507	392	4
Al-231	50.56	2.86	15.15	12.06	0.24	4.31	7.53	3.99	1.72	1.58	1.44	2.33			8	45		<2	139	147	20		25	34	502	363	5
Al-288	49.98	3.13	15.09	12.73	0.22	4.01	7.81	4.20	1.62	1.21	-0.40	0.22			11	35		7	124	193	20		26	27	500	404	5
Al-209	50.47	3.14	15.38	12.85	0.21	4.35	7.40	3.58	1.60	1.02	1.51	1.34			20	51		26	133	231	26		27	36	592	371	5
Al-236	49.07	3.22	14.48	13.57	0.24	4.36	8.24	4.10	1.31	1.41	-0.43	0.23			9	39		9	132	235	26		27	26	475	347	4
Al-263	49.61	3.09	14.72	13.21	0.24	4.17	8.08	4.15	1.34	1.39	-0.36	0.66			9	46		9	140	214	28		28	23	486	361	4
Al-232	49.96	3.04	15.47	13.08	0.22	3.16	7.79	4.29	1.54	1.45	0.39	0.62			8	60		5	133	170	27		29	30	515	393	4

	SiO_2	TiO_2	Al_2O_3	Fe_2O_3	MnO	MgO	CaO	Na_2O	K_2O	P_2O_5	LOI	H_2O-	Cr xrf	Cr inaa	Ni xrf	Co xrf	Co inaa	Cu xrf	Zn xrf	V xrf	Sc xrf	Sc inaa	Ga xrf	Rb xrf	Sr xrf	Ba xrf	Th xrf
Al-273	49.11	3.63	14.38	14.07	0.20	4.46	8.46	3.81	1.36	0.52	-0.32	0.71			21	46		17	128	323	28		25	26	417	303	4
Al-274	49.40	3.67	14.33	14.26	0.20	4.20	8.62	3.54	1.28	0.50	0.41	0.86			18	47		22	136	303	27		25	25	435	320	3
Al-46	49.65	2.92	15.24	12.70	0.23	4.25	8.11	3.99	1.58	1.33	-0.40	0.28	11		16	46		13	124	193	24		25	32	470	360	5
Al-53	49.90	2.94	15.38	12.75	0.23	4.04	7.91	3.91	1.54	1.40	0.75	1.08	12		10	54		8	137	167	28		26	30	464	356	3
Al-139	51.01	2.76	15.32	12.31	0.24	4.04	7.54	3.51	1.69	1.58	0.05	0.92	6	4.7	9	24	23.3	8	142	155	23	21.7	26	37	470	370	5
Al-141	47.27	4.00	14.33	15.58	0.23	5.05	8.71	2.75	1.00	1.08	0.54	2.10	8		21	39		24	130	281	35		25	20	472	260	2
Al-198	47.61	3.97	14.05	15.20	0.22	4.99	8.65	3.04	1.11	1.16	0.44	1.01			10	34			128				25	24	465		3
Al-138	45.67	3.85	16.14	14.87	0.22	4.76	8.87	3.47	1.05	1.10	-0.72	0.23	5	5.4	18	44	48.6	15	125	301	33	33.1	25	17	484	282	3
Al-56	49.83	3.06	15.37	12.49	0.22	4.30	7.94	4.15	1.60	1.04	-0.34	0.33	7		11	48		6	123	201	24		27	33	500	355	4
Al-159b	48.09	3.61	14.31	14.28	0.21	4.74	8.57	3.76	1.26	1.17	-0.73	0.08	13	2.6	14	47	45.1	8	116	234	28	31.2	28	27	477	320	4
Al-160	48.10	3.61	14.28	14.34	0.21	4.68	8.62	3.73	1.26	1.17	-0.78	0.10	3		15	41		14	112	232	31		27	26	482	323	3
Al-167	48.07	3.63	14.32	14.14	0.22	4.70	8.92	3.60	1.21	1.19	-0.26	0.41	3		11	44		8	128	253	29		26	24	473	309	3
Al-253	48.11	3.56	14.36	14.22	0.23	4.57	8.59	3.77	1.32	1.27	-0.68	0.20			11	36		12	120	259	26		26	23	479	336	3
Al-277	48.40	3.61	14.26	14.19	0.22	4.46	8.65	3.78	1.27	1.16	-0.73	0.59			8	41		10	131	275	28		27	22	477	333	3
Al-278	48.14	3.64	14.38	14.20	0.23	4.49	8.62	3.84	1.28	1.18	-0.95	0.71			10	38		11	147	271	26		26	22	478	353	4
Al-180	49.11	3.62	14.45	14.04	0.23	4.67	8.37	3.07	1.28	1.16	0.40	1.27	3		7	31		11	132	239	29		25	27	452	291	3
Al-179	48.67	3.51	14.39	13.62	0.21	4.48	8.67	3.97	1.30	1.18	-0.78	0.10	5		9	38		9	111	209	26		29	27	480	346	4
Al-271	48.83	3.48	14.40	13.94	0.23	4.35	8.40	3.78	1.33	1.26	-0.63	0.28			9	38		7	142	258	29		27	26	481	341	4
Al-58	48.54	3.44	14.41	14.16	0.23	4.41	8.56	3.66	1.34	1.25	-0.56	0.38	2		7	47		2	127	234	29		26	27	472	312	3
Al-24	49.82	3.11	15.27	12.75	0.22	4.21	8.02	4.02	1.53	1.05	-0.55	0.30	5		12	26		12	118	229	25		26	31	497	365	3
Al-25	50.02	3.04	15.30	12.59	0.22	4.14	7.85	4.13	1.59	1.12	-0.43	0.35	5	6.2	10	24	24.8	8	122	218	22	22.7	25	33	500	376	4
Al-159a	49.93	3.08	15.40	12.48	0.22	4.28	7.94	4.11	1.55	1.01	-0.70	0.16	9		11	38		7	126	206	21		25	32	500	355	4
Al-161	49.58	3.21	15.42	12.62	0.21	4.43	8.16	3.88	1.50	0.99	-0.30	0.34	8	6.7	12	37	38.1	9	119	214	22	24.6	24	30	498	343	4
Al-269	49.52	3.14	15.23	12.78	0.22	4.43	8.09	4.17	1.50	0.92	-0.54	0.55			16	38		8	122	244	24		28	32	502	346	5
Al-270	51.59	3.29	16.86	13.32	0.22	3.33	4.87	4.05	1.50	0.97	2.06	0.42			6	38		11	139	248	25		27	31	451	345	4
Al-284	49.70	3.13	15.29	12.43	0.22	4.46	8.12	4.26	1.46	0.93	-0.42	0.67			11	41		11	123	237	22		25	31	506	342	4
Al-285	49.38	3.16	15.30	12.70	0.22	4.36	8.19	4.25	1.50	0.94	-0.29	0.18			13	40		12	122	237	24		25	32	508	354	4
Al-75	49.41	3.17	15.32	12.69	0.21	4.47	8.14	4.09	1.52	0.98	-0.70	0.17	7		14	40		11	112	207	25		26	32	506	351	3
Al-89	49.76	3.22	15.40	12.83	0.22	4.47	8.15	3.48	1.52	0.95	-0.86	0.18	8	6.9	14	44	42.1	8	122	218	28	24.0	26	30	502	345	4
Al-251	49.42	3.17	15.30	12.76	0.22	4.36	8.14	4.18	1.51	0.94	-0.36	0.09			12	45		13	123	233	24		26	30	503	362	4
Al-252	49.55	3.17	15.38	12.59	0.22	4.42	8.12	4.10	1.50	0.95	-0.66	0.12			9	36		13	121	225	23		26	31	508	361	4
Al-183	49.64	3.11	15.44	12.47	0.21	4.45	8.03	4.19	1.50	0.96	-0.18	0.15	10		15	38		7	118	216	23		27	32	500	345	4
Al-292	49.26	3.21	15.67	12.78	0.20	4.40	8.29	3.72	1.50	0.97	0.67	0.70			5	42		13	139	207	25		26	30	647	347	4
Al-81	49.58	3.18	15.41	12.58	0.24	4.39	8.17	4.05	1.48	0.92	-0.64	0.32	5		10	34		3	140	175	22		26	25	535	344	4
Al-286	49.42	2.88	15.57	11.85	0.22	4.04	8.12	4.66	1.68	1.56	-0.30	0.37			8	25		4	154	141	20		27	31	668	408	4
Al-82	48.48	3.23	14.92	12.98	0.21	4.53	8.41	4.07	1.50	1.67	-0.50	0.27	7		11	43		9	122	208	24		26	30	499	343	4
Al-182	48.28	3.21	14.98	12.95	0.23	4.52	8.37	4.30	1.47	1.69	-0.53	0.25	3		8	32		2	125	172	21		27	25	539	356	4
Al-214	48.72	3.23	14.85	13.00	0.22	4.45	8.37	3.99	1.48	1.69	-0.27	0.13			4	23		5	134				24	32	527		4
Al-279	49.13	3.17	14.89	12.79	0.25	4.37	8.22	4.02	1.56	1.60	-0.31	0.64			8	35		<2	152	190	22		25	31	529	359	3
Al-136	48.69	3.20	14.85	12.98	0.21	4.43	8.27	4.26	1.54	1.57	0.78	0.07	2		9	36		<2	117	160	20		26	32	536	362	5
Al-280	48.88	3.16	14.87	12.78	0.24	4.32	8.34	4.26	1.55	1.60	-0.14	0.24			9	31		5	136	195	20		26	25	540	369	5
Al-218	48.66	3.16	14.99	12.71	0.24	4.48	8.31	4.37	1.51	1.57	-0.45	0.29			9	46		6	132	193	25		27	26	543	370	4
Al-188	50.12	3.01	14.76	13.16	0.24	4.17	7.82	4.04	1.48	1.20	-0.39	0.32			8	54		5	140	190	23		27	27	496	329	3
Al-281	50.17	2.99	14.83	13.12	0.24	4.20	7.77	3.94	1.52	1.22	-0.18	0.27			8	34		6	146	191	27		25	28	490	335	4
Al-189	50.85	2.96	14.99	13.12	0.26	4.05	7.41	3.69	1.44	1.23	0.21	0.48			7	35		5	155	187	24		27	30	489	335	3
Al-72	48.54	3.27	15.48	13.19	0.18	4.36	8.62	3.92	1.49	0.95	-0.66	0.37	5	3.7	13	41	46.3	22	132	191	22	24.1	28	27	645	339	3

	SiO_2	TiO_2	Al_2O_3	Fe_2O_3	MnO	MgO	CaO	Na_2O	K_2O	P_2O_5	LOI	H_2O-	Cr xrf	Cr inaa	Ni xrf	Co xrf	Co inaa	Cu xrf	Zn xrf	V xrf	Sc xrf	Sc inaa	Ga xrf	Rb xrf	Sr xrf	Ba xrf	Th xrf
Al-283	48.64	3.26	15.53	13.00	0.17	4.39	8.51	4.04	1.52	0.94	-0.70	0.55			12	38		22	108	187	20		28	31	656	377	5
Al-74	48.57	3.29	15.38	13.13	0.20	4.58	8.63	3.84	1.47	0.91	-0.49	0.24	5		13	50		20	141	201	23		27	30	646	374	4
Al-257	48.40	3.36	14.90	13.49	0.21	4.40	9.14	3.90	1.41	0.79	-0.28	0.41			20	44		29	113	311	27		26	24	450	343	3
Al-239	47.90	3.61	14.84	13.93	0.22	4.45	8.73	3.90	1.40	1.02	-0.56	0.17			21	45		17	117	285	28		26	20	451	353	4
Al-247	48.40	3.56	14.69	13.73	0.23	4.38	8.60	3.94	1.44	1.03	-0.54	0.21			13	42		25	135	294	27		26	24	444	334	4
Al-117	48.29	3.53	14.70	13.75	0.22	4.57	8.68	3.82	1.44	1.00	-0.75	0.23	4		14	48		22	123	260	27		25	26	447	329	3
Al-118	47.95	3.61	14.60	13.98	0.21	4.66	8.74	3.87	1.36	1.02	-0.69	0.23	3	2.8	16	47	48.8	20	123	254	25	28.2	27	26	454	312	4
Al-132	48.53	2.78	15.88	11.83	0.19	5.15	9.47	3.86	1.32	0.99	0.26	0.40	53	66.5	40	39	43.3	53	94	213	25	25.4	24	27	491	319	4
Al-125	50.49	2.44	18.39	10.20	0.14	3.14	9.54	3.81	1.17	0.68	0.30	0.47	13		16	38		27	82	188	22		25	18	541	271	3
Al-265	48.43	3.20	15.20	13.70	0.18	4.36	9.03	3.95	1.33	0.62	0.34	0.44			41	49		37	98	320	28		25	28	492	323	4
Al-266	48.66	3.14	15.14	13.60	0.19	4.59	8.92	3.83	1.34	0.59	0.25	0.61			25	49		39	101	338	29		25	30	480	322	4
Al-246	48.46	3.16	15.08	13.61	0.20	4.78	9.16	3.63	1.27	0.65	-0.27	0.30			25	45		37	106	319	28		25	26	490	338	4
	Mugearite (intermediate Zr/Nb)																										
Al-221	50.21	2.94	15.42	12.26	0.22	4.09	7.71	4.40	1.65	1.10	-0.37	0.11			10	45		5	125	198	22		25	34	503	390	5
Al-222	50.56	2.85	15.52	11.95	0.23	3.90	7.62	4.52	1.66	1.19	0.20	0.14			7	39		3	124	194	20		25	35	500	393	5
Al-219	50.67	2.83	15.50	11.78	0.23	3.88	7.61	4.62	1.69	1.19	-0.52	0.68			11	44		5	130	188	21		26	36	499	391	5
Al-220	50.74	2.85	15.48	11.85	0.22	3.90	7.63	4.41	1.72	1.20	-0.06	0.12			12	42		4	125	186	19		26	36	504	404	5
Al-193	50.67	2.80	15.53	11.80	0.23	3.98	7.56	4.50	1.70	1.23	-0.22	0.10			9	51		3	128	181	20		27	36	505	399	4
Al-223	50.85	2.77	15.59	11.67	0.23	3.95	7.50	4.44	1.74	1.26	-0.15	0.08			8	34		4	128	175	21		26	37	506	407	5
Al-85	51.12	2.70	15.57	11.44	0.22	3.88	7.36	4.58	1.80	1.33	-0.49	0.26	3		6	34		4	123	138	20		27	38	504	401	5
Al-194	51.97	2.48	15.73	11.03	0.23	3.62	7.02	4.71	1.92	1.29	-0.08	0.28			14	43		3	130	135	21		28	39	504	439	5
Al-192	52.31	2.40	15.83	10.77	0.24	3.57	6.92	4.72	1.94	1.30	-0.03	0.24			8	46		3	134	129	18		27	40	502	446	5
Al-50	50.59	2.65	15.47	12.06	0.24	3.99	7.40	4.36	1.78	1.46	-0.29	0.29	5		8	44		14	136	140	22		25	36	475	408	5
Al-101	50.99	2.62	15.40	11.91	0.23	3.80	7.51	4.32	1.77	1.45	0.01	0.57	5	1.9	5	33	31.5	6	144	133	22	20.5	27	34	475	402	5
Al-178	50.78	2.62	15.50	11.87	0.24	3.92	7.39	4.44	1.75	1.49	-0.13	0.44	3		8	34		3	140	141	23		27	32	478	427	5
Al-51	51.04	2.62	15.47	11.97	0.24	3.80	7.30	4.31	1.83	1.42	-0.13	0.42	4		9	39		11	146	138	21		26	36	472	419	5
Al-166	50.88	2.57	15.62	11.70	0.24	3.76	7.39	4.65	1.75	1.44	0.16	0.34	5	2.2	11	33	30.0	5	151	132	20	21.0	26	34	487	413	5
Al-276	50.82	2.61	15.54	11.91	0.26	3.76	7.29	4.61	1.75	1.45	-0.57	0.68			12	41		6	144	159	21		25	33	476	422	5
Al-191	52.31	2.61	15.65	11.93	0.25	3.70	6.93	3.48	1.76	1.38	1.16	1.59			9	46		8	144	144	23		26	36	452	397	4
Al-90	51.18	2.78	15.61	11.67	0.23	4.02	7.42	4.21	1.76	1.12	-0.22	0.33	12		6	18		4	132	162	20		25	38	493	384	4
Al-291	51.48	2.81	16.18	11.36	0.21	3.81	7.38	3.69	1.82	1.26	0.83	1.20			4	37		4	145	147	21		26	37	668	414	4
Al-38	50.94	2.74	15.50	11.92	0.23	3.86	7.41	4.41	1.72	1.27	0.37	0.33	6		13	63		8	140	156	26		26	39	604	413	6
Al-287	51.62	2.60	15.52	11.81	0.23	3.84	7.05	4.20	1.76	1.37	0.60	1.06			18	33		7	146	160	22		28	46	623	435	6
Al-296	51.80	2.55	15.59	11.84	0.25	2.92	7.19	4.69	1.79	1.38	0.58	0.34			14	35		5	142	142	23		26	38	534	420	5
Al-143	51.90	2.22	16.90	10.14	0.18	4.43	8.08	3.87	1.59	0.69	1.03	0.75	60	70.6	51	28	24.2	35	120	161	22	20.3	26	32	571	369	5
Al-145	52.54	3.15	16.20	13.15	0.20	3.36	5.91	3.51	1.31	0.67	3.31	3.11	5	6.6	17	28	26.4	20	139	170	28	15.8	28	38	435	316	7
Al-49	51.93	2.50	16.52	10.12	0.21	3.50	6.88	4.97	2.26	1.11	-0.24	0.25	5		6	29		10	132	159	21		25	53	701	573	8
Al-78	52.06	2.70	15.13	12.10	0.24	3.73	7.19	4.34	1.62	0.89	-0.22	0.37	4		12	38		11	146	129	23		27	31	471	470	4
Al-255	52.29	2.49	16.47	10.60	0.17	3.42	7.13	4.70	2.06	0.67	-0.08	0.39			17	33		26	114	215	17		26	46	636	481	6
Al-254	52.44	2.45	16.72	9.80	0.18	3.37	7.46	4.76	2.04	0.78	-0.12	0.31			13	33		22	114	192	21		26	40	592	487	7
Al-142	52.25	2.29	15.64	10.97	0.23	3.39	7.02	4.89	1.98	1.34	0.17	0.50	3		6	34		3	143	110	21		26	35	457	442	5
Al-13	52.79	2.25	15.89	11.14	0.24	3.29	6.53	4.53	2.03	1.31	0.14	0.64	3	12.0	7	11	15.4	7	143	113	20	19.2	28	41	455	497	6
Al-55	53.06	2.33	16.61	10.16	0.20	3.10	6.35	4.93	2.10	1.16	0.12	0.57	3		6	22		5	134	75	16		29	42	653	511	6
Al-80	53.06	2.20	17.68	9.34	0.15	2.89	7.52	4.54	1.84	0.78	0.14	0.66	15		13	29		15	99	138	17		26	42	557	468	6
Al-275	53.66	2.15	15.74	10.49	0.23	2.81	6.65	4.89	2.12	1.26	-0.12	1.09			7	27		6	151	106	18		27	40	452	474	6

	SiO_2	TiO_2	Al_2O_3	Fe_2O_3	MnO	MgO	CaO	Na_2O	K_2O	P_2O_5	LOI	H_2O-	Cr xrf	Cr inaa	Ni xrf	Co xrf	Co inaa	Cu xrf	Zn xrf	V xrf	Sc xrf	Sc inaa	Ga xrf	Rb xrf	Sr xrf	Ba xrf	Th xrf
AI-171	53.39	2.19	15.41	10.79	0.24	3.27	7.44	4.31	1.66	1.30	0.46	1.16	3	2.0	8	23	20.8	2	147	83	23	20.6	27	32	479	374	4
AI-84	53.81	2.21	15.57	11.09	0.26	3.12	6.37	4.55	1.82	1.20	0.16	0.90	3		7	37		4	171	78	23		28	34	486	392	4
AI-267	53.02	2.30	15.86	10.50	0.24	3.25	6.49	5.14	2.08	1.12	-0.66	0.48			10	30		3	136	122	18		27	42	467	496	6
AI-112	54.43	2.13	15.86	10.41	0.23	3.13	6.32	4.92	1.80	0.77	-0.08	0.31	4	3.7	11	28	30.7	8	142	81	22	22.6	28	34	478	502	4
AI-165	55.29	2.07	15.70	10.21	0.25	2.94	5.89	4.85	1.99	0.81	0.13	0.48	3	7.5	6	25	25.4	11	151	74	19	22.2	28	39	446	525	5
AI-113	55.18	1.94	16.21	10.16	0.26	2.77	5.71	4.49	2.26	1.02	0.94	0.70	5		10	8		6	157	81	20		27	46	513	518	5
AI-244	53.08	1.97	16.70	9.65	0.17	4.21	7.69	4.30	1.73	0.50	-0.28	0.19			47	40		28	98	174	21		25	37	444	592	6
	Benmoreite (intermediate Zr/Nb)																										
AI-185	54.74	1.96	16.83	9.26	0.26	2.88	5.59	5.30	2.20	0.98	0.56	0.36			6	37		<2	159	74	17		27	45	500	493	6
AI-184	56.72	1.74	16.61	8.55	0.23	2.23	5.23	5.59	2.30	0.80	0.13	0.46			6	62		<2	144	57	16		28	44	485	514	6
AI-130	55.31	1.86	16.09	9.91	0.25	2.53	5.44	5.43	2.34	0.84	0.24	0.12	3	3.5	5	19	18.9	3	143	63	18	17.1	28	46	433	559	6
AI-168	55.50	1.89	16.57	8.97	0.23	2.88	5.64	5.16	2.25	0.91	-0.13	0.13	4		5	24		<2	136	64	18		27	48	480	507	6
AI-57	55.33	1.92	16.37	9.09	0.22	2.84	5.81	5.15	2.27	1.00	-0.33	0.25	4		6	33		3	131	66	17		29	49	485	509	6
AI-122	55.59	1.87	16.21	9.99	0.27	2.66	5.49	4.72	2.35	0.85	0.63	0.24	5	1.7	6	7	7.7	2	165	56	20	16.0	28	49	436	540	6
AI-186a	55.46	1.89	16.07	9.41	0.26	2.76	5.47	5.52	2.22	0.94	0.01	0.16			6	49		2	142	86	21		28	43	440	488	6
AI-186	56.03	1.87	15.76	9.29	0.25	2.66	5.43	5.41	2.36	0.94	0.24	0.36			7	54		5	140	79	18		27	45	418	466	6
AI-199	56.17	1.73	16.90	8.48	0.24	2.31	5.26	5.75	2.39	0.77	0.18	0.44			5	38		<2	149	56	17		28	48	495	522	7
AI-47	56.46	1.73	16.81	8.52	0.25	2.58	5.22	5.31	2.36	0.76	0.15	0.39	4		5	47		6	155	44	18		27	48	489	528	6
AI-272	56.63	1.70	16.85	8.38	0.26	2.29	5.11	5.61	2.42	0.75	0.32	0.31			6	20		2	151	49	17		27	49	496	538	7
AI-52	56.32	1.80	16.06	9.67	0.26	2.76	5.46	4.88	1.91	0.88	0.42	0.51	4		7	34		<2	153	52	21		29	41	460	454	5
AI-54	56.69	1.70	16.08	9.33	0.24	2.63	5.32	5.15	2.07	0.79	-0.33	0.35	4	3.5	6	39	32.5	<2	148	48	21	19.5	29	43	456	455	5
AI-260	56.48	1.76	17.48	7.94	0.18	2.17	4.66	5.71	2.88	0.74	0.13	0.55			5	22		3	130	65	17		29	49	493	632	9
AI-71	57.71	1.47	16.61	8.21	0.22	2.20	4.68	5.58	2.63	0.69	-0.17	0.28	2		7	31		<2	135	38	15		29	56	422	582	8
AI-176	57.30	1.52	16.64	8.31	0.23	2.30	4.85	5.55	2.56	0.74	0.13	0.17	4	2.0	5	22	20.7	2	139	44	15	13.7	28	56	431	584	7
AI-48	57.79	1.47	17.02	7.86	0.25	2.15	4.66	5.59	2.60	0.61	0.01	0.29	3		10	29		3	147	29	15		28	52	456	576	6
AI-140	57.40	1.53	17.07	7.98	0.23	2.23	4.79	5.57	2.54	0.66	0.05	0.52	3	2.1	9	17	17.1	4	144	36	19	14.4	28	51	466	542	8
AI-92	58.40	1.44	16.92	7.53	0.21	2.13	4.55	5.60	2.65	0.57	-0.05	0.28	2		5	23		2	132	35	14		29	57	440	589	7
AI-137	60.06	1.22	16.08	8.10	0.25	1.75	4.07	5.44	2.57	0.46	0.48	0.46	3	2.2	8	17	16.4	2	163	16	18	18.1	30	51	388	567	6
AI-73	60.95	1.13	16.05	7.70	0.26	1.49	3.85	5.54	2.63	0.40	0.34	0.43	3		7	21		<2	167	12	19		31	56	374	597	7
AI-245	57.79	1.60	15.86	8.99	0.23	1.94	4.86	5.22	2.93	0.58	0.37	0.29			6	25		8	154	60	15		28	68	365	582	10
	Dark Slope Crater																										
AI-4	48.49	2.89	16.22	13.23	0.18	4.21	8.47	3.74	1.62	0.95	0.40	0.70	42	41.4	50	35	37.8	35	142	245	24	24.5	27	34	721	449	5
AI-205	48.27	2.85	15.87	12.91	0.24	4.94	8.49	3.96	1.63	0.84	0.12	0.48			51	61		38	135	241	22		26	34	717	497	5
AI-202	48.18	2.84	15.73	12.67	0.17	5.36	8.88	3.84	1.55	0.78	-0.12	0.36			37	60		42	122	233	26		26	29	729	411	5
AI-150	48.27	2.79	15.87	12.55	0.17	5.29	8.62	4.03	1.61	0.80	-0.18	0.26	22	29.1	42	52	56.1	40	107	190	20	24.2	26	36	754	423	5
AI-153	48.56	2.90	15.99	12.77	0.16	4.95	8.36	3.77	1.67	0.87	0.33	0.71	19		48	60		42	118	174	21		28	37	777	436	5
AI-154	48.33	2.89	15.86	12.81	0.17	5.09	8.62	3.82	1.57	0.84	0.02	0.46	22	24.6	41	61	57.5	39	118	203	23	25.7	26	33	719	402	5
AI-155	48.95	2.82	16.23	12.87	0.16	4.61	8.40	3.59	1.58	0.79	0.46	1.06	27	28.1	47	55	53.4	43	146	215	26	25.8	27	27	716	395	5
AI-156	49.65	2.87	16.51	12.47	0.13	4.24	8.02	3.62	1.65	0.84	0.96	1.54	28	31.2	45	47	50.5	32	143	209	24	24.4	26	27	682	374	5
AI-31	48.84	2.92	15.77	12.40	0.18	3.91	8.97	4.16	1.86	0.99	0.92	1.08	17		35	68		26	137	194	25		26	37	758	436	4
AI-2	48.51	2.72	15.73	12.88	0.18	5.20	8.13	3.92	1.82	0.91	0.18	0.72	45	51.9	52	39	38.8	36	131	221	22	21.7	25	41	782	458	5
AI-203	49.07	2.71	15.99	12.07	0.20	4.71	7.84	4.39	2.05	0.97	-0.52	0.18			28	48		40	145	163	18		30	47	902	544	7
AI-204	48.99	2.70	16.04	12.07	0.17	4.68	7.86	4.47	2.05	0.97	-0.41	0.21			28	54		35	129	166	17		29	47	894	535	7
AI-6	52.12	1.83	16.71	10.44	0.18	3.43	6.15	5.20	2.69	1.25	0.28	0.53	11	11.9	31	18	21.6	16	154	90	15	13.1	30	66	1105	720	9
AI-108	49.03	3.25	15.16	13.17	0.19	4.57	8.37	3.95	1.45	0.86	-0.36	0.36	17		29	52		29	126	280	28		27	26	605	341	6

	SiO_2	TiO_2	Al_2O_3	Fe_2O_3	MnO	MgO	CaO	Na_2O	K_2O	P_2O_5	LOI	H_2O-	Cr xrf	Cr inaa	Ni xrf	Co xrf	Co inaa	Cu xrf	Zn xrf	V xrf	Sc xrf	Sc inaa	Ga xrf	Rb xrf	Sr xrf	Ba xrf	Th xrf
Al-289	48.86	3.24	15.12	13.15	0.23	4.33	8.50	4.15	1.53	0.89	-0.24	0.42			31	43		33	125	320	27		27	34	596	378	4
Al-298	52.26	1.89	17.15	9.33	0.14	3.93	7.33	5.34	2.07	0.56	-0.43	0.48			31	41		33	108	181	18		27	50	864	524	7
Al-264	52.44	1.92	17.28	9.37	0.16	4.01	7.25	4.89	2.15	0.53	0.02	0.17			30	39		38	121	208	18		25	53	850	516	8
Broken Tooth																											
Al-88	54.67	2.15	15.64	10.04	0.23	2.99	5.95	5.08	2.22	1.03	0.21	0.57	4		7	44		6	134	94	22		27	37	418	481	5
Al-86	54.75	2.12	15.64	9.95	0.23	2.99	5.86	5.10	2.34	1.02	0.01	0.28	4		6	32		4	125	91	21		28	40	410	475	5
Al-87	54.75	2.11	15.72	9.92	0.23	3.15	5.93	5.01	2.20	0.98	0.46	0.27	3	2.7	7	31	32.7	3	131	96	21	20.4	26	37	418	482	5
Al-217	55.19	2.07	15.65	9.83	0.22	2.91	5.71	5.06	2.35	1.01	0.03	0.18			5	12		8	124				26	40	406		5
Al-77	56.48	1.83	15.81	9.04	0.22	2.41	4.96	5.49	2.78	0.98	0.69	0.36	3	2.6	5	40	34.3	7	133	82	20	19.6	28	44	339	511	4
Al-76	60.05	1.24	15.98	7.19	0.20	2.10	3.37	5.55	3.65	0.67	0.92	0.42	2	4.0	4	35	33.2	3	110	46	14	18.6	28	51	203	573	6
Al-216	58.53	1.49	15.90	8.08	0.24	2.01	4.42	5.75	2.89	0.69	-0.07	0.58			4	28		5	143	53	15		29	54	353	448	7
	Trachyte																										
Al-59	61.36	0.90	16.98	6.66	0.21	0.93	2.87	6.36	3.28	0.45	0.13	0.37	1		4	8		5	150	3	13		31	49	322	1125	8
Al-83	63.47	0.69	16.85	5.69	0.18	0.75	2.28	6.36	3.51	0.22	0.09	0.45	9		4	14		4	140	3	12		32	69	298	804	10
Al-111	63.91	0.65	16.81	4.93	0.12	0.44	1.62	6.72	4.46	0.34	0.95	0.27	9	2.0	<2	17	15.7	4	71	19	15	13.2	28	63	184	1304	6
Al-190	65.10	0.54	16.38	5.01		0.32	1.25	6.94	4.36	0.10	0.02	0.08			6	<2		<2	111				30	82	27		10
Al-119	65.29	0.69	15.82	5.33	0.13	0.44	1.71	6.00	4.38	0.21	0.25	0.32	2		3	25		6	102	10	10		30	107	135	1057	15
Al-126	65.40	0.56	16.62	4.63	0.12	0.36	1.36	6.38	4.43	0.14	0.21	0.15	2	3.3	2	13	11.3	10	105	8	8	8.7	29	104	140	990	14
Al-164	65.67	0.48	15.44	5.60	0.18	0.10	1.29	6.55	4.58	0.11	0.69	0.68	2		3	25		4	100	5	18		29	63	50	1544	7
Al-109	65.35	0.47	15.23	5.63	0.16	0.05	0.76	6.36	5.00	0.99	0.58	0.42	1	2.1	<2	15	13.5	4	110	6	13	14.0	30	69	24	1153	7
Al-163	66.06	0.43	15.23	5.44	0.20	0.08	1.06	6.41	4.86	0.23	0.13	0.25	1		<2	18		5	113	4	12		32	70	13	938	7
Al-70	65.60	0.43	16.06	4.16	0.12	0.33	2.15	6.14	4.87	0.14	0.39	0.66	3		4	11		13	73	14	11		31	84	78	373	10
Al-169	65.90	0.42	16.14	4.97	0.22	0.28	1.65	6.62	3.71	0.09	0.12	0.14	2		4	19		2	150	3	9		33	76	135	780	9
Al-116	65.99	0.43	15.87	4.79	0.18	0.25	1.20	6.73	4.49	0.07	0.23	0.15	1		2	15		4	126	4	11		30	81	13	1305	9
Al-294	66.09	0.43	15.22	5.51		0.08	1.06	6.43	5.13	0.05	-0.01	0.08			4	<2		2	126				32	80	7		9
Al-79	66.00	0.41	15.69	5.28	0.24	0.17	0.73	6.73	4.67	0.08	0.29	0.40	1	3.1	3	15	12.5	3	167	3	11	9.7	35	79	29	710	9
Al-282	66.59	0.40	15.29	5.15		0.13	0.89	6.82	4.65	0.08	0.27	0.11			6	<2		<2	165				33	84	23		10
Al-103	66.58	0.45	15.54	5.85	0.12	0.04	0.38	6.04	4.94	0.06	0.95	1.24	1	1.6	2	14	10.6	<2	151	3	12	9.2	33	81	4	644	10
Al-104	66.23	0.43	15.35	5.59	0.17	0.14	0.60	6.23	5.22	0.04	0.46	0.65	2		<2	14		2	138	4	14		33	80	8	200	9
Al-105	66.54	0.46	16.44	5.00	0.11	0.17	1.12	6.14	3.94	0.08	0.85	0.64	1		2	16		7	115	6	7		31	79	129	844	11
Al-115	66.70	0.34	15.69	4.28	0.18	0.14	1.00	6.64	4.99	0.04	0.21	0.09	1		2	16		3	145	3	10		29	97	3	641	12
Al-175	66.84	0.41	15.45	4.68	0.18	0.28	1.04	6.73	4.30	0.09	0.15	0.14	1	4.0	<2	19	15.7	3	136	7	8	10.8	31	94	24	919	11
Al-99	66.95	0.39	15.49	5.54	0.12	0.08	0.41	6.05	4.93	0.04	0.82	1.39	2		3	19		2	174	3	10		32	93	5	296	11
Al-41	66.93	0.33	15.43	4.41	0.17	0.22	1.03	6.76	4.68	0.04	0.93	0.29	<1	1.7	<2	17	12.5	4	145	4	10	11.3	31	88	15	1011	10
Al-228	67.74	0.31	15.59	4.28		0.08	0.91	6.21	4.85	0.03	0.29	0.10			6	<2		4	140				31	94	10		10
Al-91	67.39	0.35	15.60	4.32	0.13	0.09	0.40	6.57	5.10	0.05	0.25	0.47	1	3.2	2	15	11.1	3	155	4	6	5.7	33	109	7	219	14
Al-17	67.45	0.35	15.12	5.48	0.17	0.04	0.44	5.88	4.94	0.13	0.00	1.01		2.9	<2	<2	0.2	3	163	4	4	3.7	35	98	2	194	13
Al-268	67.54	0.30	15.63	4.24		0.15	1.13	6.71	4.25	0.05	0.20	0.06			4	<2		3	146				30	92	41		11
Al-66	67.56	0.35	15.23	4.46	0.15	0.13	0.88	6.09	5.11	0.04	-0.05	0.13	2		2	6		6	116	4	9		29	120	6	471	15
Al-129	68.49	0.32	14.29	4.75	0.18	0.12	0.66	6.08	5.08	0.03	0.26	0.13	4		2	15		5	172	4	7		33	142	2	33	19
Al-96	68.82	0.40	14.18	4.75	0.19	0.22	0.68	6.18	4.52	0.06	-0.08	0.29	1	1.7	<2	5	6.1	4	167	5	10	9.6	34	87	10	516	12
Al-67	67.28	0.37	15.34	4.62	0.16	0.11	0.88	6.07	5.11	0.06	0.00	0.18	2	1.5	3	8	7.3	10	126	4	9	12.2	32	117	7	554	16
Al-241	70.07	0.22	14.60	3.49		0.08	0.29	6.25	4.98	0.02	0.33	0.05			7	<2		3	129				33	129	1		15
Al-242	70.26	0.22	14.55	3.48		0.06	0.38	6.06	4.98	0.01	0.03	0.06			5	<2		2	147				33	136	1		17
Al-243	69.78	0.22	14.54	3.49		0.09	0.55	6.39	4.93	0.01	0.98	0.18			6	<2		<2	162				32	132	1		17
Al-95	69.32	0.29	14.89	4.04	0.17	0.07	0.73	6.33	4.13	0.03	0.14	0.23	1		<2	10		2	148	3	12		30	82	15	886	10

	SiO_2	TiO_2	Al_2O_3	Fe_2O_3	MnO	MgO	CaO	Na_2O	K_2O	P_2O_5	LOI	H_2O-	Cr xrf	Cr inaa	Ni xrf	Co xrf	Co inaa	Cu xrf	Zn xrf	V xrf	Sc xrf	Sc inaa	Ga xrf	Rb xrf	Sr xrf	Ba xrf	Th xrf
AI-147	69.89	0.22	14.55	3.47	0.13	0.07	0.48	6.11	5.06	0.02	0.08	0.36	3		2	8		4	149	5	5		34	132	1	72	16
AI-248	70.29	0.20	14.07	3.70	0.17	0.02	0.36	6.16	5.01	0.02	0.28	0.09			<2	23		6	167	4	4		34	143	2	14	20
AI-94	72.53	0.23	12.68	3.70	0.12	0.06	0.33	5.60	4.72	0.03	0.37	0.23	1		<2	13		<2	197	4	3		35	126	1	69	17
AI-93	72.78	0.21	12.57	3.72		0.00	0.37	5.63	4.71	0.01	0.23	0.07			5	<2		2	210				32	129	2		17
AI-261	72.97	0.22	12.41	3.68		0.00	0.36	5.69	4.66	0.01	0.37	0.09			7	<2		2	216				33	132	2		17
AI-177	73.75	0.14	12.76	2.97	0.08	0.02	0.32	5.28	4.65	0.03	0.36	0.12	<1	0.9	<2	16	14.2	4	189	5	2	1.4	35	161	1	24	19
AI-131	72.78	0.17	12.94	3.32	0.12	0.04	0.42	5.58	4.62	0.01	0.29	0.09	<1	1.4	<2	16	12.7	5	216	3	2	2.2	35	179	2	20	22
	Pumice																										
AI-19	61.07	1.11	17.40	7.06	0.25	1.17	3.47	5.50	2.54	0.43	1.98	1.43	2		2	<2		3	162	19	14		29	54	456	696	7
AI-21	62.40	0.89	16.80	6.37	0.24	0.95	2.91	5.97	3.12	0.35	1.42	0.65	3		2	<2		4	162	14	11		29	59	334	841	7
AI-20	65.57	0.61	16.53	5.31	0.21	0.75	1.73	5.37	3.70	0.22	4.69	1.85	2		<2	<2		2	152	6	11		27	60	114	1118	9
AI-15	66.68	0.38	14.59	5.68	0.22	0.03	0.87	6.41	5.00	0.14	0.27	0.83		9.8	<2	<2	0.2	4	179	3	8	7.4	31	95	3	389	11
AI-18	67.83	0.34	14.36	6.04	0.23	0.12	0.61	4.73	5.40	0.34	4.88	2.15	2		2	<2		<2	233	3	5		36	135	3	32	18
AI-135	66.56	0.40	14.44	5.81	0.22	0.34	0.86	6.03	5.29	0.05	5.45	2.33	<1	2.0	<2	54	48.9	5	203	4	8	6.7	33	118	20	49	15
AI-174	67.38	0.52	20.38	4.58	0.22	0.41	1.14	2.71	2.54	0.12	7.69	5.98	<1	3.9	2	34	31.0	2	311	9	9	7.4	25	73	74	799	8
AI-98	67.67	0.33	14.69	5.06	0.18	0.20	0.80	5.54	5.50	0.03	4.97	1.86	1		<2	101		2	202	3	8		32	115	4	114	13
AI-114	67.88	0.26	15.26	3.94	0.15	0.21	0.92	5.92	5.37	0.09	3.78	1.01	1		<2	46		5	151	5	8		30	116	8	133	15
AI-238	61.36	0.82	18.75	7.48		0.81	2.28	5.45	2.72	0.33	5.76	3.18			2	3		6	137				29	50	182		9
AI-39	66.03	0.44	16.84	4.34	0.19	0.49	1.23	5.17	5.15	0.12	5.51	1.57	<1		<2	52		<2	162	6	9		28	107	54	969	13
AI-42	72.07	0.23	13.26	4.38	0.12	0.25	0.42	3.58	5.66	0.03	5.25	2.35	<1	3.1	2	66	53.1	3	256	6	5	1.7	35	188	7	21	25
AI-43	66.95	0.39	16.51	4.79	0.15	0.61	1.29	4.99	4.27	0.05	6.00	3.08	<1		<2	62		2	162	8	13		30	83	67	705	11
AI-44	68.72	0.34	14.63	5.29	0.12	0.57	0.58	4.88	4.80	0.07	5.54	4.33	<1	2.7	<2	71	55.9	10	188	10	5	3.2	33	115	16	107	17
AI-45	50.60	3.05	15.28	13.74	0.17	4.82	7.92	3.00	0.92	0.50	1.83	4.22	24		37	68		45	141	250	34		22	25	400	174	2
AI-229	68.81	0.35	14.66	4.38		0.25	0.90	5.76	4.84	0.05	3.69	0.95			5	<2		2	178				29	119	24		15
AI-293	70.35	0.24	13.26	4.80		0.10	0.46	5.76	5.01	0.02	2.46	1.02			6	<2		<2	240				34	146	5		20
AI-143	51.90	2.22	16.90	10.14	0.18	4.43	8.08	3.87	1.59	0.69	1.03	0.75	60	70.6	51	28	24.2	35	120	161	22	20.3	26	32	571	369	5
AI-144	68.40	0.34	15.07	5.24	0.17	0.43	0.72	4.28	5.32	0.03	3.79	4.89	<1	3.7	2	48	40.8	5	209	5	6	5.6	34	115	7	84	15
AI-145	52.54	3.15	16.20	13.15	0.20	3.36	5.91	3.51	1.31	0.67	3.31	3.11	5	6.6	17	28	26.4	20	139	170	28	15.8	28	38	435	316	7
AI-146	66.68	0.45	15.03	5.02	0.16	0.41	1.46	5.35	5.13	0.31	2.72	2.77	1	7.1	2	50	47.4	8	160	13	9	7.4	31	102	47	220	12
AI-120	63.59	0.52	16.25	5.71	0.19	0.60	2.00	6.82	4.20	0.12	4.67	1.16	<1	1.9	2	62	57.2	2	149	5	12	10.3	28	75	114	868	9
AI-121	60.99	0.85	16.57	7.48	0.25	0.99	3.18	6.23	3.21	0.25	1.68	0.35	3	3.3	<2	34	29.3	<2	162	7	17	12.6	29	64	270	833	8
AI-122	55.59	1.87	16.21	9.99	0.27	2.66	5.49	4.72	2.35	0.85	0.63	0.24	5	3.0	<2	7	8.1	2	165	56	20	17.1	28	49	436	540	6
AI-123	48.87	2.55	16.17	11.42	0.20	5.91	9.59	3.06	1.24	0.99	0.22	0.24	81	83.9	63	33	32.5	49	113	195	25	23.0	21	25	492	288	3
AI-256	68.08	0.28	15.56	3.92		0.28	1.18	6.34	4.28	0.08	1.73	0.62			5	<2		2	163				30	93	57		13
AI-181	64.89	0.45	16.26	5.16	0.19	0.39	1.80	5.93	4.71	0.22	3.96	1.23	<1		2	37		<2	149	6	10		28	78	78	920	9
	Boreholes																										
	GH1																										
GH1-1	48.61	3.51	14.32	14.19		4.47	8.56	3.71	1.34	1.29	-0.63	0.19			3	32		10	102				28	29	497		4
GH1-2	48.16	3.76	14.30	14.50		4.72	8.73	3.53	1.24	1.06	-0.64	0.12			4	44		12	107				27	26	470		3
GH1-3	49.43	2.46	16.09	12.20		4.87	10.78	3.02	0.76	0.39	0.70	0.99			45	51		64	80				21	13	403		2
GH1-4	49.19	2.44	16.34	12.24		4.62	10.84	3.19	0.75	0.39	0.80	1.14			46	48		73	81				21	13	399		2
GH1-5	49.32	2.40	16.45	12.04		4.63	10.84	3.15	0.77	0.40	0.97	1.19			44	50		59	73				23	14	413		<2
	GH2																										
GH2-1	50.89	2.54	15.50	11.97		5.30	8.53	3.51	1.32	0.44	-0.25	0.23			31	46		39	88				23	30	406		4
GH2-2	51.33	2.48	15.49	11.89		5.15	8.29	3.51	1.44	0.42	-0.38	0.22			34	48		39	90				25	33	385		4
GH2-3	54.24	2.29	15.70	10.92		3.21	6.45	4.53	1.85	0.81	0.13	0.30			5	31		6	146				27	38	459		4

	SiO_2	TiO_2	Al_2O_3	Fe_2O_3	MnO	MgO	CaO	Na_2O	K_2O	P_2O_5	LOI	H_2O-	Cr xrf	Cr inaa	Ni xrf	Co xrf	Co inaa	Cu xrf	Zn xrf	V xrf	Sc xrf	Sc inaa	Ga xrf	Rb xrf	Sr xrf	Ba xrf	Th xrf
GH2-4	68.94	0.28	15.00	3.77		0.14	0.52	6.20	5.12	0.03	0.32	0.48			5	11		2	141				30	143	7		19
GH2-5	66.86	0.38	16.11	4.23		0.27	1.10	6.51	4.48	0.06	0.34	0.20			5	13		<2	108				30	111	63		14
GH2-6	67.19	0.37	16.21	4.17		0.14	0.62	6.57	4.67	0.06	0.54	0.58			4	15		<2	150				30	116	55		8
GH2-7	53.23	2.61	15.34	11.64		2.74	6.60	4.72	1.84	1.28	0.67	1.25			<2	25		6	139				26	38	478		6
GH2-8	52.40	2.63	15.13	12.18		3.08	6.80	4.69	1.80	1.29	0.49	1.13			4	25		9	134				26	36	478		5
GH2-9	55.04	2.26	15.74	10.74		2.25	5.75	5.05	2.10	1.07	0.48	1.23			2	20		3	144				26	45	458		6
GH2-10	56.35	2.18	16.00	9.88		1.85	5.28	5.26	2.19	1.01	0.40	1.03			4	17		<2	128				27	46	457		5
GH2-11	56.94	1.87	15.85	9.40		1.95	5.38	5.46	2.33	0.82	0.39	0.65			<2	18		<2	148				27	50	425		5
GH2-12	49.92	3.30	15.06	13.01		3.46	6.62	4.09	1.34	1.20	0.73	1.33			6	31		6	114				25	29	505		4
GH2-13	74.99	0.16	12.54	2.61		0.06	0.19	4.82	4.62	0.01	0.30	0.29			5	26		<2	151				30	107	2		9
GH3																											
GH3-1	47.79	3.74	15.06	13.40		4.71	8.78	3.88	1.59	1.05	-0.82	0.16			4	62		11	97				25	36	582		4
GH3-2	47.83	3.72	15.05	13.35		4.65	8.73	4.02	1.61	1.04	-0.74	0.19			6	54		18	93				24	36	582		6
GH3-3	49.93	3.06	15.11	12.79		4.35	7.84	4.17	1.59	1.16	-0.79	0.10			14	52		3	115				26	34	590		5
GH3-4	50.47	2.89	15.33	12.33		4.13	7.58	4.37	1.70	1.20	-0.74	0.10			8	43		7	120				28	37	616		5
GH3-5	48.93	2.84	15.86	12.31		4.91	6.11	4.26	1.88	0.90	-0.50	0.16			25	58		26	117				27	44	816		5
GH3-6	49.51	2.69	16.01	11.95		4.70	7.84	4.12	2.20	0.98	-0.03	0.56			22	51		24	130				26	58	866		6
GH3-7	50.51	2.16	16.45	11.41		4.30	7.06	4.78	2.28	1.05	-0.41	0.19			32	53		19	136				27	57	981		7
GH3-8	52.10	1.77	16.98	10.18		3.44	5.97	5.47	2.81	1.28	-0.27	0.23			32	37		12	144				29	75	1172		9
GH4																											
GH4-1	59.12	1.47	16.52	7.83		1.84	4.16	5.70	2.80	0.56	-0.16	0.24			3	23		<2	173				28	57	468		5
GH4-2	61.95	0.92	16.86	6.48		1.12	2.97	6.22	3.19	0.29	-0.07	0.12			6	16		<2	155				30	68	387		5
GH4-3	49.19	2.54	15.30	12.99		5.66	9.43	3.50	0.96	0.43	-0.32	0.20			34	56		58	93				23	16	457		2
GH4-4	48.81	3.30	15.39	12.99		4.56	8.54	3.95	1.52	0.94	-0.33	0.23			7	47		17	116				27	32	647		2
GH4-5	49.66	3.19	15.80	12.42		3.90	8.17	4.20	1.66	1.00	0.09	0.68			<2	39		3	124				26	36	653		2
GH4-6	48.91	3.27	15.56	12.62		4.13	6.77	3.97	1.58	0.99	0.69	0.75			5	42		12	113				27	33	647		<2
GH4-7	49.05	3.27	15.54	12.84		4.28	8.54	3.93	1.59	0.96	0.26	0.48			3	43		18	108				26	34	657		3
GH4-8	49.05	3.25	15.65	12.82		4.37	8.46	4.00	1.47	0.93	-0.20	0.34			8	42		17	110				26	31	650		<2
GH5																											
GH5-1	48.48	3.58	14.34	14.30		4.67	8.47	3.70	1.29	1.17	-0.75	0.17			<2	49		21	113				26	27	472		2
GH5-2	48.52	3.61	14.27	14.18		4.68	8.53	3.75	1.28	1.18	-0.71	0.15			4	49		8	114				28	28	477		<2
GH5-3	48.75	3.52	14.37	14.01		4.56	8.45	3.80	1.32	1.22	-0.69	0.15			4	38		16	101				27	28	485		3
GH5-4	54.66	2.16	15.67	10.48		3.05	6.16	4.72	2.02	1.08	-0.27	0.19			3	25		<2	129				28	40	473		5
GH5-5	54.64	2.18	15.63	10.52		3.10	6.14	4.71	2.00	1.08	-0.32	0.20			4	26		2	131				28	40	471		5
GH5-6	61.12	1.04	17.53	6.01		1.31	3.17	6.29	3.15	0.38	0.04	0.21			4	14		11	158				28	66	494		9
GH5-7	49.15	2.25	17.78	10.60		5.59	9.83	3.22	1.06	0.52	0.67	0.75			66	45		49	103				23	22	503		3
GH5-8	49.13	2.35	16.97	11.26		5.94	9.49	3.25	1.09	0.52	0.53	0.67			73	48		41	92				23	24	485		4
GH5-9	65.25	0.84	14.89	6.48		0.51	1.59	6.75	3.51	0.18	0.44	0.78			5	9		4	111				28	46	28		5
GH6																											
GH6-1	69.49	0.32	14.41	4.19		0.19	0.50	6.03	4.83	0.04	0.30	0.48			5	10		<2	165				33	103	6		14
GH6-2	51.26	3.64	14.93	11.70		3.12	9.30	3.76	1.30	0.99	1.64	1.52			7	42		9	102				26	22	446		3
GH6-3	48.46	3.77	14.05	14.96		4.08	9.45	3.35	1.13	0.75	2.06	2.01			11	47		15	90				23	18	403		<2
GH6-4	48.33	4.17	14.85	13.91		4.09	9.51	3.33	1.15	0.66	1.16	1.19			28	53		22	95				25	19	435		2
GH6-5	53.74	2.60	20.28	7.81		1.33	8.91	3.72	1.05	0.56	2.41	1.34			22	66		40	117				25	19	541		3
LDTGH																											
LDT-1	49.98	3.52	14.81	12.84		3.61	8.89	4.04	1.34	0.97	1.44	1.39			6	48		10	105				26	30	449		4
LDT-2	66.68	0.76	16.76	4.33		0.27	2.64	5.85	2.45	0.26	1.62	1.40			5	26		<2	160				27	48	282		6

	Th inaa	Pb xrf	Zr xrf	Hf inaa	Nb xrf	Ta inaa	Y xrf	La xrf	Ce xrf	Nd xrf	La inaa	Ce inaa	Nd inaa	Sm inaa	Eu inaa	Tb inaa	Yb inaa	Lu inaa	Zr Nb	Ba Nb	Rb Nb	La Nb	K Nb	Zr Y	K Rb	P Zr
Gabbro xenoliths																										
Al-10		<2	4		<1		3	<2	<3	<2																
Al-7		<2	7		<1		5	<2	<3	<2																
Al-32		<2	8		0.8		8																			
Al-206		<2	7		0.6		7																			
Al-3		<2	3		<1		7	2	<3	<2																
Al-35		<2	5		0.7		7																			
Al-8		<2	8		<1		11	<2	<3	<2																
Al-5		<2	3	0.17	<1	0.04	22			4		5.3	4.1	1.08	0.67	0.31	1.11	0.17								
Al-9		<2	6	0.17	<1	0.04	7	<2		2		2.4	1.2	0.47	0.45	0.09	0.41	0.06								
Al-33		<2	5		1.1		7																			
Al-34		<2	4		1.3		3																			
Al-249h		<2	22		2.6		16												8.5				255	1.4	664	89
Al-249m		<2	25		4.5		24												5.6				203	1.0	457	63
Al-249a		<2	38		7.5		88												5.1				144	0.4	1079	48
Al-249f		<2	11		2.2		11												5.0				453	1.0		190
Al-249n		<2	6		2.1		10												2.9				435	0.6		335
Mafic xenoliths in trachyte																										
Al-224		<2	217		32		70												6.8		0.56		244	3.1	433	16.5
Al-226		3	238		40		64	46	79	56									6.0	6.9	0.55	1.15	216	3.7	396	11.0
Al-227		2	287		60		628	857	1207	635									4.8	5.9	0.60	14.3	245	0.5	408	17.2
Al-225		6	735		73		69												10.1		0.67		481	10.7	717	1.4
Al-234a		<2	188		36		36	32	59	32									5.2	36.2	0.53	0.89	297	5.2	564	11.6
Al-234b		2	190		37		69	56	76	48									5.1	34.2	0.57	1.51	278	2.8	490	11.5
Al-235c		8	278		63		48												4.4		0.52		252	5.8	480	17.9
Al-235d		47	290		65		45												4.5		0.29		209	6.4	717	16.1
Al-235e		40	332		77		61												4.3		0.51		258	5.4	509	22.7
Al-235b		19	296		63		114												4.7		0.43		278	2.6	649	13.3
Al-235a		3	317		68		67												4.7		0.57		337	4.7	587	21.8
Al-240		6	357		71		221												5.0		0.56		236	1.6	419	6.2
Al-250b		2	316		62		187	100	113	96									5.1	12.3	0.65	1.61	237	1.7	367	11.3
Al-250a		3	324		71		648	528	466	404									4.6	11.6	0.48	7.44	215	0.5	449	11.3
Al-97	5.38	<2	323	6.78	70	3.94	422	294	417	224	273	400	216	44.5	11.4	7.92	22.1	3.06	4.6	13.5	0.93	4.20	238	0.8	257	11.3
Syenite xenoliths																										
Al-187d		3	174		30		27												5.8		1.03		719	6.4	696	39.9
Al-187e		4	170		42		27	33	61	28									4.0	39.7	0.67	0.79	542	6.3	812	5.9
Al-187c		<2	590		56		32	41	75	31									10.5	27.0	0.55	0.73	504	18.4	910	7.6
Al-187f		3	171		33		24												5.2		0.91		795	7.1	874	16.1
Al-187a		2	240		35		24	29	51	23									6.9	46.4	0.71	0.83	840	10.0	1175	6.5
Al-187g		4	340		44		28												7.7		0.55		607	12.1	1114	8.9
Al-187b		3	414		31		26												13.4		1.03		777	15.9	752	3.8
Al-187h		3	616		56		25												11.0		0.63		544	24.6	870	2.3
Monzonite xenoliths																										
Al-249g		4	519		74		39												7.0		1.07		433	13.3	406	7.5
Al-249j		4	798		98		61												8.1		0.63		258	13.1	408	2.6

	Th inaa	Pb xrf	Zr xrf	Hf inaa	Nb xrf	Ta inaa	Y xrf	La xrf	Ce xrf	Nd xrf	La inaa	Ce inaa	Nd inaa	Sm inaa	Eu inaa	Tb inaa	Yb inaa	Lu inaa	Zr Nb	Ba Nb	Rb Nb	La Nb	K Nb	Zr Y	K Rb	P Zr
Al-249l		3	464		55		15												8.4		0.60		475	30.9	792	2.2
Al-249b		4	395		75		47												5.3		0.69		301	8.4	434	2.1
Al-249l		4	320		81		28												4.0		0.77		246	11.4	321	0.4
Al-249k		4	368		83		28												4.4		0.94		247	13.1	263	0.5
Al-249d		4	546		92		52												5.9		0.93		338	10.5	362	3.7
Al-249e		4	716		83		48												8.6		0.60		318	14.9	528	2.3
Al-249c		5	650		108		59												6.0		0.78		271	11.0	348	1.9
Trachyte/rhyolite xenoliths																										
Al-133i		8	1420		154		146												9.2		0.68		282	9.7	413	0.6
Al-133g		8	1397		155		111												9.0		0.66		274	12.6	412	0.4
Al-133b		11	1162		194		43												6.0		0.72		218	27.0	302	1.0
Al-133c		10	1616		180		184												9.0		0.66		234	8.8	354	0.6
Al-133f		11	1817		201		258												9.0		0.65		206	7.0	317	1.2
Al-133a		11	1565		204		102												7.7		0.66		192	15.3	290	1.0
Al-133h		11	1864		213		125												8.8		0.66		186	14.9	280	0.0
Al-133d		10	1906		249		117												7.7		0.63		158	16.3	250	0.2
Al-133e		16	1613		256		164												6.3		0.67		153	9.8	229	0.1
Granite xenoliths																										
Al-262		5	1037		198		85												5.2		0.44		199	12.2	453	0.1
Al-213d		4	860		138		49	45	94	46									6.2	0.35	0.66	0.33	272	17.6	413	0.15
Al-213a		3	1346		265		114	126	222	121									5.1	0.15	0.36	0.48	142	11.8	392	0.10
Al-213f		6	894		138		52	42	81	42									6.5	0.38	0.64	0.30	275	17.2	431	0.15
Al-213c		8	1752		315		242	269	479	289									5.6	0.10	0.50	0.85	118	7.2	237	0.12
Al-213g		18	3351		374		65	66	158	75									9.0	0.11	0.48	0.18	97	51.6	202	0.23
Al-213b		2	3137		491		231	118	241	127									6.4	0.09	0.22	0.24	79	13.6	360	0.08
Al-213e		<2	852		123		57	28	63	32									6.9	0.31	0.55	0.23	290	14.9	524	0.05
High Zr/Nb basalt																										
Al-173		<2	160		29		27	17	42	23									5.5	6.7	0.59	0.59	203	5.9	347	12.0
Al-230		<2	198		32		30	20	46	27									6.2	8.2	0.53	0.63	239	6.6	449	8.6
Al-45	2.59	<2	199	4.59	34	2.38	31	19	44	23	21.3	50.3	26.1	6.21	2.20	1.15	2.57	0.38	5.9	5.1	0.74	0.56	225	6.4	305	11.0
Al-148		<2	202		34		32	20	50	28									5.9	7.4	0.59	0.59	234	6.3	398	9.1
Al-237		<2	206		34		32	18	46	27									6.1	7.4	0.50	0.53	222	6.4	444	12.1
Al-172	2.42	<2	213	4.59	35	2.09	34	21	49	28	21.8	50.2	26.1	6.38	2.29	0.98	2.32	0.31	6.1	6.1	0.57	0.60	202	6.3	353	7.2
Al-134		<2	219		38		39	23	55	36									5.8	5.6	0.55	0.61	214	5.6	387	8.8
Al-14	1.84	<2	145	3.31	26	1.65	25	18	41	20	17.7	39.8	22.0	5.22	1.85	0.78	1.68	0.23	5.6	6.6	0.50	0.69	227	5.8	453	12.9
Al-201		<2	143		25		23	16	37	20									5.7	6.3	0.56	0.64	276	6.2	492	9.5
Al-200		<2	162		29		30	22	43	24									5.6	7.3	0.41	0.76	240	5.4	581	11.0
Al-127		<2	179		31		31	21	40	22									5.8		0.48	0.68	236	5.8	487	12.2
Al-124	2.41	<2	192	4.55	32	2.25	34	19	39	23	20.9	49.0	27.9	6.74	2.29	1.09	2.57	0.38	6.0	5.9	0.44	0.59	220	5.6	504	10.2
Al-149		<2	216		38		32	22	49	29									5.7	5.7	0.50	0.58	208	6.8	415	8.7
Al-110		2	223		37		37	24	58	29									6.0	5.6		0.65	206	6.0		8.2
Al-128	3.26	<2	227	5.54	38	2.65	39	27	57	29	25.4	60.2	31.2	7.50	2.39	1.25	3.04	0.40	6.0	6.2	0.53	0.71	242	5.8	461	8.7
Al-162		<2	182		32		33	20	37	22									5.7	6.2	0.56	0.63	239	5.5	424	9.6
Al-107	2.33	<2	188	4.88	33	2.27	40	22	53	32	23.3	53.4	31.4	7.36	2.44	1.08	2.90	0.36	5.7	6.1	0.55	0.67	236	4.7	433	10.7
Al-106		<2	190		32		40	27	51	29									5.9	6.3			187	4.8		10.1
Al-233		<2	180		30		33	19	45	25									6.0	7.0	0.40	0.63	219	5.5	546	10.2

	Th inaa	Pb xrf	Zr xrf	Hf inaa	Nb xrf	Ta inaa	Y xrf	La xrf	Ce xrf	Nd xrf	La inaa	Ce inaa	Nd inaa	Sm inaa	Eu inaa	Tb inaa	Yb inaa	Lu inaa	Zr Nb	Ba Nb	Rb Nb	La Nb	K Nb	Zr Y	K Rb	P Zr
AI-215		<2	225		37		35	24	53	31									6.1	6.3	0.46	0.65	197	6.4	430	10.1
AI-36		<2	245		43		68	42	70	44									5.7	6.2	0.56		220		394	12.3
AI-37	2.94	<2	237	5.72	42	3.09	40	26	60	35	28.5	65.7	34.7	8.34	2.87	1.21	2.73	0.34	5.6	6.2	0.45	0.62	210	5.9	463	11.4
AI-40		<2	223		40		39	26	60	34									5.6	6.1	0.48	0.65	203	5.7	428	12.3
AI-64	3.69	<2	244	5.96	41	3.03	41	27	67	34	29.9	65.5	32.7	8.13	2.67	1.23	3.16	0.47	6.0	7.0	0.68	0.66	261	6.0	382	8.0
AI-65		<2	248		43		42	30	64	36									5.8	6.4	0.67	0.70	259	5.9	384	7.7
	Low Zr/Nb hawaiite																									
AI-60	4.06	<2	235	5.36	58	3.85	40	32	79	39	35.3	75.2	39.3	8.98	3.12	1.30	2.88	0.38	4.1	6.5	0.47	0.55	202	5.9	433	18.9
AI-61		2	239		58		46	35	81	42									4.1	6.7	0.50	0.60	205	5.2	409	16.8
AI-152	4.29	2	242	5.35	59	3.92	46	35	82	44	37.4	83.2	43.5	9.69	3.49	1.55	3.42	0.46	4.1	7.0	0.56	0.59	225	5.3	402	17.9
AI-151		<2	252		61		45	39	82	46									4.1	7.0	0.57	0.64	218	5.6	379	18.2
AI-157	4.67	2	256	5.67	63	4.06	47	35	76	44	37.3	83.1	46.0	10.6	3.54	1.50	3.38	0.45	4.1	6.3	0.51	0.56	217	5.4	428	18.6
AI-258		<2	251		60		42	39	80	43									4.2	6.8		0.65	217	6.0		18.3
AI-211		2	259		63		42	37	82	42									4.1	6.9	0.54	0.59	217	6.2	403	18.5
AI-207		2	257		63		41	38	82	49									4.1	6.7	0.54	0.60	210	6.3	388	17.5
AI-212		<2	257		63		43	39	73	45									4.1	6.7	0.52	0.62	215	6.0	410	19.0
AI-208		2	268		65		42	37	80	43									4.1	6.4	0.58	0.57	204	6.4	350	16.6
	Intermediate Zr/Nb basalt and hawaiite																									
AI-1	1.70	<2	140	3.35	27	1.67	30	17	40	26	17.9	42.3	26.5	6.22	2.28	1.10	2.30	0.30	5.2	5.7	0.44	0.63	203	4.7	457	20.3
AI-100	1.70	<2	145	3.51	27	2.02	31	16	41	22	17.5	42.9	24.0	5.96	2.20	1.09	2.43	0.29	5.4	5.3	0.41	0.59	200	4.7	491	17.8
AI-102		<2	150		28		32	18	40	22									5.4	5.3	0.43	0.64	193	4.7	450	18.6
AI-158	1.89	<2	150	3.70	28	2.05	32	17	40	22	18.4	43.7	24.4	6.20	2.24	1.05	2.38	0.31	5.4	5.4	0.43	0.61	193	4.7	450	17.2
AI-259		<2	143		26		31	15	39	26									5.5	6.1	0.38	0.58	185	4.6	481	19.2
AI-170		<2	230		51		41	29	70	41									4.5	5.4	0.49	0.57	210	5.6	428	18.8
AI-123	3.25	2	233	5.17	52	3.10	42	30	73	41	32.8	75.6	41.7	9.7	3.34	1.48	2.98	0.36	4.5	5.5	0.48	0.58	198	5.5	412	18.5
AI-12		<2	242		50		44	31	65	40									4.8	5.4	0.44	0.62	188	5.5	426	17.7
AI-26		2	237		49		42	28	72	41									4.8	5.3	0.51	0.57	208	5.6	408	15.7
AI-27		<2	232		48		42	26	66	39									4.8	5.6	0.48	0.54	206	5.5	429	15.2
AI-28	2.73	<2	230	5.43	48	3.70	42	25	68	36	30.0	65.1	39.0	9.15	2.95	1.30	2.91	0.39	4.8	5.5	0.48	0.52	206	5.5	429	15.9
AI-62		<2	240		50		44	26	71	39									4.8	5.4	0.42	0.52	199	5.5	474	15.6
AI-195		<2	233		47		40	27	63	40									5.0	5.8	0.49	0.57	203	5.8	415	15.2
AI-197		<2	243		50		43	28	69	45									4.9	5.7	0.50	0.56	208	5.7	415	15.6
AI-196		<2	235		48		40	26	63	41									4.9	5.7	0.50	0.54	204	5.9	408	15.0
AI-29		<2	240		49		44	30	68	37									4.9	5.6	0.45	0.61	207	5.5	460	15.3
AI-210		<2	315		65		55												4.8		0.54		206	5.7	384	19.0
AI-297		<2	323		64		55	41	95	52									5.0	5.5	0.47	0.64	191	5.9	407	17.3
AI-299		<2	334		65		55	42	94	57									5.1	6.1	0.31	0.65	199	6.1	647	16.9
AI-30	4.36	2	318	7.20	65	4.58	58	43	97	55	44.6	102	54.7	13.3	4.41	1.87	4.08	0.54	4.9	5.4	0.42	0.66	189	5.5	455	20.7
AI-290		2	320		65		58	44	100	59									4.9	5.6	0.43	0.68	201	5.5	465	20.9
AI-295		<2	340		68		62	48	103	58									5.0	5.8	0.46	0.71	198	5.5	434	20.4
AI-231		2	344		69		61	44	101	63									5.0	5.3	0.49	0.64	207	5.6	420	20.0
AI-288		<2	352		67		58	47	103	59									5.3	6.0	0.40	0.70	201	6.1	498	15.0
AI-209		<2	354		67		44	43	87	49									5.3	5.5	0.54	0.64	198	8.0	369	12.6
AI-236		<2	307		58		56	37	85	54									5.3	6.0	0.45	0.64	187	5.5	418	20.0
AI-263		<2	316		60		59	38	91	53									5.3	6.0	0.38	0.63	185	5.4	484	19.2
AI-232		<2	335		63		58	40	92	58									5.3	6.2	0.48	0.63	203	5.8	426	18.9

	Th inaa	Pb xrf	Zr xrf	Hf inaa	Nb xrf	Ta inaa	Y xrf	La xrf	Ce xrf	Nd xrf	La inaa	Ce inaa	Nd inaa	Sm inaa	Eu inaa	Tb inaa	Yb inaa	Lu inaa	Zr Nb	Ba Nb	Rb Nb	La Nb	K Nb	Zr Y	K Rb	P Zr
Al-273		<2	271		50		45	33	65	33									5.4	6.1	0.52	0.66	226	6.0	434	8.4
Al-274		2	270		50		49	35	71	37									5.4	6.4	0.50	0.70	213	5.5	425	8.1
Al-46		2	320		68		58	40	96	57									4.7	5.3	0.47	0.59	193	5.5	410	18.1
Al-53		<2	332		70		60	39	101	58									4.7	5.1	0.43	0.56	183	5.5	426	18.4
Al-139	4.89	2	353	7.46	76	4.51	63	47	111	63	49.1	115	61.4	14.1	4.72	2.10	4.89	0.57	4.6	4.9	0.49	0.62	185	5.6	379	19.5
Al-141		<2	222		46		44	30	66	41									4.8	5.7	0.43	0.65	180	5.0	415	21.2
Al-198		<2	221		46		44												4.8		0.52		197	5.0	384	22.9
Al-138	3.09	<2	221	4.85	46	3.22	48	29	74	44	30.7	73.1	37.5	9.92	3.78	1.77	3.50	0.42	4.8	6.1	0.37	0.63	189	4.6	513	21.7
Al-56		<2	316		64		49	39	84	47									4.9	5.5	0.52	0.61	208	6.4	402	14.4
Al-159b	3.77	<2	272	6.22	56	3.64	54	35	83	50	37.3	85.3	47.0	12.3	4.06	1.88	3.79	0.48	4.9	5.7	0.48	0.63	187	5.0	387	18.8
Al-160		<2	272		55		54	34	85	49									4.9	5.9	0.47	0.62	190	5.0	402	18.8
Al-167		2	277		57		53	33	83	47									4.9	5.4	0.42	0.58	176	5.2	419	18.7
Al-253		<2	288		59		55	37	89	57									4.9	5.7	0.39	0.63	186	5.2	476	19.2
Al-277		<2	282		58		54	36	87	52									4.9	5.7	0.38	0.62	182	5.2	479	18.0
Al-278		<2	282		58		62	40	93	51									4.9	6.1	0.38	0.69	183	4.5	483	18.3
Al-180		<2	279		58		52	36	85	49									4.8	5.0	0.47	0.62	183	5.4	394	18.1
Al-179		<2	292		59		56	38	88	51									4.9	5.9	0.46	0.64	183	5.2	400	17.6
Al-271		2	296		61		59	41	90	55									4.9	5.6	0.43	0.67	181	5.0	425	18.6
Al-58		<2	290		59		55	36	88	52									4.9	5.3	0.46	0.61	189	5.3	412	18.8
Al-24		3	310		62		49	36	86	49									5.0	5.9	0.50	0.58	205	6.3	410	14.8
Al-25	4.17	<2	321	7.11	64	3.87	51	37	90	47	41.9	95.9	50.6	11.5	4.12	1.83	3.95	0.50	5.0	5.9	0.52	0.58	206	6.3	400	15.2
Al-159a		<2	324		64		50	37	88	49									5.1	5.5	0.50	0.58	201	6.5	402	13.6
Al-161	4.14	<2	306	6.61	62	3.91	48	36	82	45	36.3	87.1	42.8	10.8	3.56	1.41	3.49	0.44	4.9	5.5	0.48	0.58	201	6.4	415	14.1
Al-269		<2	305		61		48	37	83	49									5.0	5.7	0.52	0.61	204	6.4	389	13.2
Al-270		49	319		64		51	36	90	52									5.0	5.4	0.48	0.56	195	6.3	402	13.3
Al-284		<2	304		61		48	36	84	47									5.0	5.6	0.51	0.59	199	6.3	391	13.4
Al-285		<2	306		62		48	34	82	46									4.9	5.7	0.52	0.55	201	6.4	389	13.4
Al-75		<2	307		62		48	38	86	43									5.0	5.7	0.52	0.61	204	6.4	394	13.9
Al-89	4.13	3	309	7.27	62	4.12	49	39	85	44	40.4	87.1	45.7	10.7	3.72	1.49	3.56	0.49	5.0	5.6	0.48	0.63	204	6.3	421	13.4
Al-251		<2	307		61		49	40	90	48									5.0	5.9	0.49	0.66	205	6.3	418	13.4
Al-252		<2	311		62		48	39	89	52									5.0	5.8	0.50	0.63	201	6.5	402	13.3
Al-183		2	310		62		48	33	85	47									5.0	5.6	0.52	0.53	201	6.5	389	13.5
Al-292		<2	334		63		42	39	94	53									5.3	5.5	0.48	0.62	198	8.0	415	12.7
Al-81		2	312		66		62	46	108	61									4.7	5.2	0.38	0.70	186	5.0	491	12.9
Al-286		<2	387		75		56	51	115	65									5.2	5.4	0.41	0.68	186	6.9	450	17.6
Al-82		<2	307		62		49	36	86	46									5.0	5.5	0.48	0.58	201	6.3	415	23.7
Al-182		<2	310		65		66	48	116	66									4.8	5.5	0.38	0.74	188	4.7	488	23.8
Al-214		<2	309		65		60												4.8		0.49		192	5.2	387	24.0
Al-279		<2	318		66		61	43	105	64									4.8	5.4	0.47	0.65	196	5.2	418	22.0
Al-136		<2	316		64		63	44	109	63									4.9	5.7	0.50	0.69	200	5.0	399	21.7
Al-280		2	320		66		61	44	108	60									4.8	5.6	0.38	0.67	195	5.2	515	21.8
Al-218		<2	321		66		61	45	108	63									4.9	5.6	0.39	0.68	190	5.3	482	21.3
Al-188		2	312		56		58	39	81	50									5.6	5.9	0.48	0.70	219	5.4	455	16.8
Al-281		2	312		57		57	39	79	51									5.5	5.9	0.49	0.68	221	5.5	451	17.1
Al-189		2	322		59		58	43	85	53									5.5	5.7	0.51	0.73	203	5.6	398	16.7
Al-72	3.99	<2	316	6.84	59	3.91	45	38	86	46	39.9	88.9	51.0	11.2	3.69	1.58	2.96	0.39	5.4	5.7	0.46	0.64	210	7.0	458	13.1

	Th inaa	Pb xrf	Zr xrf	Hf inaa	Nb xrf	Ta inaa	Y xrf	La xrf	Ce xrf	Nd xrf	La inaa	Ce inaa	Nd inaa	Sm inaa	Eu inaa	Tb inaa	Yb inaa	Lu inaa	Zr Nb	Ba Nb	Rb Nb	La Nb	K Nb	Zr Y	K Rb	P Zr
Al-283		<2	316		58		46	41	88	54									5.4	6.5	0.53	0.71	218	6.9	407	13.0
Al-74		2	313		59		46	38	87	47									5.3	6.3	0.51	0.64	207	6.8	407	12.7
Al-257		<2	277		58		45	37	74	45									4.8	5.9	0.41	0.64	202	6.2	488	12.4
Al-239		<2	285		59		51	37	85	50									4.8	6.0	0.34	0.63	197	5.6	581	15.6
Al-247		<2	298		61		52	38	83	50									4.9	5.5	0.39	0.62	196	5.7	498	15.1
Al-117		<2	296		60		51	33	78	44									4.9	5.5	0.43	0.55	199	5.8	460	14.7
Al-118	3.82	2	281	6.25	59	3.92	50	34	77	42	35.1	80.5	45.4	11.1	3.73	1.66	3.66	0.49	4.8	5.3	0.44	0.58	191	5.6	434	15.8
Al-132	3.26	<2	242	5.35	52	3.47	43	32	76	46	33.9	78.2	39.7	9.80	3.38	1.70	3.35	0.41	4.7	6.1	0.52	0.62	211	5.6	406	17.9
Al-125		<2	242		47		35	27	57	32									5.1	5.8	0.38	0.57	207	6.9	540	12.3
Al-265		<2	251		50		36	31	66	32									5.0	6.5	0.56	0.62	221	7.0	394	10.8
Al-266		<2	247		49		36	32	60	31									5.0	6.6	0.61	0.65	227	6.9	371	10.4
Al-246		<2	244		47		37	31	67	34									5.2	7.2	0.55	0.66	224	6.6	405	11.6
Mugearite (intermediate Zr/Nb)																										
Al-221		<2	333		66		52	42	96	61									5.0	5.9	0.52	0.64	208	6.4	403	14.4
Al-222		<2	340		67		53	43	98	55									5.1	5.9	0.52	0.64	206	6.4	394	15.3
Al-219		2	342		68		53	45	97	58									5.0	5.8	0.53	0.66	206	6.5	390	15.2
Al-220		2	344		68		54	44	93	57									5.1	5.9	0.53	0.65	210	6.4	397	15.2
Al-193		2	347		69		54	43	93	55									5.0	5.8	0.52	0.62	205	6.4	392	15.5
Al-223		<2	351		70		55	45	95	58									5.0	5.8	0.53	0.64	206	6.4	390	15.7
Al-85		2	361		71		57	43	101	55									5.1	5.6	0.54	0.61	210	6.3	393	16.1
Al-194		3	381		75		59	44	111	62									5.1	5.9	0.52	0.59	213	6.5	409	14.8
Al-192		<2	387		76		58	46	113	62									5.1	5.9	0.53	0.61	212	6.7	403	14.7
Al-50		4	365		78		65	50	113	65									4.7	5.2	0.46	0.64	189	5.6	410	17.5
Al-101	4.85	2	367	7.59	78	4.82	66	48	111	62	49.9	112	57.8	14.3	4.69	2.03	4.68	0.59	4.7	5.2	0.44	0.62	188	5.6	432	17.2
Al-178		2	370		78		68	53	116	64									4.7	5.5	0.41	0.68	186	5.4	454	17.6
Al-51		3	371		79		65	49	116	64									4.7	5.3	0.46	0.62	192	5.7	422	16.7
Al-166	4.89	2	373	8.39	79	4.73	65	49	116	66	51.5	114	63.4	14.9	4.72	2.08	4.79	0.62	4.7	5.2	0.43	0.62	184	5.7	427	16.8
Al-276		<2	374		79		66	48	116	64									4.7	5.3	0.42	0.61	184	5.7	440	16.9
Al-191		<2	369		78		63	50	114	69									4.7	5.1	0.46	0.64	187	5.9	406	16.3
Al-90		2	354		70		54	43	100	54									5.1	5.5	0.54	0.61	209	6.6	384	13.8
Al-291		2	394		75		49	48	98	59									5.3	5.5	0.49	0.64	201	8.0	408	14.0
Al-38		2	392		75		53	58	99	55									5.2	5.5	0.52	0.77	190	7.4	366	14.1
Al-287		2	410		77		55	47	107	60									5.3	5.6	0.60	0.61	190	7.5	318	14.6
Al-296		<2	367		70		60	50	96	57									5.2	6.0	0.54	0.71	212	6.1	391	16.4
Al-143	4.36	2	351	7.24	66	3.78	52	41	94	49	42.5	91.2	48.6	11.4	3.74	1.68	3.43	0.43	5.3	5.6	0.48	0.62	200	6.8	412	8.6
Al-145	6.65	4	470	9.33	80	4.83	93	69	110	81	71.4	109	83.5	18.5	4.63	2.63	6.84	0.90	5.9	4.0	0.48	0.86	136	5.1	286	6.2
Al-49		<2	431		91		46	54	111	52									4.7	6.3	0.58	0.59	206	9.4	354	11.2
Al-78		2	357		73		62	44	102	56									4.9	6.4	0.42	0.60	184	5.8	434	10.9
Al-255		2	419		79		38	50	103	48									5.3	6.1	0.58	0.63	216	11.0	372	7.0
Al-254		2	425		83		42	49	101	50									5.1	5.9	0.48	0.59	204	10.1	423	8.0
Al-142		<2	408		83		66	53	115	64									4.9	5.3	0.42	0.64	198	6.2	470	14.3
Al-13	5.39	5	431	9.02	87	5.12	68	56	114	66	54.6	123	64.6	14.9	4.65	2.10	5.02	0.71	5.0	5.7	0.47	0.64	194	6.3	411	13.3
Al-55		<2	426		80		56	49	117	64									5.3	6.4	0.53	0.61	218	7.6	415	11.9
Al-80		2	363		72		42	43	90	45									5.0	6.5	0.58	0.60	212	8.6	364	9.4
Al-275		2	431		86		70	57	121	69									5.0	5.5	0.47	0.66	205	6.2	440	12.8

	Th inaa	Pb xrf	Zr xrf	Hf inaa	Nb xrf	Ta inaa	Y xrf	La xrf	Ce xrf	Nd xrf	La inaa	Ce inaa	Nd inaa	Sm inaa	Eu inaa	Tb inaa	Yb inaa	Lu inaa	Zr Nb	Ba Nb	Rb Nb	La Nb	K Nb	Zr Y	K Rb	P Zr
Al-171	4.58	<2	364	7.87	69	4.27	64	42	101	56	44.0	104	56.8	13.3	4.62	1.84	4.65	0.59	5.3	5.4	0.46	0.61	200	5.7	431	15.6
Al-84		2	378		71		75	47	108	64									5.3	5.5	0.48	0.66	213	5.0	444	13.9
Al-267		2	417		85		67	54	116	66									4.9	5.8	0.49	0.64	203	6.2	411	11.7
Al-112	4.89	2	413	8.76	81	5.02	65	46	106	58	50.3	111	61.7	13.7	4.95	2.00	5.16	0.69	5.1	6.2	0.42	0.57	184	6.4	439	8.1
Al-165	5.10	4	433	9.20	85	5.26	69	53	120	63	54.4	119	62.6	14.4	5.08	2.21	5.30	0.69	5.1	6.2	0.46	0.62	194	6.3	424	8.2
Al-113		3	439		92		63	50	121	64									4.8	5.6	0.50	0.54	204	7.0	408	10.1
Al-244		3	339		63		40	37	82	39									5.4	9.4	0.59	0.59	228	8.5	388	6.4
Benmoreite (intermediate Zr/Nb)																										
Al-185		4	439		89		63	53	118	66									4.9	5.5	0.51	0.60	205	7.0	406	9.7
Al-184		3	456		91		67	58	117	63									5.0	5.6	0.48	0.64	210	6.8	434	7.7
Al-130	6.30	2	468	9.63	94	5.73	64	53	121	63	55.5	124	60.6	14.0	4.85	2.04	5.09	0.68	5.0	5.9	0.49	0.56	207	7.3	422	7.8
Al-168		3	453		87		60	49	114	59									5.2	5.8	0.55	0.56	215	7.6	389	8.8
Al-57		4	452		86		60	47	112	60									5.3	5.9	0.57	0.55	219	7.5	385	9.7
Al-122	5.74	4	460	9.26	94	5.34	64	52	120	65	54.4	120	59.8	13.9	4.76	2.06	4.93	0.64	4.9	5.7	0.52	0.55	208	7.2	398	8.1
Al-186a		3	444		80		66	53	122	69									5.6	6.1	0.54	0.66	230	6.7	429	9.2
Al-186		3	465		82		67	55	119	68									5.7	5.7	0.55	0.67	239	6.9	435	8.8
Al-199		3	474		95		71	54	120	65									5.0	5.5	0.51	0.57	209	6.7	413	7.1
Al-47		3	475		95		67	52	117	62									5.0	5.6	0.51	0.55	206	7.1	408	7.0
Al-272		3	477		95		67	55	119	66									5.0	5.7	0.52	0.58	211	7.1	410	6.9
Al-52		2	429		79		66	45	112	63									5.4	5.7	0.52	0.57	201	6.5	387	9.0
Al-54	5.55	2	445	9.86	81	5.17	68	48	113	61	49.1	116	61.0	13.8	4.74	1.94	5.19	0.70	5.5	5.6	0.53	0.59	212	6.5	400	7.7
Al-260		6	575		111		62	72	149	77									5.2	5.7	0.44	0.65	215	9.3	488	5.6
Al-71		4	540		98		63	49	115	61									5.5	5.9	0.57	0.50	223	8.6	390	5.6
Al-176	6.56	2	530	11.3	97	5.77	63	50	117	61	56.4	118	62.7	13.6	4.30	2.04	4.84	0.66	5.5	6.0	0.58	0.52	219	8.4	379	6.1
Al-48		3	524		100		70	57	123	63									5.2	5.8	0.52	0.57	216	7.5	415	5.1
Al-140	6.42	4	511	10.8	99	5.89	67	53	121	64	55.0	122	59.2	13.9	4.40	1.80	5.08	0.69	5.2	5.5	0.52	0.54	213	7.6	413	5.6
Al-92		3	524		97		63	53	118	59									5.4	6.1	0.59	0.55	227	8.3	386	4.7
Al-137	6.80	4	586	11.8	100	5.74	73	54	125	66	51.9	118	65.1	14.4	4.92	2.16	5.83	0.76	5.9	5.7	0.51	0.54	213	8.0	418	3.4
Al-73		3	610		102		73	55	126	64									6.0	5.9	0.55	0.54	214	8.4	390	2.9
Al-245		4	581		101		61	53	121	59									5.8	5.8	0.67	0.52	241	9.5	358	4.4
Dark Slope Crater																										
Al-4	4.67	3	320	6.92	64	3.95	43	44	90	51	43.4	92.3	51.7	10.7	3.76	1.60	2.95	0.38	5.0	7.0	0.53	0.69	210	7.4	396	13.0
Al-205		2	323		63		40	39	86	46									5.1	7.9	0.54	0.62	215	8.1	398	11.3
Al-202		<2	328		64		40	40	87	51									5.1	6.4	0.45	0.63	201	8.2	444	10.4
Al-150	4.78	2	330	7.03	65	4.34	38	40	87	47	41.0	88.9	45.8	9.67	3.35	1.34	2.67	0.33	5.1	6.5	0.55	0.62	206	8.7	371	10.6
Al-153		2	336		65		41	43	92	52									5.2	6.7	0.57	0.66	213	8.2	375	11.3
Al-154	4.82	2	318	6.99	63	4.23	40	39	88	46	39.6	91.2	46.9	10.2	3.37	1.29	2.75	0.34	5.0	6.4	0.52	0.62	207	8.0	395	11.5
Al-155	4.86	2	321	7.00	64	3.87	49	45	99	52	45.5	100	52.2	11.7	3.68	1.41	3.45	0.43	5.0	6.2	0.42	0.70	205	6.6	486	10.7
Al-156	4.79	2	333	6.90	66	4.10	51	45	97	53	46.6	99.5	51.5	12.1	3.88	1.68	3.57	0.46	5.0	5.7	0.41	0.68	208	6.5	507	11.0
Al-31		2	359		73		41	44	88	44									4.9	6.0	0.51	0.60	212	8.8	417	12.0
Al-2	5.44	3	364	7.83	72	4.64	37	43	96	50	45.0	97.2	48.2	10.3	3.30	1.57	2.58	0.34	5.1	6.4	0.57	0.60	210	9.8	368	10.9
Al-203		3	425		83		43	48	110	54									5.1	6.6	0.57	0.58	205	9.9	362	10.0
Al-204		4	423		82		42	49	111	60									5.2	6.5	0.57	0.60	208	10.1	362	10.0
Al-6	8.93	<2	558	11.6	110	7.35	46	73	133	67	73.2	158	67.0	14.3	4.75	1.90	3.23	0.38	5.1	6.5	0.60	0.66	203	12.1	338	9.8
Al-108		3	328		62		41	35	85	40									5.3	5.5	0.42	0.56	194	8.0	463	11.4

	Th inaa	Pb xrf	Zr xrf	Hf inaa	Nb xrf	Ta inaa	Y xrf	La xrf	Ce xrf	Nd xrf	La inaa	Ce inaa	Nd inaa	Sm inaa	Eu inaa	Tb inaa	Yb inaa	Lu inaa	Zr Nb	Ba Nb	Rb Nb	La Nb	K Nb	Zr Y	K Rb	P Zr
Al-289		<2	320		60		39	32	78	40									5.3	6.3	0.57	0.53	212	8.2	374	12.1
Al-298		2	461		85		30	48	97	41									5.4	6.2	0.59	0.56	202	15.4	344	5.3
Al-264		3	463		86		31	52	95	45									5.4	6.0	0.62	0.60	208	14.9	337	5.0
Broken T																										
Al-88		3	394		72		62	48	107	59									5.5	6.7	0.51	0.67	256	6.4	498	11.4
Al-86		3	404		72		61	42	96	57									5.6	6.6	0.56	0.58	270	6.6	486	11.0
Al-87	5.19	3	385	8.38	72	4.59	65	45	103	61	47.0	106	57.8	14.5	4.96	2.08	4.69	0.61	5.3	6.7	0.51	0.63	254	5.9	494	11.1
Al-217		3	409		72		62												5.7		0.56		271	6.6	488	10.8
Al-77	5.52	3	441	9.05	76	4.72	62	46	109	59	47.8	107	62.7	14.2	4.43	1.95	4.89	0.62	5.8	6.7	0.58	0.61	304	7.1	524	9.7
Al-76	6.45	4	516	10.5	81	4.94	57	45	102	51	49.7	106	57.3	12.5	3.61	1.83	4.92	0.69	6.4	7.1	0.63	0.56	374	9.1	594	5.7
Al-216		4	561		91		71	64	132	67									6.2	4.9	0.59	0.70	264	7.9	444	5.4
	Trachyte																									
Al-59		6	694		121		71	67	139	66									5.7	9.3	0.40	0.55	225	9.8	556	
Al-83		6	860		134		73	71	155	73									6.4	6.0	0.51	0.53	217	11.8	422	
Al-111	6.40	3	398	7.88	68	4.59	45	32	68	33	40.3	83.2	37.2	8.10	3.51	1.32	3.72	0.51	5.9	19.2	0.93	0.47	544	8.8	588	
Al-190		5	758		113		79												6.7		0.73		320	9.6	441	
Al-119		5	865		136		73	69	143	62									6.4	7.8	0.79	0.51	267	11.8	340	
Al-126	14.0	9	841	16.8	133	8.26	60	63	129	51	68.5	132	50.5	10.7	3.15	1.77	5.56	0.74	6.3	7.4	0.78	0.47	276	14.0	354	
Al-164		5	495		92		50	42	81	43									5.4	16.8	0.68	0.46	413	9.9	603	
Al-109	7.61	3	532	10.5	98	5.83	56	41	87	45	45.3	94.5	46.7	10.2	3.17	1.64	4.96	0.69	5.4	11.8	0.70	0.42	424	9.5	602	
Al-163		4	555		101		63	48	107	56									5.5	9.3	0.69	0.48	399	8.8	576	
Al-70		3	782		112		64	57	120	58									7.0	3.3	0.75	0.51	361	12.2	481	
Al-169		5	818		135		85	71	156	70									6.1	5.8	0.56	0.53	228	9.6	405	
Al-116		5	940		119		72	53	110	53									7.9	11.0	0.68	0.45	313	13.1	460	
Al-294		7	666		119		61												5.6		0.67		358	10.9	532	
Al-79	9.07	6	733	13.7	123	6.70	79	71	145	73	71.8	136	68.9	13.9	3.04	2.08	6.20	0.82	6.0	5.8	0.64	0.58	315	9.3	491	
Al-282		7	769		126		75												6.1		0.67		306	10.3	460	
Al-103	9.38	5	756	14.2	121	6.91	57	45	100	50	47.2	93.6	45.5	9.13	2.32	1.40	5.30	0.78	6.2	5.3	0.67	0.37	339	13.3	506	
Al-104		4	703		124		27	44	96	50									5.7	1.6	0.65	0.35	349	26.0	542	
Al-105		6	931		123		49	34	79	41									7.6	6.9	0.64	0.28	266	19.0	414	
Al-115		8	1204		139		84	71	149	69									8.7	4.6	0.70	0.51	298	14.3	427	
Al-175	10.7	6	823	16.3	139	8.08	45	50	112	58	56.0	115	54.1	11.3	2.80	1.66	5.20	0.79	5.9	6.6	0.68	0.36	257	18.3	380	
Al-99		4	895		138		43	73	122	89									6.5	2.1	0.67	0.53	297	20.8	440	
Al-41	10.3	5	1062	19.3	116	6.77	73	57	117	55	61.2	127	61.1	12.7	2.68	2.00	6.15	0.84	9.2	8.7	0.76	0.49	335	14.5	441	
Al-228		5	1096		117		59												9.4		0.80		344	18.6	428	
Al-91	14.3	7	1248	22.3	184	10.4	84	70	177	73	73.2	165	63.0	12.9	2.15	2.18	6.99	1.02	6.8	1.2	0.59	0.38	230	14.9	388	
Al-17	13.1	7	998	20.5	150	8.79	41	40	82	52	40.6	82.9	52.6	11.0	1.61	1.49	4.74	0.76	6.7	1.3	0.65	0.27	273	24.3	418	
Al-268		8	937		139		41												6.7		0.66		254	22.9	383	
Al-66		10	954		155		69	74	140	68									6.2	3.0	0.77	0.48	274	13.8	353	
Al-129		10	1284		186		95	94	190	82									6.9	0.2	0.76	0.51	227	13.5	297	
Al-96	11.1	7	954	20.1	134	8.06	85	64	132	70	71.9	139	68.6	15.6	3.20	2.55	7.25	1.00	7.1	3.9	0.65	0.48	280	11.2	431	
Al-67	14.3	8	940	17.9	151	9.12	62	53	119	53	61.6	115	51.6	10.3	1.98	1.72	5.91	0.89	6.2	3.7	0.77	0.35	281	15.2	363	
Al-241		6	948		167		79												5.7		0.77		248	12.0	320	
Al-242		10	1079		184		37												5.9		0.74		225	29.2	304	
Al-243		10	1048		181		102												5.8		0.73		226	10.3	310	
Al-95		8	1003		117		91	62	142	69									8.6	7.6	0.70	0.53	293	11.0	418	

	Th inaa	Pb xrf	Zr xrf	Hf inaa	Nb xrf	Ta inaa	Y xrf	La xrf	Ce xrf	Nd xrf	La inaa	Ce inaa	Nd inaa	Sm inaa	Eu inaa	Tb inaa	Yb inaa	Lu inaa	Zr Nb	Ba Nb	Rb Nb	La Nb	K Nb	Zr Y	K Rb	P Zr
Al-147		9	1025		183		38	28	97	39									5.6	0.4	0.72	0.15	230	27.0	318	
Al-248		9	1177		207		83	94	212	83									5.7	0.1	0.69	0.45	201	14.2	291	
Al-94		10	1266		177		113	78	177	88									7.2	0.4	0.71	0.44	221	11.2	311	
Al-93		12	1279		181		125												7.1		0.71		216	10.2	303	
Al-261		12	1285		184		128												7.0		0.72		210	10.0	293	
Al-177	19.4	11	968	23.8	212	13.6	137	82	181	86	91.9	189	81.0	19.1	1.21	3.59	11.9	1.56	4.6	0.1	0.76	0.39	182	7.1	240	
Al-131	20.6	14	1237	27.3	240	15.0	143	111	236	100	113	222	92.9	20.3	0.94	3.58	12.4	1.67	5.2	0.1	0.75	0.46	160	8.7	214	
	Pumice																									
Al-19		5	600		96		75	81	133	81									6.3	7.3	0.56	0.84	220	8.0	390	
Al-21		6	658		102		67	68	129	64									6.5	8.2	0.58	0.67	254	9.8	439	
Al-20		6	728		97		71	70	119	65									7.5	11.5	0.62	0.72	317	10.3	512	
Al-15	11.3	3	878	18.1	133	7.97	68	74	137	67	70.5	148	67.7	14.7	2.48	2.24	6.60	0.97	6.6	2.9	0.71	0.56	312	12.9	437	
Al-18		12	1292		212		133	155	211	136									6.1	0.2	0.64	0.73	211	9.7	332	
Al-135	13.7	8	1093	19.9	184	10.5	93	82	167	81	94.8	179	80.5	17.2	2.72	2.80	7.92	1.08	5.9	0.3	0.64	0.45	239	11.8	372	
Al-174	8.02	4	899	15.4	97	5.47	151	92	127	96	100	142	100	21.9	5.59	3.64	11.0	1.53	9.3	8.2	0.75	0.95	217	6.0	289	
Al-98		9	1375		165		111	86	180	89									8.3	0.7	0.70	0.52	277	12.4	397	
Al-114		8	1144		162		93	83	176	78									7.1	0.8	0.72	0.51	275	12.3	384	
Al-238		5	711		116		61												6.1		0.43		195	11.7	452	
Al-39		6	1032		137		62	66	140	59									7.5	7.1	0.78	0.48	312	16.6	400	
Al-42	25.1	14	1743	33.4	261	15.6	148	120	250	114	139	254	113	24.2	2.31	3.95	11.2	1.66	6.7	0.1	0.72	0.46	180	11.8	250	
Al-43		6	928		125		74	59	124	58									7.4	5.6	0.66	0.47	284	12.5	427	
Al-44	16.0	8	1187	23.3	183	12.1	88	74	152	69	85.9	165	77.5	15.7	2.24	2.44	6.51	0.94	6.5	0.6	0.63	0.40	218	13.5	346	
Al-45		<2	199		34		31	19	44	23									5.9	5.1	0.74	0.56	225	6.4	305	
Al-229		10	1062		172		101												6.2		0.69		234	10.5	338	
Al-293		14	1393		232		120												6.0		0.63		179	11.6	285	
Al-143	4.36	2	351	7.24	66	3.78	52	41	94	49	42.5	91.2	48.6	11.4	3.74	1.68	3.43	0.43	5.3	5.6	0.48	0.62	200	6.8	412	
Al-144	15.8	9	1470	25.2	177	10.2	106	97	197	96	107	209	97.9	20.7	2.49	3.23	9.06	1.21	8.3	0.5	0.65	0.55	249	13.9	384	
Al-145	6.65	4	470	9.33	80	4.83	93	69	110	81	71.4	109	83.5	18.5	4.63	2.63	6.84	0.90	5.9	4.0	0.48	0.86	136	5.1	286	
Al-146	11.9	6	1074	19.8	130	7.63	87	67	139	68	72.8	142	67.1	14.8	2.10	2.33	7.81	1.11	8.3	1.7	0.78	0.52	328	12.3	417	
Al-120	8.85	5	766	13.6	122	6.87	69	58	119	57	62.6	128	59.8	12.5	3.61	1.94	5.96	0.84	6.3	7.1	0.61	0.48	286	11.1	465	
Al-121	7.85	3	630	11.9	114	6.65	67	57	124	60	59.2	123	59.8	12.6	4.71	2.00	5.49	0.75	5.5	7.3	0.56	0.50	234	9.4	416	
Al-122	6.14	4	460	8.62	94	5.33	64	52	120	65	54.3	116	61.2	13.6	4.83	2.04	4.82	0.67	4.9	5.7	0.52	0.55	208	7.2	398	
Al-123	3.25	2	233	5.17	52	3.10	42	30	73	41	32.8	75.6	41.7	9.7	3.34	1.48	2.98	0.36	4.5	5.5	0.48	0.58	198	5.5	412	
Al-256		8	922		150		90												6.1		0.62		237	10.2	382	
Al-181		5	842		126		72	60	132	62									6.7	7.3	0.62	0.48	310	11.7	501	
	Boreholes																									
	GH1																									
GH1-1		<2	285		55		55												5.2		0.53		202	5.2	384	19.8
GH1-2		<2	269		53		49												5.1		0.49		193	5.5	393	17.2
GH1-3		<2	175		23		33												7.6		0.57		274	5.3	485	9.7
GH1-4		<2	171		23		33												7.4		0.57		271	5.2	479	10.0
GH1-5		2	169		22		32												7.7		0.64		291	5.3	457	10.3
	GH2																									
GH2-1		<2	249		42		39												5.9		0.71		261	6.4	365	7.7
GH2-2		<2	259		46		41												5.6		0.72		258	6.3	360	7.1
GH2-3		2	397		78		63												5.1		0.49		196	6.3	402	8.9

	Th inaa	Pb xrf	Zr xrf	Hf inaa	Nb xrf	Ta inaa	Y xrf	La xrf	Ce xrf	Nd xrf	La inaa	Ce inaa	Nd inaa	Sm inaa	Eu inaa	Tb inaa	Yb inaa	Lu inaa	Zr Nb	Ba Nb	Rb Nb	La Nb	K Nb	Zr Y	K Rb	P Zr
GH2-4		10	1238		173		85												7.2		0.83		247	14.6	299	
GH2-5		6	1038		141		71												7.4		0.79		263	14.6	334	
GH2-6		8	1040		140		72												7.4		0.83		277	14.4	334	
GH2-7		2	398		74		60												5.4		0.51		209	6.6	406	14.0
GH2-8		<2	390		72		60												5.4		0.50		206	6.5	413	14.4
GH2-9		3	459		81		59												5.7		0.56		214	7.8	386	10.2
GH2-10		2	487		86		60												5.7		0.53		208	8.1	388	9.1
GH2-11		3	530		90		64												5.9		0.56		213	8.3	384	6.8
GH2-12		<2	306		56		48												5.5		0.52		197	6.4	381	17.1
GH2-13		9	1004		139		113												7.2		0.77		275	8.9	357	
	GH3																									
GH3-1		<2	260		62		42												4.2		0.58		212	6.2	364	17.6
GH3-2		<2	261		63		42												4.1		0.57		211	6.2	369	17.4
GH3-3		<2	356		65		49												5.5		0.52		199	7.3	381	14.2
GH3-4		3	384		70		50												5.5		0.53		200	7.7	379	13.6
GH3-5		3	383		75		39												5.1		0.59		207	9.8	353	10.3
GH3-6		2	412		82		40												5.0		0.71		222	10.3	313	10.4
GH3-7		3	484		95		40												5.1		0.60		199	12.1	332	9.5
GH3-8		4	583		113		44												5.2		0.66		204	13.3	308	9.6
	GH4																									
GH4-1		5	627		112		68												5.6		0.51		208	9.2	408	3.9
GH4-2		5	755		122		69												6.2		0.56		217	10.9	389	1.7
GH4-3		2	225		35		34												6.4		0.46		228	6.6	498	8.3
GH4-4		2	318		58		42												5.5		0.55		216	7.6	392	12.9
GH4-5		2	337		64		42												5.3		0.56		213	8.0	378	12.9
GH4-6		<2	307		57		41												5.4		0.58		229	7.5	395	14.1
GH4-7		3	318		59		42												5.4		0.58		221	7.6	383	13.2
GH4-8		<2	287		53		42												5.4		0.58		230	6.8	394	14.1
	GH5																									
GH5-1		2	270		54		52												5.0		0.50		198	5.2	397	18.9
GH5-2		<2	267		54		52												4.9		0.52		197	5.1	379	19.3
GH5-3		3	271		53		54												5.1		0.53		207	5.0	391	19.6
GH5-4		3	459		85		68												5.4		0.47		197	6.8	419	10.3
GH5-5		2	459		85		69												5.4		0.47		195	6.7	415	10.3
GH5-6		6	696		119		57												5.8		0.55		220	12.2	396	2.4
GH5-7		2	211		37		30												5.7		0.59		238	7.0	400	10.8
GH5-8		<2	216		38		31												5.7		0.63		238	7.0	377	10.5
GH5-9		2	497		76		53												6.5		0.61		383	9.4	633	1.6
	GH6																									
GH6-1		9	1341		148		75												9.1		0.70		271	17.9	389	0.1
GH6-2		<2	293		41		50												7.1		0.54		263	5.9	491	14.7
GH6-3		<2	242		35		46												6.9		0.51		268	5.3	521	13.5
GH6-4		<2	245		36		40												6.8		0.53		265	6.1	502	11.8
GH6-5		2	230		37		34												6.2		0.51		236	6.8	459	10.6
	LDTGH																									
LDT-1		<2	285		43		49												6.6		0.70		255	5.8	365	14.9
LDT-2		5	710		84		79												8.5		0.57		240	9.0	420	1.6

		Age Ma	SiO2	87Sr 86Sr	2σ	Rb ppm	Sr ppm	87Rb 86Sr	87Sr 86Sr i	ESr	143Nd 144Nd	2σ	ENd	206Pb 204Pb	207Pb 204Pb	208Pb 204Pb	d18O WR	d18O fsp
Gabbro																		
Al-7		0		0.704107	10	1	130	0.0222	0.704107	-8.4	0.513023	40		19.461	15.660	39.186		
Al-8		0		0.702983	9	1	103	0.0281	0.702983	-24.4	0.513104	10	9.09	19.126	15.621	38.745	7.02	
Al-9		0				1	197							19.557	15.625	39.141		
low Zr/Nb																		
Al-60	H	0	47.94	0.703130	14	27	551	0.1417	0.703130	-22.3	0.512971	11	6.50				7.07	
Al-212	H	0	47.34	0.702921	11	33	574	0.1663	0.702921	-25.2	0.512972	9	6.52					
Al-157	H	0	47.69	0.702929	9	32	533	0.1736	0.702929	-25.1	0.512969	12	6.46	19.630	15.622	39.140	6.79	
Al-61	H		47.45														6.53	6.11
high Zr/Nb																		
Al-128	B	0	49.09	0.702814	11	20	418	0.1384	0.702814	-26.8	0.513060	8	8.23	19.451	15.599	39.014	7.83	5.87
Al-107	B	0	48.55	0.702811	10	18	436	0.1194	0.702811	-26.8	0.513028	12	7.61	19.566	15.605	39.106	6.12	
Al-40	B	0	47.55	0.702892	10	19	539	0.1019	0.702892	-25.7	0.512992	9	6.91					
Al-64	B	0	50.58	0.702766	12	28	414	0.1956	0.702766	-27.4	0.513066	8	8.35	19.389	15.626	39.027	6.26	
Al-172	B	0	49.64	0.702912	9	20	404	0.1432	0.702912	-25.4	0.513006	7	7.18	19.421	15.616	39.017	6.81	
Al-127	B		48.44														6.99	6.21
Al-37	B		47.59														5.69	3.42
intermed. Zr/Nb																		
Al-100	B	0	47.53	0.702831	15	11	385	0.0826	0.702831	-26.5	0.513018	10	7.41	19.482	15.607	39.062	6.37	6.79
Al-102	B		48.00														6.69	6.70
Al-158	B		47.47														6.97	5.48
Al-28	B	0	47.28	0.702942	11	23	469	0.1418	0.702942	-24.9	0.513008	7	7.22	19.740	15.685	39.370	6.86	
Al-62	B		47.38														5.54	9.96
Al-132	B	0	48.53	0.702790	10	27	491	0.1590	0.702790	-27.1	0.513038	9	7.80	19.580	15.620	39.160	7.41	5.92
Al-123	B	0	48.87	0.702941	9	25	492	0.1470	0.702941	-25.0	0.513040	7	7.84	19.446	15.623	39.008	7.41	
Al-14	B	0	49.27	0.703035	11	13	435	0.0864	0.703035	-23.6	0.513036	7	7.76				7.22	
Al-274	B	0	49.40	0.703263	10	25	435	0.1662	0.703263	-20.4	0.513011	8	7.28					
Al-125	B		50.49														6.68	6.53
Al-159b	B	0	48.09	0.702766	9	27	477	0.1637	0.702766	-27.4	0.513013	9	7.32	19.445	15.594	39.000	6.76	
Al-24	H	0	49.82	0.702845	14	31	497	0.1804	0.702845	-26.3	0.512978	9	6.63				5.03	
Al-75	H		49.41														5.27	5.47
Al-89	H		49.76														5.80	6.44
Al-72	H	0	48.54	0.702951	9	27	645	0.1211	0.702951	-24.8	0.512960	12	6.28	19.658	15.641	39.290	7.21	
Al-182	H	0	48.28	0.702791	9	25	539	0.1341	0.702791	-27.1	0.513015	7	7.35					
Al-139	B	0	51.01	0.702861	11	37	470	0.2277	0.702861	-26.1	0.513015	22	7.35	19.517	15.609	39.060	6.18	
Al-82	H		48.48														6.46	6.37
Al-143	M	0	51.90	0.702945	10	32	571	0.1621	0.702945	-24.9	0.513004	7	7.14	19.564	15.617	39.160	7.84	
Al-165	M	0	55.29	0.702844	9	39	446	0.2529	0.702844	-26.3	0.513016	11	7.37	19.516	15.603	39.054	6.48	
Al-166	M	0	50.88	0.703011	11	34	487	0.2019	0.703011	-24.0	0.513028	7	7.61	19.610	15.629	39.178	5.66	
Al-178	M		50.78														6.76	6.89
Al-80	M		53.06														6.37	5.80
Al-122	Be	0	55.59	0.702836	10	49	436	0.3250	0.702836	-26.5	0.513024	7	7.53	19.587	15.605	39.107	6.80	
Al-130	Be	0	55.31	0.702838	9	46	433	0.3072	0.702838	-26.4	0.513021	8	7.47	19.602	15.605	39.133	6.08	

		Age Ma	SiO2	87Sr 86Sr	2σ	Rb ppm	Sr ppm	87Rb 86Sr	87Sr 66Sri	ESr	143Nd 144Nd	2σ	ENd	206Pb 204Pb	207Pb 204Pb	208Pb 204Pb	d18O WR	d18O fsp
Al-176	Be	0	57.30	0.702861	10	56	431	0.3758	0.702861	-26.1	0.513006	14	7.18	19.605	15.625	39.202	5.60	
Al-71	Be		57.71														5.69	5.94
Al-137	Be	0	60.06	0.702798	10	51	388	0.3801	0.702798	-27.0	0.512982	7	6.71	19.496	15.639	39.141	7.05	
Dark Slope																		
Al-2	H	0	48.51	0.703106	10	41	782	0.1516	0.703106	-22.6	0.512967	8	6.42	19.863	15.665	39.496	5.65	
Al-6	M	0	52.12	0.703130	11	66	1105	0.1727	0.703130	-22.3	0.512918	12	5.46	19.840	15.667	39.497	6.02	
Al-154	H	0	48.33	0.703024	10	33	719	0.1327	0.703024	-23.8	0.512974	10	6.55	19.850	15.649	39.443	5.67	
Al-298	M	0	52.26	0.703107	9	50	864	0.1674	0.703107	-22.6	0.512951	10	6.11					
Broken Tooth																		
Al-76	Be	0	60.05	0.702868	10	51	203	0.7266	0.702868	-26.0	0.513091	12	8.84	19.593	15.588	39.085	7.39	5.88
Al-87	M	0	54.75	0.702859	10	37	418	0.2560	0.702859	-26.1	0.513077	11	8.56	19.599	15.605	39.128	7.48	6.43
Al-88	M		54.67														6.80	7.23
Al-187e	Sy	0	61.74	0.702860	10	30.3	266.6	0.3287	0.702860	-26.1	0.513020	9	7.45				5.73	
Malic Inclusions																		
Al-97	Be	0	55.15	0.702983	10	65	565	0.3327	0.702983	-24.4	0.512987	13	6.81	19.624	15.622	39.209	6.85	
Al-234b	M	0	51.24	0.702797	10	21	407	0.1492	0.702797	-27.0	0.513017	8	7.39					
Trachyte																		
Al-111	T	1.0	63.91	0.705038	9	63	184	0.9904	0.705024	4.6	0.513046	13	7.96	19.665	15.668	39.332	6.41	6.22
Al-79	T	1.0	66.00	0.703605	10	79	29	7.879	0.703493	-17.1	0.513024	10	7.53	19.669	15.615	39.232	7.73	7.80
Al-41	T	1.0	66.93	0.703651	9	88	15	16.97	0.703410	-18.3	0.513008	8	7.22	19.587	15.606	39.031	5.47	
Al-175	T	1.0	66.84	0.703117	8	94	24	11.33	0.702956	-24.7	0.513026	9	7.57	19.669	15.624	39.194	5.76	
Al-91	T	1.0	67.39	0.707188	11	109	7	45.05	0.706548	26.2	0.512992	6	6.91	19.746	15.644	39.339	7.56	
Al-109	T	1.0	65.35	0.705950	10	69	24	8.317	0.705832	16.1	0.513007	9	7.20	19.568	15.602	39.122	8.11	
Al-67	T	1.0	67.28	0.703715	10	117	7	48.34	0.703029	-23.7	0.512999	10	7.04	19.693	15.636	39.264	6.57	
Al-103	T	1.0	66.58	0.704755	11	81	4	58.57	0.703923	-11.0	0.513055	11	8.13	19.503	15.633	39.132	6.91	
Al-96	T	1.0	68.82	0.704053	9	87	10	25.16	0.703696	-14.2	0.513026	8	7.57	19.626	15.630	39.236	6.30	
Al-94	R	1.0	72.53	0.706306	14	126	1	364.5	0.701130	-50.6	0.513027	8	7.59					
Al-177	R	1.0	73.75	0.708917	11	161	1	465.9	0.702301	-34.0	0.513026	7	7.57	19.516	15.622	39.116	6.52	
Al-70	T		65.60														6.37	7.18
Al-104	T		66.23														6.58	6.23
Al-115	T		66.70														6.51	
Al-126	T		65.40														6.20	6.30
Pumice																		
Al-120	T	1.0	63.59	0.703255	9	75	114	1.903	0.703228	-20.9	0.513015	8	7.35	19.617	15.609	39.125	9.23	
Al-121	T	1.0	60.99	0.702898	10	64	270	0.6855	0.702888	-25.7	0.513025	18	7.55	19.569	15.608	39.118	6.41	
Al-44	T	1.0	68.72	0.706368	15	115	16	20.79	0.706073	19.5	0.513027	9	7.59	19.713	15.666	39.368	15.6	
Al-43	T	1.0	66.95	0.703498	10	83	67	3.583	0.703447	-17.8	0.513000	9	7.06					
Al-135	T		66.56			118	20										13.9	
Al-42	R	1.0	72.07	0.707603	10	188	7	77.71	0.706500	25.6	0.512998	8	7.02	19.687	15.650	39.330	16.8	

		Age Ma	SiO2	87Sr 86Sr	2σ	Rb ppm	Sr ppm	87Rb 86Sr	87Sr 86Sri	ESr	143Nd 144Nd	2σ	ENd	206Pb 204Pb	207Pb 204Pb	208Pb 204Pb	d18O WR	d18O fsp
Al-41	WR			0.703651	9													
trachyte	Fsp			0.702896	9													
	L			0.708192	10													
	LR			0.703016	30													
Al-44	WR			0.706368	15													
pumice	Fsp			0.704317	11													
	L			0.706533	42													
	LR			0.705278	20													
Al-67	WR			0.703715	10													
trachyte	Fsp			0.703029	13													
	L			0.706759	22													
	LR			0.703386	13													
Al-96	WR			0.704053	9													
trachyte	Fsp			0.703236	15													
	L			0.706357	15													
	LR			0.703273	10													
Al-103	WR			0.704755	11													
trachyte	Fsp			0.703797	10													
	L			0.708649	15													
	LR			0.703389	14													
Granite																		
Al-213c	WR	0.92	73.90	0.706920	11	152.7	4.96	89.07	0.705756	15.0							5.80	
	Fel	0.92		0.709250	10	109.9	1.18	269.5	0.705729	14.6								
	Maf	0.92		0.705850	10	27.7	8.51	9.403	0.705727	14.6								
Al-213d	WR	1.22	73.83	0.707210	10	86.7	3.80	66.00	0.706067	19.4	0.512998	8	7.02					
	Fel	1.22		0.707560	16	53.2	1.75	87.87	0.706038	19.0								
	Maf	1.22		0.706140	10	14.4	7.41	5.610	0.706043	19.1								
Boreholes																		
GH1-3	7.6	0	49.43	0.702726	9	13	405	0.0928	0.702726	-28.0	0.513045	9	7.94					
GH2-12	5.5	0	49.92	0.702819	11	29	507	0.1654	0.702819	-26.7	0.513003	19	7.12					
GH4-3	6.4	0	49.19	0.702783	11	16	459	0.1008	0.702783	-27.2	0.513009	9	7.24					
GH5-7	5.7	0	49.15	0.702830	11	22	505	0.1260	0.702830	-26.5	0.512971	8	6.50					
GH6-3	8.9	0	48.46	0.702763	11	18	405	0.1285	0.702763	-27.5	0.513042	9	7.88					
LDT-1	6.6	0	49.98	0.702787	10	30	451	0.1924	0.702787	-27.1	0.513047	11	7.98					
Guano				0.709071	10	4	1555											